

L'Université Lille 1 Sciences et Technologies

Laboratoire d'Océanologie et de Géosciences (UMR LOG 8187)

**L'Ecole Doctorale " Sciences de la Matière, du Rayonnement et de
l'Environnement " (EDSMRE-104)**

Characterisation of the coupling between oceanic turbulence and the variability of coastal waters optical properties, using in situ measurements and satellite data

By

Renosh PANNIMPULLATH REMANAN

A thesis presented for the degree of Doctor of Philosophy (Oceanography)

France

Date: 07-April-2015

In front of jury composed of:

Reviewer	Prof. Sylvain OUILLON (LEGOS, IRD, France)
Reviewer	Prof. Kevin RUDDICK (MUMM, Belgium)
Jury member	Asst. Prof. Sébastien VERRIER (CESBIO, Université de Toulouse 3, France)
Jury member	Dr. Antoine MANGIN (ACRI-ST, France)
Jury member	Asst. Prof. Alexei SENTCHEV (ULCO, LOG, France)
Jury member	Dr. Philippe ESCUDIER (CNES, Toulouse, France)
Thesis Supervisor	Prof. François G. SCHMITT (CNRS, LOG, France)
Thesis Co-Supervisor	Prof. Hubert LOISEL (ULCO, LOG, France)

DEDICATION

അച്ഛനും അമ്മയ്ക്കും...

TABLE OF CONTENTS

Table of Contents	i
List of figures	v
List of tables	xiii
Declaration	xv
Acknowledgements	xvii
Abstract	xix
Résumé	xxi
General Introduction	1
0.1 Introduction	1
0.2 Outline of the thesis	5
1 Introduction to homogeneous turbulence and intermittency	7
1.1 Fully developed turbulence	7
1.2 Intermittency and cascades	11
1.3 Multifractal properties	13
1.4 Scaling concepts to deal with intermittency in turbulence	15
1.5 Universal stochastic scaling models	17

1.6	Summary	19
2	Introduction to marine optics and ocean colour remote sensing	21
2.1	Composition of natural waters	21
2.1.1	Dissolved matter	22
2.1.2	Particulate matter	23
2.2	Optical properties of the water	24
2.3	Particle Size Distributions (PSD)	25
2.4	Absorption, Scattering and Attenuation coefficients	27
2.5	The principle of ocean colour radiometry	31
2.6	Bio-optical algorithms for Chlorophyll-a	33
2.7	Remarks	34
3	High frequency variability of particle size distribution and its dependency on turbulence over the sea bottom during re-suspension processes	37
3.1	Introduction	38
3.2	Data and methods	40
3.2.1	Study area	40
3.2.2	Data	42
3.2.3	Methods	43
3.3	Results	46
3.3.1	Meteorological and hydrodynamic conditions	46
3.3.2	Stokes number	47
3.3.3	Temporal variability of the velocity field	49
3.3.4	Temporal variability patterns of particles concentration and size parameters in relation with hydrodynamical forcing.	50
3.4	Discussion and Conclusion	55
4	Intermittent particle dynamics in marine coastal waters	59
4.1	Introduction	60
4.2	In-situ data	61

4.2.1	Separation into size classes	61
4.2.2	PSD slope (ξ)	62
4.3	Intermittent dynamics	65
4.3.1	Velocity intermittency	65
4.3.2	Dynamics of the entropy of particle size	65
4.3.3	Intermittent dynamics of different size classes	67
4.3.4	Intermittent concentration dynamics	69
4.4	Conclusions	70
4.5	Appendices	72
5	Scaling analysis of ocean surface turbulent heterogeneities from satellite remote sensing: use of 2D structure functions.	77
5.1	Introduction	78
5.2	Methods	80
5.2.1	Data analysis techniques	80
5.2.2	Tests on 2D stochastic simulation	82
5.3	Comparison of the CG and SF methods	87
5.3.1	Scaling analysis on a Chl-a image of MODIS aqua	89
5.3.2	Scaling analysis of MODIS SST	90
5.4	Discussion: the role of signs	92
5.5	Conclusion	93
6	Multi-Scale analysis of Ocean Colour and Sea Surface Temperature images of MODIS-Aqua: statistical characterisation using turbulence tools	97
6.1	Introduction	98
6.2	Materials and methods	100
6.2.1	Data and study areas	100
6.2.2	Significance of the study regions	101
6.2.3	Chlorophyll-a (Chl-a)	107
6.2.4	Sea Surface Temperature (SST)	109

6.2.5	Remote sensing reflectance (R_{rs})	109
6.2.6	Homogeneous isotropic turbulence	110
6.2.7	1D Power spectra	111
6.2.8	2D Power spectra	111
6.2.9	Structure Function (SF) method	112
6.2.10	Cumulants and cumulant scaling analysis	113
6.3	Results and discussions	115
6.3.1	1D and 2D scaling	115
6.3.2	Structure function method	118
6.3.3	Cumulant scaling	122
6.4	Conclusions	123
7	Conclusions and perspectives	127
	Bibliography	133
	Appendices	156
	Appendix A: Curriculum Vitae of the author	156
	Appendix B: Published papers	161
	Appendix C: Submitted paper	189

LIST OF FIGURES

- 1 Illustration of time and space scales of physical oceanographic phenomena varying from very small bubbles to oceanic circulations associated with earth’s orbit variations. 2
- 1.1 Illustration of the cascade process: Energy is injected at large scales, eddies are broken at inertial scales until the Kolmogorov scale η , where energy is converted into heat (Richardson, 1922). 9
- 1.2 A surrogate of the dissipation is given by the squares of the derivative of the velocity $(dV)^2$. It shows intermittency. 11
- 1.3 A schematic representation of a discrete multiplicative cascade 12
- 2.1 Schematic diagram of various seawater constituents in the broad size range from molecular size of the order of 10^{-10} m to large particles and bubbles of order of 10^{-3} - 10^{-2} m in size [Figure reprint from Stramski et al. (2004)]. 22
- 2.2 Illustration of absorption, scattering and transmission [Figure reproduced from Mobley et al. (2011)]. 29
- 2.3 Illustration of light rays contributing to L_u as measured above the sea surface (after Mobley et al. (2011)). 31

2.4	Instruments (bio-optical and hydro-graphic) mounted over the sea-spider for the in situ sampling; done in the laboratory of oceanology and geosciences, Wimereux.	34
3.1	Location (blue dot) of the sampling area in the eastern English Channel together with the isobaths (A). Zoom on the sampling area (blue dot), the meteorological station (red dot) and SOMLIT stations (green dot) in (B).	41
3.2	Time series of A) the significant wave height H_s , B) peak wave period T_p , C) peak wave direction D_p , and D) water level.	46
3.3	Time series of water level evolution along with tide (black line), time series of VACV (in red) and contour map showing the vertical structure of the current velocity.	48
3.4	Time series of U (A) and V (B). The insets represent a small portion of the time series to show the fluctuations. (C) Power spectra of U (blue curve) and V (green curve). The two straight lines correspond to two different scales with slopes of -1.72 (near to -5/3 slope of Kolmogorov) in light green and -0.58 in red and the humps in the energy value at high frequency represents a small scale forcing of high energy wave breaking.	50
3.5	PSD for volume concentration (A) and for number concentration (B). The inset in (A) is a log-log plot emphasizing the power-law relations for the volume concentrations.	51
3.6	The PDF of A) ξ , B) D_A , C) $c_p(670)$ and normalised volume concentration of the different size classes of particles (VC_{silt} (D), VC_{fine} (E), VC_{coarse} (F) and VC_{macro} (G)), superposed to a Gaussian fit with the same mean and variance. The inset in all figures is a semi log plot emphasizing extremes, showing that all $PDFs$ are non-Gaussian.	53

3.7	Time series of A) $\xi(t)$, B) D_A , C) $c_p(670)$ and the normalised volume concentration of different size classes of particles (VC_{silt} (D), VC_{fine} (E), VC_{coarse} (F) and VC_{macro} (G)) superposed to VACV data.	54
3.8	(A) Scatter plot of $c_p(670)$ versus H_s and (B) ξ versus H_s .	55
3.9	Power spectra of ξ , D_A , $c_p(670)$ and the total volume concentrations of different size classes of particles showing different scale regimes as indicated by the different slope values for different frequency ranges.	56
4.1	Time series of 3000 samples of volume concentrations of different size classes of PSD. (A) Silt/Clay, (B) Fine particles, (C) Coarse/Micro particles (D) Macro particles/flocs.	63
4.2	Time series of 3000 samples of PSD slope (ξ) (A) and PSD slope of the entire dataset with a power-law fit of slope $\bar{\xi} = 2.9 \pm 0.16$ (B).	64
4.3	Turbulent power spectra of U and V components of velocity fields showing different scaling regimes same for both FFT and HSA (A). The scaling exponents estimated using the HSA method: the curve for U is more nonlinear than the one for V. The Hurst exponents H_U and H_V are negative (B).	66
4.4	Time series of 3000 samples of Shannon entropy in (A), PDF of Shannon entropy along with a Gaussian fit in semi-log plot (inset) in (B) and the Autocorrelation of Shannon entropy in (C).	67
4.5	Power spectra for different size classes of PSD estimated for Fourier and Hilbert transform Silt/Clay (A), Fine (B), Coarse/Micro (C) and Macro particles/flocs (D). The red lines shows the scaling range and the slope of the best fit in this range.	68
4.6	Scaling exponents $\zeta(q)$ estimated for different particle sizes, using the HSA method. In all cases the Hurst exponent is negative, with values between -0.17 and -0.38. The curves are all slightly nonlinear, sign of intermittency.	69

4.7	Time series of 3000 samples of $c_p(670)$ in (A), Time series of 3000 samples of $C_{vol-total}$ in (B), Turbulent power spectrum of $c_p(670)$ and turbulent power spectrum of $C_{vol-total}$ showing different scaling regimes (The scaling regime indicated as red is used for the scaling exponent computation) in (C and D) and scaling moment function of $c_p(670)$ and $C_{vol-total}$ in (E). The Hurst exponent values are very small but the curve is strongly non-linear.	71
4.8	Time series of $c_p(670)$ in (A), IMF retrieved through the EMD methods in (B), the time scale is increasing with the mode from C1 to C17 .	73
4.9	Representation of the joint pdf in log scale of the $c_p(670)$ fluctuations in an amplitude-frequency space.	74
5.1	A) simulation of a 2D β model with $n = 2^{10}$ and $\beta = 0.9$ (ϵ is displayed), B) coarse grained moments for $q=1$ to 5 and C) moment scaling function $K(q)$, where the experimental estimation is shown in dots compared to the theoretical prediction as a dotted line, with $c = 0.15$	84
5.2	A) Simulation of a 2D log-normal image using a discrete cascade model with $\mu = 0.3$, B) coarse grained moments from $q=1$ to 5 and C) the corresponding moment scaling function experimentally estimate as dots and theoretical value $K(q) = \frac{\mu}{2}(q^2 - q)$ as a dotted line. . .	86
5.3	A) Simulation of 2D fractional Brownian motion for various Hurst exponents ($H = 0.1, 0.2 \dots, 0.9$). The white rectangles are the space where the data have been removed to test this method for deriving H using spatial Structure function method. The 2D structure function was applied to each full image and also to the same image with white rectangles removed, in order to show that this scaling method can be applied to irregular images. B) For each image, comparison of the H value estimated using the structure function for the full image and for images with missing values.	88

5.4	A) Simulation of a 2D log-normal multifractal image with $H = 0.35$ and $\mu = 0.1$. B) Scaling of the SF; C) Scaling analysis when gradient modulus is applied on the image shown in A; D) representation of different exponents.	89
5.5	A) Chl-a image from MODIS Aqua from the Mauritanian coast sampled on 11 March 2003; the square indicates the 512×512 pixel of cloud free image chosen for the analysis of Chl-a. B) Gradient modulus estimated for the latter square image. C) Power-spectrum of the Chl-a image showing a scaling exponent $\alpha = 1.79$. D) Moment scaling function for the square image, using the CG and SF methods. Eq. 5.19 is tested and found not to be correct for $q \geq 1.7$	91
5.6	A) SST image from MODIS from the Mauritanian coast sampled on 11 March 2003. B) 2D power-spectrum of the image showing a scaling exponent $\alpha = 1.80$. C) Moment scaling function, using the CG and SF method. Eq. 5.19 is approximately valid, coming from the fact the $K_{CG}(q)$ is very small, corresponding to a very regular field.	93
5.7	The gradient sign information of the 2D fBm derived for $H=0.6$ in A) and its moment scaling function in B).	94
6.1	Study area maps from different regions of world ocean	101
6.2	Chl-a, SST, R_{rs-443} and R_{rs-555} from AC region sampled on 10/07/2013. The square indicates the 512×512 pixel of cloud free image chosen for the analysis.	102
6.3	Chl-a, SST, R_{rs-443} and R_{rs-555} from MC region sampled on 10/01/2013. The square indicates the 512×512 pixel of cloud free image chosen for the analysis.	103
6.4	Chl-a, SST, R_{rs-443} and R_{rs-555} from NEAS region sampled on 02/12/2013. The square indicates the 512×512 pixel of cloud free image chosen for the analysis.	104

6.5	Different parameters from the Angola Namibia coastal waters sampled on 30-April-2013, Chl-a in A), SST in B), R_{rs} -443 in C) and R_{rs} -555 in D). The square indicates the 512×512 pixel of cloud free image chosen for the analysis.	105
6.6	Chl-a, SST, R_{rs} -443 and R_{rs} -555 from PCC region sampled on 30/05/2012. The square indicates the 512×512 pixel of cloud free image chosen for the analysis.	106
6.7	Chl-a, SST, R_{rs} -443 and R_{rs} -555 from CS region sampled on 29/03/2012. The square indicates the 512×512 pixel of cloud free image chosen for the analysis.	107
6.8	Chl-a, SST, R_{rs} -443 and R_{rs} -555 from EM region sampled on 31/12/2009. The square indicates the 512×512 pixel of cloud free image chosen for the analysis.	108
6.9	Various power spectra, log centered 2D power spectrum of Chl-a sampled from ANC on 30-April-2013 in A), averaged zonal and meridional power spectra (1D) of various parameters in B), radially summed power spectra of Chl-a, SST, R_{rs} -443 and R_{rs} -555 in C). These 2 types of spectra show good scaling for Chl-a, SST, R_{rs} -443 and R_{rs} -555.	116
6.10	Comparison of 1D and 2D spectral slope β derived for Chl-a in A), SST in B), R_{rs} -443 in C) and R_{rs} -555 in D).	117
6.11	The 2D structure function scaling of Chl-a in A), SST in B), R_{rs} -443 in C), R_{rs} -555 in D) and the ratio between R_{rs} -443 to R_{rs} -555 in E) showing good scaling, especially for R_{rs} -443.	119
6.12	The moment scaling function derived by 2D structure function of various parameters from the ANC sampled on 30-April-2013.	120
6.13	H- μ plot clustering of parameters (Chl-a, SST, R_{rs} -443, R_{rs} -555 and the ratio between R_{rs} -443 to R_{rs} -555) for different regions. The colour code corresponds to the parameters, and the shape to the geographical location.	120

6.14	The second characteristic function $\Phi_l(q)$ derived for different l values of Chl-a sampled from ANC on 30-April-2013 in A). The first cumulant derived for the same image in B) and the second cumulant in C).	122
6.15	H derived through cumulant scaling versus H derived through structure function scaling for Chl-a in A) and SST in B).	123



LIST OF TABLES

3.1	Biogeochemical and optical data collected from SOMLIT before the time series measurements from the stations C and L (shown in Figure 1B).	42
5.1	The exponents (H and α) derived for Chl-a and SST images for Mauritanian region. The Hurst exponent H derived through SF ($H = \zeta(1)$).	90
6.1	The geographical locations with sampling date	101
6.2	The spectral slope β derived in 1D, for various parameters sampled from different regions.	116
6.3	The spectral slope β derived in 2D, for various parameters sampled from different regions.	117
6.4	The Hurst parameter H derived through SF method for various parameters sampled from different regions. For each case the mean and standard deviation are estimated by doing statistics over the number of images. For PCC, CS and EM cases there is only 1 image.	121
6.5	The intermittency parameter μ derived through SF method for various parameters sampled from different regions. For each case the mean and standard deviation are estimated by doing statistics over the number of images. For PCC, CS and EM cases there is only 1 image.	121



DECLARATION



This thesis was funded by The Centre National d'Etudes Spatiales (CNES) and Centre National de la Recherche Scientifique (CNRS). This work was also supported by CNES in the framework of COULCOT2 project of TOSCA program.

This thesis is a presentation of my original research work. I declare that it has not been submitted before for any degree or examination in any other university and that all the sources. I have used or quoted have been indicated and acknowledged as complete references.

RENOSH P. R.

ACKNOWLEDGEMENTS

First I would like to express my profound and heartfelt thanks my two supervisors, Prof. François G. Schmitt and Prof. Hubert Loisel for their constant support and motivation. I would like to express my special thanks to François to introduce me in the challenging field of turbulence. Hubert's comments and suggestions always amazed me and it helped me to improve my research. It was really a great experience to work with you both.

Centre National d'Etudes Spatiales (CNES) and Centre National de la Recherche Scientifique (CNRS) are acknowledged for funding my Ph.D. thesis.

Meteo France is acknowledged for providing wind data. Service d'Observation en Milieu Littoral (SOMLIT), INSU-CNRS, Wimereux was also acknowledged for providing the biogeochemical data. Goddard Space Flight Centre is also acknowledged for providing the SST and ocean colour data of MODIS Aqua.

I specially want to express my gratitude to Dr. Alexei Sentchev, Xavier Mériaux, Arnaud Cauvin and Eric Lecuyer for helping me to collect the in situ data. I also appreciate Dr. Ole Mikkelsen for his valuable comments on the LISST data. I also wish to thank Dr. Yongxiang Huang providing the Matlab scripts for EMD method.

I also very grateful to my colleagues especially Dr. Zied, Dr. Jonathan, Dr. Mikael, Dr. Antoine, Dr. Eric, Dr. Fabien, Dr. Muriel, Dr. Virginie, Céline, Valerie, Michelle and Evelyne for their ceaseless help and support in various aspects to fulfil my goals.

I take this opportunity to recollect my teachers, those who inspired and treated me well, as a student and a research scholar.

Words do not suffice the gratitude I owe to my parents, for their constant support and pray for me to achieve my goals and to provide me a chance to study. I am also thankful to my sisters for their constant support and pray.

Then very special thanks to my wife Dr. Anumol for her perpetual support, motivation and understanding under tough phases of life. As a new part of my life, I wish to thank my son Arnav.

Last but not the least my sincere gratitude to all those who (mainly my classmates and friends from Goa University) directly or indirectly contributed for the successful completion of my thesis.

ABSTRACT

The objective of this thesis is to understand the processes responsible for the high spatial and temporal variability of particulate matter as assessed from optical measurements performed in situ or/and from ocean colour observations. We particularly focus on coupling processes between turbulence and particulate matter (suspended sediment and phytoplankton).

The first part of the thesis is on in situ measurements performed under different meteorological situations. Here the objective was to understand the coupling between the turbulent velocity field and suspended particles. We selected the attenuation coefficient as a proxy for the total concentration of particles and in situ measurement of particle size distribution (PSD) spectrum. This study showed that the dynamics of the PSD is controlled by many oceanographic parameters such as tidal currents, waves and turbulence. We also studied the multifractal characteristics of these PSD for various size classes (silt, fine, coarse and macro particles). For that, we used Empirical Mode of Decomposition (EMD) along with the Hilbert Spectral Analysis (HSA).

The second part of the thesis focuses on the multi-scale analysis of satellite ocean colour and SST images. The spatial heterogeneity of oceanic scalars (phytoplankton and sea surface temperature) under the turbulence influence is considered at different scales. For this, we used the satellite image of Chlorophyll-a and SST at high spatial resolution (1000 m) of MODIS aqua. We have used different multi-scale ap-

proaches (Power spectra, Coarse-Graining (CG) and 2D Structure Functions (SF)) to characterize scalar fluctuations under the turbulence influence (passive scalars). Here we proposed to adapt the structure functions for 2D fields for analysing the 2D image. The CG method is tested and verified on different cascade models such as the β -model and lognormal model. The SF method was tested by applying it to a 2D fractional Brownian simulation with different Hurst exponent (H) values. This method also worked with images having missing data, which is helpful since non-averaged instantaneous images have often missing values due to cloud coverage. Finally, this methodology using 2D structure functions, was applied to real images of Chl-a, SST, R_{rs} -443 and R_{rs} -555. It is possible to characterize, for all spatial scales and all intensities, the heterogeneities and intermittencies of the studied scalar fields, using a few parameters (2 parameters in the framework of the lognormal approximation). The values of these parameters, for 7 different locations, are discussed and compared.

L'objectif de cette thèse est de comprendre les processus responsables de la forte variabilité spatiale et temporelle de la matière particulaire telle qu'elle est évaluée à partir de mesures optiques réalisée in situ et / ou à partir d'observations de couleur de l'océan. Nous avons mis particulièrement l'accent sur des processus de couplage entre la turbulence et la matière particulaire (sédiments en suspension et phytoplancton).

La première partie de la thèse porte sur des mesures in situ effectuées sous différentes situations météorologiques. L'objectif était de comprendre le couplage entre le champ de vitesse turbulent et les particules en suspension. Nous avons considéré le coefficient d'atténuation, indicateur de la concentration totale de particules in situ, et le spectre de tailles des particules in situ (particle size distribution - PSD). Cette étude a montré que la dynamique de la PSD est contrôlée par plusieurs paramètres océanographiques, tels que les courants de marée, les vagues et la turbulence. Nous avons également étudié les caractéristiques multifractales de ces PSD pour diverses classes de taille (limon, sable fin, sable grossier, particules macro). Pour cela, nous avons utilisé la décomposition modale empirique (empirical mode decomposition - EMD) avec avec l'analyse spectrale de Hilbert (HSA).

La deuxième partie de la thèse porte sur l'analyse multi-échelle d'images couleur de l'océan et SST (sea surface temperature). L'hétérogénéité spatiale des scalaires océaniques (phytoplancton et la température de surface de la mer), sous l'influence

de la turbulence est considérée à différentes échelles. Pour cela, nous avons utilisé l'image satellite de chlorophylle a et SST à haute résolution spatiale (1000 m × 1000 m) d'Aqua MODIS. Nous avons utilisé différentes approches multi-échelles (spectres de puissance, coarse graining (CG) et Fonctions de structure 2D (SF)) pour caractériser les fluctuations de scalaires sous l'influence de la turbulence (scalaires passifs). Ici nous avons proposé d'adapter les fonctions de structure de champs 2D pour analyser des images 2D. Le Méthode CG est testée et vérifiée avec différents modèles de cascade multiplicatives tels que le modèle beta et le modèle log-normal. La méthode SF a été testée en l'appliquant à un champ 2D simulé de mouvement Brownien fractionnaire avec différents exposants de Hurst (H). Cette méthode fonctionne également avec des images ayant des données manquantes, ce qui est utile, car des images instantanées, non moyennées, ont souvent des valeurs manquantes en raison de la couverture nuageuse. Enfin, cette méthodologie, en utilisant les fonctions de structure 2D, a été appliquée à des images réelles de Chl-a, SST, Rrs-443 et Rrs-555. Il est possible de caractériser, pour toutes les échelles spatiales et toutes les intensités, les hétérogénéités et intermittences des champs scalaires étudiés, à l'aide de quelques paramètres (deux paramètres dans le cadre de l'approximation log-normale). Les valeurs de ces paramètres, pour sept endroits différents du globe, sont examinés et comparés.

0.1 Introduction

Coastal areas contribute around 60% of the world population (within 100 km from the coastal line) and around 75-90 % of global sink of suspended river run-off takes place in coastal waters. The coastal zone provides an area ($\approx 26 \times 10^6 \text{ km}^2$) about 7 % of the surface area of the ocean ($\approx 360 \times 10^6 \text{ km}^2$). This coastal zones experience 20 % of the total annual primary production of total ocean primary production (6.0 Gt C year⁻¹ and 24.0 Gt C year⁻¹ in the coastal ocean and open ocean respectively) (Wollast, 1998; Doney, 2010). So the improved study of coastal water physical processes and their effects on biological, chemical and geological aspects need to be better monitored and understood.

The traditional approaches of oceanographic cruises and in-situ samplings over coastal waters are time-consuming, expensive and sometimes uncertain to yield significant results on a studied phenomena, especially at synoptic scales. This is basically due to the high variability of the physical and biogeochemical processes occurring in coastal areas. Prediction and dynamics of material particles dispersed and transported in a turbulent flow remains a challenge for the oceanographic community. Understanding these variability of physical, hydrographic, biological, and optical properties and the relationships among these properties are necessary for the designing of accurate coupled physical-biogeochemical models and for the in-

terpretation of remote sensing data in the near-shore coastal ocean.

In the remote sensing context, the biological and physical parameters are a very powerful tool for performing large-scale studies. Satellite observations provide global coverage on a routine basis at a sufficiently high spatial and temporal resolution to observe a variety of important physical and biogeochemical processes and the linkages among them, especially when different satellite observations (ocean colour, SST, surface winds, sea surface height) are combined with in situ data in an analysis of numerical models. Satellite data are well suited for estimating scales and variability of physical and biological properties of the ocean surface. These data sets serve to constrain models of physical and biogeochemical processes and for estimating global primary production, calcite, fluorescence line height, chromophoric dissolved organic matter absorption, photosynthetic available radiation, and sea surface temperature, winds, and sea surface height are generated operationally.

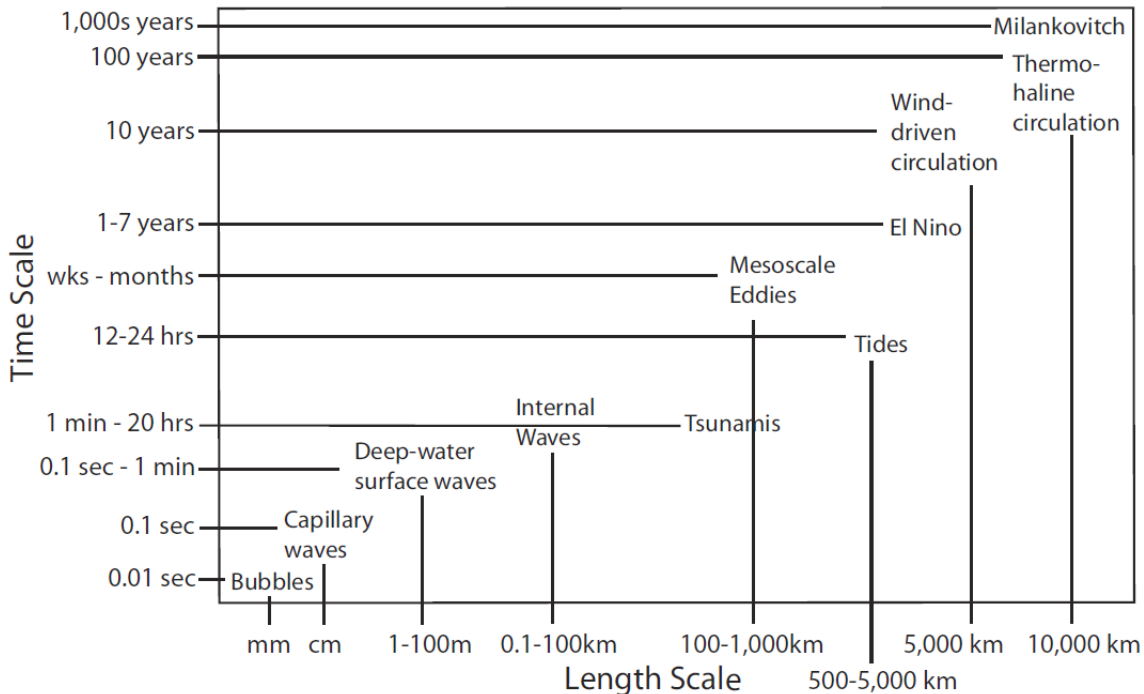


Figure 1: Illustration of time and space scales of physical oceanographic phenomena varying from very small bubbles to oceanic circulations associated with earth's orbit variations.

The oceans are highly complex systems in which organism distributions are af-

affected spatially and temporally by the physical and biogeochemical processes occurring at multiple scales (Lubchenco and Petes, 2010; Doney et al., 2012). Theories of geophysical fluid dynamics can explain many of these basic processes at different scales such as local turbulence, eddy systems and ocean circulation (Pedlosky, 1982). The understanding, modelling and prediction of hydrologic processes is needed over a broad range of scales from few mm to 10,000 km in space and from few seconds to many years in time (Fig. 1).

Figure 1 illustrates the scale problem of oceanic fluctuations, for spatial and temporal scales spanning 10 orders of magnitude. In fact, one way to tackle this problem is to consider, as in Fig. 1, some special cases, giving them names and separating their study from other cases. Another way to tackle the scale problem is to consider scaling processes, having statistics which have scale invariant properties: the properties at a given scale are then considered to be similar with the properties at another scale, with a rescaling factor. This is the framework of fully developed turbulence. We have used here this framework to consider scaling properties of particle concentration and remotely sensed parameters. The objectives of such approach are to be able to understand, to model and characterize, the intermittency of these fields in relation with turbulence.

In the framework of this Ph.D. thesis, our objective is to analyse the interactions of turbulence and bio-optical properties for in situ and satellite observations.

In-situ aspects. The research on coastal ocean bio-optical properties are difficult because physical processes in this region are not only affected by shelf slope dynamics, but also by river flow, bottom topography, and the shape of the coastline. The suspended particles are the ubiquitous components of oceanic waters which plays an important role in the biogeochemical cycles of the marine environment (Wells and Goldberg, 1992). Important examples are: the absorption and scattering of light, the exchange of substances between solid and liquid phases, the transport of the substances through ocean and to the seabed and also a huge group of biological

processes. At certain extent, these processes strongly depend on the suspended particle size distributions. In-situ measurements of particle size are currently limited to a few locations and relatively short periods (Fennessy et al., 1994; Ellis et al., 2004; Mikkelsen et al., 2006). In the present thesis, we mainly concentrate on the dependency of turbulence on particle size distributions (PSD) along with other physical processes like tidal currents and waves. From the PSD measurements, we will consider PSD slope ($\xi(t)$) at each time step (every second) using automatic regression analysis. This provides the relative concentration of small and large particles: the steeper the PSD slope (the greater ξ), the more small particles relative to large particles are present in the water column (and vice versa). The previous studies quantified ξ for oceanic waters range between 2.5 and 5 (Jonasz, 1983; Boss et al., 2001b; Loisel et al., 2006; Buonassissi and Dierssen, 2010; Reynolds et al., 2010; Neukermans et al., 2012a). The turbulence theory predicts that passively advected scalars exhibit small-scale structure similar to the fluid motion. We will study this passive scalar characteristic of PSD from highly dynamic coastal environment. The scaling and intermittency properties of high frequency measurements of PSD and different size classes of the PSD are also studied using different approaches such as Fourier power spectra, Empirical mode of decomposition along with Hilbert spectral analysis (Huang et al., 1998, 2008). The results from in-situ aspects of the studies are explained in Chapters 3 and 4.

To understand the temporal heterogeneity of the bio-optical properties, we have conducted 3 campaigns of high frequency time series with all bio-optical instruments (AC-S, ECO-FLRT, ECO-FLCDRT and LISST-100X type C) and current measurements (ADCP and ADV) from highly dynamic coastal waters of Eastern English Channel. Regarding the first two samplings, we found that the quality of the data was very poor, so we discarded these data from my thesis. For the third campaign, we have received high-quality data of LISST, ADV and ADCP. and some of the instruments did not work (AC-S, ECO-FLRT and ECO-FLCDRT). So we could not incorporate much IOPs in the present thesis.

Satellite aspects. It is common to observe high spatial and temporal heterogeneity in ocean colour products (Chl-a and R_{rs}) and SST. In the present thesis, we try to understand these heterogeneities using different tools borrowed from the field of turbulence, statistical physics and signal processing. 2D images are analysed using 2D power spectra, coarse graining (CG) method, 2D structure function (SF) method and cumulant scaling of these images. The results from satellite aspects of the studies are explained in Chapters 5 and 6.

Multi-scale dynamics are relevant for many phenomena extending from turbulence (Frisch, 1995; Sreenivasan and Antonia, 1997), finance (Schmitt et al., 2000; Muzy et al., 2001) to geosciences (Schmitt et al., 2009; Lovejoy and Schertzer, 2012). Multi-scale/Multifractal studies have been widely applied to time series, but there are not many studies in the field of ocean colour remote sensing. Montera et al. (2011) tested and derived the multifractal parameters for satellite-derived Chl-a. It is a well-known fact that natural images possess power law scaling which reflects their scale-invariant nature. These scaling properties are associated with the power spectrum, that is usually related to the fractal characteristics of the image (Burton and Moorhead, 1987; Field, 1987). These scaling properties of satellite-derived ocean colour (Chl-a and R_{rs}) and SST have been tested with 1D and 2D power spectra. For the multi-scaling analysis, we have adopted and adapted the methodology of 2D structure function method. This method has been applied to various oceanic environments and their multifractal parameters also derived using lognormal intermittency model fit.

0.2 Outline of the thesis

This Ph.D. dissertation is organized as follows:

- Chapter 1 describes the introduction to homogeneous turbulence and intermittency. Here we give brief explanations of fully developed turbulence, intermittency, cascades, multifractality, scaling and stochastic scaling processes.

- Chapter 2 depicts the introduction of marine optics and ocean colour remote sensing through radiative transfer theories. Here we explain briefly the composition and optical properties of the natural waters. As this Ph.D. mainly focuses on scattering processes, we explain some of the properties of PSD, absorption, scattering and attenuations, because these are directly linked with the remote sensing reflectance.
- Chapter 3 shows the impact of the tidal currents, waves and turbulence on the particle re-suspension over the sea bottom in a highly dynamic coastal environment of eastern English Channel. Here we show different power spectra's of PSD along with particle concentration $c_p(670)$, a proxy for suspended particulate matter concentration) and analysed the dynamics with different forcing parameters.
- Chapter 4 analyses the intermittency properties of the PSD. Here we decomposed the PSD into different size classes and analysed their intermittency using different techniques like Empirical mode of decomposition (EMD) and Hilbert transform (HT) using arbitrary order Hilbert spectral analysis (AHSA).
- Chapter 5 derives a new methodology to analyse the multi-scale properties of 2D satellite images. Here we proposed a new methodology of directly estimate SF scaling exponents.
- Chapter 6 uses the 2D SF method for different regions of the global ocean having large heterogeneity in the bio-mass distribution. Here we derive the multifractal parameters μ and H using lognormal intermittency model fitting and discuss their values.
- Chapter 7 conclude this thesis with some future perspectives.

CHAPTER 1

INTRODUCTION TO HOMOGENEOUS TURBULENCE AND INTERMITTENCY

Abstract

In this chapter, I recall some of the important terminologies and concepts in the field of fully developed turbulence, including intermittency and scaling concepts. These will be used in other chapters for data analysis: particle size distribution time series analysis as well as ocean colour image analysis.

1.1 Fully developed turbulence

Turbulence belongs to the field of fluid mechanics. It corresponds to a flow with a large Reynolds number:

$$Re = \frac{VL}{\nu} \quad (1.1)$$

where V is a typical velocity, L is typical scale and ν the kinematic viscosity (m^2/s). Since $\nu \approx 10^{-5} m^2/s$ in the air and $10^{-6} m^2/s$ in water (at usual temperature). Natural flows in the atmosphere, ocean or hydrology are most often in a state of fully developed turbulence ($Re \gg 1$). When Re is very small, the flow is considered as laminar and fluid motion is regular. There is a transition value at which fluid motion

changes from laminar to turbulent and instabilities occur. Turbulence is characterized by irregular motion, with lack of predictability, enhanced mixing, and apparent stochastic fluctuations. The governing equations are known since 1822 and are the Navier-Stokes equations:

$$\frac{\partial u_i}{\partial t} + u_j \frac{\partial u_i}{\partial x_j} = -\frac{\partial p}{\partial x_i} + \nu \nabla^2 u_i \quad (1.2)$$

and the continuity equation:

$$\frac{\partial u_i}{\partial x_i} = 0 \quad (1.3)$$

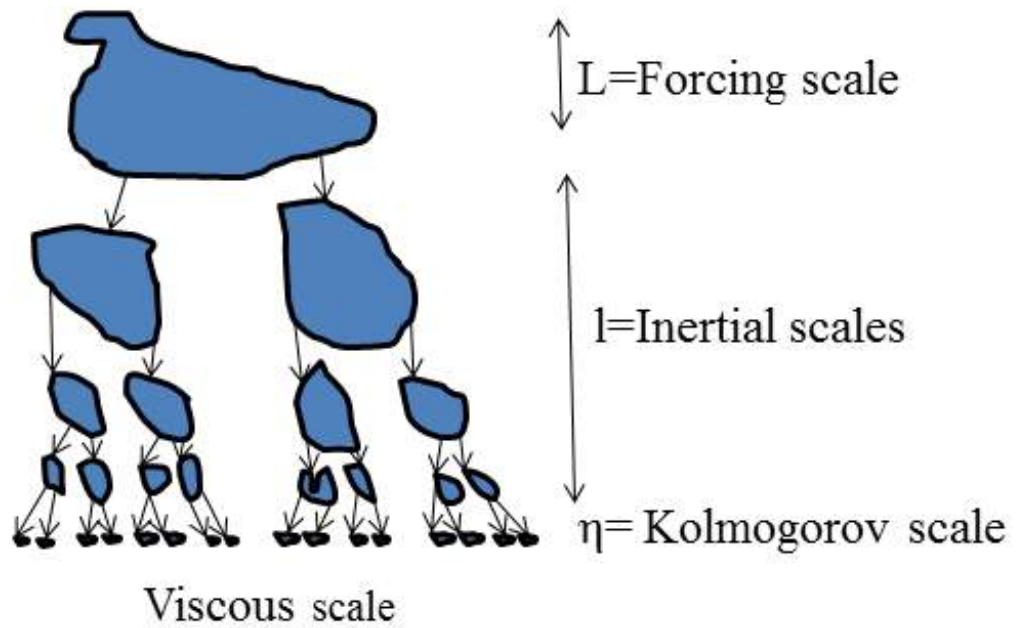
where $\vec{u} = (u_i)$ is the velocity vector, p the pressure, and ν the kinematic viscosity of the fluid. These equations are known for almost 200 years but are still unsolved, due to their non-linear character.

An inspiring concept in the theory of turbulence is Richardson's energy cascade process (Fig. 1.1). For large Reynolds numbers, the non-linear term dominates the viscosity according to dimensional analysis, for the large-scale structures. In the cascade process, the inertial term is responsible for the transfer of energy to smaller and smaller scales until small enough scales are reached for which viscosity becomes important. At those smallest scales, kinetic energy is finally dissipated into heat. It should be emphasized that turbulence is a dissipative process; no matter how large the Reynolds number is, viscosity plays a role at the smallest scales.

Such description has been proposed by Lewis Fry Richardson in a book in 1922, with the following poem (Richardson, 1922):

“Big whorls have little whorls
That feed on their velocity
And little whorls have lesser whorls
And so on to viscosity”

This was later quantified by the probabilist A.N. Kolmogorov in a very famous paper published in 1941 (Kolmogorov, 1941a). Kolmogorov assumed that for large enough Reynolds number, at intermediary scales the turbulence statistics are isotropic



Lewis Fry Richardson (1881-1953)

Figure 1.1: Illustration of the cascade process: Energy is injected at large scales, eddies are broken at inertial scales until the Kolmogorov scale η , where energy is converted into heat (Richardson, 1922).

(i.e. independent of direction). He assumed that the velocity fluctuations at scale l as ΔV_l , depends only on the scale and on the dissipation of kinetic energy ϵ defined as:

$$\epsilon = 2\nu \langle S_{ij} S_{ij} \rangle \quad (1.4)$$

where $S_{ij} = \frac{1}{2} \left(\frac{\partial u_i}{\partial x_j} + \frac{\partial u_j}{\partial x_i} \right)$ is the fluctuating rate of strain tensor. He obtained dimen-

sionally the following law:

$$\langle \Delta V_l \rangle = C \epsilon^{1/3} l^{1/3} \quad (1.5)$$

This is now considered as valid for scales belonging to the so called “inertial range”, from the large scale where energy is injected to the small scale where energy is dissipated, now called the Kolmogorov scale.

Simultaneously to this, his student Obukhov proposed a similar law in Fourier space (Obukhov, 1941a,b):

$$E_v(k) = C' \epsilon^{2/3} k^{-5/3} \quad (1.6)$$

where $E_v(k)$ is the Fourier power spectrum of the velocity, C' is a constant and k is the wavenumber. This has been verified with many studies in atmosphere (Gurvich, 1960), the ocean (Grant et al., 1962) and in the laboratory (Champagne, 1978). It has soon become universal to describe fully developed turbulence.

K41 theory can also be used to express the Re using the scale ratio. For a given scale l , belonging to the inertial range, ΔV_l is the velocity fluctuations at this scale, and the local Re corresponding to this can be written as:

$$Re_l = \frac{\Delta V_l l}{\nu} \quad (1.7)$$

We can introduce the scale η , also known as Kolmogorov scale, for which $Re_\eta \approx 1$. Then $\Delta V_\eta \eta = \nu$ and using Kolmogorov relation $\Delta V_l \approx \epsilon^{1/3} l^{1/3}$ for $l = \eta$ we have $\epsilon^{1/3} \eta^{4/3} = \nu$, then the Kolmogorov scale η is given by:

$$\eta = \left(\frac{\nu^3}{\epsilon} \right)^{1/4} \quad (1.8)$$

This is the smallest scale of turbulent motion; below this scale there are viscous scales. Kolmogorov scale separates the turbulent scales and viscous scales. Using the distinctive values of the dissipation and viscosity in the atmosphere and ocean, it is found that η is of the order of millimeters, both in the atmosphere and ocean. The scale η depends on both ν , characterizing the fluid, and ϵ , characterizing the

flow. Further, using $\Delta V_\eta \eta = \nu$, we find

$$Re_l = \left(\frac{l}{\eta} \right)^{4/3} \quad (1.9)$$

showing that the local Reynolds number depends on a scale ratio, for scales l belonging to the inertial range.

1.2 Intermittency and cascades

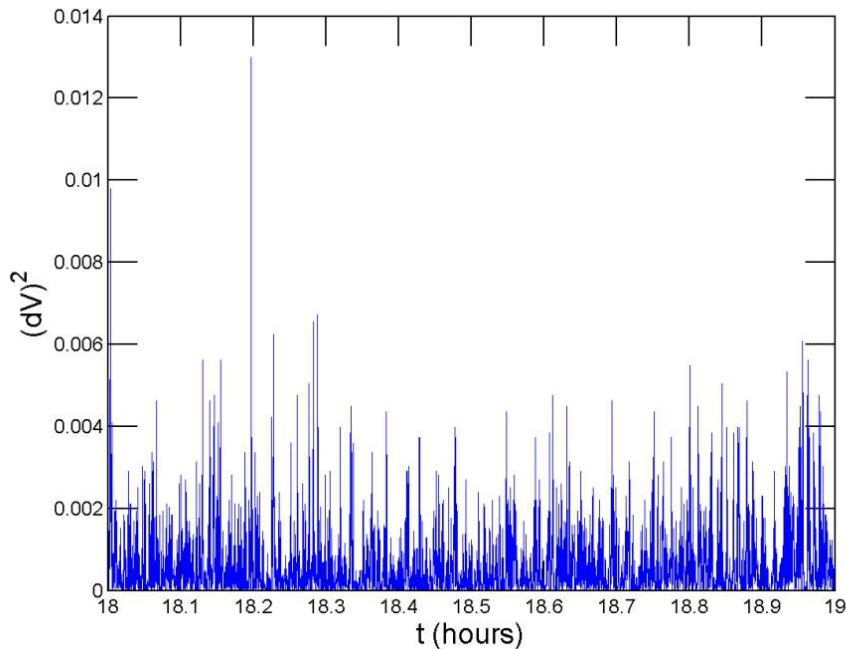


Figure 1.2: A surrogate of the dissipation is given by the squares of the derivative of the velocity $(dV)^2$. It shows intermittency.

The central assumption of K41 theory is the local homogeneity of dissipation rates, where ϵ is assumed to be smooth and even constant. However, experimental measurements estimated ϵ from the local derivative $\left(\frac{\partial V}{\partial t} \right)^2$ and found that this proxy of local dissipation is extremely variable (Fig. 1.2). This was called by [Batchelor and Townsend \(1949\)](#) as “intermittency”.

After the discovery of intermittency in the late 1940s, [Kolmogorov \(1962\)](#) have proposed some new formulations involving lognormal fluctuations for the velocity.

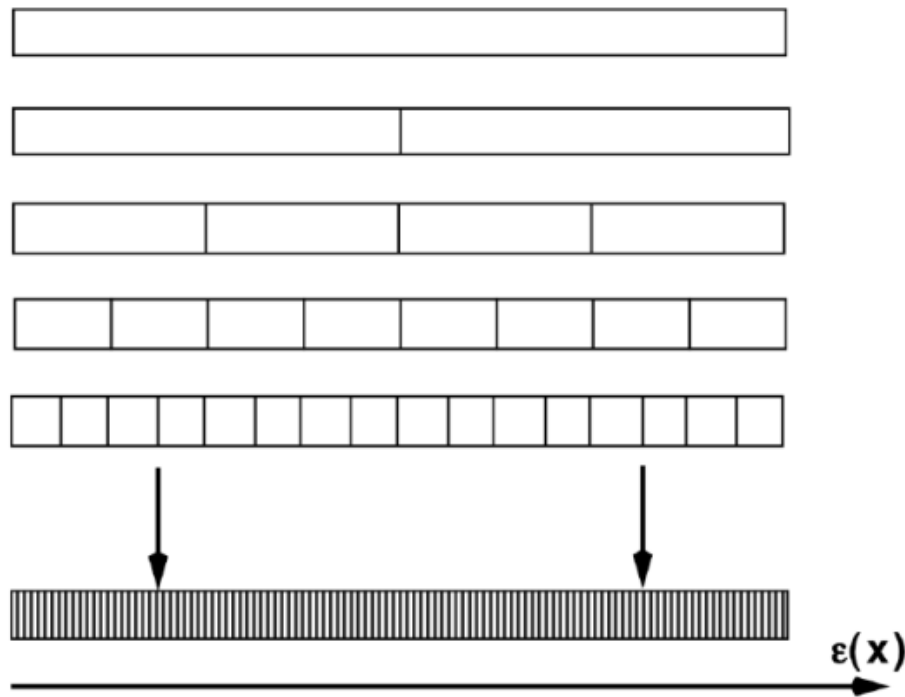


Figure 1.3: A schematic representation of a discrete multiplicative cascade

A few years later, [Yaglom \(1966\)](#), a student of Kolmogorov, has proposed a toy model to generate intermittency and mimic the energy cascade from large to small scale (Fig. 1.3).

The cascade of turbulent eddies in Yaglom's model can be seen as the ensemble of cells, each cell being associated with a random variable. All the variables are assumed to be positive and independent, and they obey the same statistical law. The largest external scale is associated with a single cell of size L . The largest cell divided into 2 cells, each of them having a length scale of $L/2$. This process is iterated, and at the step m , there are 2^m cells, each of size $L/2^m$, until the viscous scale $l = L/2^n$. Whatever the spatial position the turbulence dissipation rate ϵ_λ at scale ratio $\lambda = L/l = 2^n$ can be written as a product of n independent random variable as;

$$\epsilon_\lambda = \langle \epsilon \rangle \prod_{i=1}^n X_i \quad (1.10)$$

where X_i is a positive random variable associated with the level i in the cascade pro-

cess. Following the previous hypothesis of independence of variables, it is straightforward to calculate the moment of the turbulence-dissipation rate ϵ_λ that is expressed as

$$\langle (\epsilon_\lambda)^q \rangle = \langle \epsilon \rangle^q \left\langle \left(\prod_{i=1}^n X_i \right)^q \right\rangle = \langle \epsilon \rangle^q \prod_{i=1}^n \langle (X_i)^q \rangle = \langle \epsilon \rangle^q \langle X^q \rangle^n \quad (1.11)$$

The moments of the dissipation rate ϵ_λ are then given by:

$$\langle \epsilon_\lambda^q \rangle \approx \lambda^{K(q)} \quad (1.12)$$

with

$$K(q) = \log_2 \langle X^q \rangle \quad (1.13)$$

This expression is the second Laplace characteristic function of the random variable $\gamma = \log X$; as such it is a convex function. There is also $K(0) = 0$ and $K(1) = 0$ by conservation. Such cascade generate a multifractal process.

1.3 Multifractal properties

A fractal is a rough or fragmented geometrical object that can be subdivided into parts, each of which is (at least approximately) a reduced-size copy of the whole. The shape of the smaller features is like the shapes of the larger features. If the replication is exactly the same at every scale, it is called a self-similar pattern. Fractals are generally self-similar and independent of scale and are characterized by a fractal dimension. A multifractal is a set of intertwined fractals. A deviation from a strict self-similarity is also called intermittency. A single exponent is not enough to describe the dynamics of a multifractal; instead, a continuous spectrum is required, called as singularity spectrum.

In the multiplicative cascade framework the following relation is found:

$$\Pr(\epsilon_\lambda \geq \lambda^\gamma) \sim C'' \lambda^{-C(\gamma)} \quad (1.14)$$

where C'' is a constant, γ is called a singularity and $C(\gamma)$ is a co-dimension function,

related to the fractal dimension associated to the support of the singularity γ , $d(\gamma)$, by:

$$C(\gamma) = d - d(\gamma) \quad (1.15)$$

where d is the dimension of the field ($d=1,2$ or 3). For a monofractal field there is only one value for $d(\gamma)$, for a multifractal field an infinite number of values. $C(\gamma)$ and $K(q)$ are related through a Legendre transform. Indeed let us write the moments:

$$\langle \epsilon_\lambda^q \rangle = \int \epsilon_\lambda^q P(\epsilon_\lambda) d\epsilon_\lambda = \int \epsilon_\lambda^q \lambda^{-C(\gamma)} d\epsilon_\lambda \quad (1.16)$$

using the change of variable $\epsilon_\lambda = \lambda^\gamma$ this gives:

$$\langle \epsilon_\lambda^q \rangle \approx \int \lambda^{q\gamma} \lambda^{-C(\gamma)} d\gamma \approx \lambda^{\max_\gamma \{q\gamma - C(\gamma)\}} \quad \text{for } \lambda \gg 1. \quad (1.17)$$

This shows that:

$$K(q) = \max_\gamma \{q\gamma - C(\gamma)\} \quad (1.18)$$

This is a Legendre transform and relates the co-dimension function $C(\gamma)$ to the moment function $K(q)$. Whenever $C(\gamma)$ is non-linear, $K(q)$ also. Reciprocally when $K(q)$ is non-linear, this is a sign of multifractality.

The Legendre transform can be written also as:

$$\begin{cases} \gamma = K'(q) \\ C(\gamma) = q\gamma - K(q) \end{cases} \quad (1.19)$$

or

$$\begin{cases} q = C'(\gamma) \\ K(q) = q\gamma - C(\gamma) \end{cases} \quad (1.20)$$

Such Legendre transform is also found in statistical physics (Thermodynamics or large deviation theory).

1.4 Scaling concepts to deal with intermittency in turbulence

Since a proposal of [Kolmogorov \(1962\)](#) the velocity fluctuations at scale l , ΔV_l are related to the energy cascade flux at scale l , ϵ_l , by:

$$\Delta V_l \stackrel{d}{=} (\epsilon_l)^{1/3} l^{1/3} \quad (1.21)$$

where “ $\stackrel{d}{=}$ ” means equality in distribution and ϵ_λ is obtained from a cascade process. This leads to a scaling form of the structure functions:

$$\langle \Delta V_l^q \rangle \sim l^{\zeta(q)} \quad (1.22)$$

where $\zeta(q)$ is the moment function that characterizes the scale dependence of the moments of order q of the increment ΔV_l . Kolmogorov’s (1962) relation gives

$$\zeta(q) = \frac{q}{3} - K\left(\frac{q}{3}\right) \quad (1.23)$$

This relates the energy cascade statistics $K(q)$ and the velocity scaling law $\zeta(q)$. Kolmogorov’s (1941) relation corresponds to no intermittency; $K(q) = 0$ and $\zeta(q) = q/3$. Wherever there is intermittency, we have seen that $K(q)$ is concave with $K(1) = 0$ hence $\zeta(q)$ is convex with $\zeta(3) = 1$. The power spectrum of the velocity field is the following:

$$E_v(k) \sim k^{-\beta} \quad (1.24)$$

This is a scaling relation with β the scaling exponent. Furthermore the previous relation gives

$$\beta = 1 + \zeta(2) = 5/3 - K(2/3) \quad (1.25)$$

Usually $K(2/3)$ is small and negative hence there is a so-called scaling power spectrum with a scaling exponent slightly larger than $5/3$. This is called intermittency effect and usually $\beta \simeq 1.69$ ([Sreenivasan and Kailasnath, 1993](#)).

From the relation Eq.(1.23), we see that the probability distribution chosen for the cascade, which determines $K(q)$, determines also the shape of $\zeta(q)$. Hence $\zeta(q)$ has different shapes for different models. Many cascade models have been proposed in the turbulence literature. Below we recall only 4 famous models.

The β model. This model was introduced by Frisch et al. (1978) but was already presented by Mandelbrot (1974). This model is monofractal and linear, it has only one fractal dimension. The exponents for β model are:

$$K(q) = \mu(q-1); \quad \zeta(q) = \frac{q}{3} - \mu\left(\frac{q}{3} - 1\right) \quad (1.26)$$

The power spectral exponent is $\beta = \frac{5}{3} + \frac{\mu}{3}$. The parameter μ is related to β by $\mu = -\log_2 \beta$.

The log-normal model. This model was introduced by Yaglom (1966). The exponents $K(q)$ (derived from the moment of dissipation rate) and $\zeta(q)$ (derived from the moment of velocity fluctuations using structure function) for the log-normal model are;

$$K(q) = \frac{\mu}{2}(q^2 - q); \quad \zeta(q) = \frac{q}{3} - \frac{\mu}{18}(q^2 - 3q) \quad (1.27)$$

where μ is called as intermittency parameter: $\mu = K(2) = 2 - \zeta(6)$. The equation for the power spectral exponent is $\beta = 5/3 + \mu/9$. This model is classical and can be considered as a generic example of multifractal process. Hence we take this model for fitting data analysis in application chapters.

The log-Lévy/log-stable model. The log-Lévy, also called as universal multifractal model was proposed by Schertzer and Lovejoy (1987). This is based on the Lévy stable law (Lévy and Borel, 1954). The exponents $K(q)$ and $\zeta(q)$ characterizing the dissipation rates and the velocity fluctuations are:

$$K(q) = \frac{C_1}{\alpha - 1}(q^\alpha - q); \quad \zeta(q) = \frac{q}{3} - \frac{C_1}{\alpha - 1} \left[\left(\frac{q}{3}\right)^\alpha - \frac{q}{3} \right] \quad (1.28)$$

where C_1 is the co-dimension of the mean event ($0 \leq C_1 \leq d$), where d is the dimension of the space and α is the Lévy index. The α is bounded between 0 and 2, when $\alpha = 2$ the lognormal model is recovered and when $\alpha = 0$ the β -model is found. This model has been used in many studies in turbulence and the geosciences (Schmitt et al., 2009).

The log-Poisson model. Based on the Poisson distribution, this model was proposed in the mid 1990s (She and Leveque, 1994; Dubrulle, 1994; She and Waymire, 1995). The moment function using the dissipation rate $K(q)$ and velocity fluctuations $\zeta(q)$ are:

$$K(q) = c[(1 - \gamma)q - 1 + \gamma^q]; \quad \zeta(q) = \frac{q}{3} - c \left[(1 - \gamma) \frac{q}{3} - 1 + \gamma^{q/3} \right] \quad (1.29)$$

where $c > 0$ is the co-dimension of the most extreme events and γ , $0 < \gamma < 1$ is linked to the maximum singularity reachable from a finite sample. The constants $c = 2$ and $\gamma = \frac{2}{3}$ provided a relation with no adjustable parameters.

1.5 Universal stochastic scaling models

In this section we consider some of the important scaling models and their scaling moment functions. Since they will be used for methodological purpose in later chapters.

Brownian motion. Let us consider the normal distribution $N(\mu, \sigma^2)$ with mean μ and variance σ^2 . Then the 1D Brownian motion can be defined as a continuous stochastic process having Gaussian stationary increments such that $X(t + l) - X(t)$ belong to $N(0, l)$. The scaling moment function $\zeta_B(q)$ for Brownian motion is given by:

$$\zeta_B(q) = \frac{q}{2} \quad (1.30)$$

The β for Brownian motion is $\beta = 2$.

Fractional Brownian motion. Fractional Brownian motion (FBM), is a generalization of Brownian motion and was introduced by [Kolmogorov \(1940\)](#) and later studied by [Mandelbrot and Van Ness \(1968\)](#). A possible definition is as follows: for $0 \leq H \leq 1$, a fractional Brownian motion $B_H(t)$ of parameter H is defined as a Gaussian process of mean 0 and covariance $\langle B_H(t)B_H(s) \rangle = \frac{1}{2}(|t|^{2H} + |s|^{2H} - |t-s|^{2H})$. The scaling moment function is given by:

$$\zeta_H(q) = qH \quad (1.31)$$

For $H = 1/2$ the Brownian motion is recovered and when $0 \leq H \leq 1/2$, increments are negatively correlated, whereas when $1/2 \leq H \leq 1$ increments are positively correlated. We also have $\beta = 1+2H$, so that time series modelled by FBM have a spectral exponent between 1 and 3.

Lévy stable motion. Lévy stable laws are generalizations of the Gaussian law, named after the French mathematician Paul Lévy (1886-1971).

The Lévy stable motion also are scaling, but because of the divergence of the moments of order α , the moment function is peculiar. For $q \leq \alpha$, one has $H = 1/\alpha$ and the moment function is linear of the form $\zeta_L(q) = q/\alpha$. For $q > \alpha$, the consequence of the divergence of moments is that it depends on the number of realizations, [Schmitt et al. \(1999\)](#); [Nakao \(2000\)](#) have shown this moment function to be bilinear. The equation for the scaling moment function is given by:

$$\zeta_L(q) = \begin{cases} \frac{q}{\alpha}; & q \leq \alpha \\ 1; & q > \alpha \end{cases} \quad (1.32)$$

this saturation for moments $q > \alpha$ comes from a cancellation of the effect of integration and of divergence of moments.

The power spectrum is not considered for such process, since this corresponds to a second order moment, for $\alpha < 2$, the second moment is not defined since it is diverging.

1.6 Summary

In this chapter, we have presented turbulence and the way turbulent fluctuations are statistically characterized, using scaling approaches such as power spectra and structure functions. Such framework helps to characterize intermittency for 1D or 2D processes. Such framework will be used to study in-situ (1D) data and satellite 2D data. The chapters 3 and 4 are dealing with the in-situ data of the Particle Size Distributions along with the current and tide. The chapters 5 and 6 deal with the satellite data of Chl-a and SST from the MODIS aqua using these turbulent tools.

CHAPTER 2

INTRODUCTION TO MARINE OPTICS AND OCEAN COLOUR REMOTE SENSING

Abstract

In this chapter, I will give brief descriptions of the composition of the natural waters, mainly oceanic. Then I briefly recall some of the major optical properties of the natural waters along with their units. I briefly recall Particle Size Distribution (PSD) and its importance in the aquatic sciences. I also provide the link between some of the properties like Absorption, Scattering and Attenuation to the reflectance of the water.

2.1 Composition of natural waters

Natural waters are complex composite physical-chemical-biological media of dissolved and particulate matter assemblages ([Stramski et al., 2004](#)). Together with air bubbles and pure sea water, these components determine the bulk inherent optical properties (IOPs) of natural water bodies. The constituents of natural waters are traditionally divided into “Dissolved” and “Particulate” matter, of organic and inorganic origins, living and non-living. When filtering a water sample, everything that passes through a filter paper of pore size $0.2 \mu m$ is called dissolved matter and

everything retained on the filter is called particulate.

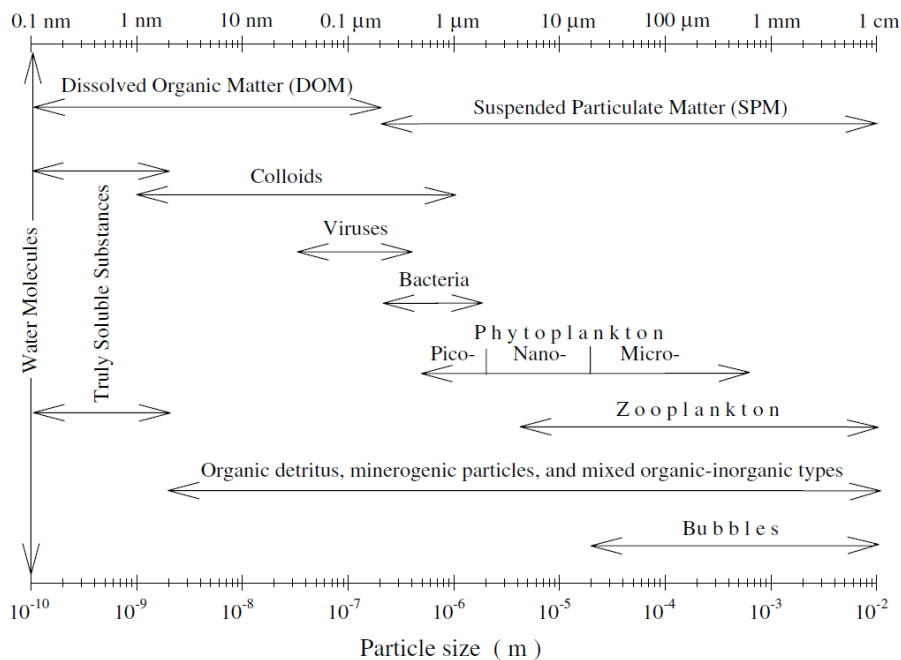


Figure 2.1: Schematic diagram of various seawater constituents in the broad size range from molecular size of the order of 10^{-10} m to large particles and bubbles of order of 10^{-3} - 10^{-2} m in size [Figure reprint from [Stramski et al. \(2004\)](#)].

2.1.1 Dissolved matter

The constituents of the dissolved matter are further classified into “Organic” and “Inorganic” origins.

Dissolved organic matter. Dissolved organic matter (DOM) concentrations in natural waters are consequences of either photosynthetic activity of phytoplankton, bacterial activity or direct inputs of terrestrially matter. The transformation of phytoplankton into DOM is a consequence of photolysis, hydrolysis and bacterial decomposition of the phytoplanktonic cellular structures. These compounds are produced by the decay of plant matter and consist mostly of various humic and fulvic acids ([Carder et al., 1989](#)). These compounds are generally brown in colour and in sufficient concentrations they can colour the water in yellowish brown. For this reason, these compounds are referred to yellow matter or coloured dissolved organic matter (CDOM). This substance is also referred as Gelbstoff. The biogeochemical

cycle of CDOM is driven by several physical and biological processes such as river input, biogeneration and photo-bleaching that act as primary sinks and sources of CDOM (Kirk, 1994; Vantrepotte et al., 2007; Loisel et al., 2014). The CDOM plays a central role in many physical, chemical and biological processes in aquatic ecosystems, including inhibiting attenuation of harmful ultraviolet radiation, affecting carbon budgets, nutrient availability and ecosystem productivity (Coble, 2007; Stedmon et al., 2007).

Dissolved inorganic matter. The pure sea water consists of pure water along with various dissolved salts, which average about 35 parts per thousand (35 ‰) by weight. These salts increase scattering above that of pure water by about 30 % (Mobley, 1994). These salts have a negligible effect on absorption at visible wavelengths, but it is likely that they increase an absorption somewhat at ultraviolet wavelengths (Mobley, 1994).

2.1.2 Particulate matter

The particulate matter in the ocean and coastal waters is composed of heterotrophic bacteria, phytoplankton, detritus, zoo-plankton, and mineral particles from biogenic or minerogenic origin. This particulate matter can directly be generated from biological processes occurring in water (primary production, the degradation process by bacteria activity, etc) or bring from land through local run-off, river plums, and dust deposition. These particulate matter are the major determiner of both the absorption and scattering properties of natural waters. They have both biogenic and minerogenic material whose relative amounts are variable in the ocean (Stramski et al., 2004; Balch et al., 2009).

Particulate Organic Matter. Organic particles include two major categories of particulate matter: living plankton micro-organisms (viruses, bacteria, and various phytoplankton and zoo-plankton species) and non-living organic detritus (break-down products of micro-organisms). Particulate organic matter, usually present ev-

erywhere, is an important component in floc formation since it acts as the glue that holds particles together. Particles of a given size are destroyed by breaking apart after death, by flocculation into larger aggregate particles or by setting out of the water column. The particles formed by organisms largely consist of organic matter (Riley, 1963).

Particulate Inorganic Matter. Inorganic particles include the various mineral species (clay minerals, quartz, feldspars, calcite and many others). The particulate inorganic matter are created primarily by weathering of terrestrial rocks and soils. The mechanisms which produce particulate inorganic matter in the aquatic environment are by inorganic processes (precipitation and flocculation) and break-up of sediments and rocks (erosion and re-suspension). These particles enter the water by wind-blown dust settled on the sea surface, as the river carry eroded soil to the sea, or as currents re-suspend bottom sediments.

2.2 Optical properties of the water

Natural waters, both fresh and saline, are a mixture of dissolved and particulate matter. These solutes and particles are both optically significant and highly variable in kind and concentration. Therefore, the optical properties of natural waters show large temporal and spatial variations and rarely resemble that of the pure water. The large-scale optical properties of natural waters are handily divided into two mutually exclusive classes: Inherent and Apparent (Mobley, 1994).

Inherent Optical Properties (IOPs) These are optical properties, which depend only upon the medium and, therefore, are independent of the ambient light field within the medium. Some of the *IOPs* are absorption coefficient, volume scattering function, index of refraction, beam attenuation coefficient and single scattering albedo.

Apparent Optical Properties (AOPs) These are the optical properties which depend both on the medium (*IOPs*) and on the geometric structure of the ambient light field. *AOPs* exhibit enough regular features and stability, so it can be used as useful descriptors of the water body. Some of the commonly used *AOPs* are the irradiance reflectance, the average cosines and various diffuse attenuation coefficients.

In the frame of this Ph.D. thesis we will mainly focus on scattering (or backscattering) processes, which will be used to assess the concentration of particles, as well as the Particle Size distribution, and the remote sensing reflectance. For that purpose, the following parts are dedicated to the definition of Particle size Distribution, scattering, absorption (as it affects the remote sensing reflectance), and the remote sensing reflectance (with introduction to ocean colour observation principles).

2.3 Particle Size Distributions (PSD)

The concentration and species composition of organic and inorganic particles vary greatly in the ocean. The particle size distribution in the ocean, which describes the particle concentration as a function of particle size/number, typically shows a rapid decrease in concentration with increasing size from a sub-micrometer range to hundreds of micrometers. This feature is common to all the suspended particles and also for plankton micro-organisms ([Jackson et al., 1997](#); [McCave, 1983](#); [Sheldon et al., 1972](#); [Stramski and Kiefer, 1991](#)).

Particles are 3-dimensional objects, and unless they are perfect spheres, they cannot be fully described by a single dimension such as a radius or diameter. In order to simplify the measurement process, it is often convenient to define the particle size using the concept of equivalent spheres. In this case, the particle size is defined by the diameter of an equivalent sphere having the same volume.

Weighted distribution. A particle size distribution can be represented in different ways with respect to the weighting of individual particles. The weighting mechanism will depend upon the measuring principle being used.

Number weighted distributions. A counting technique such as image analysis will give a number weighted distribution where each particle is given equal weighting irrespective of its size. This is often useful for deriving the PSD slope (ξ).

Volume weighted distributions. Static light scattering techniques such as laser diffraction will give a volume weighted distribution. In volume weighted distribution, the contribution of each particle distribution are related to the volume of that particle (equivalent to mass if the density is uniform), i.e. the relative contribution will be proportional to $(size)^3$. In the present study, we used LISST-100X type C instrument, which works on laser diffraction principle and derive volume concentrations of particle between 2.5 - 500 μm in 32 logarithmically spaced size classes.

Intensity weighted distributions. Active/Dynamic light scattering technique, sometimes called as Quasi Elastic Light Scattering (QELS) is a non-invasive well established technique for measuring the size and size distribution of molecules and particles typically in the sub-micron region. The active light scattering techniques will give an intensity weighted distribution, where the contribution of each particle in the distribution related to the intensity of light scattered by the particle. From Rayleigh approximation, the relative contribution of very small particles will be proportional to $(size)^6$.

It is possible to convert particle size data from one type of distribution to another, however this requires certain assumptions about the form of the particle and its physical properties. We cannot expect that the volume weighted particle size distribution measured using image analysis agree exactly with a particle size distribution measured by laser diffraction.

The variability of the marine particle size distribution (*PSD*) impacts the differ-

ent biological processes occurring in oceanic waters and vice versa. For instance, trophic interactions are tightly linked to the size distribution of the different living and non-living particles involved all over the trophic system (McCave, 1984). The size of the particles in the aquatic environment is measured in various ways. Visible microscopy can be used for particles greater in size than a few wavelengths of light; electron microscopy can be used for particles as small as nano-meters in size. These two methods are extremely tedious and time consuming if large number of the particles are counted and sized. Laser diffraction technique is the other technique to derive the volume concentration of the particles in the aquatic environment (Agrawal and Pottsmith, 2000).

More details of PSDs and its importance in the aquatic environments are given in the chapters 3 and 4.

2.4 Absorption, Scattering and Attenuation coefficients

The propagation of photons within a natural water body will undergo scattering and absorption interactions with the optically significant matter of natural water body (Mobley, 1994; Bukata et al., 1995). Both scattering and absorption interactions change the original subsurface radiance distribution as the photon flux propagates through the aquatic medium. Absorption and scattering processes combine to reduce the intensity of the radiance distribution while the scattering processes also change the directional character of the radiance distribution.

Absorption coefficient. A convenient form of Beer's Law (the absorbance of light is directly proportional to the thickness of the media through which the light is being transmitted multiplied by the concentration of absorbing chromophore) results from the consideration of the loss of energy from a beam of light (photons comprised of a spectrum of energy values $h\nu$). The absorption loss of beam energy from an initial radiant flux value of Φ_{inc} to a final radiant flux value of Φ_{trans} subsequent

to passing through an attenuating medium of thickness Δr would then be given by:

$$\Phi_{trans} - \Phi_{inc} = -a\Phi_{inc}\Delta r \quad (2.1)$$

where the constant of proportionality a is defined as the absorption coefficient. Since the beam attenuation coefficient is a function of wavelength λ , it follows from the above equation that:

$$\Phi(r, \lambda) = \Phi(0, \lambda)e^{-a(\lambda)r} \quad (2.2)$$

from which

$$a(\lambda) = -\frac{1}{\Phi(r, \lambda)} \frac{\partial \Phi(r, \lambda)]_{abs}}{\partial r} \quad (m^{-1}) \quad (2.3)$$

This provides the general definition of the absorption coefficient $a(\lambda)$ as the fraction of radiant energy absorbed from a beam as it travels an infinitesimal distance ∂r . To this point, we have considered attenuation of a photon flux or a radiant flux as due solely to absorption processes and independent of any attenuation due to scattering processes.

As IOPs are additive in nature, the bulk IOPs are the sum of pure seawater and all its individual constituents. Then the total absorption coefficient $a(\lambda)$ can be written as:

$$a(\lambda) = a_w(\lambda) + a_{DOM}(\lambda) + a_p(\lambda) \quad (2.4)$$

where w , DOM and p are the pure water, dissolved organic matter and particulate matter, respectively. The particulate are again subdivided into phytoplanktons and non algal particles.

Scattering coefficient. The radiant flux, however is also subject to attenuation due to scattering and in a manner similar to the development of absorption coefficient, the scattering coefficient $b(\lambda)$, defined as fraction of radiant energy scattered from a beam per unit distance as it travels an infinitesimal distance ∂r , is mathematically expressed as:

$$b(\lambda) = -\frac{1}{\Phi(r, \lambda)} \frac{\partial \Phi(r, \lambda)]_{scatt}}{\partial r} \quad (m^{-1}) \quad (2.5)$$

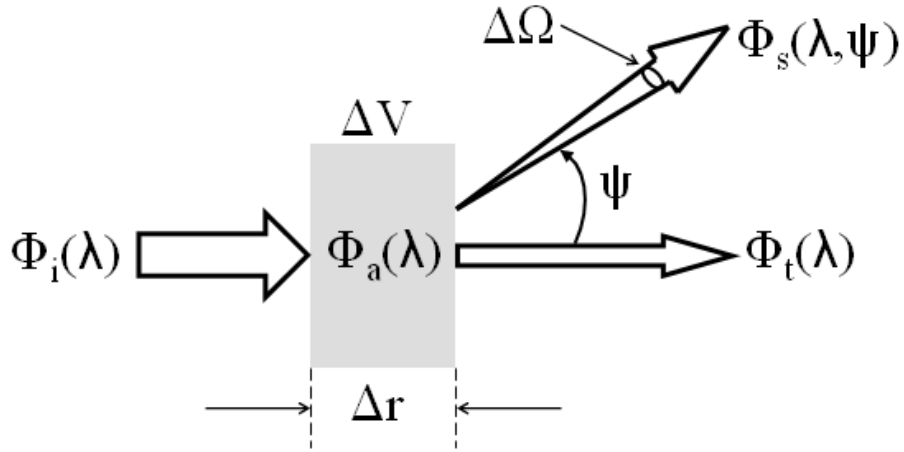


Figure 2.2: Illustration of absorption, scattering and transmission [Figure reproduced from Mobley et al. (2011)].

where the subscript *scatt* denotes that the diminution of radiant energy as it traverses an infinitesimal distance ∂r is due entirely to scattering processes. The above equation describes the attenuation of a radiant flux of wavelength λ in the absence of absorption processes in the same way of the absorption coefficient describes the attenuation of radiant flux of wavelength λ in the absence of scattering processes.

This $b(\lambda)$ is obtained by integration of volume scattering function $\beta(\theta, \phi, \lambda)$ over all scattering directions θ and ϕ :

$$b(\lambda) = \int_0^{4\pi} \beta(\theta, \phi, \lambda) d\Omega = \int_0^{2\pi} \int_0^{\pi} \beta(\theta, \phi, \lambda) \sin\theta d\theta d\phi \quad (2.6)$$

where θ and ϕ are the nadir and azimuthal scattering angles and Ω is the solid angle in the direction of (θ, ϕ) . The back scattering coefficient $b_b(\lambda)$ can be derived by integration over back directions. In natural waters, particles are assumed to be randomly oriented, so that:

$$\begin{cases} b(\lambda) = 2\pi \int_0^{\pi} \beta(\theta, \lambda) \sin\theta d\theta \\ b_b(\lambda) = 2\pi \int_{\pi/2}^{\pi} \beta(\theta, \lambda) \sin\theta d\theta \end{cases} \quad (2.7)$$

In general, the components of natural water responsible for the scattering are the pure water and particulate matter. Then total back scattering of natural water be-

comes:

$$b_b(\lambda) = b_{bw}(\lambda) + b_{bp}(\lambda) \quad (2.8)$$

where $b_{bw}(\lambda)$ and $b_{bp}(\lambda)$ are backscattering due to pure water and particulate matter, respectively.

Beam attenuation coefficient. In a natural medium such as air and water where both absorption and scattering processes are responsible for attenuation, the beam attenuation coefficient, $c(\lambda)$ is defined as the fraction of radiant energy removed from an incident beam per unit distance as it traverses an infinitesimal distance ∂r due to the combined processes of absorption and scattering. The beam attenuation coefficient is then mathematically defined as the sum of the absorption coefficient and the scattering coefficient.

$$c(\lambda) \equiv a(\lambda) + b(\lambda) \quad (2.9)$$

or, equivalently,

$$c(\lambda) \equiv -\frac{1}{\Phi(r, \lambda)} \left[\left(\frac{\partial \Phi(r, \lambda)_{abs}}{\partial r} \right) + \left(\frac{\partial \Phi(r, \lambda)_{scatt}}{\partial r} \right) \right] \quad (m^{-1}) \quad (2.10)$$

The units of $a(\lambda)$, $b(\lambda)$ and $c(\lambda)$ are all m^{-1} .

Measurements of $a(\lambda)$, $b(\lambda)$ and $c(\lambda)$. The most widely used in situ instruments for measuring absorption $a(\lambda)$ and attenuation $c(\lambda)$ are the WET Labs ac-9 (multi-wavelength) and ac-s (hyper-spectral). The particulate scattering $b_p(\lambda)$ is measured from these instruments as the difference between the simultaneous measurements of $a(\lambda)$ and $c(\lambda)$ after proper correction have been applied to ultra-pure Milli-Q (Sullivan et al., 2005).

The other instruments which measure the backscattering are the WET Labs BB-9 and HOBI Labs Hydroscat (Jonasz and Fournier, 2011). These instruments are widely used to measure the backscattering based on single angle measurements of

$\beta(\theta, \lambda)$.

2.5 The principle of ocean colour radiometry

Reflectance. The commonly used *AOP* is the spectral irradiance reflectance $R(z; \lambda)$, defined as the ratio of spectral upwelling to downwelling plane irradiances:

$$R(z; \lambda) \equiv \frac{E_u(z; \lambda)}{E_d(z; \lambda)} \quad (2.11)$$

$R(z; \lambda)$ is often evaluated in the water just below the surface; we denote this depth by $z = w \approx 0$.

Remote sensing reflectance. The spectral remote sensing reflectance R_{rs} is defined as the ratio of up-welling radiance to downwelling irradiance.

$$R_{rs}(\theta, \phi; \lambda) \equiv \frac{L(z = a; \theta; \phi; \lambda)}{E_d(z = a; \lambda)} \quad (sr^{-1}) \quad (2.12)$$

$$L_u(\text{in air}, \theta, \phi, \lambda) = L_w(\theta, \phi, \lambda) + L_r(\theta, \phi, \lambda)$$

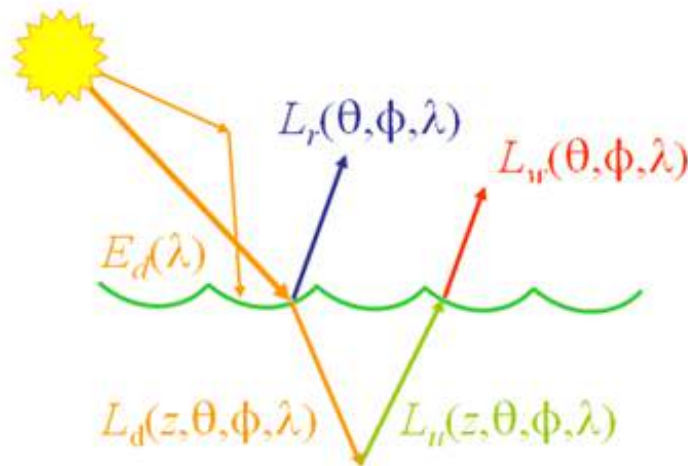


Figure 2.3: Illustration of light rays contributing to L_u as measured above the sea surface (after Mobley et al. (2011)).

Here depth $z = a$ indicates that R_{rs} is evaluated using upwelling radiance L_u and downwelling irradiance E_d in the air, just above the water surface; this L_u is

often called as “water-leaving” radiance. Ocean colour radiance is the wavelength-dependent solar energy captured by an optical sensor looking at the sea surface. These water-leaving radiances contain information on the ocean albedo and information on the optical constituents of the sea water, in particular phytoplankton pigments (e.g., chlorophyll-a). It is also affected by sun and sky reflection that should be corrected. A specific geometric observation configuration is adopted for field measurement to reduce this reflection effects. Data analysis is not easy as at satellite altitudes the relatively weak ocean colour radiance signal (5-15% of incident solar radiation) propagates through the atmosphere before detection.

[Gordon et al. \(1988\)](#) proposed a simplified reflectance model for the direct link between IOPs and AOPs as:

$$r_{rs}(\lambda) = \frac{f'}{Q} \frac{b_b(\lambda)}{a(\lambda) + b_b(\lambda)} \quad (2.13)$$

where r_{rs} is the subsurface remote sensing reflectance.

$$r_{rs}(\lambda) = \frac{L_w(\theta, \phi, \lambda, 0-)}{E_d(\lambda, 0-)} \quad (2.14)$$

f' is the dimensionless reflectance model factor ([Morel and Gentili, 1991](#)) and Q is the ratio of subsurface upwelling radiance to the subsurface upwelling radiance in the viewing direction. The subsurface remote sensing reflectance can be related to remote sensing reflectance by:

$$\pi \Xi r_{rs}(\lambda) = \pi R_{rs}(\lambda) \quad (2.15)$$

where Ξ represents reflection and refraction effects at sea surface. The typical value of this Ξ is derived by [Morel and Gentili \(1996\)](#) as $\Xi = 0.529$. The value of f'/Q found for sediment dominated waters: $f'/Q = 0.13$ by [Loisel and Morel \(2001\)](#).

The remote sensing reflectance is a measure of how much of the downwelling light that is incident onto the water surface is eventually returned through the surface in direction (θ, ϕ) , so that it can be detected by a radiometer pointed in the

opposite direction. Both R and R_{rs} are of great role in the satellite oceanography.

2.6 Bio-optical algorithms for Chlorophyll-a

Satellite remote sensing is the adequate method for monitoring the phytoplankton biomass in the coastal and oceanic waters synoptically. The task of estimating Chl-a from remotely-sensed ocean colour has been considerably difficult at regional and local scales because the spectral inherent optical properties (IOPs) of the ocean influencing the colour of the ocean are both diverse and complex.

The first use of the ocean colour measurements was carried out by on-board Nimbus 7 satellites sensor of CZCS (Coastal Zone Colour Scanner) launched in 1978 followed by many sensors like SeaWiFS, OCM, MERIS, MODIS and GOCI. The images provided by the CZCS sensor have completely changed the oceanographic concepts of the distribution of biomass in the coastal waters (Bricaud et al., 1987; McGillicuddy et al., 2001). In our study, we are interested in the MODerate resolution Imaging Spectroradiometer (MODIS) sensor, from which the images were acquired. The R_{rs} measured by the satellite is the input for the algorithms which compute the Chl-a concentrations. In this thesis, we used Chl-a derived using OC3M (O'Reilly et al., 2000) algorithm of MODIS Aqua. The form of the OC3M algorithm is:

$$\log[Chl - a] = a_0 + a_1X + a_2X^2 + a_3X^3 + a_4X^4 \quad (2.16)$$

where

$$X = \left[\frac{\max(R_{rs} - 443, R_{rs} - 488)}{R_{rs} - 547} \right] \quad (2.17)$$

and the coefficients a_0, a_1, a_2, a_3, a_4 are 0.2424, -2.7423, 1.8017, 0.0015 and -1.2280 respectively.

2.7 Remarks

The main objective of this Ph.D. thesis is to understand the high temporal variability of suspended particulate matter and its spatial distribution in relation to some physical forcing processes occurring during relatively short time periods. To understand the temporal heterogeneity we have conducted time series measurements of 3 field samplings from the Eastern English channel. We have used AC-S, ECO-FLRT, ECO-FLCDRT, LISST-100X type C, Troll, Nortek Vector Velocimeter and ADCP RD instruments.



Figure 2.4: Instruments (bio-optical and hydro-graphic) mounted over the sea-spider for the in situ sampling; done in the laboratory of oceanology and geosciences, Wimereux.

AC-S measures absorption and attenuation coefficients, ECO-FLRT measures

the Chlorophyll-a fluorescence, ECO-FLCDRT measures the CDOM fluorescence, LISST-100X measures the volume concentration of the particles from 2.5-500 μm , Troll measures the turbidity along with temperature and salinity, Nortek Velocimeter measures the point measurement of velocity components (x,y and z directions) and ADCP measures the velocity profiles of x,y and z components at every 0.4 m.

Concerning the first two sampling, after retrieving the instruments, unfortunately we found that the quality of the data was very poor, so we discarded that data from my thesis. For the third sampling, some of the instruments did not work (AC-S, ECO-FLRT and ECO-FLCDRT). That is why we could not incorporate many of the bio-optical data sets in the present thesis.

CHAPTER 3

HIGH FREQUENCY VARIABILITY OF PARTICLE SIZE DISTRIBUTION AND ITS DEPENDENCY ON TURBULENCE OVER THE SEA BOTTOM DURING RE-SUSPENSION PROCESSES

This chapter was published as Renosh et al., 2014. In open access available from <http://www.sciencedirect.com/science/article/pii/S0278434314000454>

Renosh, P. R., Schmitt, F. G., Loisel, H., Sentchev, A., Meriaux, X., 2014. High frequency variability of particle size distribution and its dependency on turbulence over the sea bottom during re-suspension processes, *Continental Shelf Research*, 77, 51-60.

Abstract

The impact of tidal current, waves, and turbulence on particles re-suspension over the sea bottom is studied through eulerian high frequency measurements of velocity and particle size distribution (PSD) during 5 tidal cycles (65 hours) in a coastal environment of the eastern English Channel. High frequency variability of PSD is observed along with the velocity fluctuations. Power spectral analysis shows that turbulent velocity and PSD parameters have similarities in their spectral behaviour

over the whole range of examined temporal scales. The low frequency variability of particles is controlled by turbulence ($\beta \simeq -5/3$) and the high frequency is partly driven by dynamical processes impacted by the sea bottom interactions with turbulence (wall turbulence). Stokes number (St), rarely measured in situ, exhibits very low values, emphasizing that these particles can be considered as passive tracers. The effect of tide and waves on turbidity and PSD is highlighted. During slack tide, when the current reaches its minimum value, we observe a higher proportion of small particles compared to larger ones. To a lower extent, high significant wave heights are also associated with a greater concentration of suspended sediments and the presence of larger particles (larger Sauter's diameter D_A , and lower PSD slope ξ).

3.1 Introduction

Marine particles cover a broad range in diameters from nanometers, mainly as colloids, to few millimeters and even centimeters in presence of big *Phaeocystis* colonies, diatoms chains, or cyanobacteria filaments. Intermediate size particles include viruses, heterotrophic bacteria, pico-, nano-, and micro-, phytoplankton, micro-, meso-, and macro-zooplankton, non-living particles, and mineral particles (Stramski et al., 2004). These particles do not solely appear as individual entities in the water column, but are mainly present as marine algal flocs and aggregates (Eisma, 1986; Fowler and Knauer, 1986; Hill, 1998; Boss et al., 2009). The variability of the marine particle size distribution (PSD), impacts the different biological processes occurring in oceanic waters, and vice versa. For instance, trophic interactions are tightly linked to the size distribution of the different living and non-living particles involved all over the trophic system (McCave, 1984). On the other way, blooms of specific phytoplankton species modify the general PSD shape by affecting one given size class. Phytoplankton degradation processes as well as zooplankton grazing also affect the PSD shape by promoting the small particles size classes compared to larger ones. Physical processes occurring in the water col-

umn are also related to the PSD. For example, the settling velocity of the suspended matters is strongly controlled by the particles size. In contrast, the size distribution of floc or aggregate depends on the balance between aggregation and breakage, two processes driven by diffusive turbulent transport and differential settling (McCave, 1984). McCave suggested that particles in the Brownian range ($< 1.0 \mu m$) are pumped rapidly into larger size classes by aggregation. The instantaneous turbulent kinetic energy modifies the proportion between particles/floccule, fine and coarse microflocs, and macroflocs (Lefebvre et al., 2012). The re-suspension of marine sediments are also strongly size dependent (Wells and Goldberg, 1992; Mikkelsen and Pejrup, 2001; Fettweis et al., 2006).

Turbulence is one of the most important physical phenomenon which determines the re-suspension and settling of the suspended particles in the coastal as well as oceanic waters (Eisma, 1986; Van Leussen, 1988; Umlauf and Burchard, 2005; Fettweis et al., 2006; Burchard et al., 2008; Van der Lee et al., 2009). For instance, observations on floc in the field show that smaller flocs occur in high energy environments (Kranck and Milligan, 1992; Berhane et al., 1997). At a critical magnitude of turbulence, shear overcomes the binding strength of flocs and tends to destroy aggregates (Eisma, 1986). For primary (disaggregated) particles significantly larger than $1.0 \mu m$, and for the process of smaller flocs (microflocs) growing into larger flocs (macroflocs), turbulent shear is thought to be the dominant collision mechanism, except during periods of slack current velocities when differential settling of suspended particles on to one another may be responsible for most of the flocs formation and rapid clearing of the water (Van Leussen, 1988).

Studies done by Wolanski and Gibbs (1995) in Fly River Estuary show that the mean floc size was affected by the turbulence of tidal currents. The largest floc size were observed in the low tidal currents ($< 0.5 m/s$) and comparatively smaller floc sizes were observed in the high tidal currents ($> 0.5 m/s$).

In the present study, we analyse the dynamics of PSD and its relation with turbulence from in situ measurements. We conducted simultaneous measurements of velocity and PSD from instruments fixed on a frame positioned on the sea floor in

the coastal waters of eastern English Channel. This study area, characterized by low depth, exhibits a large range of variability of bio-optical properties related to the occurrence of difference phytoplankton blooms, bottom sediments re-suspension confined in the coastal areas, and numerous river inputs (Velegrakis et al., 1999; Loisel et al., 2007; Vantrepotte et al., 2007). The study carried out by Velegrakis et al. (1999) showed that re-suspension of fine-grained particles takes place during the spring tides and correlates well with the distribution of the bottom lithological type. In this paper, we will assess whether the re-suspended particles are passive tracers, or have an inertia that influences their transport by turbulence. For this, we estimate from in situ measurements their Stokes number St , which is a dimensionless number explaining the effect of inertia on the particles in a fluid motion. The impact of hydro-dynamical forcing on the particles behaviour is examined for different size classes of particles (silt/clay, fine, micro/coarse and macro flocs).

In the first section we present the study area as well as the different measurements and methods used to assess the coupling between turbulence and the particles behaviour over the sea bottom. The meteorological and hydrodynamic contexts occurring during the field measurements are then provided in the next section. The velocity field and particle size distribution variability are described and their relationships are analysed. The Stokes numbers of these different particles, rarely measured in situ, are also estimated.

3.2 Data and methods

3.2.1 Study area

The measurements were conducted in the coastal waters of the eastern English Channel at a fixed station ($50^{\circ}45.676N$, $01^{\circ}35.117E$) from the 25 to the 28 of June 2012 (Fig. 3.1A). The different instruments (explained in the data section) are fixed on a structure which was positioned on the seafloor. The English Channel is a mega tidal sea having a tidal range that varies from 3 to 9 m, and experiencing a tidal

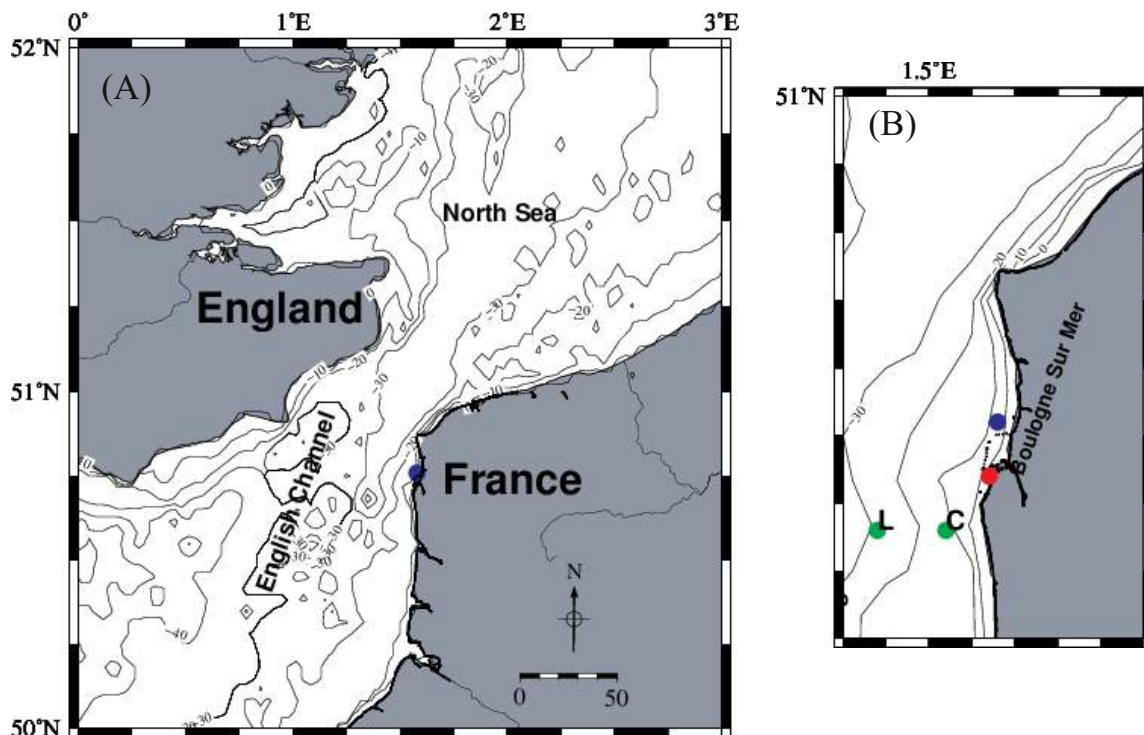


Figure 3.1: Location (blue dot) of the sampling area in the eastern English Channel together with the isobaths (A). Zoom on the sampling area (blue dot), the meteorological station (red dot) and SOMLIT stations (green dot) in (B).

current of amplitude close to 1.0 m/s (Desprez, 2000; Seuront and Schmitt, 2005; Korotenko et al., 2012). The biogeochemical environment during the particular sampling period is defined from in-situ data collected few days before the experiment (the 21 of June) in the frame of the SOMLIT program in two different areas and in high tide period (Fig. 3.1B). A strong stratification can be noticed, especially for the suspended particulate matter (SPM), which increases by a factor of 15 from the surface to the bottom at the coastal station (Table 3.1). However the SPM values are relatively low for a coastal environment, in good agreement with the summer low fresh water discharge, and the absence of phytoplankton bloom. The particulate carbon concentration is however relatively high. Besides, the relatively high POC/Chl-a ratio values, a proxy of the carbon mass of living and non-living organisms with respect to the autotrophic organisms (Loisel et al., 2007), indicates that the particulate organic fraction is largely dominated by detritus and heterotrophic bacteria.

Site	Date	Depth	Temp.(°c)	Salinity(psu)	POC($\mu\text{g/l}$)	SPM(mg/l)	Chl-a($\mu\text{g/l}$)
C	21-06-2012	Surface	15.83	34.43	341.9	0.1	0.5
C	21-06-2012	Bottom	14.82	34.76	239.67	1.54	0.5
L	21-06-2012	Surface	14.88	34.93	220.9	0.48	1.21
L	21-06-2012	Bottom	13.92	35.06	85.804	1.63	0.18

Table 3.1: Biogeochemical and optical data collected from SOMLIT before the time series measurements from the stations C and L (shown in Figure 1B).

3.2.2 Data

High frequency time series data were collected at 0.5 meter depth above the sea bottom from different instruments fixed on the same platform moored on the sea bed. The three following instruments were used for the present study: a LISST-100x type C (Laser In-Situ Scattering and Transmissometry, Sequoia Scientific), a Nortek Vector ADV current meter, and a RDI ADCP. The LISST measures the volume concentration of particles having diameters ranging from 2.5 to 500 μm in 32 size classes in logarithmic scale (Agrawal and Pottsmith, 2000). It also records the beam attenuation (c) at 670 nm ($\pm 0.1\text{ nm}$) over a 5 cm path length with an acceptance angle of 0.0135° . The particulate beam attenuation coefficient c_p has been derived from c after calibration with MilliQ water before and after the field campaign, using the assumption that chromophoric dissolved organic matter (CDOM) does not absorb the light at 670 nm. The volume concentration and c_p are measured with a sampling frequency of 1.0 Hz. The Nortek Vector ADV current meter measured the North, East and up components of the local velocity components with an accuracy of $\pm 0.5\%$ at every 1 Hz. The available range of the velocity value measured by the instrument is from 0.01 to 7.0 m/s ($\pm 0.01\text{ m/s}$). A 1.2 MHz upward-looking four beam broadband RDI ADCP was also deployed on the bottom, along with the previous cited instruments clubbed in a structure. The ADCP was operated in the fast ping mode, providing two profiles per second. Each velocity was an average of six short pulse measurements over a 2 Hz interval. The velocities were recorded in Cartesian co-ordinates with 0.4 m vertical resolution. The significant wave height H_s , peak wave period T_p , and peak wave direction D_p are derived from the ADCP data using manufacture provided software WavesMon (Teledyne RD Instruments).

These wave parameters were computed for 10 minutes burst duration with a moving window of 5 minutes interval providing one data point every 5 minutes. The wind data were provided by the meteorological station of harbour, Boulogne-Sur-Mer light house (Meteo-France) with a temporal resolution of 1 hour.

3.2.3 Methods

Particle Size Distributions and power law of PSD. The scattering patterns of particles at 670 nm are recorded in 32 logarithmically size scattering angles by the LISST-100X type C (Agrawal and Pottsmith, 2000). This instrument measures the volume concentration $C_{vol,i}$ ($\mu l/l$) of the particles in 32 size classes from 2.5 to 500 μm through diffraction technique. Because of instability in the smallest and largest size classes, the data recorded in the first five inner and last outer rigs are excluded from further analysis (Traykovski et al., 1999; Jouon et al., 2008; Reynolds et al., 2010; Neukermans et al., 2012a). These instabilities observed in the smaller size classes have also been related to effects of stray light (Reynolds et al., 2010). Due to multiple scattering effects and signal to noise ratio sensitivity, the data for which optical transmission values are less than 30% and greater than 98% are also disregarded from the statistical analysis (personal communication with Ole Mikkelsen).

The volume concentration distributed on a particle size class can also be expressed as the concentration $C_{vol}(\sigma)$ per unit volume per unit bin width (Jouon et al., 2008):

$$C_{vol}(\sigma) = \frac{C_{vol,i}}{\sigma_{\max}(i) - \sigma_{\min}(i)} \quad (3.1)$$

where σ is the median diameter of the particle size class i , $\sigma_{\max}(i)$ and $\sigma_{\min}(i)$ are respectively the maximum and minimum particle size of the class i . This resulting volumetric PSD is expressed in $\mu l l^{-1} \mu m^{-1}$. The number of particles for a size σ of the PSD is estimated by a normalisation by their volume (Jouon et al., 2008). We obtain the number density $n(\sigma)$, which is also the product of the probability density

function of the size, $p(\sigma)$, times N , the total number of particles:

$$n(\sigma) = Np(\sigma) = \frac{C_{vol}(\sigma)}{\frac{4}{3}\pi(\sigma/2)^3} \quad (3.2)$$

The PSD of this density number classically follows a power law distribution for aquatic particles in suspension (Sheldon et al., 1972; Kitchen et al., 1982; Jonasz, 1983; Boss et al., 2001a; Twardowski et al., 2001; Loisel et al., 2006; Reynolds et al., 2010).

$$n(\sigma) \sim K\sigma^{-\xi} \quad (3.3)$$

where K is a constant and ξ is the PSD slope. The value of $\xi(t)$ is here estimated at each time step (every second) from the LISST measurements, using an automatic regression analysis. The ξ value provides information on the relative concentration of small and large particles: the steeper the slope (the greater ξ), the more small particles relative to large particles are present in the water (and vice versa).

Mean particulate diameters. Sauter's diameter (D_A) is the mean diameter of an equivalent sphere which has the same specific surface area as that of the PSD. This diameter is commonly used in sedimentology to represent size distribution in fluid flow calculation. The Sauter's diameter D_A is also computed from the PSD using the following equations (Neukermans et al., 2012a; Filippa et al., 2012):

$$D_A = \frac{\sum_{i=6}^{31} [AC]_i \sigma_i}{[AC]} = \frac{\int_{\sigma_6}^{\sigma_{31}} n(\sigma) \sigma^3 d\sigma}{\int_{\sigma_6}^{\sigma_{31}} n(\sigma) \sigma^2 d\sigma} = \frac{\int_{\sigma_6}^{\sigma_{31}} p(\sigma) \sigma^3 d\sigma}{\int_{\sigma_6}^{\sigma_{31}} p(\sigma) \sigma^2 d\sigma} \quad (3.4)$$

$$[AC]_i = \frac{3}{2\sigma_i} C_{vol}(\sigma) \quad (3.5)$$

where $[AC]_i$ is the cross sectional area concentration of particles in bin i , and $[AC]$ is the total cross sectional area.

The following size classification has been adopted: silt/clay ($< 30\mu m$), fine ($< 105\mu m$), coarse/micro ($< 300\mu m$) and macro-floc ($> 300\mu m$) (Lefebvre et al., 2012). The volume concentration of each size class has been analysed using statistical and

dynamical approaches.

Stokes number. In turbulent flows, the largest turbulent eddies break-up into smaller eddies through an energy cascade and finally dissipate at small scale due to molecular viscosity. The length of these smallest eddies is the Kolmogorov length scale. The eddies at this scale have typical life time τ_η which is the smallest time scale of turbulence. The Stokes number St is defined as the non-dimensional ratio of an inertial characteristic time scale τ_p , to τ_η . It is one of the fundamental parameter characterising particle-turbulence interactions: for $St \ll 1$, particles follow passively the fluid flow, whereas for $St \gg 1$, large inertia particles are not influenced by turbulence, and follow their own trajectories. It can also be related to the particles and fluid characteristics (Wang et al., 2000; Schmitt and Seuront, 2008; Xu and Bodenschatz, 2008) as follows:

$$St = \frac{\tau_p}{\tau_\eta} = C_p \left(\frac{\sigma}{\eta} \right)^2 \quad (3.6)$$

with $C_p = B/18$, where $B = \rho_p/\rho$ is the ratio of the particle density to the fluid density, and $\eta = (\nu^3/\epsilon)^{1/4}$ is the Kolmogorov length scale, where ν and ϵ are the kinematic viscosity of the fluid (in m^2s^{-1}) and the dissipation rate (in m^2s^{-3}), respectively.

The value of the dissipation rate ϵ is estimated using the power spectrum of the velocity time series, assuming a local isotropic Kolmogorov relation of the form (Pope, 2000).

$$E(k) = C\epsilon^{2/3}k^{-5/3} \quad (3.7)$$

where $E(k)$ is the Fourier power spectrum, $C = 1.5$ is a constant and k is the wavenumber. Since the power spectrum is here estimated from a time series in a fixed point, we estimate $E(f)$ where f is the frequency. Frequency and wavenumber are related with the horizontal component of the velocity V : $k = 2\pi f/V$. This gives the following estimation of the dissipation, from the power spectrum (Sethuraman et al., 1978; Lien and D'Asaro, 2006; Gerbi et al., 2009; Huang et al., 2012; Thomson et al.,

2012):

$$\epsilon = \left(\frac{C_0}{C}\right)^{3/2} \left(\frac{2\pi}{\sigma_V}\right)^{5/2} \quad (3.8)$$

where σ_V is the standard deviation of V and C_0 is the constant such that $E(f) = C_0 f^{-5/3}$ is a best fit estimated over a range of frequencies corresponding to the inertial range.

3.3 Results

3.3.1 Meteorological and hydrodynamic conditions

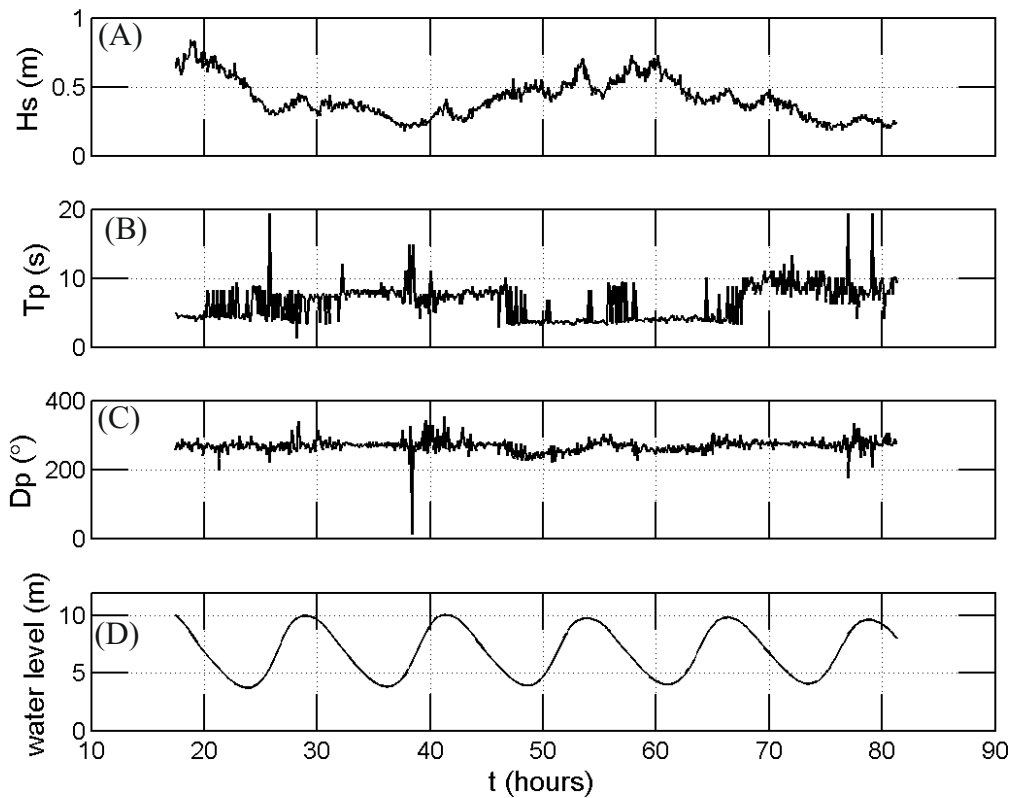


Figure 3.2: Time series of A) the significant wave height H_s , B) peak wave period T_p , C) peak wave direction D_p , and D) water level.

Figure 3.2 shows the hydrodynamic conditions prevailing in the study area during the observations. The significant wave height H_s exhibits relatively large vari-

ability in its magnitude during the entire time series observation (from 0.18 to 0.84 meters). The mean and standard deviation values of H_s are 0.41 and 0.14 m, respectively. The peak wave period, T_p , also presents a relatively great variability from few seconds to 20 seconds, with a mean and standard deviation values of 6.41 and 2.44 s, respectively. In contrast, the peak wave direction, D_p , is almost constant during the entire experiment, with a mean value around 268° , which reveals that, the waves are coming from the West. The water level shows typical semi diurnal tidal characteristics with a period of 12.42 hours. The total water column depth observed during the low tide time and high tide time is 3.74 m and 10.07 m, respectively, revealing the spring tide conditions.

Relatively large wind fluctuations in terms of amplitude and direction are observed during the experiment. Relatively high wind speed values (above 4 ms^{-1}) are generally associated with South West wind (except at the end of the experiment); whereas relatively low wind speeds values (less than 4 ms^{-1}) are generally associated with South East wind.

From the water level evolution and current data set provided by ADCP, the effect of tidal current on the PSD can be analysed. The interval when the speed of the tidal current is very weak or zero, usually refers to the period of reversal between ebb and flood currents, and also refers to the slack tide. The vertically averaged current velocity (VACV) has been derived for the entire time series (Fig. 3.3). VACV shows minimum values during the current reversal time, and two maxima, the main ones corresponding to the high tide (high water), and the second ones, reached at low tide (low water) (Fig. 3.3). The consecutive intervals of time between flood to ebb and ebb to flood is (7-7.34 h) greater than ebb to flood and flood to ebb (5.1 - 5.42 h), evidencing a pronounced asymmetry of tidal currents (Fig. 3.3).

3.3.2 Stokes number

The estimation of horizontal power spectra (U and V components) were used to estimate the constant C_0 in equation(3.8) and hence the dissipation rate. The mean

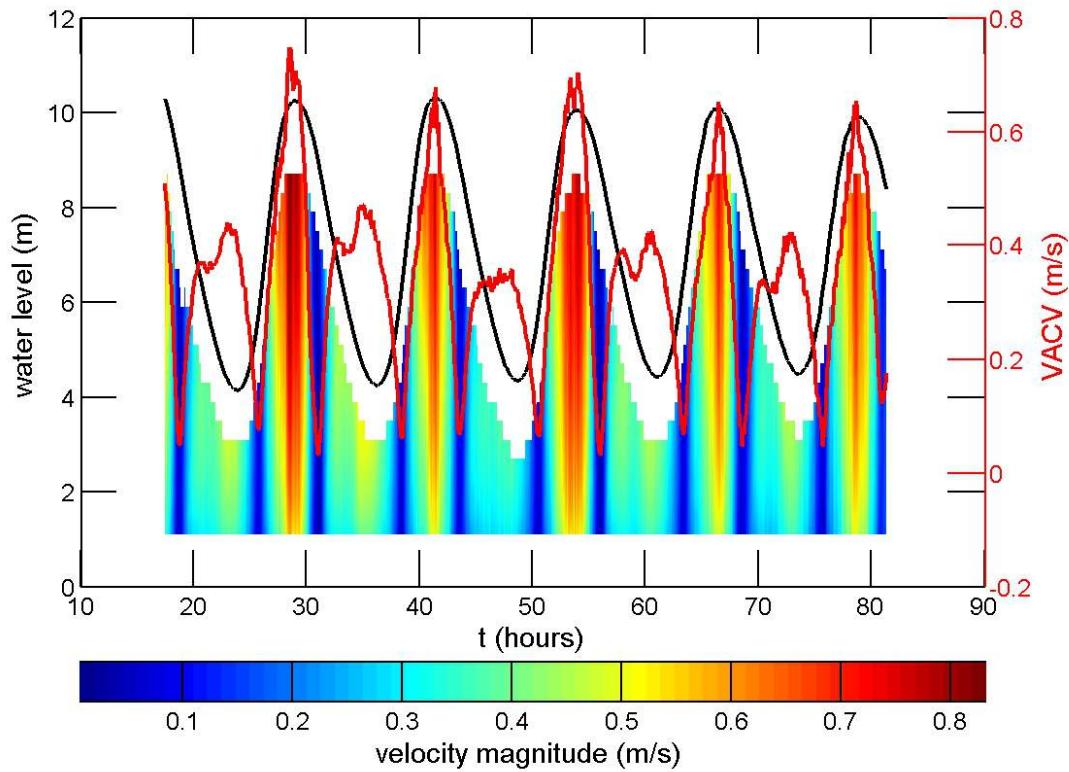


Figure 3.3: Time series of water level evolution along with tide (black line), time series of VACV (in red) and contour map showing the vertical structure of the current velocity.

value of the dissipation rate over the sampling day is $\epsilon = 7.65 \times 10^{-7} \text{ m}^2\text{s}^{-3}$. Since the mean temperature value is $T = 16.11^\circ\text{C}(\pm 0.10)$, the viscosity value is fixed at $\nu = 1.133 \times 10^{-6} \text{ m}^2\text{s}^{-1}$ (Kestin et al., 1981) and hence the Kolmogorov dissipation length scale $\eta = (\nu^3/\epsilon)^{1/4} = 1.2 \text{ mm}$. Because the mass density is not measured in the present study, two extreme values are imposed to assess the ratio of the particle density to the fluid density, B . The mass density of mineral and organic particles are $\rho_p = 2.7 \pm 0.15 \text{ gcm}^{-3}$ and $\rho_p = 1.06 \pm 0.03 \text{ gcm}^{-3}$, respectively (Chiappa-Carrar et al., 2006); resulting in B values of $2.7 \pm 0.15 \text{ gcm}^{-3}$ and 1.06 ± 0.03 , respectively. Using equation (3.6), these range of values for B , the estimation of ϵ and the range of particle sizes detected by the LISST (6.20 to 390 μm), we obtain Stokes numbers ranging from 6.8×10^{-7} to 0.03 for mineral particles and from 2.66×10^{-7} to 0.01 for organic particles. The largest values of the Stokes number are found for the largest

particles ($\sim 0.39 \text{ mm}$), which are still almost four times smaller than the Kolmogorov scale. This shows that the Stokes numbers are here always very small, and that these particles are likely to be passive tracers and move along with the fluids.

3.3.3 Temporal variability of the velocity field

The time series of along-shore (U) and cross-shore (V) components of the velocity and their corresponding power spectra were estimated using the ADV data (Fig. 3.4). The along and cross shore velocity components are characterized by a periodicity of 12.42 hours, and a large small scale variability with a coefficient of variation (i.e., a ratio of standard deviation to the mean value of the absolute velocity also called as turbulent intensity) value for the along-shore and cross-shore components of 64.28 and 50.48 %, respectively (Fig. 3.4 A-B). These velocity records are tightly linked to the tidal cycle which also exhibits a period of 12.42 hours. The along-shore component is characterized by a higher variability compared to the cross-shore component. The variability patterns of U and V are analysed through their power spectra (Fig. 3.4C). At low frequency scaling ranges, the power spectra of the two horizontal components (U and V) are characterized by a power law with a slope (β) close to $-5/3$ associated with 3D homogeneous turbulence (Kolmogorov scaling). From $T = 1000s \sim 17min$ there is a transition to a regime for which the power spectra is characterized by a lower slope value (close to -0.6). Similar kind of β value has been observed in the 1-min summer rainfall time series data with a scaling regime from 1 h to one day (Yonghe et al., 2013). At high frequencies (0.1 to 0.3 Hz, hence on the range 3 to 10 s), the energy spectra exhibit the impact of a localized forcing. Such forcing has previously been attributed to the high energy associated with wave breaking scales (Schmitt et al., 2009).

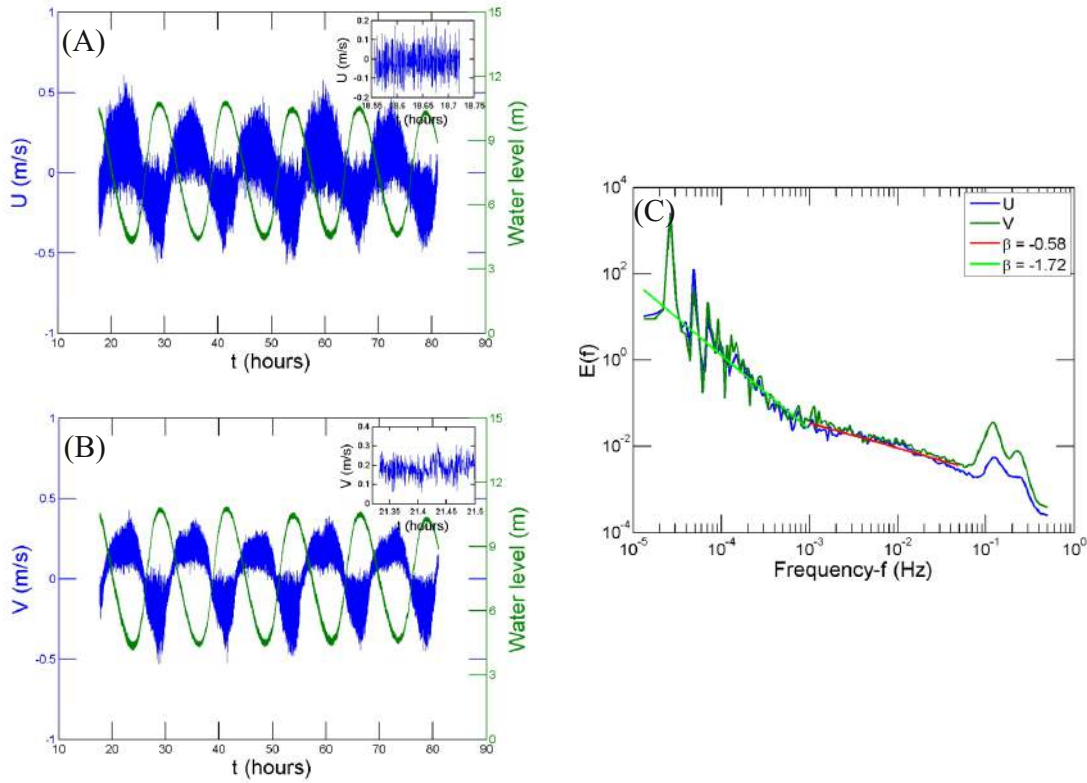


Figure 3.4: Time series of U (A) and V (B). The insets represent a small portion of the time series to show the fluctuations. (C) Power spectra of U (blue curve) and V (green curve). The two straight lines correspond to two different scales with slopes of -1.72 (near to $-5/3$ slope of Kolmogorov) in light green and -0.58 in red and the humps in the energy value at high frequency represents a small scale forcing of high energy wave breaking.

3.3.4 Temporal variability patterns of particles concentration and size parameters in relation with hydrodynamical forcing.

The size parameters considered here are the slope ξ of the PSD, as well as D_A and the normalised volume concentration of different size classes (silt/silt, fine, coarse/micro and macro-floc) of aggregates (Lefebvre et al., 2012). The turbidity dynamics is also considered through the particulate attenuation coefficient, $c_p(670)$, which is proportional to the particle concentration, at first order (Neukermans et al., 2012b). The number of particles in size class i per unit volume and per unit diameter increment $n(\sigma)$ is computed for the entire size classes at each time step (Fig. 3.5). The PSD of the present data set is well represented by a power-law distribution throughout the whole time series. The slope values, ξ , of the particulate size distri-

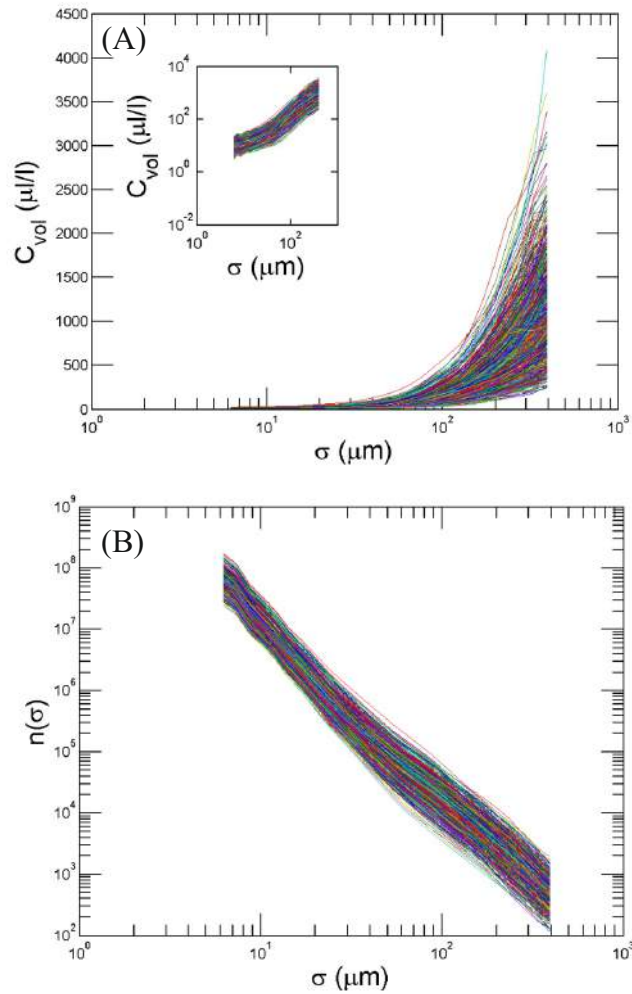


Figure 3.5: PSD for volume concentration (A) and for number concentration (B). The inset in (A) is a log-log plot emphasizing the power-law relations for the volume concentrations.

bution range between 2.57 and 3.94, with a mean value of 2.9 and a standard deviation of 0.16. These values are in good agreement with previous studies (Jonasz, 1983; Boss et al., 2001b; Loisel et al., 2006; Buonassissi and Dierssen, 2010; Reynolds et al., 2010; Neukermans et al., 2012a).

The Probability Density Function (PDF) of the concentrations and size parameters followed non-Gaussian distributions (Fig. 3.6). The inset of each panel in Figure 6 shows the PDF and the Gaussian fit in a semi log scale, in order to emphasize extreme values. All the parameters show an asymmetry, and some are showing a heavy tail in their distribution (Fig. 3.6C, 3.6D and 3.6E). In addition, chi-square

goodness-of-fit tests have been performed to test the normal distribution; the test result rejects the null hypothesis that these parameters come from a normal distribution with a mean and variance computed from these parameters, at 5% significance level with a p -value of 0 and $h=1$.

The temporal variability of $\xi(t)$ is analysed along with the vertically averaged current velocity (VACV) showing the tidal information as well as the current reversal (Fig. 3.7A). At the time of the current reversal, that is when VACV is minimum, $\xi(t)$ generally exhibits a well pronounced peak. This pattern indicates that the proportion of small particles compared to larger ones increases at this particular time. The mean diameter D_A , estimated for each time step, exhibits strong high frequency variability and has a mean value of $116.57 \mu m$ and standard deviation of $\pm 20.43 \mu m$ (Fig. 3.7B). D_A presents a well pronounced trough in magnitude during the current reversal time, in agreement with the $\xi(t)$ patterns. This impact of current reversal on particles size distribution is also well evidenced through the temporal evolution of the normalized volume concentration of each considered size class (Fig. 3.7D-G). During slack tide the normalised volume concentration presents relatively higher values (a peak) in the lower size classes (silt/clay and fine) (Fig. 3.7D-E) and lower values (a trough) in the complementary higher size classes (coarse/micro and macro-flocs) (Fig. 3.7F-G). The time series of $c_p(670)$, a proxy of the suspended particulate concentration, exhibits strong high frequency variability (coefficient of variation of 53 %), with numerous peaks which generally occur when the VACV is maximum (Fig. 3.7C). The mean and standard deviation of $c_p(670)$ are 10.38 and $5.53 m^{-1}$, respectively.

Besides the apparent impact of the vertically averaged current velocity on the particles concentration and size distribution, the significant wave height also slightly contributes to the re-suspension effects ($r^2 = 0.23$). The larger the mean significant wave height, the more the concentration of re-suspended particles (Fig. 3.8A). Moreover, significant wave height seems to affect PSD, by promoting the concentration of larger particles compared to smaller ones (Fig. 3.8B). However, according to the low determination coefficient value additional data are needed to confirm this last

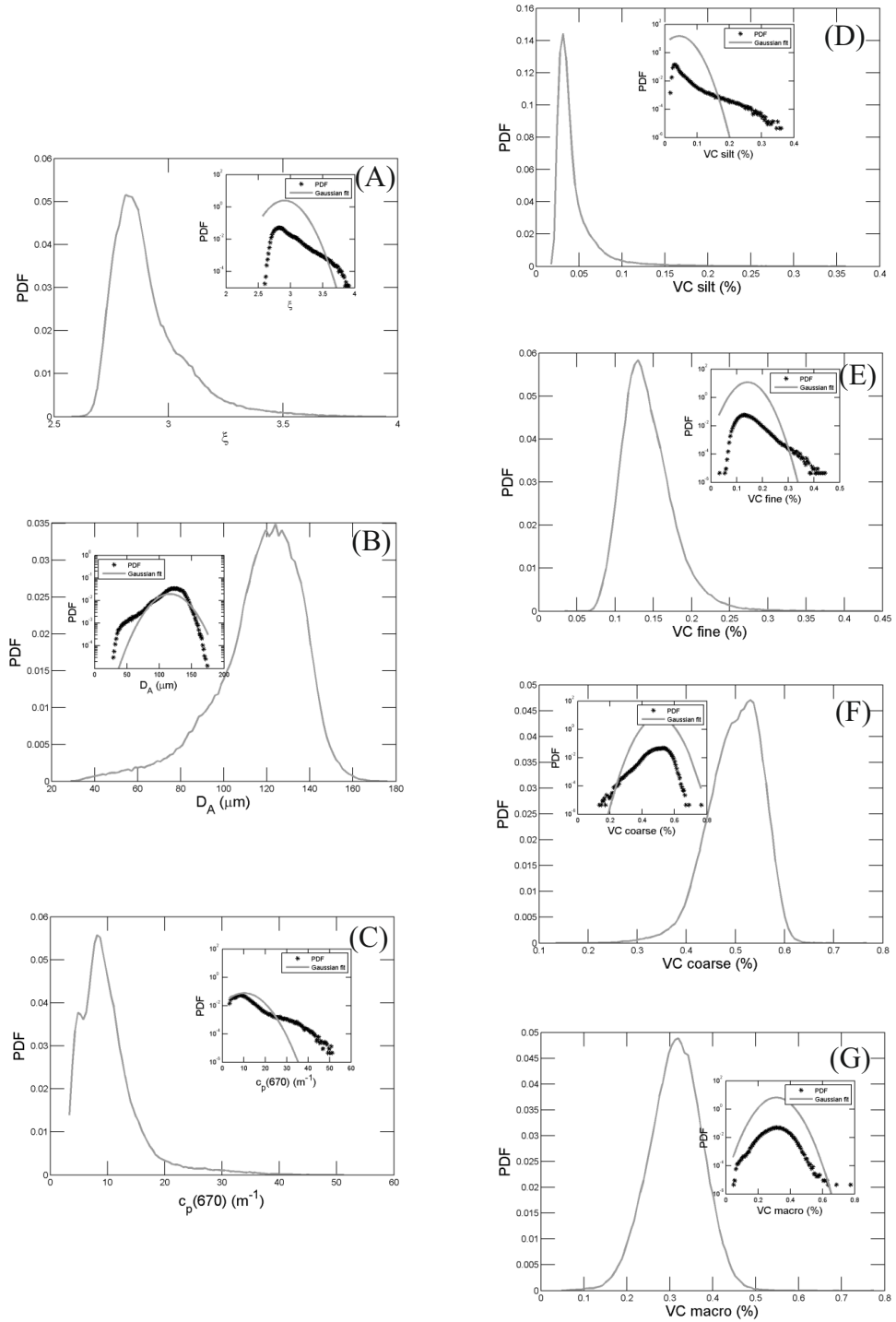


Figure 3.6: The *PDF* of A) ξ , B) D_A , C) $c_p(670)$ and normalised volume concentration of the different size classes of particles (*VCsilt* (D), *VCfine* (E), *VCcoarse* (F) and *VCmacro* (G)), superposed to a Gaussian fit with the same mean and variance. The inset in all figures is a semi log plot emphasizing extremes, showing that all *PDFs* are non-Gaussian.

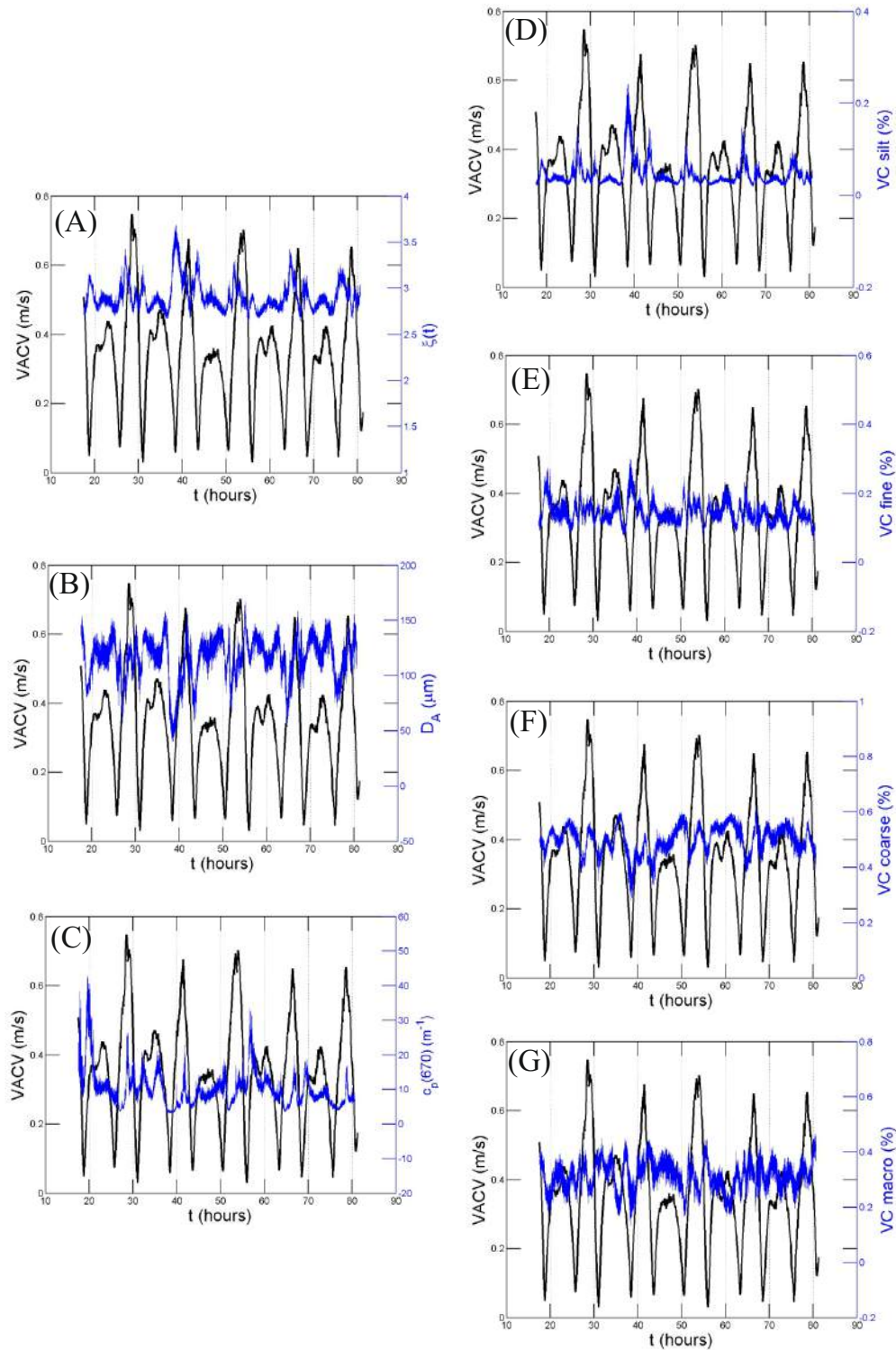


Figure 3.7: Time series of A) $\xi(t)$, B) D_A , C) $c_p(670)$ and the normalised volume concentration of different size classes of particles (VC_{silt} (D), VC_{fine} (E), VC_{coarse} (F) and VC_{macro} (G)) superposed to VACV data.

point.

Since we have high frequency time series of $\xi(t)$, $D_A(t)$, $c_p(670)(t)$ and normalised

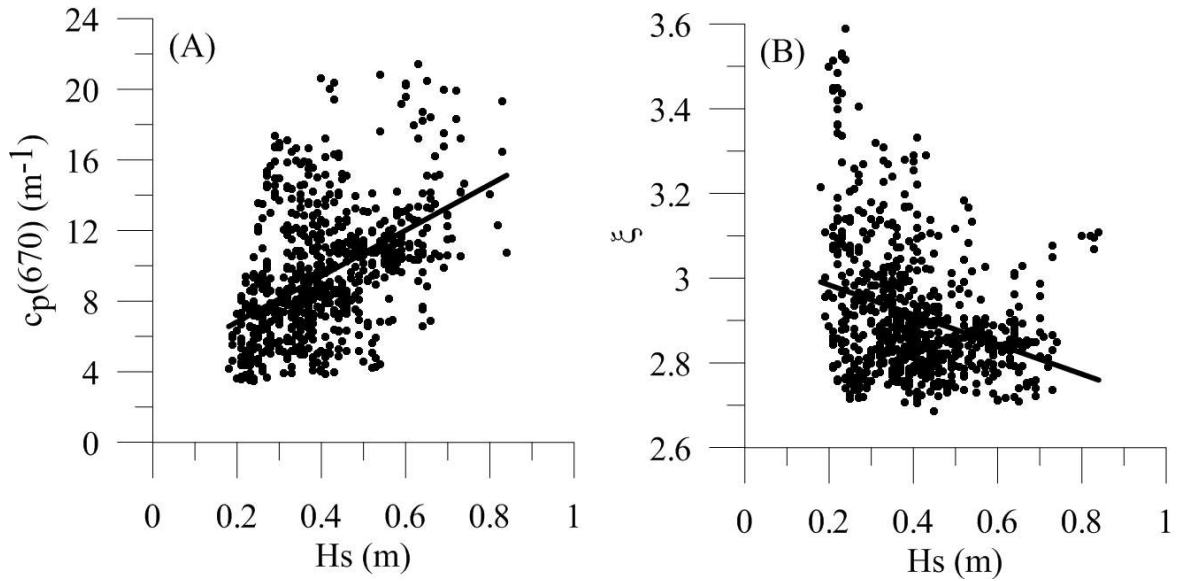


Figure 3.8: (A) Scatter plot of $c_p(670)$ versus H_s and (B) ξ versus H_s .

volume concentration of each size classes of particles, we can explore their dynamical properties. The dynamics of ξ , D_A and $c_p(670)$ has been estimated through power spectral analysis (Fig. 3.9A-C). Two scaling regimes characterized by different slope values are observed on either side of the period of $T=1000\text{s}$, similarly to the velocity period. These parameters in the low frequency regime present the same spectral slope (β close to $-5/3$) similar to the velocity field, indicating that the dynamics of the particles is influenced by turbulence at low frequencies. At higher frequencies, the slope values of these parameters and velocity field are significantly different but remain similar to the velocity spectra. With a slope value close to -0.8 in the frequency range $[0.001; 0.1 \text{ s}^{-1}]$, the dynamics of the particles seems to be partly driven by dynamical processes likely impacted by the interaction with the sea floor, for which a slope of -1.0 is expected (Perry et al., 1986; Katul et al., 1995; Katul and Chu, 1998). Similar power spectra are also observed in the case of normalised volume concentrations of different size classes of particles (Fig. 3.9D).

3.4 Discussion and Conclusion

Large temporal variability in the hydrodynamic fields, particle concentration and size distribution were observed during the in-situ experiment reported here. The

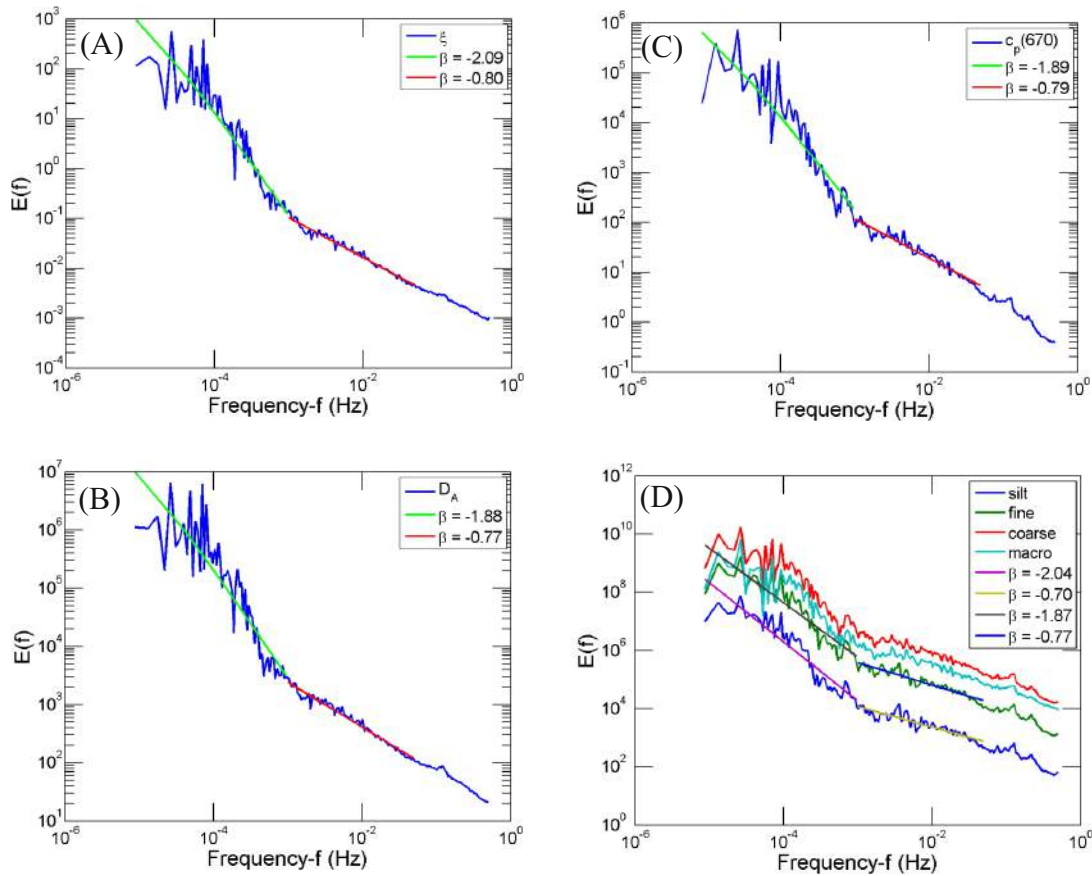


Figure 3.9: Power spectra of ξ , D_A , $c_p(670)$ and the total volume concentrations of different size classes of particles showing different scale regimes as indicated by the different slope values for different frequency ranges.

hydrodynamic conditions, along with the high turbulence level encountered, provide favourable conditions for the re-suspension of particle. The present data set has shown that tidal current and waves have a significant role in the particle re-suspension and further water column turbidity. This is in good agreement with [Velegrakis et al. \(1999\)](#) who observed large scale particle re-suspension processes generated by the tidal current and coastal waves for the same region. During the current reversal, when the VACV is minimum, all the size parameters examined here indicate a modification in the particle size distribution. The proportions of small particles tend to increase compared to bigger ones (Fig. 3.7). Two processes can explain this pattern. First, hydrodynamic forcing is not sufficient to re-suspend large particulate assemblages from the bottom. Second, during the period of slack current, the differential settling of particles one over the other takes place

inducing a washing of the water column, especially of heavy flocs. These observations agree with the study carried out by [Van Leussen \(1988\)](#). To a lesser extent, the occurrence of waves induces an increase of the suspended particulate matter concentration (i.e. $c_p(670)$), and especially of large particulate assemble (Fig. 3.8).

Turbulence has been extracted from the along shore and cross-shore components of the current velocity, which show periodic fluctuations in their magnitude. The power spectra of velocity components follow three different regimes depending on the scale. The first one, with typical inertial range, has a slope close to $-5/3$. The second one is characterized by a flatter slope of -0.6 with a transition scale of 1000 seconds. At last, the energy spectra at high frequencies (3-10 s) shows a localised forcing attributed to waves forcing, similarly to the previous results obtained in the same region ([Schmitt et al., 2009](#)). From $T=1000$ s \sim 17 min there is a transition to a regime for which the power spectra is characterized by a lower slope value (close to -0.6). While there is still no theoretical explanation of such low slope value, theoretical studies have shown that the power spectra of velocities close to the sea floor may be characterized by a slope value of -1.0 ([Panchev, 1972](#); [Kader and Yaglom, 1984](#); [Katul and Chu, 1998](#)). The theoretical and experimental studies carried out by [Perry et al. \(1986\)](#); [Katul et al. \(1995\)](#); [Katul and Chu \(1998\)](#) showed that the turbulent boundary layer was characterized by a power-spectral slope of -1.0 at the low wave number values.

Thus, the power spectra of size parameters and $c_p(670)$ exhibit very similar turbulent scaling in the lower and higher frequency region compared to the velocity field. The Stokes number derived from the present measurements exhibit very low values ($\ll 1$), showing that the particles in the fluid motion behave like tracers and move along with the fluid.

We found that turbulence has a great role in the dynamics of the particles in the present region. Low frequency variability of the particles is controlled by the turbulence ($\beta \simeq -5/3$) and high frequency variability is controlled by the physical processes which are related to the sea bottom interactions (wall turbulence), tidal currents and waves. A next step related to this work will be to analyse the turbu-

lent intermittency scaling of these parameters using empirical mode decomposition ([Huang et al., 2008](#)). Other measurement campaigns will be performed in coastal waters to compare with the present study and assess its possible universality.

CHAPTER 4

INTERMITTENT PARTICLE DYNAMICS IN MARINE COASTAL WATERS

Abstract

Marine coastal processes are highly variable over different space and time scales. In this paper we analyse the intermittency properties of particle size distribution (PSD) recorded every second using a LISST instrument (Laser In-Situ Scattering and Transmissometry). The particle concentrations has been recorded over 32 size classes from 2.5 to 500 μm , at 1 Hz resolution. Such information is used to estimate at each time step the hyperbolic slope of the particle size distribution, and to consider its dynamics. Shannon entropy, as an indicator of the randomness, is estimated at each time step and its dynamics is analysed. Furthermore, particles are separated into four classes according to their size, and the intermittent properties of these classes are considered. The empirical mode decomposition (EMD) is used, associated with arbitrary order Hilbert spectral analysis (AHSA), in order to retrieve scaling multi-fractal moment functions, for scales from 10 *sec* to 8 minutes. The intermittent properties of two other indicators of particle concentration are also considered on the same range of scales: the total volume concentration $C_{vol-total}$ and the particulate beam attenuation coefficient $c_p(670)$. Both show quite similar

intermittent dynamics and are characterized by the same exponents. Globally we find here negative Hurst exponents for each time series considered, and non-linear moment functions.

4.1 Introduction

Ocean data fields show a high variability over many different time and space scales. Such variability is often associated with turbulence, and multi-scaling properties of oceanic fields have been reported and studied in many previous studies: sea state (Kerman, 1993); phytoplankton concentration (Seuront et al., 1996b,a, 1999; Lovejoy et al., 2001a); rainfall and cloud radiance (Tessier et al., 1993; Lovejoy and Schertzer, 2006); satellite images of ocean colour, chlorophyll-a and sea surface temperature (Lovejoy et al., 2001b; Nieves et al., 2007; Pottier et al., 2008; Turiel et al., 2009; Montera et al., 2011; Renosh et al., 2015). Here we focus on coastal waters and consider particles transported by oceanic currents in this highly energetic medium (Svendsen, 1987; Schmitt et al., 2009). The solid phases in the environment has been described by hyperbolic particle size distributions (PSD) of clay aggregates in water (Amal et al., 1990), biological aggregate and marine snow (Jiang and Logan, 1991; Logan and Wilkinson, 1991), aerosol agglomerates (Wu and Friedlander, 1993) and flocs produced in the water and waste water discharge (Li and Ganczarczyk, 1989).

PSD has major influence in biological, physical and chemical processes in the aquatic environment (Boss et al., 2001a; Twardowski et al., 2001; Reynolds et al., 2010). For instance, PSD is strongly involved in the trophic interaction within the plankton community and in the chemical/geological aspects. The shape of the PSD is also uses in computing the sinking rate of the sediment fluxes. The study carried out by Renosh et al. (2014) using the same in situ data set than the present study showed that the dynamics of the PSD is controlled by many oceanographic parameters like tidal currents, waves and turbulence. The present study is a continuation of this work.

All environmental and geophysical data sets are non-linear and non-stationary

at many different scales of time and space. Intermittency is a property that occurs in fully developed turbulence ranging between the large scale injection and the small scale dissipation (Frisch, 1995; Pope, 2000). The main objective of this study is to analyse the intermittency properties of particle size distribution (PSD). In this study we mainly focus on the dynamics of the PSD along with the velocity data. For that we decomposed the PSD into different size classes and also derived the Shannon entropy from the probability density function (PDF) of the PSD.

Empirical Mode of Decomposition (EMD) together with Hilbert spectral analysis (HSA) is a well-known time-frequency analysis method for non-stationary and non-linear time series (Huang et al., 1998, 1999). Such analysis is done in two parts: the EMD is an algorithm to decompose a time series into a sum of mono-chromatic modes, and HSA extends for each mode into characteristic amplitude and frequency. Hence this method is a time-amplitude-frequency analysis, which is recalled in appendices A and B. This approach can be generalised to extract intermittency exponents (Huang et al., 2008, 2011). This is presented in Appendix C.

The first part of the paper present the study area and in-situ data, which contains the separation of different size classes and the hyperbolic shape shape of the PSD. Intermittency analysis using the EMD-AHSA method (presented in the appendices) are then provided in the next section followed by the conclusion.

4.2 In-situ data

The same data sets presented in the chapter 3 will be used for this present study.

4.2.1 Separation into size classes

The volume concentration distributed of a particle size class can also be expressed as the concentration $C_{vol}(\sigma)$ per unit volume per unit bin width (Jouon et al., 2008):

$$C_{vol}(\sigma) = \frac{C_{vol,i}}{\sigma_{\max}(i) - \sigma_{\min}(i)} \quad (4.1)$$

where σ is the median diameter of the particle size class i , $\sigma_{\max}(i)$ and $\sigma_{\min}(i)$ are respectively the maximum and minimum particle size of the class i . This resulting volumetric PSD is expressed in $\mu l.l^{-1}.\mu m^{-1}$. The total volume concentration of the PSD ($C_{vol-total}$) has been derived at each time step:

$$C_{vol-total}(t) = \sum_{i=6}^{31} C_{vol,i}(t) \quad (4.2)$$

This quantity gives the total volume of the particles in $\mu l/l$. For the present study we deal with 4 different size classes, using the following classification: Silt/Clay ($\sigma < 30\mu m$), Fine ($30 < \sigma < 105\mu m$), Coarse/Micro ($105 < \sigma < 300\mu m$) and Macro flocs/particles ($\sigma > 300\mu m$) (Lefebvre et al., 2012; Renosh et al., 2014). Fig. 4.1 shows the time series of normalized volume concentrations (VC) of different size classes of PSD. All 4 size classes are showing large temporal fluctuations in their magnitude. Their statistical and dynamical properties are considered below.

4.2.2 PSD slope (ξ)

The particle size distribution in the ocean, which describes the particle concentration as a function of particle size/number, typically shows a rapid decrease in concentration with increasing size from a sub-micrometer range to hundreds of micrometers. This feature is common to all the suspended particles and also for plankton micro-organisms (Sheldon et al., 1972; McCave, 1983; Stramski and Kiefer, 1991; Jackson et al., 1997). The number of particles for a given size σ is estimated by a normalisation by their volume (Jouon et al., 2008). We obtain the number density $n(\sigma)$, which is also the product of the probability density function of the size, $p(\sigma)$, times N , the total number of particles:

$$n(\sigma) = Np(\sigma) = \frac{C_{vol}(\sigma)}{\frac{4}{3}\pi(\sigma/2)^3} \quad (4.3)$$

The PSD of this density number classically follows a power law distribution for aquatic particles in suspension (Sheldon et al., 1972; Kitchen et al., 1982; Jonasz,

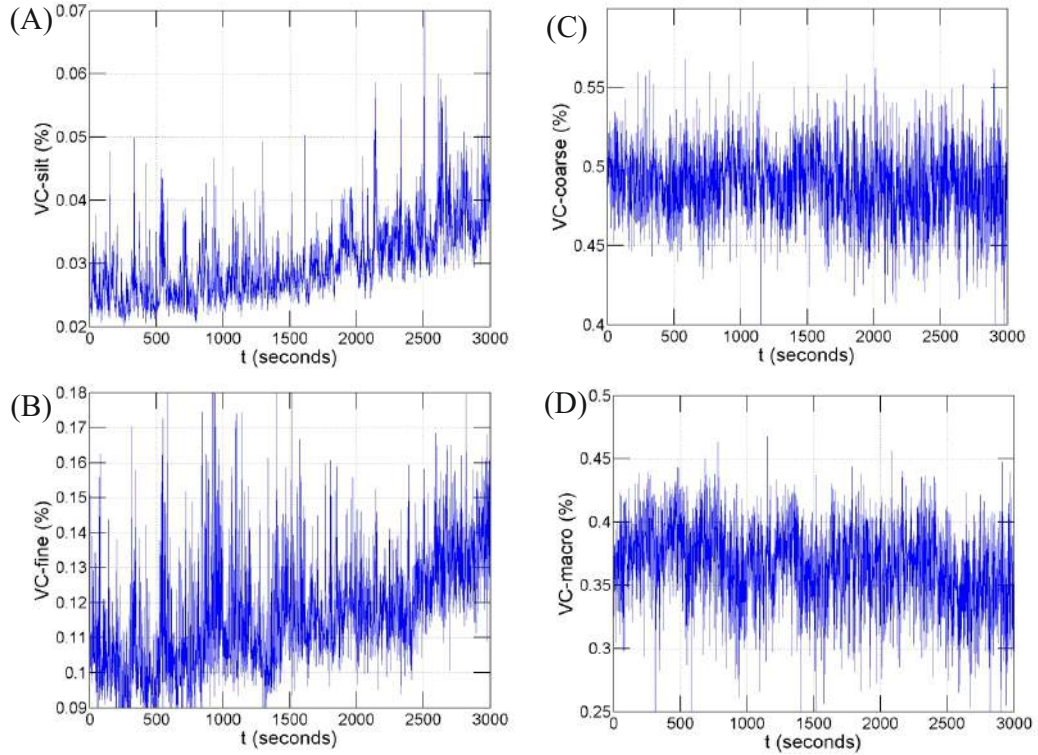


Figure 4.1: Time series of 3000 samples of volume concentrations of different size classes of *PSD*. (A) Silt/Clay, (B) Fine particles, (C) Coarse/Micro particles (D) Macro particles/flocs.

1983; Boss et al., 2001a; Twardowski et al., 2001; Loisel et al., 2006; Reynolds et al., 2010; Renosh et al., 2014):

$$n(\sigma) \sim K\sigma^{-\xi} \quad (4.4)$$

where K is a constant and $\xi > 0$ is the *PSD* hyperbolic slope. Since the LISST provides size class information at each time step, the power-law distribution can be fitted at each time step, providing the exponent as a time series $\xi(t)$. The ξ value provides information on the relative concentration of small and large particles: the steeper the slope (the greater ξ), the more small particles relative to large particles are present in the water (and vice versa). A small portion of 3000 samples of ξ is shown in Fig. 4.2A: large temporal fluctuations in its magnitude are visible. When considering all size classes in all the time steps, a hyperbolic PDF is also obtained,

represented in Fig. 4.2B with a slope value of $\bar{\xi} = 2.9 \pm 0.16$.

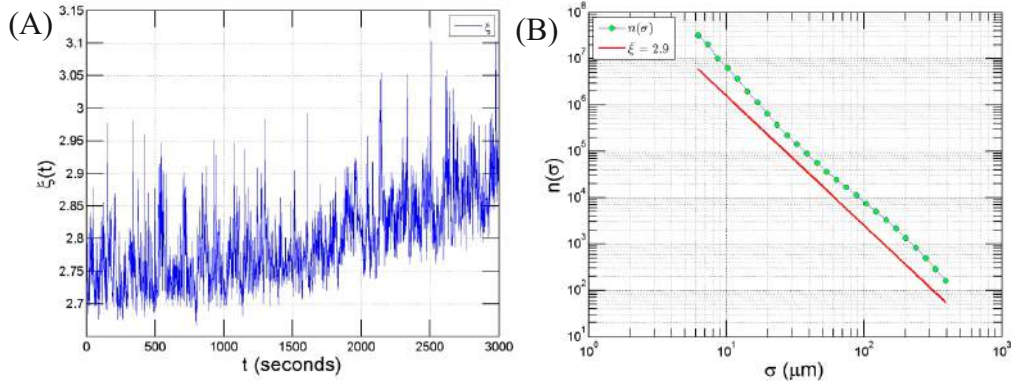


Figure 4.2: Time series of 3000 samples of PSD slope (ξ) (A) and PSD slope of the entire dataset with a power-law fit of slope $\bar{\xi} = 2.9 \pm 0.16$ (B).

The study carried out by [Renosh et al. \(2014\)](#) considered the dynamics of the $\xi(t)$ in relation with different hydrodynamic quantities like waves, tidal currents and turbulence. It showed that turbulence has a major role in the re-suspension of the particles in the aquatic environment. It also showed that along-shore (U) and cross-shore (V) components of velocity have power spectra showing different scaling regimes in low frequency and high frequency regions (Fig. 4.3). At low frequency scale there is a typical Kolmogorov $-5/3$ slope and at high frequency a scaling regime with a 0.6 slope. For high frequencies there is a hump like structure, which can be identified as the high energy associated with surf zone wave breaking ([Schmitt et al., 2009](#)).

The study of [Renosh et al. \(2014\)](#) showed that the low frequency variability of $\xi(t)$ and $c_p(670)$ are controlled by turbulence and that the high frequency part is related to dynamical processes impacted by the sea bottom. The present study is a continuation of [Renosh et al. \(2014\)](#); it considers the high frequency scaling regimes and studies the intermittency of particle concentration in this range of scales.

4.3 Intermittent dynamics

4.3.1 Velocity intermittency

We first consider here the scaling and intermittency properties of the velocity. Fig. 4.3A shows the Fourier and Hilbert (HSA) estimation of the U and V components of the velocity. Scaling range are found from 20 to 500 seconds with a slope of about -0.6. In this range of scales the AHSA method has been applied to characterise intermittency in a multi-fractal framework (see Appendix C for the AHSA method). First a negative Hurst exponent is found: $H_U = -0.26$ and $H_V = -0.24$. Such negative sign for H values indicates that small scales show larger fluctuations than the larger scales in a scaling way (Lovejoy and Schertzer, 2012). Both curves become quite different for larger moments: the U curve is more non-linear, associated to larger intermittency (Fig. 4.3B).

4.3.2 Dynamics of the entropy of particle size

The LISST system records at each time step a discretized PDF of the particle size. Hence it is possible to estimate at all time step the entropy of the particle size distribution as:

$$S(t) = - \sum_{i=6}^{31} P_i(t) \log P_i(t) \quad (4.5)$$

where $P_i(t) = n(\sigma_i)(t)/N(t)$. The Shannon Entropy $S(t)$ is estimated at each time step; it possesses some variability with value centered around $\bar{S} = 1.59 \pm 0.03$. Fig. 4.4A shows a sample of $S(t)$ and Fig. 4.4B shows its PDF, which is centered around \bar{S} with values ranging mainly between 1.5 and 1.7. As a stochastic process, in order to consider the dynamics of $S(t)$, we plot in Fig. 4.4C the autocorrelation of $S(t)$. A memory time of the entropy series can be estimated as:

$$T = \int_0^{T_0} C_s(t) dt \quad (4.6)$$

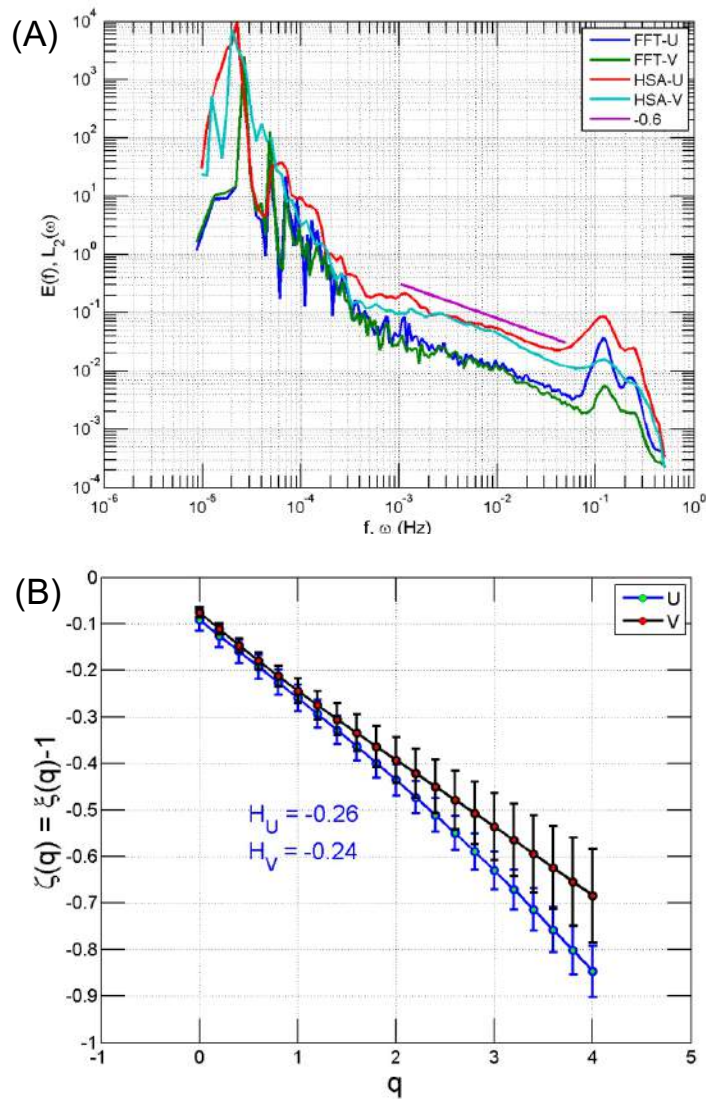


Figure 4.3: Turbulent power spectra of U and V components of velocity fields showing different scaling regimes same for both FFT and HSA (A). The scaling exponents estimated using the HSA method: the curve for U is more nonlinear than the one for V. The Hurst exponents H_U and H_V are negative (B).

where T_0 is the first time for which $C_s(t) = 0$; we find here $T_0 = 7826s$ and we compute $T = 2176s = 36.26min$. This characteristic time scale could be related to the transition scale (Fig. 4.3A) between two scaling regimes of low frequency injection scale and high frequency wave breaking scale.

The entropy of particle sizes characterises the “disorder” of the size distribution, its information content. We showed here that the dynamics of such quantity can be considered by using LISST data. One of the very interesting feature of LISST

measurements is hence to be able to characterise non-linear classical indicators such as the Shannon entropy, in a dynamical way.

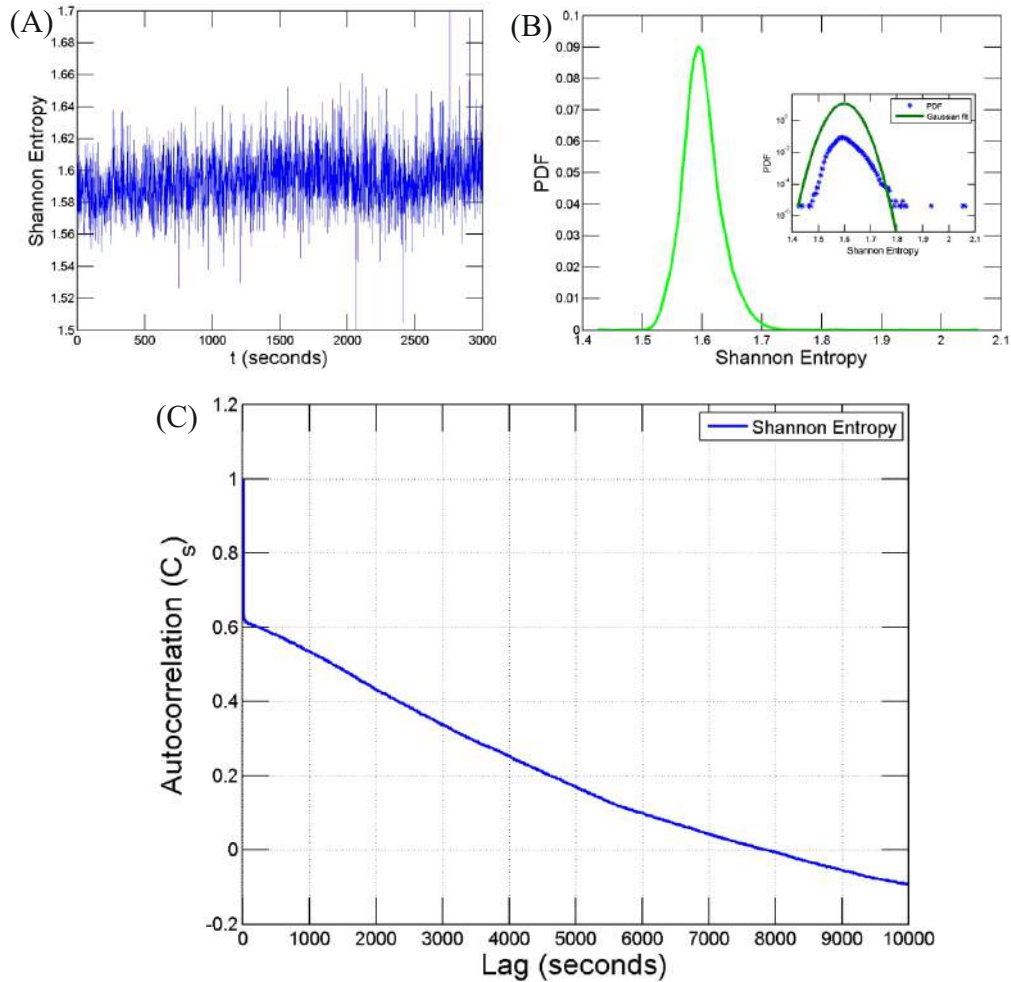


Figure 4.4: Time series of 3000 samples of Shannon entropy in (A), PDF of Shannon entropy along with a Gaussian fit in semi-log plot (inset) in (B) and the Autocorrelation of Shannon entropy in (C).

4.3.3 Intermittent dynamics of different size classes

As explained above, the PSD is decomposed into 4 different size classes of particles (Silt/Clay, Fine particles, Coarse/Micro particles and Macro particles/flocs). The power spectra of these 4 size classes have been derived using Fourier as well as Hilbert transform (Fig. 4.5) for understanding the turbulent characteristics. Similar spectra are found from Fourier and Hilbert transform and there is a good power-law

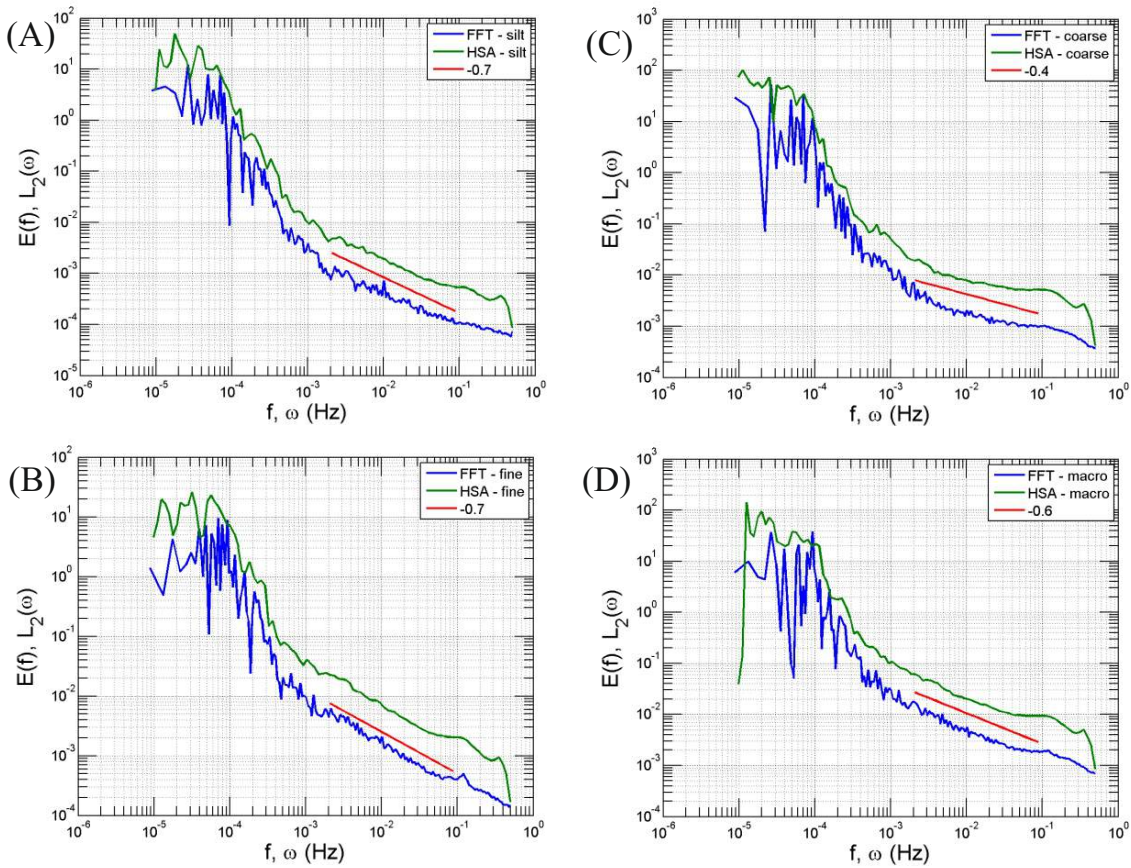


Figure 4.5: Power spectra for different size classes of PSD estimated for Fourier and Hilbert transform Silt/Clay (A), Fine (B), Coarse/Micro (C) and Macro particles/flocs (D). The red lines shows the scaling range and the slope of the best fit in this range.

behaviour observed in the high frequency region (0.09Hz - 0.002Hz).

This scale range has been taken for the extraction of the scaling exponents. The scaling exponent function $\xi(q)$ has been extracted for all size classes using arbitrary order Hilbert spectral analysis (Appendix C). The exponent $\zeta(q) = \xi(q) - 1$ is computed. Non-linear functions are visible for each size classes (Fig. 4.6). The Hurst number $H = \zeta(1) = \xi(1) - 1$ is estimated for each classes: we find $H = -0.17$; -0.19 ; -0.38 ; -0.26 for increasing size classes. The high H values are observed in the larger size classes and low H values are observed in lower size classes. This parameter determines the rate at which mean fluctuations grow ($H > 0$) or decrease ($H < 0$) with the scale. We found negative H values in the present study. Negative H values have not been found in many studies. Recently in [Lovejoy and Schertzer \(2012,](#)

2013) it was argued that Haar wavelet analysis can be used to extract the H values with any sign for the exponent ($-1 < H < 1$). Such sign indicate that small scales show larger fluctuation than large scales. If $\zeta(q)$ is linear, the statistical behaviour is mono-scaling; if $\zeta(q)$ is non-linear and concave/convex, the behaviour is defined as multi-scaling, corresponding to a multi-fractal process. The concavity of this function is a characteristic of the intermittency: the more concave is the curve, the more intermittent is the process (Frisch, 1995; Schertzer et al., 1997; Vulpiani and Livi, 2003; Lovejoy and Schertzer, 2012). The slight curvature which is found here for all size classes (Fig. 4.6) is hence a signature of intermittency in the particle dynamics.

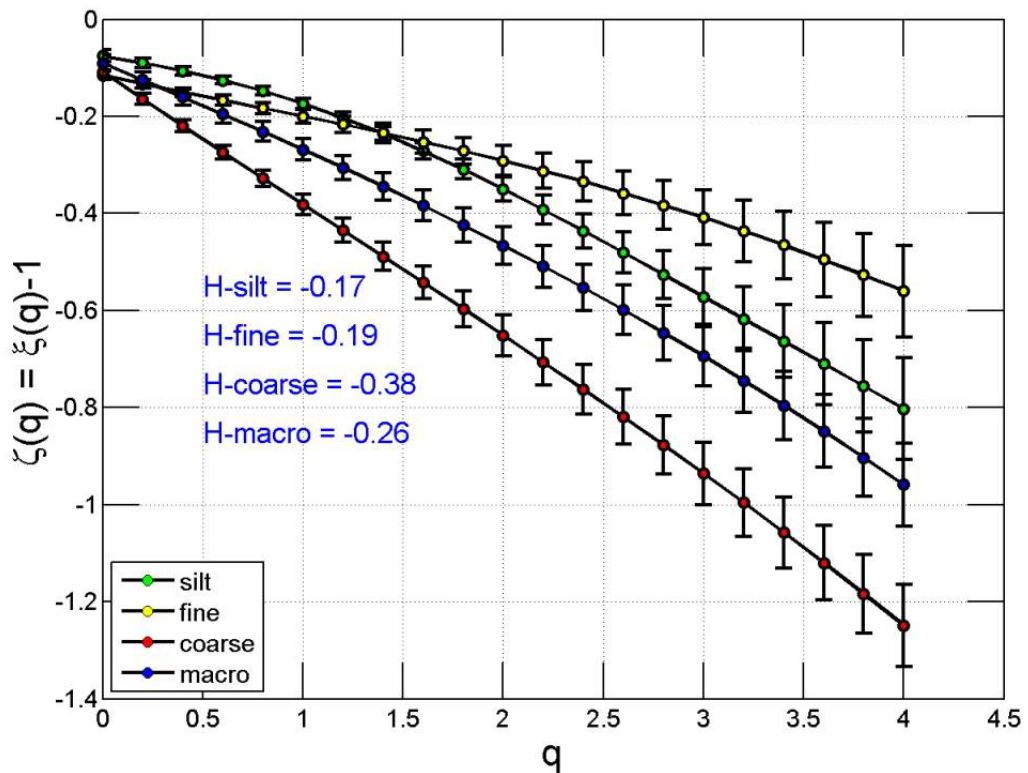


Figure 4.6: Scaling exponents $\zeta(q)$ estimated for different particle sizes, using the HSA method. In all cases the Hurst exponent is negative, with values between -0.17 and -0.38. The curves are all slightly nonlinear, sign of intermittency.

4.3.4 Intermittent concentration dynamics

We perform here an analysis of intermittency of concentration dynamics considering two indicators of this particle concentration: $c_p(670)$ and total volume con-

centration ($C_{vol-total}$). At first order, $c_p(670)$ is driven by the suspended particulate matter (SPM). We observe here a large variability in the $c_p(670)$ data (Fig. 4.7A). The total volume concentration of the PSD has been derived for each time step using Eqn. 4.2. The derived $C_{vol-total}$ shows large fluctuation in its magnitude (Fig. 4.7B). The turbulent power spectrum derived for these series shows 2 scaling regimes similar to the size classes (Fig. 4.7C and Fig. 4.7D). A good scaling between 0.002Hz - 0.09Hz is observed (Fig. 4.7C and Fig. 4.7D). Hence the region between 0.002 to 0.09 Hz (10 sec. to 8 min.) has been identified for the multi-scaling analysis. The structure function scaling moment function derived for this series shows a non-linearity and concavity in its shape (Fig. 4.7E). The H value derived for the $C_{vol-total}$ is slightly negative; $H = -0.08$. The scaling moment function of the $c_p(670)$ showed a non-linearity in its behaviour showing its intermittent characteristics (Fig. 4.7E). We find here $H = -0.06$ which is quite similar to $C_{vol-total}$. Globally, for power spectra as well as for their intermittency properties, both proxies of SPM show similar scaling properties. These two different indicators of particle concentrations show quite similar dynamics and statistical intermittent properties.

4.4 Conclusions

This work analysed the intermittency and scaling properties of particles using the AHSA method. The intermittent transport of particles in complex flows, like in coastal waters, is very important for the study of partition dynamics, erosion processes, ecosystem modelling, sediment transport and turbidity dynamics. Suspended particle dynamics in turbulent flows are complex; some studies showed preferential concentration (Eaton and Fessler, 1994; Squires and Eaton, 1991) and some other studies showed multifractal repartition according to the Stokes number (Bec, 2005; Yoshimoto and Goto, 2007). We thus expect here also, in the natural environment to find intermittent particle dynamics.

This work has analysed the intermittency and scaling properties of the PSD using different aspects. We have time series of normalized volume concentration of

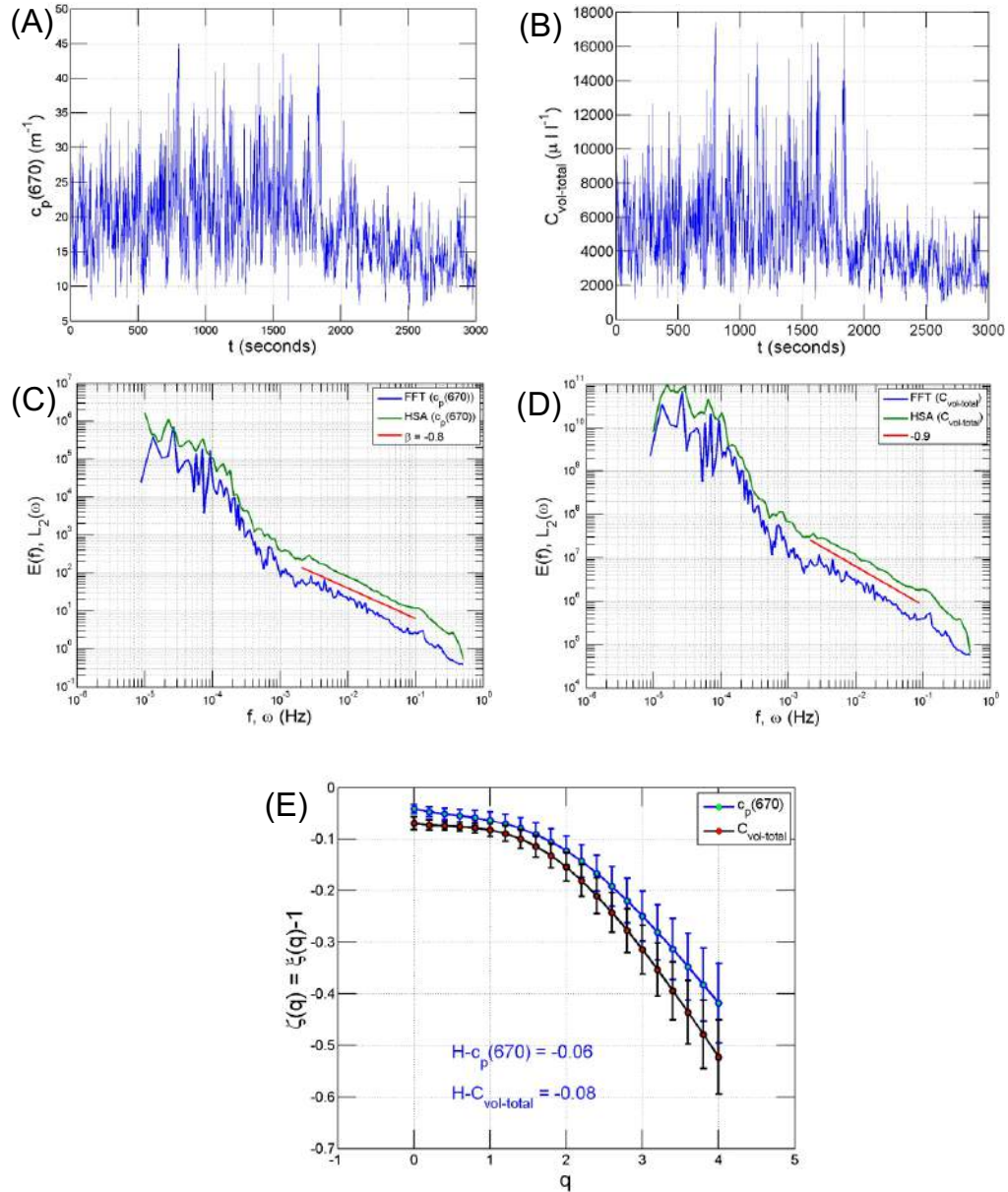


Figure 4.7: Time series of 3000 samples of $c_p(670)$ in (A), Time series of 3000 samples of $C_{vol-total}$ in (B), Turbulent power spectrum of $c_p(670)$ and turbulent power spectrum of $C_{vol-total}$ showing different scaling regimes (The scaling regime indicated as red is used for the scaling exponent computation) in (C and D) and scaling moment function of $c_p(670)$ and $C_{vol-total}$ in (E). The Hurst exponent values are very small but the curve is strongly non-linear.

different size classes of PSD and Shannon entropy which have been derived from number density of PSD. Here we showed the intermittency of particles for different size classes. The $c_p(670)$, a proxy of the suspended sediment concentration, and the total volume concentration ($C_{vol-total}$) showed an intermittent and multiscaling

properties in their dynamics.

Turbulent scaling of these parameters has been derived through both Fourier power spectra and spectra derived through HSA. The scaling moment function derived for $C_{vol-total}$ and $c_p(670)$ are showing similar non-linear curve stressing the intermittency in their dynamics. The scaling moment functions derived for each size class of the particle are also non-linear. The curvature of the spectrum for various size class shows the intermittency of the particles dynamics in different sizes.

We may note also that the Hurst exponent derived for the velocity components and the particle concentrations are negative. This negative sign indicates that small scales show larger fluctuations than large scales. We have here no theoretical interpretation to propose to these values, which could be related to the particular statistical characteristics of a bottom boundary layer flow.

This multi-scaling analysis has been tested only in the bottom of the highly dynamic coastal waters of the Eastern English channel. Such analysis is an illustration of the potential provided by LISST data, with many particle size classes recorded at each time steps. It may be applied to other time series in the open ocean, coastal waters and also fresh water situations, in order to provide comparison and help to look for universal properties.

4.5 Appendices

Appendix A Empirical Mode of Decomposition (EMD)

Hilbert Spectral Analysis (HSA) and Empirical Mode of Decomposition (EMD) have been introduced by Norden Huang and collaborators in the end of the 1990s ([Huang et al., 1998](#)) to locally extract amplitude and frequency information in a time series. It was mainly introduced for non-linear and non-stationary time series. The first step of this approach is EMD. The objective of the EMD method is to decompose a signal into a series of modes. Each component is defined as an intrinsic mode function (IMF) satisfying the following conditions: (1) In the whole data set, the

number of extrema and the number of zero crossings must either equal or differ at most by one. (2) The mean value of the envelope defined using the local maxima and the envelope defined using the local minima are zero (Huang et al., 1998; Huang and Wu, 2008). An iterative algorithm was proposed to extract successive IMF from time series. We do not reproduce all the details of this algorithm here and refer to original publications (Huang et al., 1998, 1999).

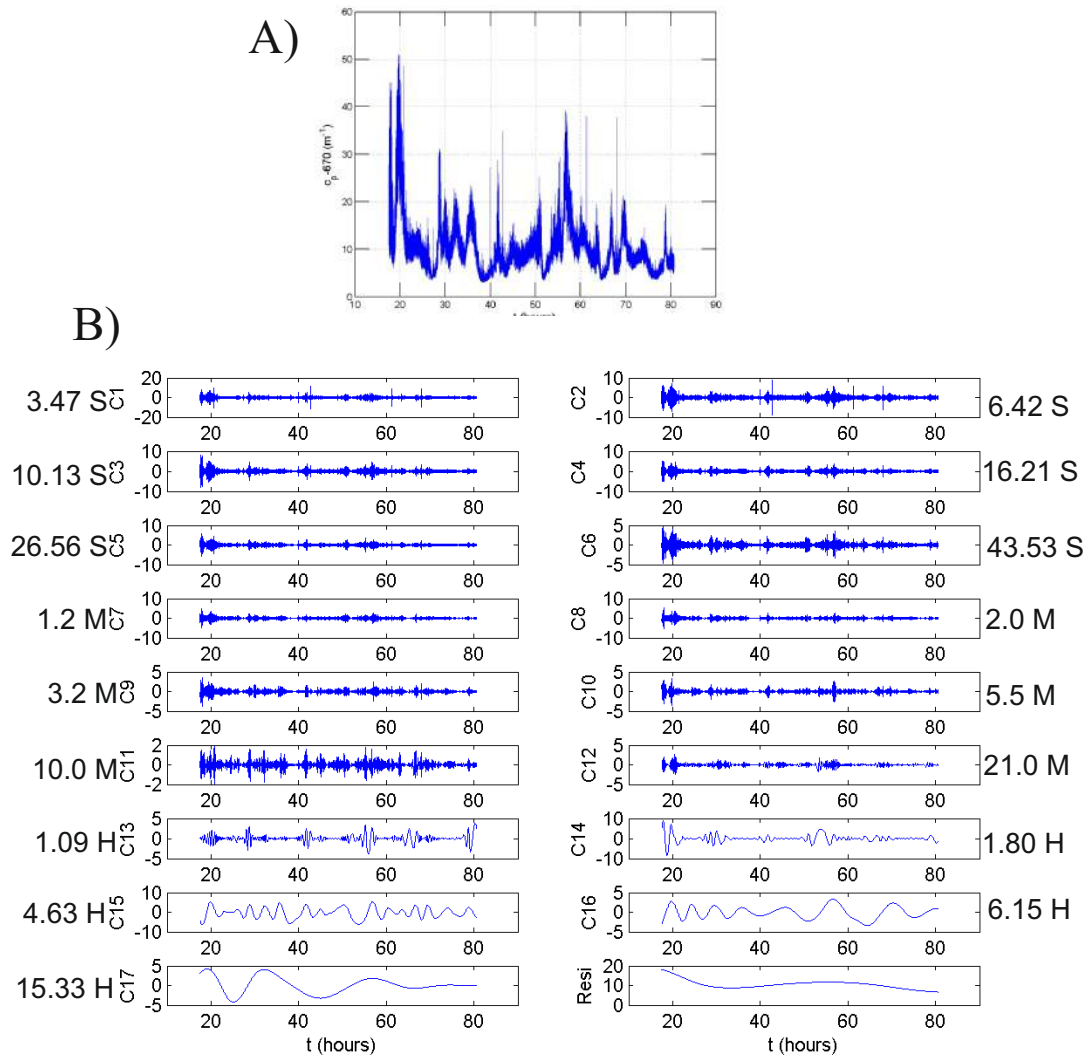


Figure 4.8: Time series of $c_p(670)$ in (A), IMF retrieved through the EMD methods in (B), the time scale is increasing with the mode from C1 to C17

The decomposition process stops when the residue, r_n , becomes a monotonic function or a function with only one extrema from which no more IMF can be extracted.

At the end of the decomposition, the original time series $x(t)$ is decomposed into a sum of n modes and a residue:

$$x(t) = \sum_{j=1}^n c_j(t) + r_n(t) \quad (4.7)$$

where $c_j(t)$ are IMFs and $r_n(t)$ is the residue. In this decomposition, each mode has a decreasing characteristic frequency. If N is the number of points of the original series, we have: $n \approx \log_2(N)$, hence in general, $10 \leq n < 20$ (Flandrin and Goncalves, 2004; Huang et al., 2008).

Appendix B Hilbert Spectral Analysis (HSA)

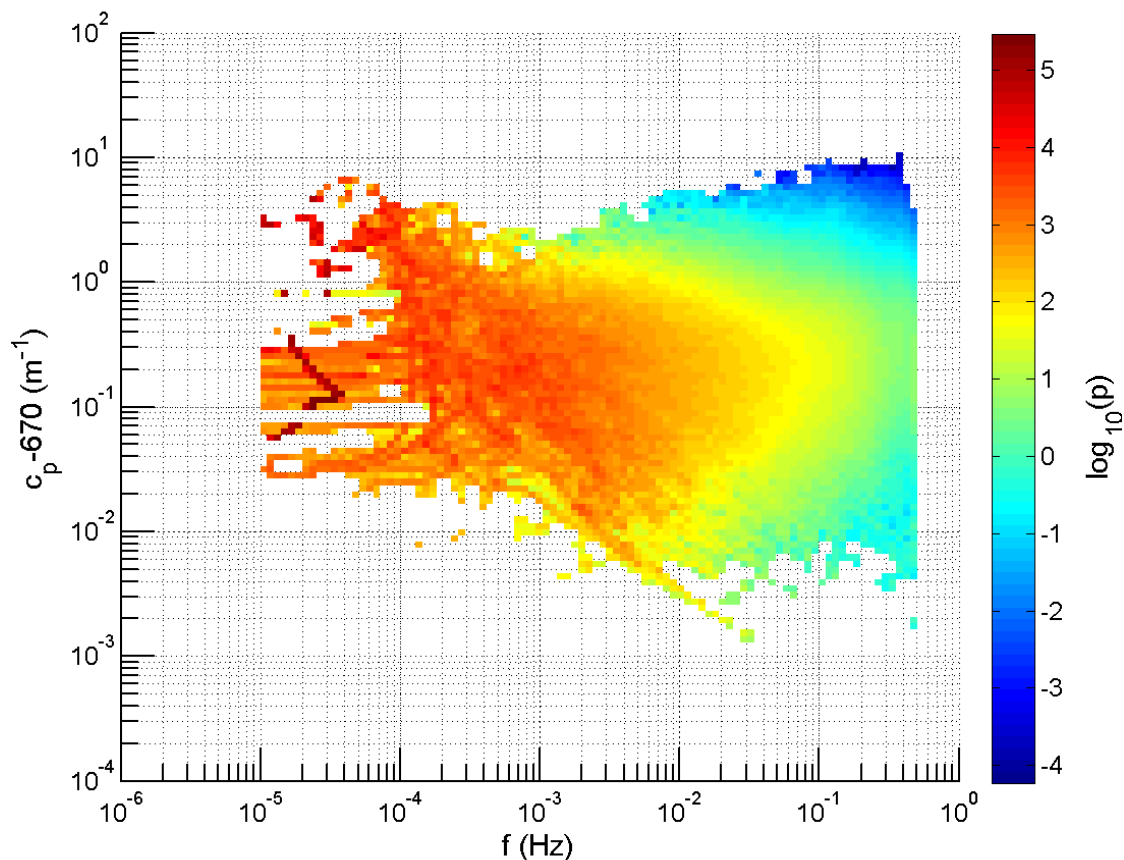


Figure 4.9: Representation of the joint pdf in log scale of the $c_p(670)$ fluctuations in an amplitude-frequency space.

Hilbert Spectral Analysis (HSA) is the second step of the analysis, which is ap-

plied to each mode $c_j(t)$ extracted for the time series $x(t)$ using the procedure discussed in Appendix A. For any function $x(t)$, its Hilbert transform $y(t)$ is written as:

$$y(t) = H\{x\}(t) = \frac{1}{\pi} \int_{-\infty}^{+\infty} \frac{x(\tau)}{t - \tau} d\tau \quad (4.8)$$

The analytic function $z(t)$ estimated from $x(t)$ using the Hilbert transform $y(t)$:

$$z(t) = x(t) + iy(t) = x(t) + iH\{x\}(t) \quad (4.9)$$

where $i = \sqrt{-1}$. The analytical function is estimated for each mode and at each time step. For each mode and each time step a local amplitude a and phase function θ can be estimated:

$$a(t) = (x^2 + y^2)^{1/2} \quad (4.10)$$

$$\theta(t) = \tan^{-1}(y/x) \quad (4.11)$$

The local frequency is estimated from the phase function:

$$\omega = \frac{d\theta}{dt} \quad (4.12)$$

The *HSA* represents a time-amplitude-frequency analysis. This helps to estimate a joint PDF $p(\omega, A)$ of frequency and amplitude. From this, a marginal spectrum is estimated:

$$h(\omega) = \int_0^{\infty} p(\omega, A) A^2 dA \quad (4.13)$$

This $h(\omega)$ spectral analysis is done through a Hilbert transform and can be compared to the Fourier spectrum $E(f)$ obtained through the classical Fourier analysis ([Huang et al., 2008](#)).

Appendix C Arbitrary order Hilbert Spectral Analysis (AHSA)

The equation obtained in the previous section giving $h(\omega)$ is a second order statistical moment; it can be generalised into arbitrary order moment (Huang et al., 2008, 2011), by taking a moment of order q :

$$L_q(\omega) = \int_0^\infty p(\omega, A) A^q dA \quad (4.14)$$

where $q \geq 0$. In case of scale invariance we can write

$$L_q(\omega) \approx \omega^{-\xi(q)} \quad (4.15)$$

where $\xi(q)$ is the corresponding scaling exponent, which is related to the classical structure function by $\xi(q) = 1 + \zeta(q)$ (Huang et al., 2008). For example for a fractional Brownian motion $\xi(q) = 1 + qH$. Here we are interested by the ‘‘Hurst’’ exponent given by $H = \zeta(1) = \xi(1) - 1$. H can positive or negative and it characterises the degree of stationarity of the scaling process. The non-linearity of $\zeta(q)$ is related to the intermittency of the time series: the more non-linear the scaling exponent $\zeta(q)$, the more intermittent is the series (Schmitt and Huang, 2015).

CHAPTER 5

SCALING ANALYSIS OF OCEAN SURFACE TURBULENT HETEROGENEITIES FROM SATELLITE REMOTE SENSING: USE OF 2D STRUCTURE FUNCTIONS.

This chapter was published as Renosh et al., 2015. In open access available from <http://journals.plos.org/plosone/article?id=10.1371/journal.pone.0126975>

Renosh P. R., Schmitt F. G., Loisel H., (2015) Scaling Analysis of Ocean Surface Turbulent Heterogeneities from Satellite Remote Sensing: Use of 2D Structure Functions. PLoS ONE 10(5): e0126975. doi:10.1371/journal.pone.0126975.

Abstract

Satellite remote sensing observations allow the ocean surface to be sampled synoptically over large spatio-temporal scales. The images provided from visible and thermal infra-red satellite observations are widely used in physical, biological and ecological oceanography. The present work proposes a method to understand the multi-scaling properties of satellite products such as the Chlorophyll-a (Chl-a), and the Sea Surface Temperature (SST), rarely studied. The specific objectives of this study are to show how the small scale heterogeneities of satellite images can be

characterised using tools borrowed from the fields of turbulence. For that purpose, we show how the structure function, which is classically used in the frame of scaling time series analysis, can be used also in 2D. The main advantage of this method is that it can be applied to process images which have missing data. Based on both simulated and real images, we demonstrate that coarse-graining (CG) of a gradient modulus transform of the original image does not provide correct scaling exponents. We show, using a fractional Brownian simulation in 2D, that the structure function (SF) can be used with randomly sampled couple of points, and verify that 1 million of couple of points provides enough statistics.

5.1 Introduction

One of the main features of geophysical fields is their huge fluctuations occurring over wide ranges of spatio-temporal scales. Here we consider the heterogeneities and intermittencies in 3D ocean turbulence. We use for this the framework of homogeneous and locally isotropic turbulence that originated in the work of Kolmogorov ([Kolmogorov, 1941b](#)). In this framework, energy is supplied, introduced or produced in the fluid at a relatively large scale, and is successively passed by interactions between eddies or their instabilities. This is performed through a spectrum of smaller and smaller eddies where inertial forces are dominant. After successive cascades steps, these eddies are conveyed to eddies of size comparable to the Kolmogorov length scale η , where viscosity plays a major role in transferring their kinetic energy into heat. This was formalised using the velocity fluctuations at scale l ; for time series it writes $\Delta V_l = |V(x+l) - V(x)|$ (V is the velocity); and for an isotropic 2D field it can be written $\Delta V_l = \|V(M) - V(N)\|$, where M and N are two points and $l = d(M, N)$:

$$\langle \Delta V_l \rangle = C \epsilon^{1/3} l^{1/3} \quad (5.1)$$

where $\langle \rangle$ means statistical average, C is a constant and ϵ represents the dissipation. This can also be written in the spectral space as follows (Obukhov, 1941b):

$$E_v(k) = C_1 \epsilon^{2/3} k^{-5/3} \quad (5.2)$$

where C_1 is another constant, $E_v(k)$ is the Fourier spectral energy of velocity, and k is the wave number. This corresponds to a situation of scale invariance: velocity fluctuations have no characteristic scale with a power-law scale dependence. A similar scale dependence can be obtained for a passive scalar θ , with a power-law of the form (Obukhov, 1949; Corrsin, 1951):

$$E_\theta(k) = C_2 \epsilon^{-1/3} \chi k^{-5/3} \quad (5.3)$$

where $E_\theta(k)$ is the Fourier spectral energy of passive scalar, C_2 is another constant, and χ is the dissipation of scalar variance (analogous to ϵ as dissipation of kinetic energy). It is now realized for a long time that turbulence produces intermittency, i.e. huge local fluctuations in energy and passive scalar fluxes ϵ and χ , and large variations in velocity and passive scalars (Frisch, 1995). Since the proposals of Obukhov and Kolmogorov in 1962 (Obukhov, 1962; Kolmogorov, 1962) those quantities are characterized using local averages ϵ_l and χ_l at scale l :

$$\epsilon_l(x) = \frac{1}{a_l} \int_{B_l(x)} \epsilon(x') dx'; \quad \chi_l(x) = \frac{1}{a_l} \int_{B_l(x)} \chi(x') dx' \quad (5.4)$$

where $B_l(x)$ is a bowl of radius l centered in x and $a_l = \frac{4}{3}\pi l^3$ is its volume. This is called the ‘‘coarse graining’’ method (CG). This method is used to change the resolution of a positive, intermittent field. These local averages have scaling statistical properties of the form (Frisch, 1995; Lovejoy and Schertzer, 2013):

$$\langle \epsilon_l^q \rangle \approx l^{-K_\epsilon(q)}; \quad \langle \chi_l^q \rangle \approx l^{-K_\chi(q)} \quad (5.5)$$

where q is the statistical moment, $K_\epsilon(q)$ and $K_\chi(q)$ are scale invariant moment functions; these are also second Laplace characteristic function and as such are convex functions. They verify $K_\epsilon(1) = 0$ and $K_\chi(1) = 0$ by conservation of fluxes. Another approach to characterize intermittency and local fluctuations in the studied fields is to directly characterize the fluctuations of velocity and passive scalar using structure functions (Frisch, 1995):

$$\langle \Delta V_l^q \rangle \approx l^{\zeta_v(q)}; \quad \langle \Delta \theta_l^q \rangle \approx l^{\zeta_\theta(q)} \quad (5.6)$$

where $\zeta_v(q)$ and $\zeta_\theta(q)$ are the scaling moment functions that characterize the fluctuations of velocity and passive scalar (Schmitt et al., 1996). This is called the structure function method (SF). In the following, we focus on the passive scalar case, since we will consider Chlorophyll-a and Sea Surface Temperature, which are transported scalars and may be compared to passive scalars. The scaling moment functions for both CG and SF methods are derived using remotely sensed 2D Chl-a and SST images from MODIS Aqua.

In the next section we present the two-dimensional data analysis techniques using CG and SF methods. The next section deals with the test of these two methods for various 2D stochastic simulations. Finally as an illustration, the methods are applied to two real images (Chl-a and SST) measured from MODIS Aqua. An often assumed link between scaling exponents estimated using CG and SF methods is tested on these images and shown to be wrong except for low order moments.

5.2 Methods

5.2.1 Data analysis techniques

Multifractal methods have been widely applied to time series, but there are not many studies applying such approaches to 2D data, especially in the field of ocean color remote sensing. Some of them considered a local gradient transform in order to identify currents and oil spills (Turiel et al., 2005, 2009; Nieves et al., 2007; Yahia

et al., 2008). Other studies transformed satellite Chl-a or SST image data into a positive singular field using a gradient modulus transform (Montera et al., 2011; Lovejoy et al., 2001b). Below we will consider this method and compare it to the structure functions method.

Coarse Graining (CG) method. One method which has been applied in several studies is to produce a positive field, called “multifractal random measure”, from a non stationary field such as Temperature and Chlorophyll-a (Turiel et al., 2005, 2009; Montera et al., 2011). For that purpose, the gradient modulus of the field θ is calculated as follows:

$$\varphi = \sqrt{\left(\frac{\partial\theta}{\partial x}\right)^2 + \left(\frac{\partial\theta}{\partial y}\right)^2} \quad (5.7)$$

using at the smallest resolution the discrete transformation:

$$\varphi_{i,j}^2 = \left(\frac{\theta_{i+1,j} - \theta_{i,j}}{a}\right)^2 + \left(\frac{\theta_{i,j+1} - \theta_{i,j}}{a}\right)^2 \quad (5.8)$$

where a is a constant corresponding to grid size and $\theta_{i,j}$ is the value of the field θ at pixel position (i, j) . This relates a fluctuating field θ (a passive scalar) to an intermittent and passive field φ . The latter is taken as the multifractal measure at the best resolution l_0 . The field φ_l at larger scales $l \geq l_0$ is then estimated by coarse graining:

$$\varphi_l(x, y) = \frac{1}{a_l} \int_{B_l(x,y)} \varphi(x_0, y_0) dx_0 dy_0 \quad (5.9)$$

This is usually done by taking an image of size $2^n \times 2^n$, and degrading the resolution in p steps until scale $l = 2^p l_0$ ($2 \leq p \leq n$). At each step, one goes from resolution l to $2l$ by taking a local average in a square of 4 values and giving to the larger scale cell this average value. The resolution is degraded recursively. As given by Eq. (5.5), the scale-dependant field has scaling statistics with a scale invariant moment function $K(q)$, $\langle \varphi_l^q \rangle \approx l^{-K(q)}$. Experimentally, the function $K(q)$ is estimated as the regression of $\log \langle \varphi_l^q \rangle$ versus $\log(l)$, for each value of q (in practice $q \geq 0$ varies from 0 to 5).

Structure Function (SF) method. In fact the application of the gradient modulus method is not necessary to consider the intermittency properties of a 2D field, θ , such as temperature and Chlorophyll-a. Let us consider two points M and N belonging to the field, and their distance $d(M, N)$. The moments $\langle |\theta(M) - \theta(N)|^q \rangle$ versus $d(M, N)$ are considered. This can be estimated directly by taking all couple of points (M, N) in the 2D domain and discretizing the distance $d(M, N)$ in small intervals. A log-log regression of $\langle |\theta(M) - \theta(N)|^q \rangle$ versus $d(M, N)$ gives the exponent ζ_θ , following the law

$$\langle |\theta(M) - \theta(N)|^q \rangle \approx d(M, N)^{\zeta_\theta(q)} \quad (5.10)$$

where “ \approx ” means scaling relation. In practice, for an image of size $n \times n$, M is chosen among $n \times n$ values and the same for N , which corresponds to consider n^4 couple of points. If $n = 10^3$, this will provide 10^{12} couple of points, which is usually much too computationally expensive, even for modern computers. It is then necessary to use a numerical method to optimize the computations. M and N are here randomly taken. The N_p number of couple of points ($N_p \ll n^4$) are taken small enough for a computational realistic time (less than half an hour for each image for a powerful personal computer), and large enough to have converged statistics. The exponent function $\zeta_\theta(q)$ is directly estimated from such images using the randomly selected couple of points, N_p .

5.2.2 Tests on 2D stochastic simulation

CG Method. In the following, the coarse graining method is tested in 2D with two classical cascade models: the β model and the Log-normal model.

β model 2D cascade. This is one of the first and simplest cascade models to describe the intermittency in turbulence, also called as the black and white model (Frisch et al., 1978). This model was introduced under this name by Frisch et al. (Frisch et al., 1978), but it has already been discussed by Mandelbrot (Mandelbrot, 1974) using a “pulses into pulses” approach originally proposed by Novikov

and Stewart (Novikov and Stewart, 1964). The β -model is a discrete multiplicative model. The multiplicative cascade yields a small scale field $\epsilon(x)$ at the smallest scale, as the product

$$\epsilon(x) = \prod_{i=1}^n W_{i,x} \quad (5.11)$$

of n independent realisations $W_{i,x}$ of a random variable W (here x is the position and i is the level in the cascade).

The β -model is a binomial model with only 2 possibilities for the value of W ($0 < \beta < 1$):

$$\begin{cases} \Pr(W = 0) = 1 - \beta \\ \Pr\left(W = \frac{1}{\beta}\right) = \beta \end{cases} \quad (5.12)$$

We can verify that such field is normalized:

$$\langle W \rangle = \sum W_i \Pr(W_i) = \left(\frac{1}{\beta}\right) \beta = 1 \quad (5.13)$$

The statistical moments of the random variable W are:

$$\langle W^q \rangle = \int W^q \Pr(W) dw = \sum_{i=1}^n W_i^q \Pr(W_i) = \beta^{1-q} \quad (5.14)$$

The cascade field ϵ is built by multiplying n independent realisations of W . Hence its moments write:

$$\langle \epsilon^q \rangle = \left\langle \left(\prod_{i=1}^n W_{i,x} \right)^q \right\rangle = \prod_{i=1}^n \langle (W_{i,x})^q \rangle = \langle W^q \rangle^n = \beta^{(1-q)n} \quad (5.15)$$

Since each cascade step is associated with a scale ratio of 2 from one scale to the next, we have $\lambda = 2^n$, where λ is the total scale ratio. Hence we have the scaling relation for moments $\langle \epsilon^q \rangle = \lambda^{K(q)}$ with $K(q) = c(q-1)$, where $c = -\log_2 \beta$ is the co-dimension. Which give rise to Eq. (5.5) by coarse-graining. The scaling moment function $K(q)$ is linear, and corresponds to a mono-fractal process. A realisation with $n = 10$ and $\beta = 0.9$ is shown in Fig. 5.1A. Fig. 5.1B shows the CG method applied to this field

and Fig. 5.1C, the scaling moment function.

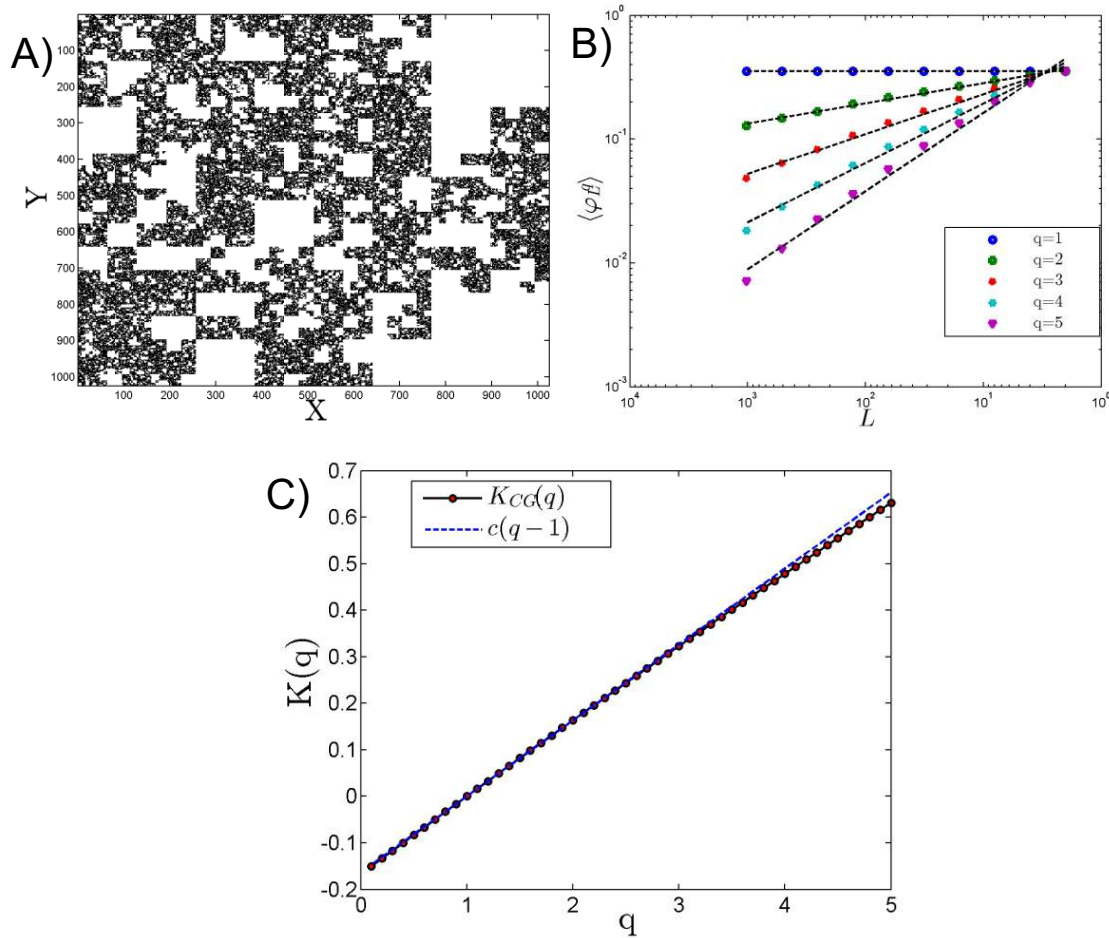


Figure 5.1: A) simulation of a 2D β model with $n = 2^{10}$ and $\beta = 0.9$ (ϵ is displayed), B) coarse grained moments for $q=1$ to 5 and C) moment scaling function $K(q)$, where the experimental estimation is shown in dots compared to the theoretical prediction as a dotted line, with $c = 0.15$.

Lognormal 2D cascade. The cascade generation for the log-normal model is similar to the β model cascade. The only difference is that here we use $W = e^g$, where g is Gaussian. As above, the scaling moment function for the dissipation is $\langle \epsilon^q \rangle = \lambda^{K(q)}$, where $K(q) = \log_2 \langle W^q \rangle$. To understand the scaling moment function, some basic characteristics of a log-normal random variable are now provided. The moment generating function of a log-normal series (X) of mean m and standard deviation σ (of $\log X$) is $\langle X^q \rangle = \exp(qm + q^2 \sigma^2 / 2)$. This can be applied to the moment generating

function for dissipation:

$$K(q) = \log_2 \langle W^q \rangle = \frac{qm + q^2 \sigma^2 / 2}{\log 2} \quad (5.16)$$

Since we want to have $K(q) = \frac{\mu}{2}(q^2 - q)$, where $\mu = K(2)$ is the intermittency parameter, the adequate choice for the discrete log-normal cascade is to take for g , a Gaussian random variable of mean $m = \frac{-\mu \log 2}{2}$ and variance $\sigma^2 = \mu \log 2$.

A realisation of discrete log-normal cascade has been produced with $n = 10$ and $\mu = 0.3$ (Fig. 5.2A). The coarse-gaining method is applied to this image in Fig. 5.2B, and the resulting $K(q)$ function provided by Eq. (5.16) in Fig. 5.2C. The agreement is excellent until moment of order 3; this is a statistical bound of the estimation of moments which is theoretically predicted (Schertzer and Lovejoy, 1992).

SF Method. The proposed structure function method has been validated with a 2D fractional Brownian field with H value varying from 0.1 to 0.9 with an increment of 0.1.

Fractional Brownian motion (fBm). A generalization of Brownian motion, was introduced by Kolmogorov in 1940 (Kolmogorov, 1940). This has been extensively studied by Mandelbrot and his co-workers in 1960s (Mandelbrot and Van Ness, 1968) and since then, it is considered as a classical scaling stochastic process for time series analysis. For time series, a *fBm*, denoted by $B_H(t)$, is a zero-mean Gaussian process with stationary increments characterized by the self-similarity parameter H , also known as the Hurst exponent. It possesses the following rescaling property:

$$B_H(\Lambda t) \stackrel{d}{=} \Lambda^H B_H(t), \quad \forall \Lambda > 0 \quad (5.17)$$

Where $\stackrel{d}{=}$ means equality of probability distributions. It leads to linear moment functions using structure functions Eq. (5.6): $\zeta(q) = qH$. This can be done also in 2D. The bi-dimensional isotropic fractional Brownian motion with Hurst parameter

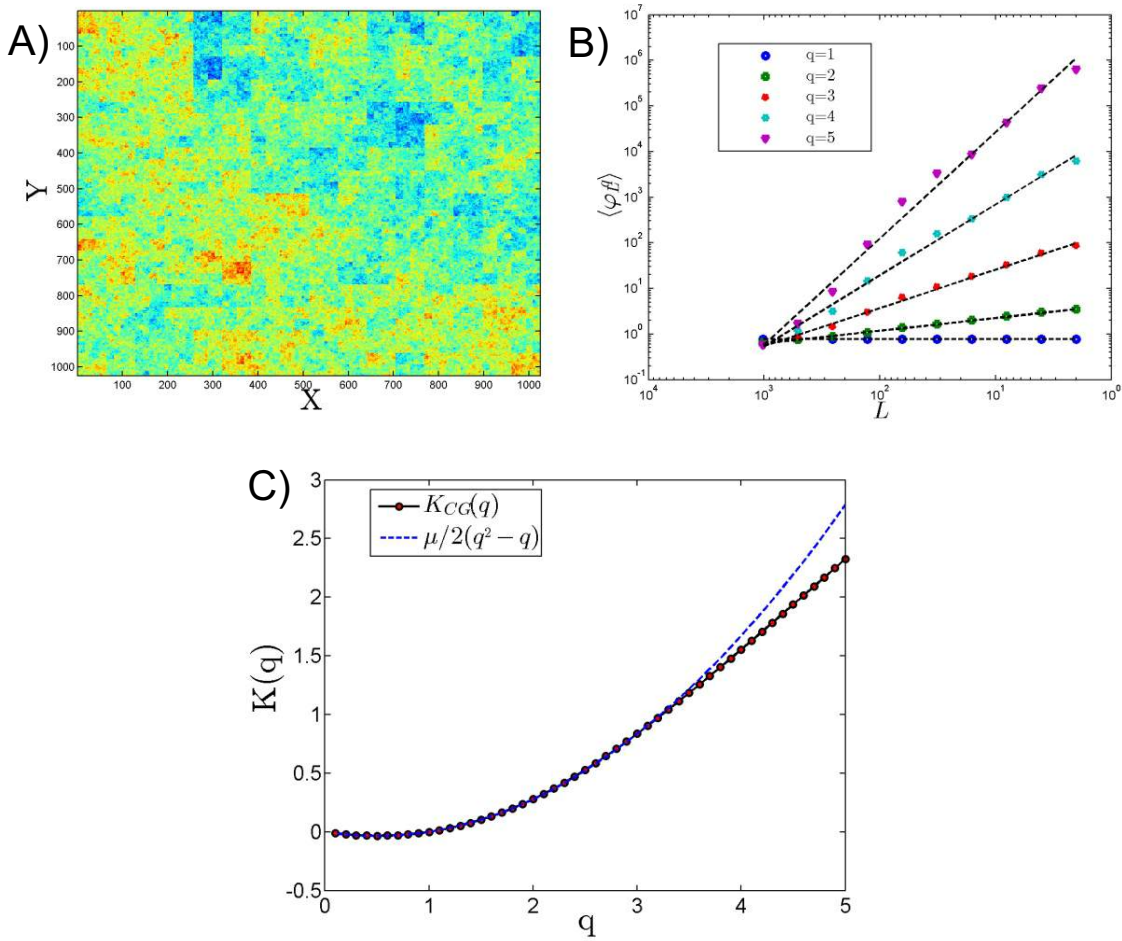


Figure 5.2: A) Simulation of a 2D log-normal image using a discrete cascade model with $\mu = 0.3$, B) coarse grained moments from $q=1$ to 5 and C) the corresponding moment scaling function experimentally estimate as dots and theoretical value $K(q) = \frac{\mu}{2}(q^2 - q)$ as a dotted line.

H is a centered Gaussian field B_H with an autocorrelation function (Kamont, 1995):

$$\langle B(\vec{x})B(\vec{y}) \rangle \propto \|\vec{x}\|^{2H} + \|\vec{y}\|^{2H} - \|\vec{x} - \vec{y}\|^{2H}; \quad 0 < H < 1 \quad (5.18)$$

where $\vec{x}, \vec{y} \in \mathbb{R}^2$ and $\|\cdot\|$ is the usual Euclidean norm.

In the present study we simulated 2D fractional Brownian field for various H values ($H = 0.1, 0.2 \dots, 0.9$) using an algorithm and code described in recent works (Barrière, 2007; Nicolis et al., 2011) (Fig. 5.3A). These images are analysed using 2D SF method for various randomly selected data ($N_p = 0.1$ million, 0.5 million, 1.0 million, 5.0 million and 10.0 million). The scaling moment function has been

derived for each image for different iteration number. H has been derived from the moment scaling function using $H = \zeta(1)$. Since satellite images often have missing values due to cloud coverage, we have also applied the SF approach to irregular images, where some part of the image have been removed. Fig. 5.3A shows some simulations for various values of H and Fig. 5.3B compares H estimations for full images and for images with some rectangles removed. This is tested for various values of N_p . We see that for $N_p = 10^6$ the method works very well (with an error of 3.88 %) even when there are missing values, and the estimated exponents are very precise. In the following we thus choose $N_p = 10^6$, since it is computationally reasonable and provide converged statistics for scaling exponents. To estimate the standard deviation of the estimated values with respect to full image and percentage of missing values will need a systematic study, which will be the topic of a future work.

5.3 Comparison of the CG and SF methods

Two recent studies have proposed to analyse the scaling of satellite images by applying first a gradient modulus approach (Montera et al., 2011; Nieves et al., 2007), in order to have a positive intermittent field, and then applying the CG method. The $K_{CG}(q)$ exponent function is retrieved and the authors assume that:

$$K_{CG}(q) = qH - \zeta(q) \quad (5.19)$$

where $\zeta(q)$ is the scaling exponent characterizing the Chl-a or SST fluctuations. Based on one simulated image, and two real satellite images we compare this latter approach with the one proposed here. We extract $K_{CG}(q)$ as described above, and we directly estimate $\zeta(q)$ using the 2D structure functions. We then compute $K_{CG}(q) + \zeta(q)$: if Eq. 5.19 is correct this should be linear ($= qH = q\zeta(1)$).

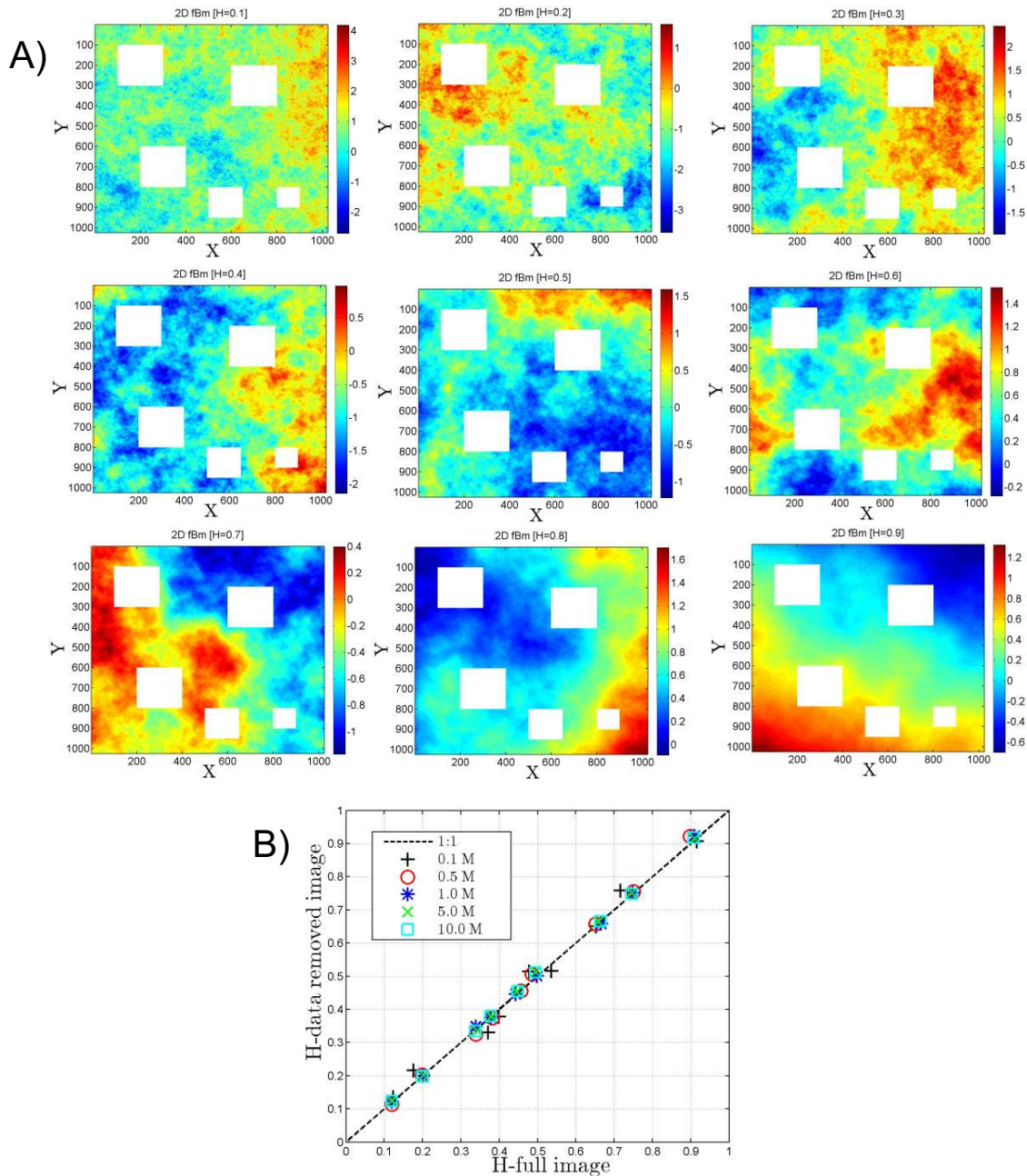


Figure 5.3: A) Simulation of 2D fractional Brownian motion for various Hurst exponents ($H = 0.1, 0.2 \dots, 0.9$). The white rectangles are the space where the data have been removed to test this method for deriving H using spatial Structure function method. The 2D structure function was applied to each full image and also to the same image with white rectangles removed, in order to show that this scaling method can be applied to irregular images. B) For each image, comparison of the H value estimated using the structure function for the full image and for images with missing values.

Multifractal field from cascade and fractional integration

We first test Eq. 5.19 using a multifractal simulation done by performing a cascade and then a fractional integration (Schertzer et al., 1997). As done in Lovejoy

et al. (Lovejoy et al., 2001b), we simulate a 2D log-normal multifractal image with $H = 0.35$ and $\mu = 0.1$ (Schertzer and Lovejoy, 1989) (Fig. 5.4A). The SF is directly applied to the image itself and the CG is applied to its gradient modulus. The scaling moment spectrum is derived for each method (Fig. 5.4B and 5.4C). The moment scaling functions for both SF and CG are derived for various moments from 0.1 to 5 with an interval of 0.1. $K_{CG}(q)$ is non-linear and $\zeta(q)$ is almost linear and Eq. 5.19 is not verified: $K_{CG}(q) + \zeta(q)$ is close to qH for $q \leq 2$ but for larger moments it is no more the case (Fig. 5.4D).

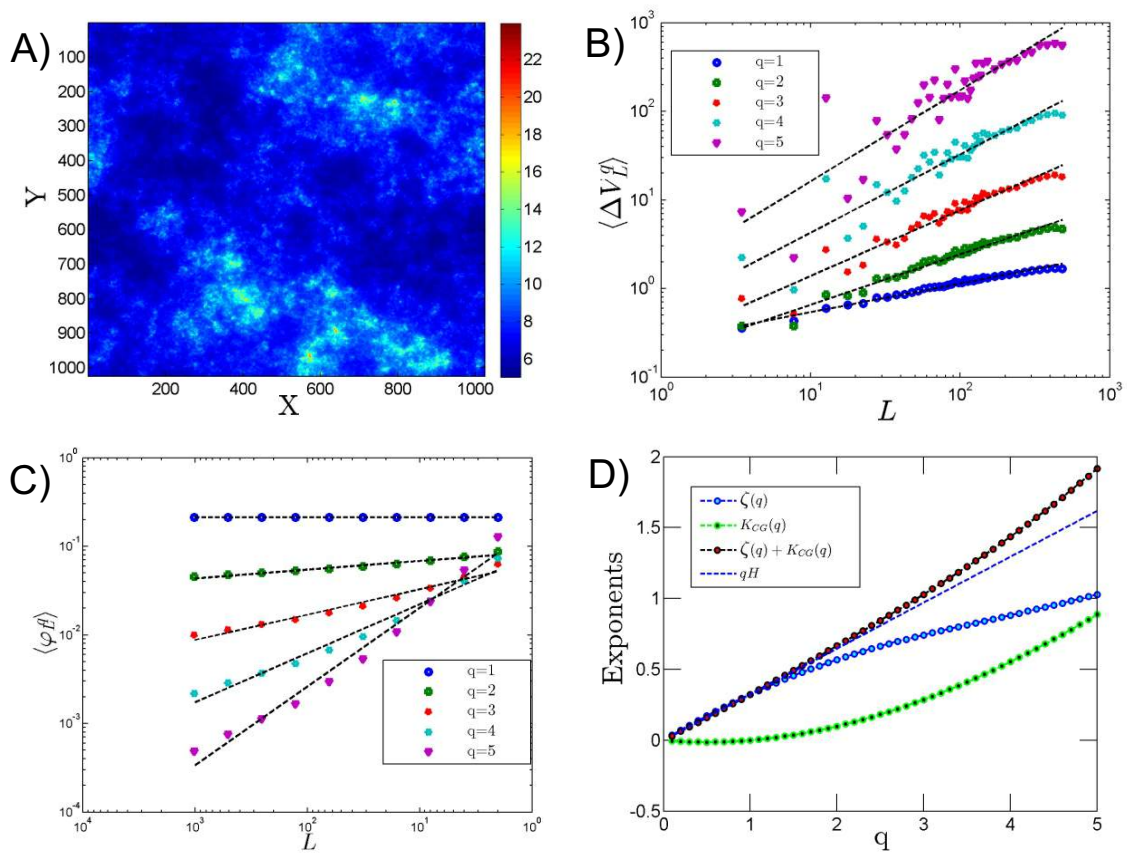


Figure 5.4: A) Simulation of a 2D log-normal multifractal image with $H = 0.35$ and $\mu = 0.1$. B) Scaling of the SF; C) Scaling analysis when gradient modulus is applied on the image shown in A; D) representation of different exponents.

5.3.1 Scaling analysis on a Chl-a image of MODIS aqua

The standard MODIS Chl-a imagery available from the Goddard Space Flight Centre is produced via OC3M algorithm (O'Reilly et al., 2000) has been used for the

present study. The *OC3M* algorithm is a fourth order polynomial equation and applies the maximum ratio of the remote sensing reflectance at 443 *nm* (blue) to 550 *nm* (green) or 490 *nm* (blue) to 550 *nm* (green). These proposed methods have been applied to real images of Chl-a from the Mauritanian coast sampled on 11-March-2003 (Fig. 5.5A). A cloud free image (512×512 pixels) has been extracted for the analysis (square region marked in Fig. 5.5A). The gradient modulus of Chl-a (Δ Chl-a) has been derived from the Chl-a image (Fig. 5.5B). This gradient modulus generates a positive field, the CG method is adopted for analysing this positive field. The SF method has been applied directly to the Chl-a image. We have chosen the random picking method tested in section 2 with $N_p = 10^6$ couple of points. Here also we could observe the power-law behaviour of the SF. The radially summed power-spectra of the Chl-a image has been derived for the cloud free part of the image (512×512 pixel). The derived spectral exponent α for the radially summed image is 1.79 (Fig. 5.5C). The constants derived for the Chl-a image are shown in Table 5.1. The $\zeta(q)$ derived for the Chl-a image also follows a non-linear convex curve showing intermittency in the spatial distribution of Chl-a (Fig. 5.5C). Fig. 5.5D shows that Eq. 5.19 is not verified for $q \geq 1.7$.

Region	Sampling date	Parameter	H	α
Mauritanian Coast	11-Mar-2003	Chl-a	0.37	1.79
Mauritanian Coast	11-Mar-2003	SST	0.41	1.80

Table 5.1: The exponents (H and α) derived for Chl-a and SST images for Mauritanian region. The Hurst exponent H derived through *SF* ($H = \zeta(1)$).

5.3.2 Scaling analysis of MODIS SST

These proposed methods (CG and SF) have also been applied to an image of SST sampled simultaneously with Chl-a from the Mauritanian coast on 11-March-2003. A cloud free image (512×512 pixels) has been extracted for the analysis (Fig. 5.6A). The 2D power-spectra of the SST image has been derived. It follows a power-law behaviour with a spectral slope $\alpha = 1.8$ (Fig. 5.6B) with some noise observed at smaller scales. Similarly to Chl-a, the gradient modulus of the SST has been derived and CG

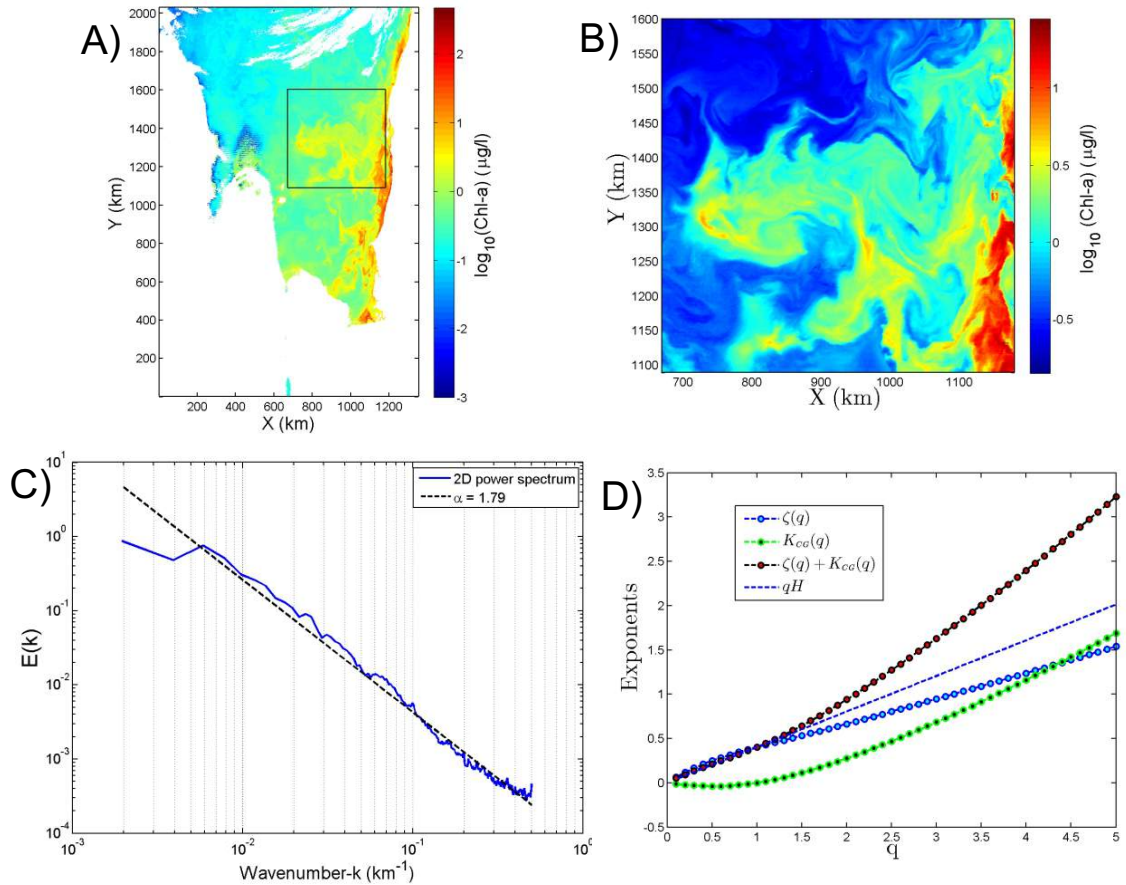


Figure 5.5: A) Chl-a image from MODIS Aqua from the Mauritanian coast sampled on 11 March 2003; the square indicates the 512×512 pixel of cloud free image chosen for the analysis of Chl-a. B) Gradient modulus estimated for the latter square image. C) Power-spectrum of the Chl-a image showing a scaling exponent $\alpha = 1.79$. D) Moment scaling function for the square image, using the CG and SF methods. Eq. 5.19 is tested and found not to be correct for $q \geq 1.7$.

method applied. Here also the scaling moment function derived for the SST follows a non-linear concave curve showing the spatial intermittent characteristics of SST (Fig. 5.6C). However its small value shows that this field is not very intermittent. The proposed SF method has been directly applied to the SST image. The moment scaling function of SST image derived follows a non-linear convex shape, showing the intermittent characteristics of the spatial distribution of the SST (Fig. 5.6C). The H derived through the SF method is $H = 0.41$ ($H = \zeta(1)$). The constants derived for the SST image are shown in Table 5.1. Here we also can see that these two exponents fall away from the typical linear qH line for $q \geq 1.5$.

The values of the spectral exponent α derived here for the Chl-a and SST satel-

lite images are in good agreement with the range of α values derived from in situ measurements of fluorescence (as a proxy of Chl-a) and temperature (Seuront et al., 1996b). The estimated values of the scaling parameter H for Chl-a and SST show also very good agreement with previous studies (Seuront et al., 1996b; Lovejoy et al., 2001a; Verrier et al., 2014). Concerning the μ value, let us note that this intermittency parameter could be more sensitive to the local conditions. It can be estimated using structure functions as $\mu = K_{CG}(2) = 2\zeta(1) - \zeta(2)$. For Chl-a and SST we obtain here 0.13 and 0.012 respectively. For Chl-a, this value is larger than the one estimated from Eulerian time series, ranging from 0.065 to 0.074 (Seuront et al., 1996b,a). On the other hand, the SST field considered here seems smoother than found in other studies since $\mu = K_{CG}(2)$ in other published studies range from 0.05 to 0.19 (Seuront et al., 1996b; Lovejoy et al., 2001a; Verrier et al., 2014; Seuront et al., 1996a, 1999).

5.4 Discussion: the role of signs

We have considered here the scaling exponent $K_{CG}(q)$ obtained by coarse-graining a positive field, and the exponent $\zeta(q)$ obtained directly through structure functions. We found, using a simulation and two satellite images, that Eq. 5.19 is not verified, an equation assuming that the gradient modulus applied to a non-stationary field retrieves the basic scaling information. In fact, such relation is not verified because the local sign contains information; when performing a gradient modulus, the sign information is lost. We check this hypothesis here by considering a fBm simulation with $H = 0.6$. We estimated a sign information from the 2D fBm simulation as follows. We computed the two components of the gradient (in the x and y directions) and took the sum of the two terms. If this sum is positive, we choose to consider a sign information as 1 and 0 if the sum is negative. This way the sign information of the gradient is transformed into a matrix containing only 0 and 1 values. The figure obtained (Fig. 5.7A) does not seem to be a noise; to check this we consider its scaling by using a coarse-graining (Fig. 5.7B). We obtain a scaling law of the form $\mu(q - 1)$

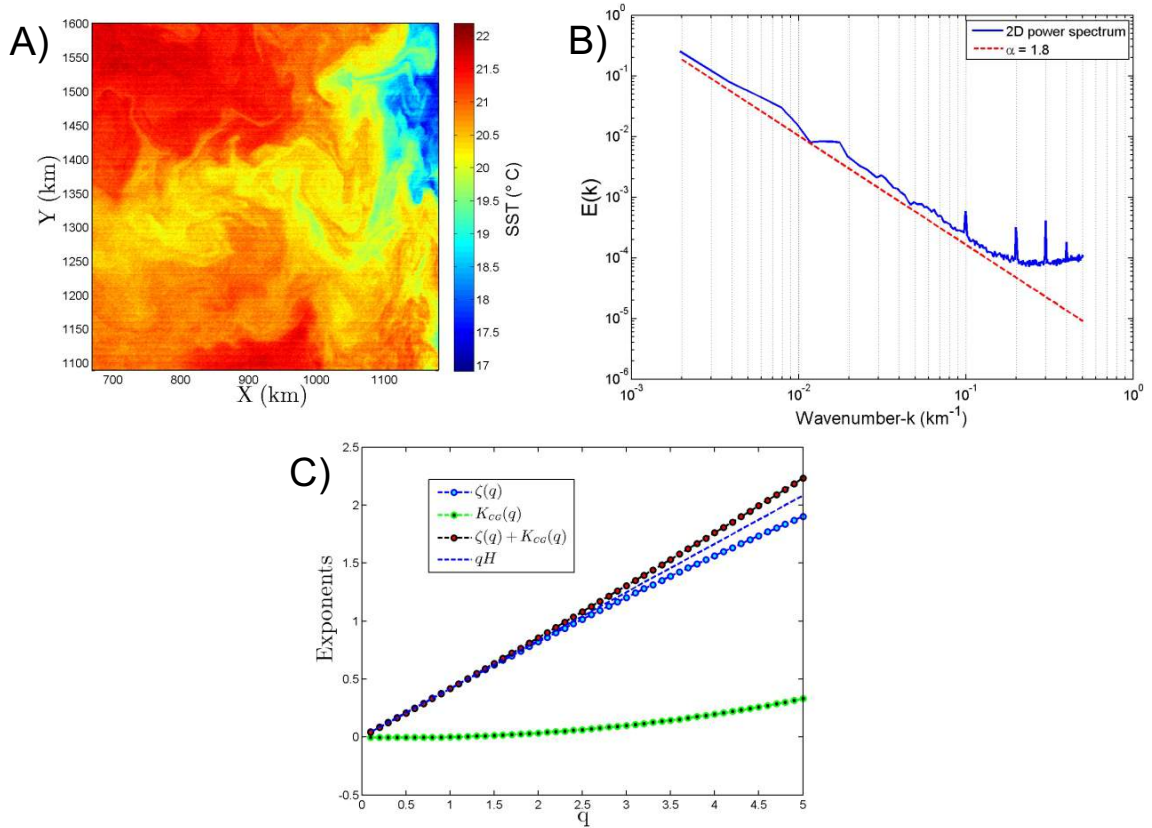


Figure 5.6: A) SST image from MODIS from the Mauritanian coast sampled on 11 March 2003. B) 2D power-spectrum of the image showing a scaling exponent $\alpha = 1.80$. C) Moment scaling function, using the CG and SF method. Eq. 5.19 is approximately valid, coming from the fact the $K_{CG}(q)$ is very small, corresponding to a very regular field.

with $\mu = 0.09$. This is similar with β -model and shows that the sign information has a structure; such structure is lost when performing a modulus and we can assume the same property for real images: such analysis is left for future studies.

5.5 Conclusion

We have considered here several methods to estimate the scaling properties of ocean colour images, in relation with turbulence. We have first recalled data analysis methods, mainly coarse graining after taking the gradient modulus, and 2D structure functions. Similar to many atmospheric processes, oceanic processes are also governed by complex turbulent processes. These processes cannot be fully characterised by a single scaling exponent such as α . Additional multifractal parameters

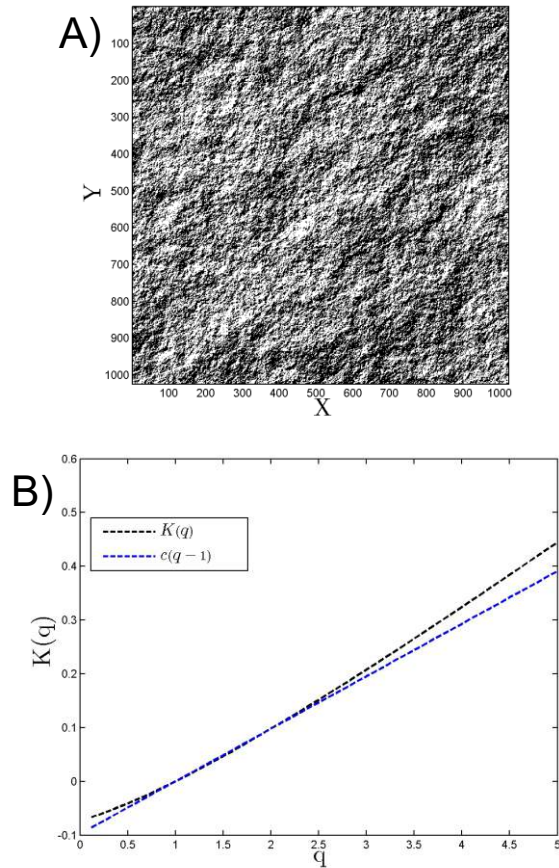


Figure 5.7: The gradient sign information of the 2D fBm derived for $H=0.6$ in A) and its moment scaling function in B).

are required to fully characterise these multi-scaling properties. Even though the CG method is successful in many applications, it suffers from several approximations that can add some uncertainties in the estimation of multifractal parameters. In this context, we highlighted here an alternative tool such as 2D structure function to overcome the approximations related to the CG method. This method of 2D structure functions has rarely been documented and studied for geophysical image analysis due to computational complexity constraints. We have obtained several results in this framework:

- Since the structure function approach needs to consider n^4 couple of points, where n is the linear size (in pixels) of an image, it is too much computer time consuming. We shown using fBm simulations that taking 10^6 couple of points randomly is enough for an adequate estimation of the structure func-

tion scaling exponents. We showed also that this method works for images with missing data, an important aspect since many real images have missing pixels due to cloud coverage.

- We compared the Coarse graining scaling exponent $K_{CG}(q)$ from the gradient modulus, to $qH - \zeta(q)$, and found that such relation is not verified, indicating that the gradient modulus loses information (the signs have a scaling structure) and hence this method cannot be safely used instead of SF.
- We considered two images from MODIS Aqua (Chl-a and SST) and showed on these examples that scaling approach using SF and $N_p = 10^6$ couple of points is adequate; we also showed that the spectral exponent for these examples is close to $5/3$ characteristic of passive scalar fully developed turbulence. Such 2D multifractal property of Chl-a and SST is a 2D generalistic of previous results obtained for time series (Seuront et al., 1996b,a, 1999).
- Since Chl-a and SST are not conservative, Chl-a can be influenced by biological activities and SST can be influenced by the surface heat flux. These biological and physical processes can have influence on the scaling exponents. These two parameters may show different scaling properties for in situ measurements as shown in other studies (Seuront et al., 1996b,a). The spectral exponent α derived for Chl-a and SST satellite images are in good agreement with the in-situ measurements of fluorescence by Chl-a and temperature (Seuront et al., 1996b,a, 1999).
- The present paper compared CG and SF methods on a real image. We have considered here the question of missing data on a synthetic fBm field; the same has been done on real images and it was confirmed that the method is also providing the same scaling exponents for real images (not shown here).

Let us note that this method can also be applied to the 2D velocity field obtained from altimeter data, since the velocity can also be intermittent and scaling. As a perspective, in a following work, we will use the SF method with $N_p = 10^6$ couple

of points, to estimate the $\zeta(q)$ function, fit with the data using a log-normal approximation with 2 parameters ($H = \zeta(1)$ and $\mu = 2H - \zeta(2)$) and consider the values of these parameters in several locations (open ocean, coastal waters, upwelling region, etc.). For that purpose, several images collected over different oceanic regions characterised by contrasted biological and physical environment will have to be studied.

CHAPTER 6

MULTI-SCALE ANALYSIS OF OCEAN COLOUR AND SEA SURFACE TEMPERATURE IMAGES OF MODIS-AQUA: STATISTICAL CHARACTERISATION USING TURBULENCE TOOLS

Abstract

Satellite remote sensing is a powerful tool for understanding many of oceanic processes synoptically. The scaling and multi-scaling properties of these satellite products have been studied hardly in the framework of the turbulence theory. The main objective of the present study is to understand the multi-scaling and multifractal properties of the satellite images of ocean colour and sea surface temperature for various oceanic regions using tools borrowed from the turbulence theory. For this purpose, we have selected satellite ocean colour products of Remote sensing reflectance (R_{rs}), Chlorophyll-a (Chl-a) and thermal infra-red Sea Surface Temperature (SST). For understanding the spatial scaling associated with turbulence, it is important to have a daily imagery of these products. As far as ocean colour remote sensing is considered, it is very difficult to have a cloud free images for the understanding of scaling behaviour.

For that purpose, we have identified seven contrasted regions of the global ocean, characterised by high spatial heterogeneity in Chl-a and SST. Power spectral analysis, a widely used tool in the marine environment and marine ecology to assess the scaling properties of these scalars, especially in connection with turbulence have been used for the present study. Here we use 1D and 2D Fourier power spectra to understand the spatial scaling of Chl-a and SST. The 2D spectral slope β is derived from the 2D power spectrum using radial sum of the power spectrum. The multi-scaling properties of these images are also studied using the Structure Function (SF) method. Using a lognormal fit, we have derived the multifractal parameters (Hurst exponent H and intermittency parameter μ) of these images using SF method. The β derived through power spectra and SF method show good agreement except SST images. The derived multifractal parameters show variability in their values depending upon the region. The scatter plot of μ versus H shows some clustering of these parameters. The SST is showing low intermittency, R_{rs} high, and Chl-a shows intermittency in between SST and R_{rs} for all the regions.

Cumulant scaling of these images is also performed for deriving H using log-normal intermittency model. The H values derived through the SF method and the cumulant scaling method also show good agreement with Chl-a data.

6.1 Introduction

The ocean is a complex physical system in which organism distributions are affected spatially and temporally by the physical and biogeochemical processes on multiple scales (Lubchenco and Petes, 2010; Doney et al., 2012). Theories of geophysical fluid dynamics can explain many of the basic processes at different scales such as local turbulence, eddy systems and ocean circulation (Pedlosky, 1982). The ocean colour remote sensing is a tool used for the understanding of these spatial and temporal changes synoptically. The spatial/temporal scale of a variable is the distance/period over which it is relatively unchanged (Powell, 1995). The spatial heterogeneity of the ocean is omnipresent and occurs at all scales (Steele, 1991; Levin and Whitfield,

1994; Mitchell et al., 2008). These heterogeneities are quite common in biogeochemical (Gruber, 2011; Hales et al., 2012), biophysical (Hsieh et al., 2005) and trophic interactions (Litzow and Ciannelli, 2007; Brander, 2010) of the the aquatic environments.

The distribution of phytoplankton does provide key information about the physical and biological processes in the aquatic ecosystems (Denman et al., 1977; Steele, 1989; Abraham et al., 2000). Phytoplankton distribution has a unique feature at all spatial scales. For instance, at global scale it defines rich ocean regions and outline ocean biomasses at mesoscales (Falkowski et al., 1998). It highlights the importance of the upwelling for the primary production and role of mixing in dispersion and the ability of fronts to confine and accumulate phytoplankton (Yoder et al., 1994).

The Sea Surface Temperature (SST) is an important variable for the study of the earth's climate system, for weather forecasting, and for oceanographic research. Patterns of SST reveal the complexity of the ocean surface currents, and large scale SST anomalies in critical oceanic areas presage climate perturbations, such as El-Nino events. The SST is a controlling variable in the coupling of the ocean and atmosphere in terms of the fluxes of heat, moisture, momentum and greenhouse gasses, such as CO₂. The global distribution of the SST and its change with time and space is of growing importance to many agencies worldwide (Donlon et al., 2007). It includes climate variability monitoring, seasonal forecasting, operational weather and ocean forecasting, military and defence operations, validating or forcing ocean and atmospheric models, ecosystem assessment, and tourism and fisheries research. The multiscale/multifractal properties of SST simulated from NEMO are studied by Verrier et al. (2014). This study has been quantified the Hurst exponent H (one of the important multifractal parameter) for SST simulation range from 0.32 to 0.76.

In Renosh et al. (2015) the 2D structure function methodology was proposed for satellite image analysis. It was tested on simulated data and also on 2 sample MODIS images. The present study is the continuation of this work, with more images analysed in several parts of the ocean.

The interpretation and analysis of data acquired by remote sensing are based on

physical laws linked to the optical properties of the constituents of the ocean. Therefore, it is essential to understand their spectral responses to explain the behaviour of the various components of the surface layer of the oceans and their relationships with their physical environment. The present study fits into this framework to characterise the effect of turbulence on physical and biological processes. The distinctive feature of our work is to understand the large spatial variability of ocean colour (Chl-a) and SST. Studies based on the spectral analysis of these parameters from satellite imagery are in most cases corresponding to average measurements over a week, a month or even years. However, averaging measurements corresponds to lose the information on small spatial scales. For this reason in our study, we focus on instantaneous measurements of Chl-a, SST and remote sensing reflectance (R_{rs}).

6.2 Materials and methods

6.2.1 Data and study areas

We used MODerate resolution Imaging Spectrometer (MODIS) derived Chl-a, SST, R_{rs} -443, and R_{rs} -555 data for the present study. MODIS is a sensor on-board Aqua (Earth Observation System PM) satellite which capture data in 36 spectral bands ranging in wavelength from $0.4 \mu m$ to $14.4 \mu m$, and at varying spatial resolutions (2 bands at 250 m, 5 bands at 500 m and 29 bands at 1 km). MODIS Aqua gives a global vision of the earth surface during 3 days. Each MODIS image spans a distance of 2330 km with a spatial resolution of 1 km for the bands of interest here (Chl-a, SST, R_{rs} -443, and R_{rs} -555). The most difficult task for selecting a region was the cloud coverage. Level 2 imagery consists in the derived geophysical variables, such as Chl-a, SST, R_{rs} -443, and R_{rs} -555 at 1 km spatial resolution covering the same area as the original scene. In the present study we have selected 7 different regions (Argentina Coastal waters (AC), Mauritanian Coastal waters (MC), North Eastern Arabian Sea (NEAS), Angola Namibia coastal waters (ANC), Peru Chile coastal waters (PCC), Celtic Sea (CS) and Eastern Mediterranean (EM)). The level 2 (spatial resolution 1.0

km) products of MODIS-Aqua (Chl-a, SST, R_{rs-443} , and R_{rs-555}) for cloud-free days has been selected for the present study. The date of sampling and the geographical location of the study area are shown in Table 6.1.

AC	MC	NEAS	ANC	PCC	CS	EM
08/07/2013	05/02/2014	02/12/2013	05/04/2013	30/05/2012	29/03/2012	31/12/2009
10/02/2014	10/01/2013	05/03/2013	06/05/2012	–	–	–
19/04/2013	12/02/2014	07/01/2014	12/04/2014	–	–	–
30/07/2012	12/01/2013	12/10/2012	14/07/2011	–	–	–
–	–	20/01/2013	23/04/2013	–	–	–
–	–	20/11/2013	30/04/2013	–	–	–
–	–	21/03/2013	30/07/2013	–	–	–

Table 6.1: The geographical locations with sampling date

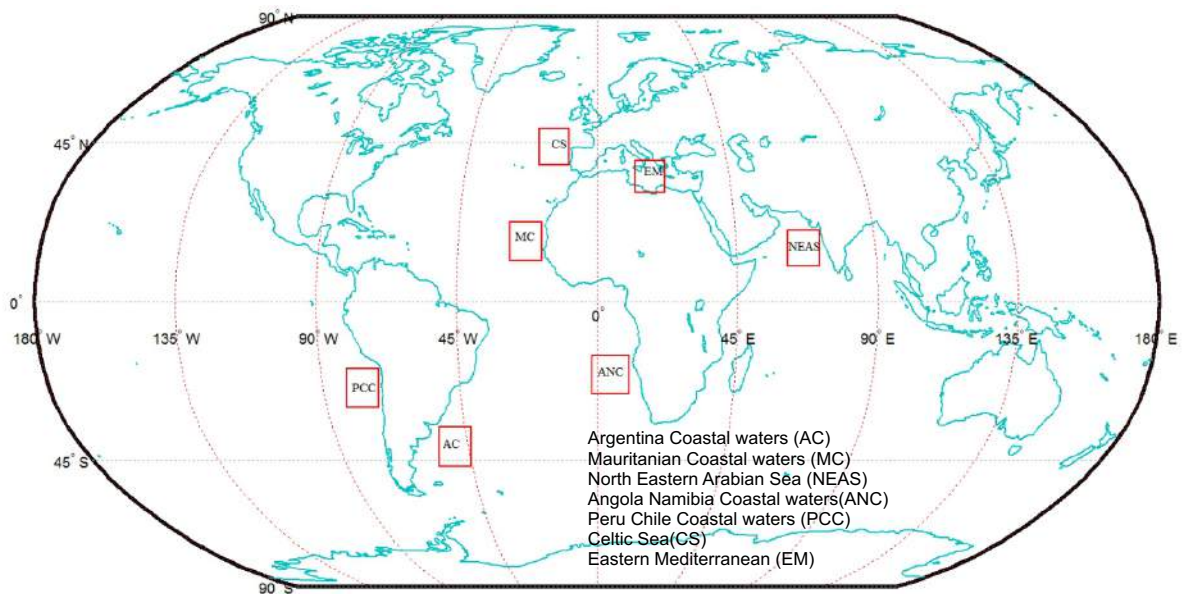


Figure 6.1: Study area maps from different regions of world ocean

6.2.2 Significance of the study regions

In this study, we have selected 7 different regions of the world ocean (Fig. 6.1) which show high spatial heterogeneity in their biomass. The physical and biological features of these areas are provided below.

Argentina Coastal waters (AC) Argentina coastal ocean is known to be an eutrophic ocean. Three large rivers discharge in this region: the Rio de la Plata, the

Rio Negro and the Rio Colorado. The water masses of the Northern Argentine Continental Shelf are derived from the advected waters of subantarctic origin, local source of continental river run-off and a locally generated salinity maximum (Lucas et al., 2005). This region is also famous for the small scale local frontal zones (Acha et al., 2004).

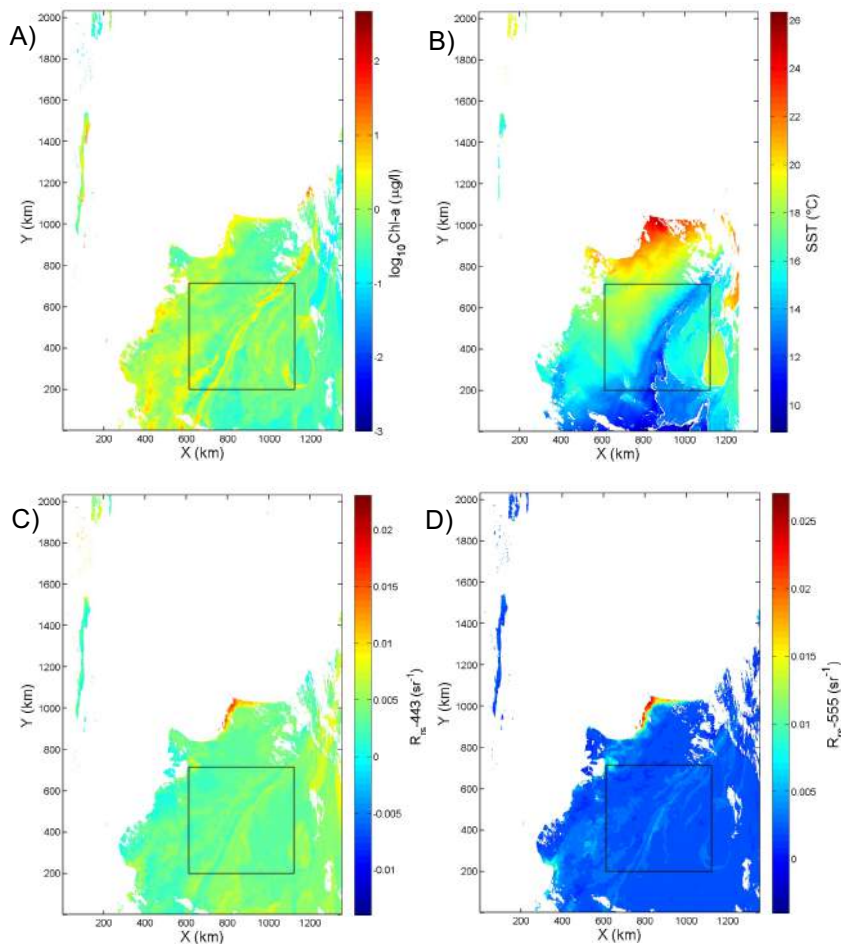


Figure 6.2: Chl-a, SST, R_{rs-443} and R_{rs-555} from AC region sampled on 10/07/2013. The square indicates the 512x512 pixel of cloud free image chosen for the analysis.

Mauritanian Coastal waters (MC). The equatorial Atlantic ocean is a complex region dominated by large scale westward currents (North Equatorial Current *NEC*) and eastward counter currents (North Equatorial Counter Current *NECC*). The North-West African upwelling region, where surface waters are driven away from the coast by easterly trade-winds and cold, nutrient-rich waters, ascends from the

deep to fertilize the euphotic layer. Mauritanian coastal waters are the region having high productivity and plankton biomass along with strong seasonal fluctuations in the North-East Atlantic Ocean (Kuipers et al., 1993).

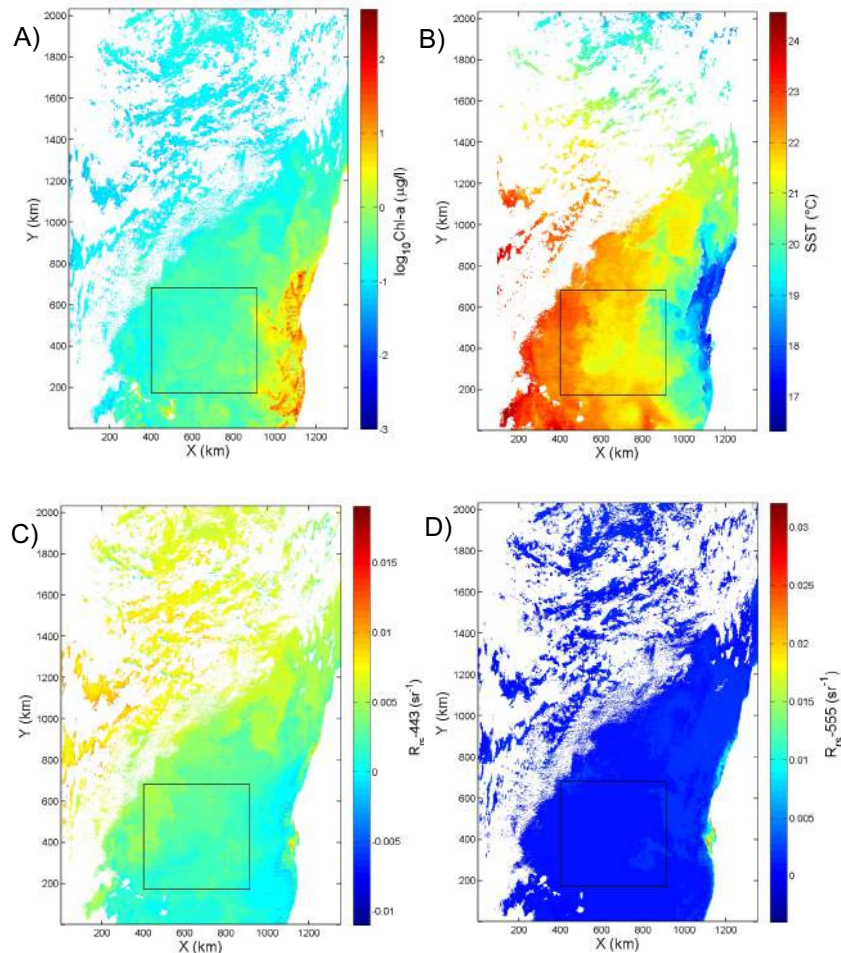


Figure 6.3: Chl-a, SST, R_{rs-443} and R_{rs-555} from MC region sampled on 10/01/2013. The square indicates the 512×512 pixel of cloud free image chosen for the analysis.

North Eastern Arabian Sea (NEAS). The Arabian Sea is one of the most biologically productive oceanic regions, mainly due to the upwelling of nutrients during the south-west monsoon (summer). The northern Arabian Sea continues to sustain fairly high biological production after the upwelling season and during much of the north-east monsoon season (winter) (Banse, 1987). The cooling of surface waters in the winter season triggers the convection mechanism for injecting the high nutrient subsurface waters into the surface, and cause high productivity during the winter

season (Madhupratap et al., 1996).

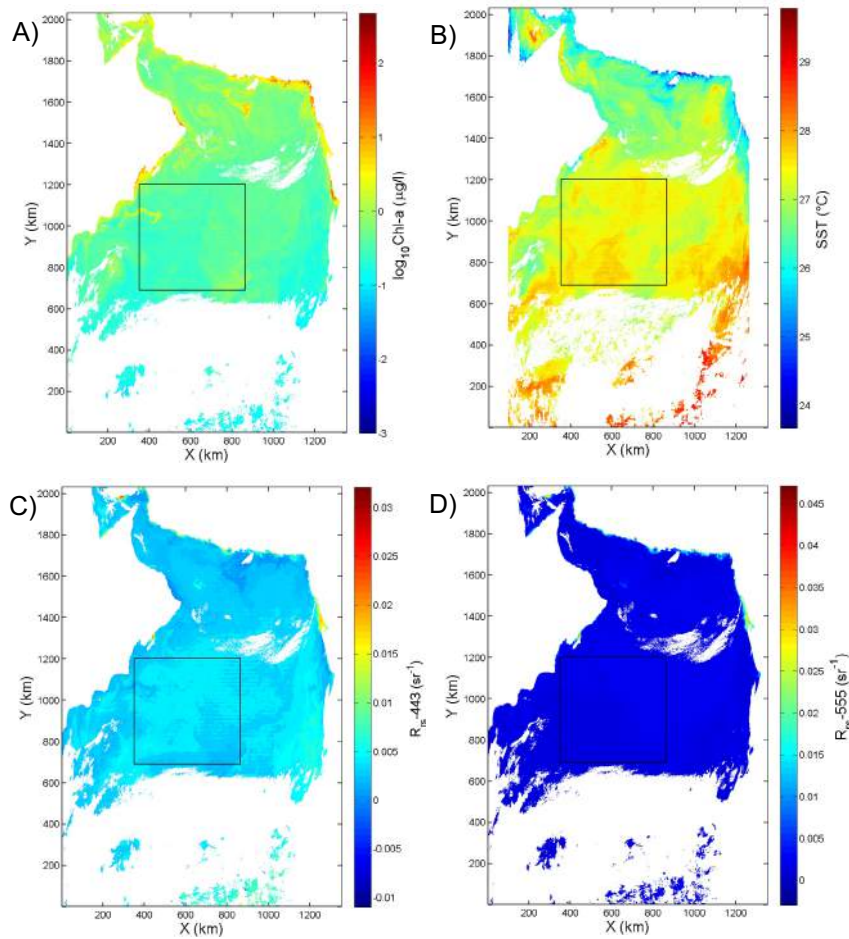


Figure 6.4: Chl-a, SST, R_{rs-443} and R_{rs-555} from NEAS region sampled on 02/12/2013. The square indicates the 512×512 pixel of cloud free image chosen for the analysis.

Angola Namibia Coastal waters (ANC). ANC is located in a region influenced by a fast narrow and stable Angola Current of 250-300 m depth covering both the shelf regions and the continental slope (Moroshkin et al., 1970). This water mass usually has a temperature greater than 24°C and a salinity of more than 36.4 psu in the upper mixed layer. This water mass gradually becomes colder and less saline as it travels south (Lass et al., 2000). During winter and spring, the hot Angola Current waters, with temperatures between 27 and 30°C, retreat to the north-west and are replaced by slightly cooler waters with temperatures between 20 and 26°C. This periodic south-east advance and north-west retreat of the Angola Current seems

to be linked to the intensity of upwelling that occurs later off the Namibian coast (Meeuwis and Lutjeharms, 1990).

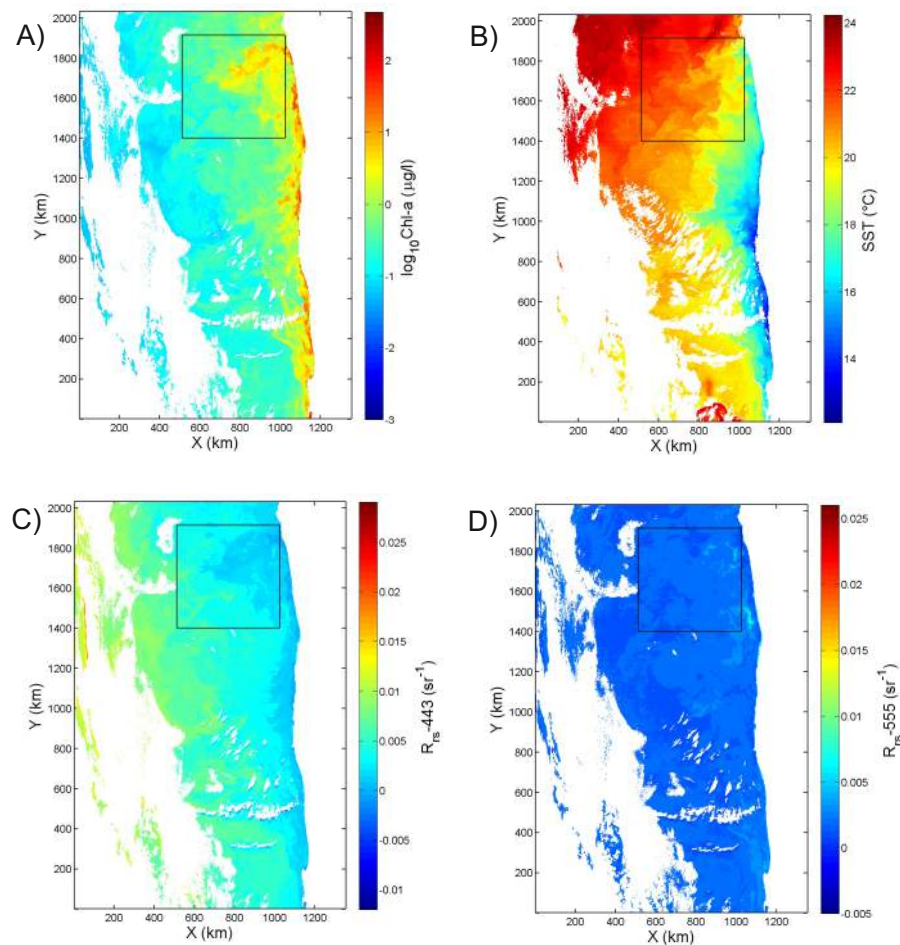


Figure 6.5: Different parameters from the Angola Namibia coastal waters sampled on 30-April-2013, Chl-a in A), SST in B), R_{rs-443} in C) and R_{rs-555} in D). The square indicates the 512×512 pixel of cloud free image chosen for the analysis.

Peru Chile coastal waters (PCC). The Peru-Chile current system is characterised by a high biological production, supporting some of the largest fisheries on the planet (Chavez and Messié, 2009). The inter-annual variability of Chl-a in this region is mainly associated with El Nino-Southern Oscillation (ENSO) perturbations (Correa-Ramirez et al., 2012).

Celtic Sea (CS). CS is an extensive shallow area bordering the eastern North Atlantic in 50° North. It is separated from the deep ocean by a rapidly descending

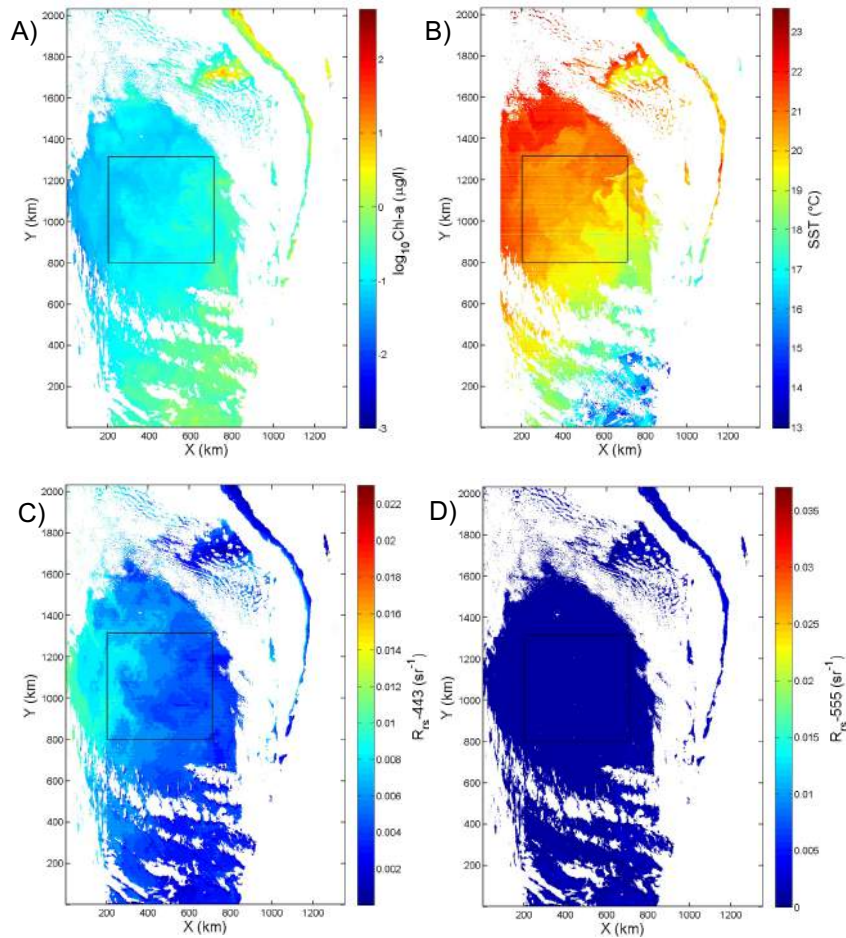


Figure 6.6: Chl-a, SST, R_{rs-443} and R_{rs-555} from PCC region sampled on 30/05/2012. The square indicates the 512×512 pixel of cloud free image chosen for the analysis.

shelf break and is strongly stratified over much of its interior throughout the summer months. Phytoplankton productivity and taxonomic composition in the CS depend on the water column structure. Diatoms dominate well mixed areas with high nutrient content and show a high rate of productivity, while dinoflagellates and micro flagellates are found in stratified waters exhibiting lower rates of productivity (Raine et al., 2002; Cooper, 1961).

Eastern Mediterranean (EM). Eastern Mediterranean is one of the most famous oligotrophic waters of the world ocean (Azov, 1991). It is because low nutrient content in the deep waters, when they are upwelled or mixed into the photic zone, produce less primary production. Because of the clarity of the water, Eastern Mediter-

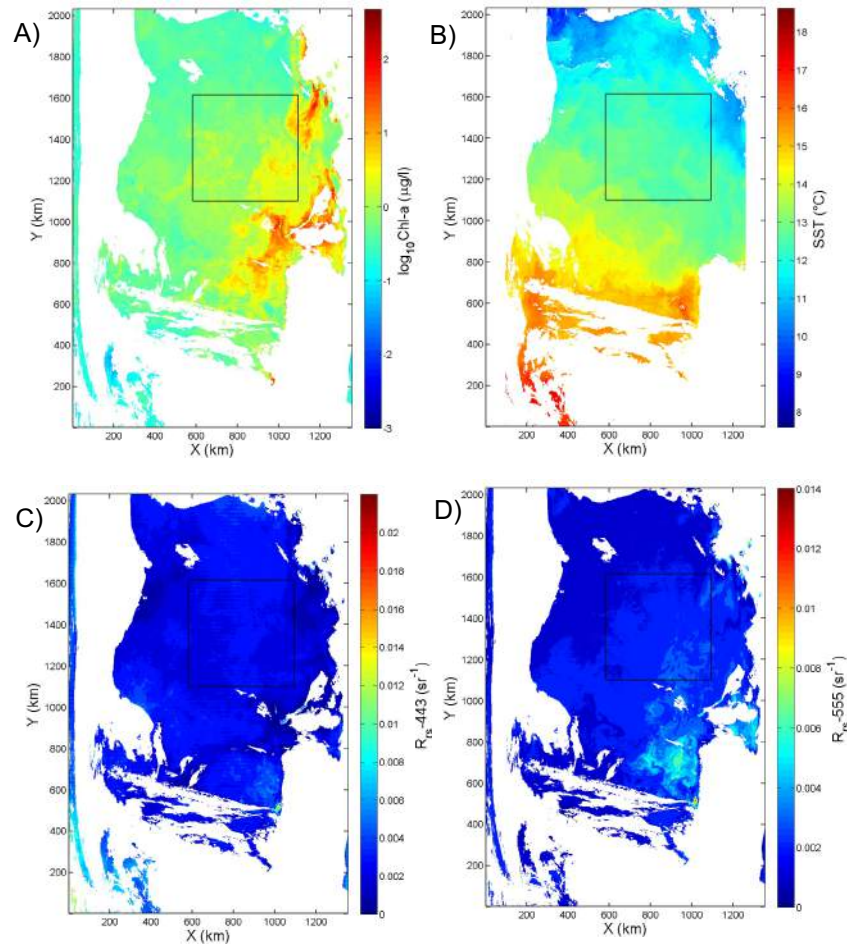


Figure 6.7: Chl-a, SST, R_{rs} -443 and R_{rs} -555 from CS region sampled on 29/03/2012. The square indicates the 512×512 pixel of cloud free image chosen for the analysis.

anean has deeper euphotic zones.

Here we considered a broad range of regions from highly eutrophic sea of AC region to highly oligotrophic waters of EM. These regions differ also by the hydrography and river run-off. Except EM, all other regions are famous for the coastal upwelling and high primary production.

6.2.3 Chlorophyll-a (Chl-a)

The standard MODIS Chl-a imagery available from Goddard Space Flight Centre is produced via the OC3M algorithm. The OC3M algorithm is an extension of the empirical OC4v4 algorithm derived for SeaWiFS, based upon 2853 field measurements collected across a range of bio-optical marine provinces (O'Reilly et al., 2000). The

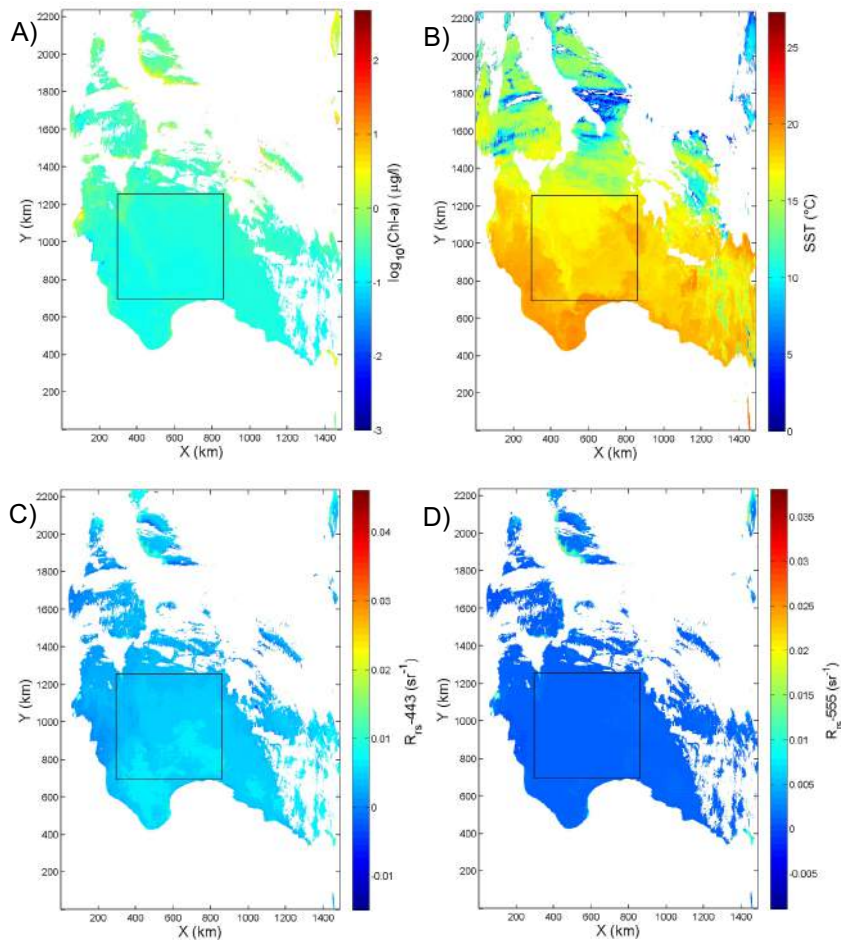


Figure 6.8: Chl-a, SST, R_{rs-443} and R_{rs-555} from EM region sampled on 31/12/2009. The square indicates the 512×512 pixel of cloud free image chosen for the analysis.

OC3M algorithm is in the form of a fourth order polynomial equation and applies the maximum of the ratio of the remote sensing reflectance at 443 nm (blue) to 550 nm (green) or 490 nm (blue) to 550 nm (green). Chl-a is the pigment in the majority of the photosynthetic organisms, therefore it is considered as an excellent indicator of biomass. It is used to estimate the primary production of the water column (Jeffrey and LeRoi, 1997), also used to track the phytoplankton dynamics (Brentnall et al., 2003) and included in templates of the biogeochemical cycle especially in the carbon cycle (Behrenfeld et al., 2005). As far as fisheries are considered, Chl-a is used as an important input to many dynamic models. A sample data of Chl-a used for the present study is shown in Fig. 6.5A and the square shows the cloud-free part

of 512×512 pixels. This is later used in our study.

6.2.4 Sea Surface Temperature (SST)

The SST represents the temperature of a thin layer of the ocean of 0.01 m deep. The algorithm described for the measurement of the SST is based on the measurements of brightness temperature. MODIS SST algorithms use either band 22 and 23 at 3.959 and 4.050 μm or bands 31 and 32 at 11 and 12 μm . Bands 31 and 32 in the long-wave infra-red part of the spectrum are applied during the day as they are not affected by the reflected sunlight; however they are potentially affected by water vapour in the atmosphere. While bands 22 and 23 in the short-wave infra-red are less affected by water vapour, they are applied only to night imagery due to contamination by sunlight (Brown et al., 1999). Daytime SST imagery has been selected for the present study as it is collected simultaneously to Chl-a (Fig. 6.5B). The study areas have been selected in such a way that Aerosol Optical Depth (AOD) has minimum values.

6.2.5 Remote sensing reflectance (R_{rs})

The standard R_{rs} products of MODIS Aqua are downloaded from the Goddard Space Flight Centre. For the present study, we choose two different wavelengths, 443 nm and 555 nm, R_{rs} -443 and R_{rs} -555 (Fig. 6.5C and Fig. 6.5D). The use of these two wavelengths represents the minimum (555 nm) and maximum (443 nm) absorption of phytoplankton. Because of that the ratio of these two R_{rs} (R_{rs} -443/ R_{rs} -555) approximates the concentration of Chlorophyll-a and the biomass. As Chl-a values are retrieved from these two R_{rs} values using a non-linear equation, the Chl-a and R_{rs} spatial patterns and their relation to turbulence could be different. In this context, we will specifically examine if R_{rs} -443 is a better proxy than space retrieved Chl-a to assess the effect of turbulence.

6.2.6 Homogeneous isotropic turbulence

The analysis of the data is done in the methodological framework of turbulence. Turbulent flows have been investigated for more than a century; however no general approach to the problems in turbulence exists. There is no general solution of the Navier-Stokes equations, which drive the turbulent flows. For fully developed turbulence (with large Reynolds number $Re = UL/\nu$ where U is a typical velocity scale, L a typical length scale and ν the kinematic viscosity) a classical picture is the Kolmogorov-Richardson energy cascade. In this framework energy is supplied, introduced or produced in the fluid at a relatively large scale, and is successively passed by interactions between eddies or their instability through a spectrum of smaller and smaller eddies, within which inertial forces, rather than the viscosity forces, are dominant. Finally energy is conveyed to eddies of size comparable to Kolmogorov length scale η , where viscosity is effective in transferring their kinetic energy into heat. This was formalised using the velocity fluctuations by Kolmogorov using the below-mentioned equation ([Kolmogorov, 1941b](#)):

$$\Delta V_l = C\epsilon^{1/3}l^{1/3} \quad (6.1)$$

where V is the velocity, ΔV_l is the velocity difference between position, l is the scale and ϵ the dissipation. This relationship is valid for homogeneous and isotropic turbulence and for the scales belonging to the inertial regime $\eta \leq l \leq L$. It is the smaller scale of the inertial regime, written as:

$$\eta = \left(\nu^3/\epsilon\right)^{1/4} \quad (6.2)$$

In the ocean η is often of the order of 0.5 mm to a few cm. Below this η scale, viscosity dominates. [Obukhov \(1941b\)](#) has written the K41 theory in spectral space as:

$$E_v(k) = C_1\epsilon^{2/3}k^{-5/3} \quad (6.3)$$

where $E(k)$ is the power spectrum, k is the wave number and C_1 is a constant. A similar scale dependence can be obtained for a passive scalar θ , with a power-law of the form (Obukhov, 1949; Corrsin, 1951):

$$E_\theta(k) = C_2 \epsilon^{-1/3} \chi k^{-5/3} \quad (6.4)$$

where $E_\theta(k)$ is the Fourier spectral energy of passive scalar, C_2 is another constant, and χ is the dissipation of scalar variance (analogous to ϵ as dissipation of kinetic energy). This energy spectrum is calculated using the fast Fourier transform of the data with a regular sampling. The resulting energy spectra are represented in log-log plot which allows good visualisation of the scale dependence.

6.2.7 1D Power spectra

A major difficulty in the analysis of ocean colour images is the missing values due to cloud cover. In the present study, we extracted 512×512 pixels of cloud free Chl-a and SST of different regions of the coastal oceans. One-dimensional power spectra are performed from the pixel values taken from zonal (rows) and meridional (columns) of the MODIS image. For such analysis, 512 realizations of 1D power spectra are averaged, providing an ensemble average power spectra.

6.2.8 2D Power spectra

The 2D spatial scaling of the image has been analysed using the radially averaged 2D power spectra. The 2D Fourier transform of the image $F(u, v)$ becomes,

$$F(u, v) = \int_{-\infty}^{+\infty} \int_{-\infty}^{+\infty} IMG(x, y) e^{-2\pi i(xu+yv)} dx dy \quad (6.5)$$

Here u, v are the spatial frequencies. The function $F(u, v)$ is a complex spectrum which gives the weight of harmonics components in the linear combination. The

discrete version of this is:

$$F(u, v) = \frac{1}{MN} \sum_{m=0}^{M-1} \sum_{n=0}^{N-1} IMG(m, n) \exp \left[-2\pi i \left(\frac{mu}{M} + \frac{nv}{N} \right) \right] \quad (6.6)$$

Here $u=0,1,\dots,M-1$; $v=0,1,\dots,N-1$; M = number of rows of the image and N =number of columns of the image. The power spectrum of the image is computed using:

$$P(u, v) = |F(u, v)|^2 = R^2(u, v) + I^2(u, v) \quad (6.7)$$

Due to the symmetries of the spectrum the quadrant positions can be swapped diagonally and the low frequencies fall in the middle of the image. The radially averaged power spectrum $E(k)$ is derived using the centered power spectrum with the origin of the coordinate system. To obtain this we first convert the Cartesian co-ordinate system into polar coordinate axis and the low-frequency spectrum falls close to the origin. The radial power spectrum can be derived from summing or averaging of the concentric circles with unit frequency increment. For a scaling process, the radially summed power spectrum of the 2D image has the same slope β as the 1D sections of the image.

6.2.9 Structure Function (SF) method

In the following we analyse image fluctuations in the framework of passive scalar turbulence ([Frisch, 1995](#)):

$$\langle \Delta \theta_l^q \rangle \approx l^{\zeta_\theta(q)} \quad (6.8)$$

where $\zeta_\theta(q)$ is the scaling moment functions that characterize the fluctuations of passive scalar ([Schmitt et al., 1996](#)). We focus on the passive scalar case, since we will consider Chlorophyll-a and Sea Surface Temperature, which are transported scalars and may be compared to passive scalars. The scaling moment functions are derived using remotely sensed 2D Chl-a, SST, R_{rs-443} and R_{rs-555} images from MODIS Aqua.

Let us consider two points M and N belonging to the field, and their distance $d(M, N)$. The moments $\langle |\theta(M) - \theta(N)|^q \rangle$ versus $d(M, N)$ are considered. This can be estimated directly by taking all couple of points (M, N) in the 2D domain and discretizing the distance $d(M, N)$ in small intervals. A log-log regression of $\langle |\theta(M) - \theta(N)|^q \rangle$ versus $d(M, N)$ gives the exponent ζ_θ , following the law

$$\langle |\theta(M) - \theta(N)|^q \rangle \approx d(M, N)^{\zeta_\theta(q)} \quad (6.9)$$

where “ \approx ” means scaling relation.

The exponent function $\zeta_\theta(q)$ is directly estimated from such images using randomly selected couple of points. In [Renosh et al. \(2015\)](#), we have presented and tested this methodology and showed that 10^6 couple of points is convenient for statistical convergence and computing time. The present work is hence a continuation of this methodological work.

For scaling ranges this approach was used to extract $\zeta(q)$ as a log-log fit of the moments. Then, in the framework of a lognormal scaling model, we have proposed a fit of $\zeta(q)$ of the following form:

$$\zeta_{LN}(q) = qH - \frac{\mu}{2}(q^2 - q) \quad (6.10)$$

where $H = \zeta_{LN}(1)$ is the Hurst parameter, and characterizes the mean scaling invariance of the field, and $\mu = 2H - \zeta_{LN}(2)$ is the intermittency parameter: the larger this parameter, the more the field is intermittent. The values (H, μ) are used here to characterize the scaling and intermittency of satellite images, for the scales where Eq.6.9 is valid, i.e. the scales for which there is scale invariance.

6.2.10 Cumulants and cumulant scaling analysis

The cumulant analysis corresponds to characterize the fluctuations at a single scale, and fit the moment function using 2 parameters. We then consider the scale dependence of these 2 parameters. For a fixed scale l , the cumulant generating function of

the generator $g_l = \log|\Delta V_l|$ is defined as $\Phi_l(q) = \log\langle|\Delta V_l|^q\rangle$ (Gardiner, 2004; Schmitt et al., 2007). Here we apply the difference of passive field separated between two points M and N as $\theta(M) - \theta(N)$ instead of ΔV_l . The distance $d(M, N)$ between these two points M and N is noted as l for the cumulant scaling:

$$\Phi_l(q) = \log\langle|\theta(M) - \theta(N)|^q\rangle \quad (6.11)$$

The function $\Phi_l(q)$ is also the second Laplace characteristic function of the generator: $\Phi_l(q) = \log\langle e^{qg_l}\rangle$. As second characteristic function, it is convex (Feller, 2008) and can be developed using the cumulants:

$$\Phi_l(q) = \sum_{p=1}^{\infty} C_p(l) \frac{q^p}{p!} \quad (6.12)$$

where $C_p(l)$ is the n^{th} cumulant. Let us recall that $C_1(l) = \langle g_l \rangle$, $C_2(l) = \langle g_l^2 \rangle - C_1(l)^2$, and C_n depends on all moments $\langle g_l^p \rangle$ ($1 \leq p \leq n$). The other way to derive $C_2(l)$ is from the the intercept of the linear fit between $\log(\Phi(q) - C_1(l)q)$ versus $\log q$; the exponential of the intercept gives $C_2(l)$. On the other hand, since we have $\langle|\theta(M) - \theta(N)|^q\rangle = B_q l^{\zeta(q)}$, its logarithm writes:

$$\Phi_l(q) = \log\langle|\theta(M) - \theta(N)|^q\rangle = \zeta(q) \log(l) + \log B_q \quad (6.13)$$

let us write $\zeta(q)$ for the lognormal model:

$$\zeta_{LN}(q) = qH - \frac{\mu}{2}(q^2 - q) \quad (6.14)$$

where $H = \zeta_{LN}(1)$ and μ is the intermittency parameter. Then:

$$\Phi_l(q) = [q(H + \frac{\mu}{2}) - \frac{\mu}{2}q^2] \log(l) + \log B_q \quad (6.15)$$

$$= C_1(l)q + \frac{C_2(l)}{2}q^2 + \log B_q \quad (6.16)$$

From the above two equations, the 2 cumulants for the scaling lognormal model are:

$$\begin{cases} C_1(l) = \left(H + \frac{\mu}{2}\right)\log(l) + A \\ C_2(l) = -\mu\log(l) + B \end{cases} \quad (6.17)$$

where H and μ are the multifractal parameters and A and B constants that may come out from the B_q parameter. For pure scaling processes, the structure function and cumulant give the same results. However for cases where the scaling is not perfect the cumulant approach may be a good alternative to the SF approach, since $\Phi_l(q)$ can be estimated perfectly at any scale l and the first two cumulants estimated. In the following for 2D images, the cumulant scaling analysis has been performed and the first two cumulants expressions have been used to extract the H and μ values.

6.3 Results and discussions

6.3.1 1D and 2D scaling

First we have selected the regions having no missing data in 512×512 pixels. We have identified 7 regions for the present study. The scaling behaviour of the Chl-a, SST, R_{rs-443} , R_{rs-555} and R_{rs-443}/R_{rs-555} images have been analysed using the power spectrum. For this, we have considered two types of power spectra: one dimensional (1D) and two dimensional (2D) power spectra using fast Fourier transform. Cloud free image of 512×512 pixels of each parameter were selected for the power spectral scaling for all regions.

We show first the resulting images for a typical case, in order to illustrate the scaling behaviour which was found for almost all images considered. The case chosen here concern the ANC region sampled on 30/4/2013. The 2D power spectrum of Chl-a sampled from ANC on 30/4/2013 is shown in Fig. 6.9A. The 1D power spectral energy is derived by slicing the image zonally and meridionally and deriving power spectral energy for each slice and averaging it. From this average, the power spectrum is derived from power spectral energy versus wavenumber in log-

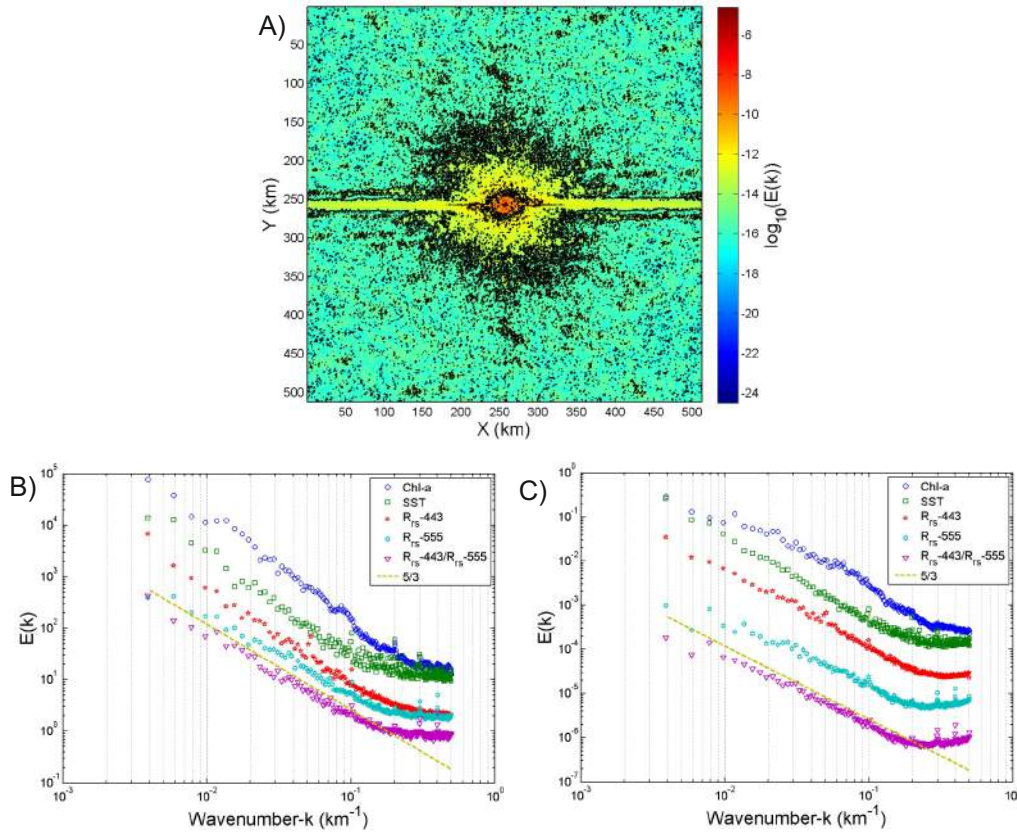


Figure 6.9: Various power spectra, log centered 2D power spectrum of Chl-a sampled from ANC on 30-April-2013 in A), averaged zonal and meridional power spectra (1D) of various parameters in B), radially summed power spectra of Chl-a, SST, R_{rs} -443 and R_{rs} -555 in C). These 2 types of spectra show good scaling for Chl-a, SST, R_{rs} -443 and R_{rs} -555.

log scale and the exponent β is also derived. Here we found that the 1D power spectra of these parameters follow a clear power law behaviour with some disturbance in the high wavenumbers ($0.1 - 1 \text{ km}^{-1}$) (Fig. 6.9B). The β derived values for 1D approach for various parameters show large variability (Table 6.2), as well as for the 2D case (Table 6.3).

β -1D	AC	MC	NEAS	ANC	PCC	CS	EM	Global
Chl-a	1.66 ± 0.21	1.12 ± 0.39	1.41 ± 0.12	1.13 ± 0.33	1.64	1.53	1.50	1.34 ± 0.32
SST	1.54 ± 0.06	1.52 ± 0.13	1.42 ± 0.22	1.60 ± 0.14	1.45	1.43	1.67	1.52 ± 0.16
R_{rs} -443	1.50 ± 0.15	1.40 ± 0.11	1.12 ± 0.23	1.46 ± 0.24	1.38	1.10	1.23	1.33 ± 0.24
R_{rs} -555	1.35 ± 0.34	1.33 ± 0.09	1.02 ± 0.31	1.26 ± 0.28	1.42	1.16	0.96	1.20 ± 0.29
R_{rs} -443/ R_{rs} -555	1.18 ± 0.16	1.36 ± 0.10	1.14 ± 0.12	1.41 ± 0.13	1.39	1.04	0.99	1.26 ± 0.18

Table 6.2: The spectral slope β derived in 1D, for various parameters sampled from different regions.

The 1D β derived for the Chl-a image ranges from 0.65-1.87 with a mean value

β -2D	AC	MC	NEAS	ANC	PCC	CS	EM	Global
Chl-a	1.69±0.26	1.27±0.45	1.29±0.18	1.06±0.42	1.74	1.68	1.51	1.31±0.38
SST	1.77±0.04	1.85±0.12	1.79±0.17	1.89±0.11	1.70	1.74	1.84	1.83±0.12
R_{rs} -443	1.72±0.19	1.62±0.18	1.20±0.32	1.62±0.19	1.73	1.07	1.41	1.49±0.31
R_{rs} -555	1.48±0.45	1.45±0.20	1.18±0.46	1.31±0.27	1.69	1.38	0.76	1.30±0.36
R_{rs} -443/ R_{rs} -555	1.45±0.17	1.56±0.19	1.33±0.21	1.61±0.15	1.73	1.25	1.37	1.48±0.21

Table 6.3: The spectral slope β derived in 2D, for various parameters sampled from different regions.

of 1.34 and standard deviation 0.32. Similarly, for SST it varies from 1.06-1.77 with a mean value of 1.52 and standard deviation 0.16. The 1D β derived for the R_{rs} -443 also shows large variability in its value and ranges from 0.86-1.77 with a mean of 1.33 and standard deviation 0.24. Similarly for R_{rs} -555, the β ranges from 0.59-1.76 with a mean of 1.20 and standard deviation 0.29. This is the first report of the scaling exponent computation for the remote sensing reflectance.

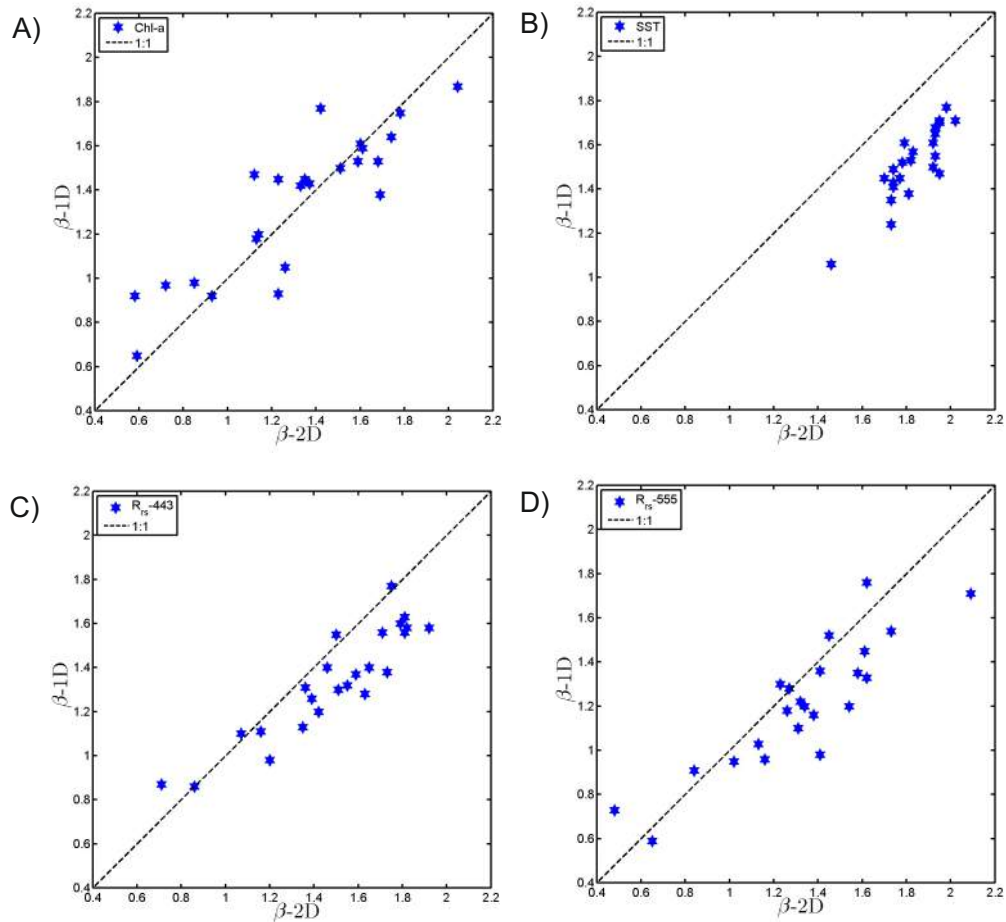


Figure 6.10: Comparison of 1D and 2D spectral slope β derived for Chl-a in A), SST in B), R_{rs} -443 in C) and R_{rs} -555 in D).

2D power spectrum (Fig. 6.9A) is derived for these parameters and β is derived from the slope value obtained from radial sum of the power spectrum versus the wavenumber in log-log scale (Fig. 6.9C). Here also we could find a large variability in the slope values for each parameter. The 2D β for the Chl-a images, ranges from 0.58-2.04 with an average of 1.31 and standard deviation 0.38. Likewise, SST also shows large variability in its β values with a mean value of 1.83 and standard deviation 0.12. The β value derived for the present study falls inside the range of the β values (1.5-2.5) of previous studies (Abraham and Bowen, 2002; Montera et al., 2011; Piontkovski et al., 1997). Similarly for R_{rs} -443, the scaling exponent found a mean 1.49 and standard deviation 0.31 and for R_{rs} -555 a mean of 1.30 and standard deviation 0.36.

The comparison of the β derived through each method is done for each parameter (Fig. 6.10). Here we can see that the β values for Chl-a from different approaches fall near to the 1:1 line (Fig. 6.10A). For the SST image, we found that the points are systematically below the 1:1 line (Fig. 6.10B): the exponents derived from 2D show a higher value than 1D. We can say that scaling pattern of 1D and 2D are different from SST images. This could be explained by a lack of isotropy which could be more important for the SST field. While coming to the R_{rs} -443 the points are near to the 1:1 (Fig. 6.10C) line, and still we observe high values in the 2D exponent compared to 1D. Similar results are also observed in the R_{rs} -555 images (Fig. 6.10D).

6.3.2 Structure function method

The SF method is directly applied to the images. Here we found good scaling for all 4 parameters and the ratio between R_{rs} -443 to R_{rs} -555 (Fig. 6.11). The interesting thing we can see that the R_{rs} -443 and R_{rs} -555 have nice scaling, much better than Chl-a. It means that these fluctuations are artificially introduced by the bio-optical algorithm. The scaling moment function $\zeta(q)$ has been derived from these images. Here we found that all the four images show a non-linear curve (convex/concave)(Fig. 6.12). This is a clear indication of intermittency in the spatial

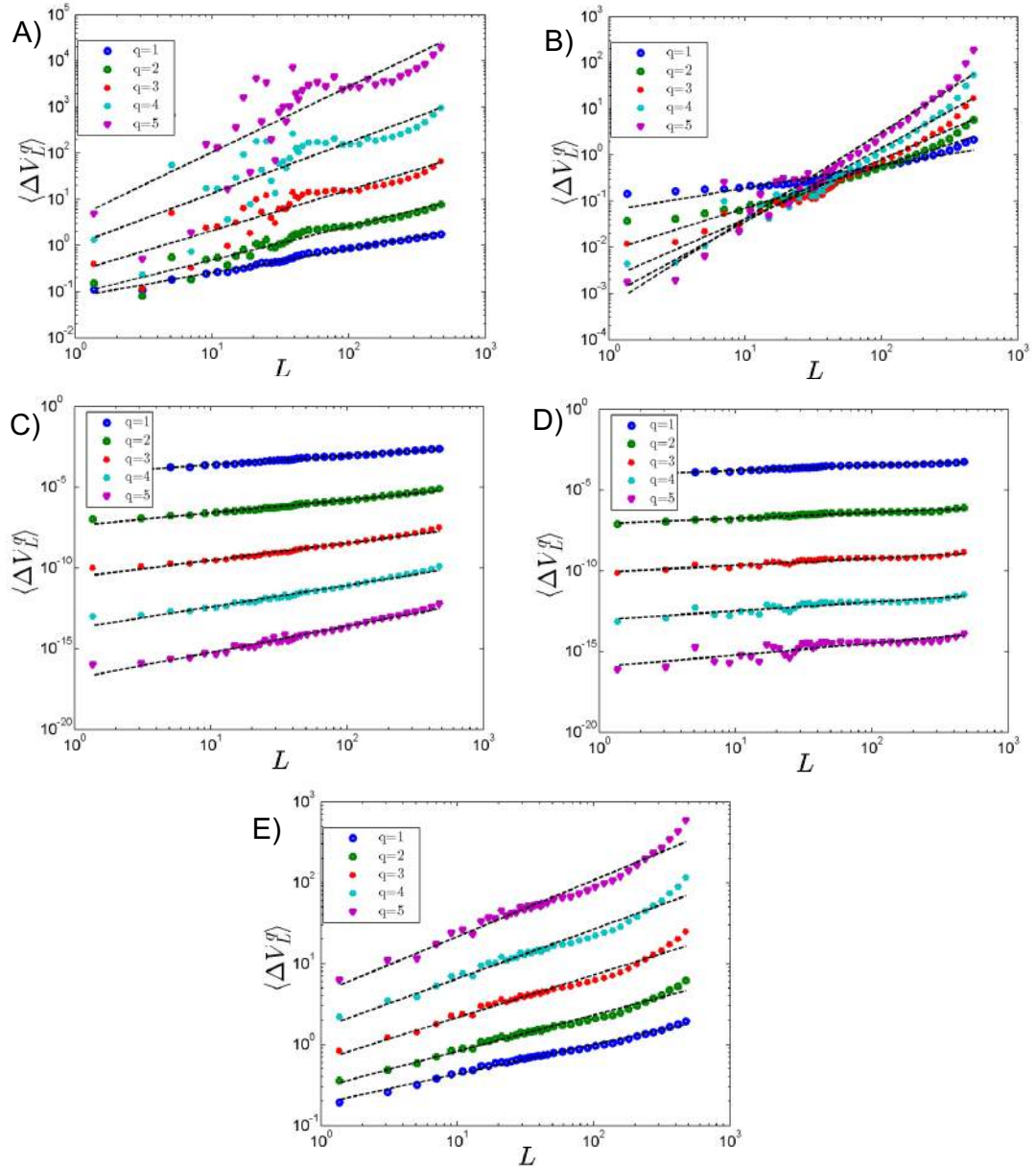


Figure 6.11: The 2D structure function scaling of Chl-a in A), SST in B), R_{rs-443} in C), R_{rs-555} in D) and the ratio between R_{rs-443} to R_{rs-555} in E) showing good scaling, especially for R_{rs-443} .

distribution of these parameters.

To understand the intermittency characteristics we consider the classical lognormal intermittency model $\zeta(q) = qH - \frac{\mu}{2}(q^2 - q)$. The multifractal parameters (H and μ) derived through this method show variability depending on the region and parameter (Table 6.4- 6.5). The spatial pattern of these two variables for the 7 regions is shown in Fig. 6.13 by considering a (H - μ) plot. As we know the H value for typical

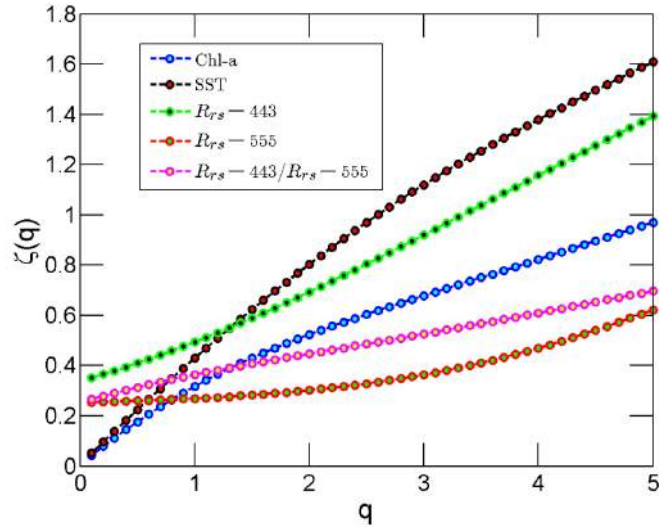


Figure 6.12: The moment scaling function derived by 2D structure function of various parameters from the ANC sampled on 30-April-2013.

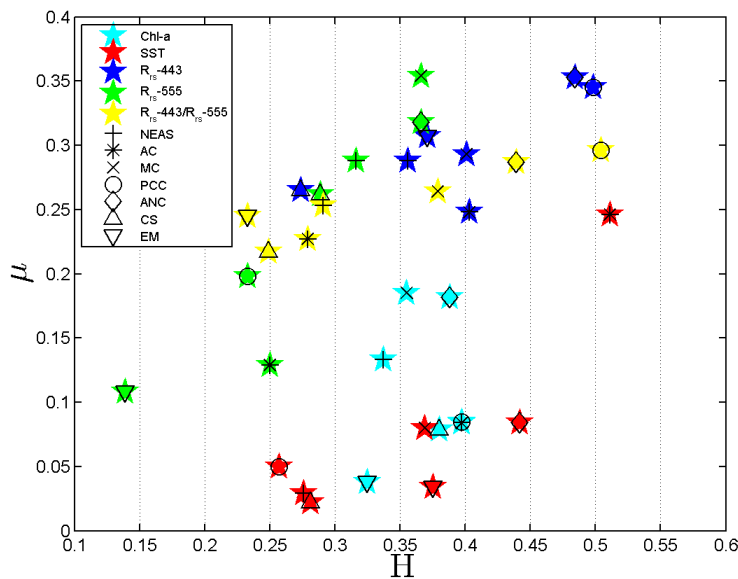


Figure 6.13: H - μ plot clustering of parameters (Chl-a, SST, R_{rs} -443, R_{rs} -555 and the ratio between R_{rs} -443 to R_{rs} -555) for different regions. The colour code corresponds to the parameters, and the shape to the geographical location.

turbulence is close to $1/3$ and for Brownian motion is $1/2$; here we found that the H values for all the parameters fall between 0.25 and 0.45 ($H = 0.35 \pm 0.1$) except 7 cases. We can also see a high level intermittency in R_{rs} values compared to Chl-a and SST. Here we find low level of intermittency in SST for all the regions except the AC region. In the AC region, the SST is showing high value of μ and follows a close

H	AC	MC	NEAS	ANC	PCC	CS	EM	Global
Chl-a	0.40±0.09	0.35±0.06	0.34±0.06	0.39±0.08	0.40	0.38	0.33	0.37±0.07
SST	0.51±0.03	0.37±0.04	0.28±0.11	0.44±0.06	0.26	0.28	0.37	0.38±0.11
R _{rs} -443	0.40±0.08	0.40±0.08	0.36±0.05	0.48±0.04	0.50	0.27	0.37	0.41±0.08
R _{rs} -555	0.25±0.11	0.37±0.06	0.32±0.11	0.37±0.07	0.23	0.29	0.11	0.31±0.1
R _{rs} -443/R _{rs} -555	0.28±0.03	0.38±0.09	0.29±0.06	0.44±0.06	0.50	0.25	0.23	0.35±0.01

Table 6.4: The Hurst parameter H derived through SF method for various parameters sampled from different regions. For each case the mean and standard deviation are estimated by doing statistics over the number of images. For PCC, CS and EM cases there is only 1 image.

μ	AC	MC	NEAS	ANC	PCC	CS	EM	Global
Chl-a	0.08±0.03	0.18±0.10	0.13±0.02	0.18±0.08	0.08	0.08	0.04	0.14±0.07
SST	0.25±0.02	0.08±0.04	0.03±0.02	0.08±0.04	0.05	0.02	0.03	0.09±0.08
R _{rs} -443	0.25±0.03	0.29±0.04	0.29±0.07	0.35±0.10	0.35	0.27	0.31	0.30±0.07
R _{rs} -555	0.13±0.09	0.35±0.07	0.29±0.14	0.32±0.10	0.20	0.26	0.11	0.27±0.12
R _{rs} -443/R _{rs} -555	0.23±0.03	0.26±0.04	0.25±0.03	0.29±0.02	0.30	0.22	0.24	0.26±0.03

Table 6.5: The intermittency parameter μ derived through SF method for various parameters sampled from different regions. For each case the mean and standard deviation are estimated by doing statistics over the number of images. For PCC, CS and EM cases there is only 1 image.

to Brownian scaling exponent ($H \approx 0.5$). The large scale river run-off in the Atlantic continental shelf develops a large diversity of mesoscale fronts (Acha et al., 2004). These fronts cover several scales in space and time. This may be the main reason for showing large intermittency value in SST compared to the other regions. With regards to Chl-a in all the regions, the distributions are very close to 0.35. In contrast, the intermittency patterns are quite variable depending on the regions. Chl-a shows high intermittency in high productive coastal waters of ANC and low intermittency in clear oligotrophic waters of EM. The level of intermittency observed for Chl-a lays between the SST and R_{rs}.

R_{rs} is characterised by a high range of H values compared with that of Chl-a. Compare to R_{rs}-443, R_{rs}-555 show lower H value. The R_{rs}-555 values for clear oligotrophic waters of EM shows low intermittency and maximum intermittency has been observed in the upwelling region of the MC. Due to less productivity, the clear oligotrophic waters reflects more in the blue bands compared with the green bands. This may be the reason for low intermittency of R_{rs}-555 in EM. The ratio of R_{rs}-443 to R_{rs}-555 shows a stable μ values for all the seven regions with a broad range of H

values.

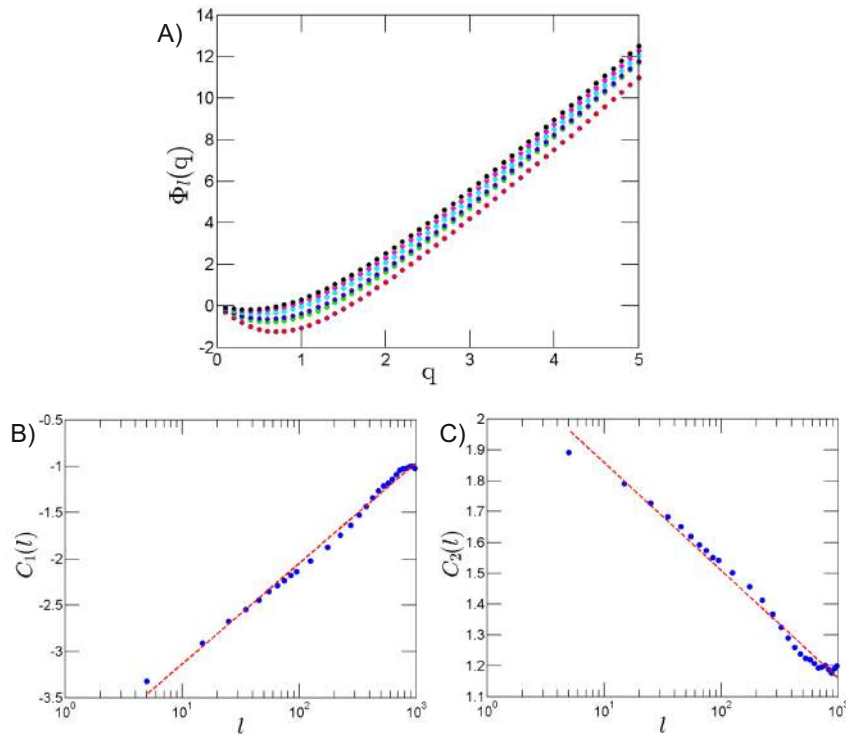


Figure 6.14: The second characteristic function $\Phi_l(q)$ derived for different l values of Chl-a sampled from ANC on 30-April-2013 in A). The first cumulant derived for the same image in B) and the second cumulant in C).

6.3.3 Cumulant scaling

The cumulant scaling has been done for the Chl-a and SST images using structure cumulant scaling method. The second characteristic function is derived for each image (Fig. 6.14A). The second characteristic function shows a non-linear concave curve with different moments. The first and second cumulant have been derived for each image at different scales. These cumulants show good scaling in semi-log scale as expected from Eq.(6.17)(Fig. 6.14B-C). Here also we applied the lognormal intermittency model, the slope of the first cumulant versus l in semi-log scale is related with $H + \frac{\mu}{2}$ and the slope of the second cumulant is related with $-\mu$. This enables another estimation of H and μ .

Using these relations, we derived the H values for each Chl-a and SST images. This cumulant derived H values are compared with SF derived H values for Chl-a

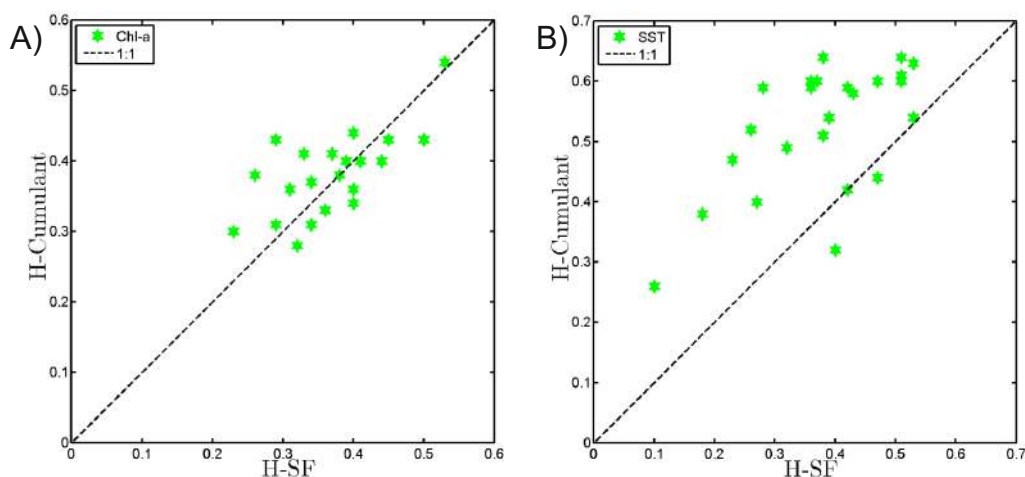


Figure 6.15: H derived through cumulant scaling versus H derived through structure function scaling for Chl-a in A) and SST in B).

and SST (Fig. 6.15). For Chl-a images, these two H values show very good agreement whereas the agreement is not so good for SST. This may come from a lack of very good scaling for SST: when the scaling is not perfect the cumulant approach is more reliable since the scaling fit is done at the end of the process. We may note also from Fig. 6.15 that values of H cluster around 0.3-0.4 for Chl-a, as expected for a passive turbulence situation.

6.4 Conclusions

In the present study, we use ocean colour (R_{rs} and Chl-a) and thermal infra-red SST images to characterise the heterogeneity of turbulence by analysing the biophysical coupling of ocean colour and SST. We use the 2D structure function which was proposed and tested in [Renosh et al. \(2015\)](#), as well as a cumulant method. For that purpose, we have selected 7 different regions of oceanic waters which show large heterogeneity in terms of biomass (Chl-a) as well as differences in the physical forcing environment. All the data used in the present study are from the MODIS-Aqua sensor with a spatial resolution of $1 \times 1 \text{ km}^2$.

We first analyse the spatial scaling of these images using Fourier power spec-

tra. For that, we used the 1D and 2D different approaches. We found that the derived spectral exponent β calculated from these two approaches show relatively good agreement with each other. These derived β values calculated for Chl-a and SST show good agreement with previous studies (Abraham and Bowen, 2002; Montero et al., 2011; Piontkovski et al., 1997). This is the first report which shows the spatial scaling of remote sensing reflectance. Here we have chosen 2 different wavelengths of remote sensing reflectance at 443 nm and 555 nm, their ratio is directly linked with the biomass.

Multi-scale properties of these images have been analysed using two different methods; one is the structure function method and the other one is the cumulant scaling. The multifractal parameters (μ and H) have been derived from these methods using the lognormal intermittency model. Clustering of each parameter can be seen from the scatter plot of μ versus H for all variables from different regions. Here we find that SST has a minimum intermittency and R_{rs} has the maximum value of intermittency, Chl-a showed an intermittency value in between the SST and R_{rs} ones. The Hurst exponent derived for the each parameter cluster near to the typical turbulent H value of 0.35 ± 0.10 except 7 data points.

Argentina Coastal waters are famous for the frontal zones and the high run-off region (Acha et al., 2004), the SST measured from this region shows high value of μ and follows a close to Brownian scaling exponent ($H \approx 0.5$). The large scale river run-off along with the formation of the frontal zones may be the main reason for showing large intermittency value in SST compared to the other regions. We found that the spatial distributions of Chl-a could be driven by turbulence (H value close to 1/3) for all 7 regions (Fig. 6.13). The H values derived for SST maps belongs to the range (0.23-0.76) with the H values of simulated SST from NEMO (Verrier et al., 2014). For Chl-a, the intermittency differs depending upon the region. Chl-a shows high intermittency in high productive coastal waters of ANC and low intermittency in clear oligotrophic waters of EM.

The R_{rs} shows high range of H values compared with the Chl-a. The R_{rs} -555 shows less H compared with R_{rs} -443. The R_{rs} -555 for clear oligotrophic waters

of EM shows minimum intermittency and the maximum intermittency has been observed in the upwelling high productive region of the MC.

The cumulants and cumulant scaling of Chl-a and SST have been derived for all study areas. The derived first cumulant and the second cumulant followed good scaling. Using the lognormal intermittency model fit the Hurst exponent has been derived for Chl-a and SST. The cumulant scaling derived H values of Chl-a and SST shown good agreement with the H value derived from the SF method.

Such approach may be generalised to other satellite products, and to other environmental situations, in order to assess the relationship between environmental situations and lognormal multifractal parameters.

Conclusions. The aim of the present thesis is to better understand the characterisation of coupling between oceanic turbulence and the variability of coastal water optical properties using in situ and satellite data. For that purpose, the thesis was split into two parts devoted to an analysis of in-situ and satellite data.

For the in-situ analysis, we mainly focused on the Particle size distribution and its dependency on turbulence. We have conducted simultaneous measurements of PSD along with the current velocity from the sea bottom from highly dynamic coastal waters of the eastern English Channel. From the analysis of this high frequency sampling, we found that there is a significant influence of tidal currents, waves and turbulence on the particle re-suspension and its dynamics. The power spectral analysis of $c_p(670)$, proxy for SPM concentration along with current data showed similar scaling regimes in lower and higher frequency region. The Stokes number derived from this PSD exhibits very low values ($\ll 1$), showing that the particles in the fluid motion behave like tracers and move along with the fluid. The present study has shown that tidal current and waves have a significant role in the particle re-suspension and further water column turbidity. The study carried out by [Velegrakis et al. \(1999\)](#) observed large-scale particle re-suspension processes generated by the tidal current and coastal waves for the same region. Our present study has shown good agreement with the above study. During the current reversal, when

the vertically averaged current velocity (VACV) is minimum, all the size parameters examined here indicate a modification in the particle size distribution. At the time of current reversal, we found that the proportions of small particles tend to increase compared to bigger ones (Fig. 3.7). This is explained by two processes mainly: First, the hydrodynamic forcing is not enough to re-suspend large particulate assemblages from the bottom. Second, during the period of slack hour, the differential settling of particles takes place inducing a washing of the water column, especially of heavy flocs. These observations from the present study have good agreement with the study carried out by [Van Leussen \(1988\)](#). We also found that turbulence has a major role in the dynamics of the particles in the present region. Low-frequency variability of the particles is controlled by the turbulence ($\beta \approx 5/3$) and high frequency variability is controlled by the physical processes that are get along with the sea bottom interactions especially wall turbulence, tidal currents and waves.

The intermittent characteristics of the PSD have been analysed using EMD, HSA and AHSA methods. For that purpose, we have selected the total volume concentration and $c_p(670)$, which is the proxy for total SPM concentration ([Neukermans et al., 2012b](#)). We have also analysed the intermittent characteristics of different size classes of PSD in relation to particle sizes ([Lefebvre et al., 2012](#); [Renosh et al., 2014](#)). Here we considered 4 different size classes mainly Silt/Clay, Fine particles, Coarse/Micro particles and Macro particles/flocs. Turbulent scaling of these parameters has been derived through both Fourier power spectra and spectra derived through HSA. Here we find similar turbulent scaling of these parameters (different size classes of PSD, $C_{vol-total}$ and $c_p(670)$). The scaling moment function derived for $C_{vol-total}$ and $c_p(670)$ showed similar non-linear curve, indicating that their dynamics is intermittent. The scaling moment function derived for each size class of the particles are also showing non-linear curves. The curvature of the spectrum for various size class showed the intermittency characteristics of the particles in different sizes. The curvature of the silt and macro was large compared with fine and coarse particles. Here we observed different levels of intermittency in their dynamics. We also derived the Shannon entropy from the number density of PSD. It was estimated

at each time step of one second and has shown some variability with values centered at a mean of 1.59 ± 0.03 .

For the satellite aspects, we have developed a new methodology for multi-scale analysis of remote sensing data. Here we found that the way of extracting scaling exponent through a passive scalar gradient modulus fail to give the exact scaling exponent. So we derived a new methodology for computing the 2D structure function scaling exponent. We showed that this method works for images with missing data, an important aspect since many real images have missing pixels because of cloud coverage. We considered two images from MODIS Aqua (Chl-a and SST) and showed in these examples that scaling approach using SF and $N_p = 10^6$ couple of points are adequate. We also showed that the spectral exponent for these examples is close to $5/3$, characteristic of passive scalar fully developed turbulence. Such 2D multifractal property of Chl-a and SST is a 2D generalisation of previous results obtained for time series ([Seuront et al., 1996b,a, 1999](#)).

This methodology has been applied to various oceanic regions showing high spatial heterogeneity in their biomass. We mainly used Chl-a, SST, R_{rs-443} and R_{rs-555} images derived from MODIS Aqua with a spatial resolution 1×1 km. First we analysed the spatial scaling of these images using Fourier power spectra. For that, we used 2 different approaches, 1D and 2D. We found that the derived spectral exponent β for these two approaches were in relatively good agreement with each other. These derived β for Chl-a and SST showed good agreement with the old studies 1.5-2.5 ([Abraham and Bowen, 2002](#); [Montera et al., 2011](#); [Piontkovski et al., 1997](#)).

To have a complementary approach to characterise variability without relying on pure scaling, we have analysed multi-scale properties of these images using two different methods; one was the structure function method and the other one was the cumulant scaling. The multifractal parameters were derived using the lognormal intermittency model. We derived μ and H using the SF method. The scatter plot of μ versus H for all variables showed a sort of clustering for each parameter. Here we found that the multifractal parameter μ for various parameters for various region clusters together. We also found that SST has minimum intermittency and

R_{rs} has the maximum value of intermittency, and Chl-a showed an intermittency value in between the SST and R_{rs} . The Hurst exponent derived for the each area fell near to the typical turbulent H value of 0.35 ± 0.10 except for 5 cases. The Argentina coastal waters are famous for the frontal zones and the high run-off region (Acha et al., 2004): the SST measured from this region showed a high value of μ and follow a Brownian scaling exponent ($H \approx 0.5$) compared with other regions. We also observed that the spatial distributions of Chl-a are driven by turbulence (very close to 0.35) for all 7 regions. For the R_{rs} s, a broad range of H values have been observed compared with the Chl-a, and for the R_{rs} -555 less values of H have been observed compared with R_{rs} -443. The R_{rs} -555 for clear oligotrophic waters of EM shows least intermittency, and maximum intermittency has been observed in the upwelling high productive region of the MC.

The cumulants and cumulant scaling of Chl-a and SST have been derived for all study areas. The derived first cumulant and the second cumulant followed good scaling. A lognormal intermittency model fit was also performed to extract the Hurst exponents for Chl-a and SST. The cumulant scaling derived H values of Chl-a and SST showed good agreement with the H value derived from the SF method.

Globally these results showed that:

- Turbulence, tidal currents and waves play a major role in the dynamics and the re-suspension processes of the particles in highly dynamic coastal waters.
- The Stokes number derived for the particles exhibits very low values ($\ll 1$), showing that the particles in the fluid motion behave as tracers and move along with the fluid.
- Particles in different size classes of PSD showed intermittency characteristics in their dynamics.
- Heterogeneity in remote sensing images has scaling properties and can be related to turbulence.

- Such heterogeneity can be characterized using a few parameters in the lognormal model.
- The parameters can be, in some respect, related to local physical and environmental conditions.

Limitations. The present study is limited to PSD and its dependency on the hydrodynamic conditions such as tidal currents, waves and turbulence. We could not extend this work with some bio-optical properties (IOPs) such as absorption and scattering at different wavelengths along with different hydrodynamic conditions. We also failed to study the Chl-a fluorescence (a proxy for Chl-a concentration) and CDOM fluorescence (a proxy for coloured dissolved organic matter concentration) dynamics and its dependency with turbulence.

The present study focused only on MODIS Aqua products of ocean colour (Chl-a and R_{rs}) and infra-red SST with a spatial resolution $1000 \times 1000 m^2$. We could not broaden this work with high resolution data ($300 \times 300 m^2$) of ocean colour from MERIS for various coastal sites. This study was limited with only one satellite sensor. This is the main drawback of the present study.

Perspectives. Concerning in-situ sampling, we mainly analysed PSD and its dependency with turbulence. The dependency of IOPs such as $a(\lambda)$, $b(\lambda)$ and $c(\lambda)$ with turbulence is still to be analysed. This could be an interesting topic for the ocean colour community. Here we found some good scaling regime with a slope 0.6. More investigations and explanations need to be done on this β value in highly dynamic coastal environments. For that, we have to do more field campaigns in the present area as well as other oceanic regions for understand the universality in its distributions. This is the first perspective of the present work.

Concerning satellite aspects, the present study has been tested only with MODIS aqua. There are other sensors that measure these parameters(SeaWiFS, MERIS and GOCI): these should also be analysed using our methodology. GOCI has eight spectral bands from 412 to 865 nm with spatial resolution 500 m and an hourly mea-

surement during daytime from 9:00 to 16:00 local time, i.e., eight images per day. Analysis of these high resolution data shall provide more information on the daily dynamics of intermittency parameters in a specified region. These images give the daily temporal heterogeneity in the reflectance and Chl-a dynamics. The spatial scaling and multi-scale properties of Sea Surface Salinity (SSS), another passive scalar from the Aquarius need to be analysed using our methods.

Furthermore, as recalled above, our results have provided first links between intermittency parameters and local environmental conditions. This needs to be confirmed, perhaps with more precision, and also theoretically explained.

BIBLIOGRAPHY

- Abraham, E. R. and Bowen, M. M.: Chaotic stirring by a mesoscale surface-ocean flow, *Chaos: An Interdisciplinary Journal of Nonlinear Science*, 12, 373–381, 2002.
- Abraham, E. R., Law, C. S., Boyd, P. W., Lavender, S. J., Maldonado, M. T., and Bowie, A. R.: Importance of stirring in the development of an iron-fertilized phytoplankton bloom, *Nature*, 407, 727–730, 2000.
- Acha, E. M., Mianzan, H. W., Guerrero, R. A., Favero, M., and Bava, J.: Marine fronts at the continental shelves of austral South America: physical and ecological processes, *Journal of Marine systems*, 44, 83–105, 2004.
- Agrawal, Y. and Pottsmith, H.: Instruments for particle size and settling velocity observations in sediment transport, *Marine Geology*, 168, 89–114, 2000.
- Amal, R., Raper, J. A., and Waite, T. D.: Fractal structure of hematite aggregates, *Journal of Colloid and interface Science*, 140, 158–168, 1990.
- Azov, Y.: Eastern Mediterranean: a marine desert?, *Marine Pollution Bulletin*, 23, 225–232, 1991.
- Balch, W. M., Plueddeman, A., Bowler, B., and Drapeau, D.: Chalk-Ex-Fate of CaCO₃ particles in the mixed layer: Evolution of patch optical properties, *Journal of Geophysical Research: Oceans*, 114, 2009.

- Banse, K.: Seasonality of phytoplankton chlorophyll in the central and northern Arabian Sea, *Deep Sea Research Part A. Oceanographic Research Papers*, 34, 713–723, 1987.
- Barrière, O.: Synthèse et estimation de mouvements browniens multifractionnaires et autres processus à régularité prescrite: définition du processus auto-régulé multifractionnaire et applications, Ph.D. thesis, Nantes, 2007.
- Batchelor, G. and Townsend, A.: The nature of turbulent motion at large wavenumbers, *Proceedings of the Royal Society of London. Series A. Mathematical and Physical Sciences*, 199, 238–255, 1949.
- Bec, J.: Multifractal concentrations of inertial particles in smooth random flows, *Journal of Fluid Mechanics*, 528, 255–277, 2005.
- Behrenfeld, M. J., Boss, E., Siegel, D. A., and Shea, D. M.: Carbon-based ocean productivity and phytoplankton physiology from space, *Global biogeochemical cycles*, 19, 2005.
- Berhane, I., Sternberg, R. W., Kineke, G. C., Milligan, T., and Kranck, K.: The variability of suspended aggregates on the Amazon Continental Shelf, *Continental Shelf Research*, 17, 267–285, 1997.
- Boss, E., Pegau, W. S., Gardner, W. D., Zaneveld, J. R. V., Barnard, A. H., Twardowski, M. S., Chang, G., and Dickey, T.: Spectral particulate attenuation and particle size distribution in the bottom boundary layer of a continental shelf, *Journal of Geophysical Research: Oceans*, 106, 9509–9516, 2001a.
- Boss, E., Twardowski, M. S., and Herring, S.: Shape of the particulate beam attenuation spectrum and its inversion to obtain the shape of the particulate size distribution, *Applied Optics*, 40, 4885–4893, 2001b.
- Boss, E., Slade, W., and Hill, P.: Effect of particulate aggregation in aquatic environments on the beam attenuation and its utility as a proxy for particulate mass, *Optics Express*, 17, 9408–9420, 2009.

- Brander, K.: Impacts of climate change on fisheries, *Journal of Marine Systems*, 79, 389–402, 2010.
- Brentnall, S. J., Richards, K. J., Brindley, J., and Murphy, E.: Plankton patchiness and its effect on larger-scale productivity, *Journal of Plankton Research*, 25, 121–140, 2003.
- Bricaud, A., Morel, A., and Andre, J.: Spatial/temporal variability of algal biomass and potential productivity in the Mauritanian upwelling zone, as estimated from CZCS data, *Advances in Space Research*, 7, 53–62, 1987.
- Brown, O. B., Minnett, P. J., Evans, R., Kearns, E., Kilpatrick, K., Kumar, A., Sikorski, R., and Závody, A.: MODIS Infrared Sea Surface Temperature Algorithm Algorithm Theoretical Basis Document Version 2.0, University of Miami, 1999.
- Bukata, R. P., Jerome, J. H., Kondratyev, A. S., and Pozdnyakov, D. V.: *Optical properties and remote sensing of inland and coastal waters*, CRC press, 1995.
- Buonassissi, C. and Dierssen, H.: A regional comparison of particle size distributions and the power law approximation in oceanic and estuarine surface waters, *Journal of Geophysical Research: Oceans*, 115, 2010.
- Burchard, H., Craig, P. D., Gemrich, J. R., van Haren, H., Mathieu, P.-P., Meier, H. M., Smith, W. A. M. N., Prandke, H., Rippeth, T. P., Skillingstad, E. D., et al.: Observational and numerical modeling methods for quantifying coastal ocean turbulence and mixing, *Progress in oceanography*, 76, 399–442, 2008.
- Burton, G. and Moorhead, I. R.: Color and spatial structure in natural scenes, *Applied Optics*, 26, 157–170, 1987.
- Carder, K. L., Steward, R. G., Harvey, G. R., and Ortner, P. B.: Marine humic and fulvic acids: Their effects on remote sensing of ocean chlorophyll, *Limnology and oceanography*, 34, 68–81, 1989.

- Champagne, F.: The fine-scale structure of the turbulent velocity field, *Journal of Fluid Mechanics*, 86, 67–108, 1978.
- Chavez, F. P. and Messié, M.: A comparison of eastern boundary upwelling ecosystems, *Progress in Oceanography*, 83, 80–96, 2009.
- Chiappa-Carrar, X., Rioja-Nieto, R., and Mascaro, M.: Mass density assessment: Comparison of three methods using *Oikopleura dioica* (Appendicularia) as a model system, *Caribbean Journal of Science*, 42, 231, 2006.
- Coble, P. G.: Marine optical biogeochemistry: the chemistry of ocean color, *Chemical reviews*, 107, 402–418, 2007.
- Cooper, L.: The Oceanography of the Celtic Sea I. Wind Drift, *Journal of the Marine Biological Association of the United Kingdom*, 41, 223–233, 1961.
- Correa-Ramirez, M. A., Hormazabal, S. E., and Morales, C. E.: Spatial patterns of annual and interannual surface chlorophyll-a variability in the Peru–Chile Current System, *Progress in Oceanography*, 92, 8–17, 2012.
- Corrsin, S.: On the spectrum of isotropic temperature fluctuations in an isotropic turbulence, *Journal of Applied Physics*, 22, 469–473, 1951.
- Denman, K., Okubo, A., and Platt, T.: The chlorophyll fluctuation spectrum in the sea¹, 2, *Limnology and Oceanography*, 22, 1033–1038, 1977.
- Desprez, M.: Physical and biological impact of marine aggregate extraction along the French coast of the Eastern English Channel: short-and long-term post-dredging restoration, *ICES Journal of Marine Science: Journal du Conseil*, 57, 1428–1438, 2000.
- Doney, S. C.: The growing human footprint on coastal and open-ocean biogeochemistry, *Science*, 328, 1512–1516, 2010.
- Doney, S. C., Ruckelshaus, M., Emmett Duffy, J., Barry, J. P., Chan, F., English, C. A., Galindo, H. M., Grebmeier, J. M., Hollowed, A. B., Knowlton, N., et al.: Climate

- change impacts on marine ecosystems, *Annual review of marine science*, 4, 11–37, 2012.
- Donlon, C., Rayner, N., Robinson, I., Poulter, D., Casey, K., Vazquez-Cuervo, J., Armstrong, E., Bingham, A., Arino, O., Gentemann, C., et al.: The global ocean data assimilation experiment high-resolution sea surface temperature pilot project, *Bulletin of the American Meteorological Society*, 88, 1197–1213, 2007.
- Dubrulle, B.: Intermittency in fully developed turbulence: Log-Poisson statistics and generalized scale covariance, *Physical review letters*, 73, 959, 1994.
- Eaton, J. K. and Fessler, J.: Preferential concentration of particles by turbulence, *International Journal of Multiphase Flow*, 20, 169–209, 1994.
- Eisma, D.: Flocculation and de-flocculation of suspended matter in estuaries, *Netherlands Journal of Sea Research*, 20, 183–199, 1986.
- Ellis, K., Bowers, D., and Jones, S.: A study of the temporal variability in particle size in a high-energy regime, *Estuarine, Coastal and Shelf Science*, 61, 311–315, 2004.
- Falkowski, P. G., Barber, R. T., and Smetacek, V.: Biogeochemical controls and feedbacks on ocean primary production, *Science*, 281, 200–206, 1998.
- Feller, W.: *An introduction to probability theory and its applications*, vol. 2, John Wiley & Sons, 2008.
- Fennessy, M., Dyer, K., and Huntley, D.: INSSEV: an instrument to measure the size and settling velocity of flocs in situ, *Marine geology*, 117, 107–117, 1994.
- Fettweis, M., Francken, F., Pison, V., and Van den Eynde, D.: Suspended particulate matter dynamics and aggregate sizes in a high turbidity area, *Marine Geology*, 235, 63–74, 2006.

- Field, D. J.: Relations between the statistics of natural images and the response properties of cortical cells, *Journal of Optical Society of America*, 4, 2379–2394, 1987.
- Filippa, L., Trento, A., and Álvarez, A. M.: Sauter mean diameter determination for the fine fraction of suspended sediments using a LISST-25X diffractometer, *Measurement*, 45, 364–368, 2012.
- Flandrin, P. and Goncalves, P.: Empirical Mode Decompositions as Data Driven Wavelet-Like Expansions, *JWMIP*, 2(4), 477–496, 2004.
- Fowler, S. W. and Knauer, G. A.: Role of large particles in the transport of elements and organic compounds through the oceanic water column, *Progress in Oceanography*, 16, 147–194, 1986.
- Frisch, U.: *Turbulence: the legacy of AN Kolmogorov*, Cambridge University Press, 1995.
- Frisch, U., Sulem, P.-L., and Nelkin, M.: A simple dynamical model of intermittent fully developed turbulence, *Journal of Fluid Mechanics*, 87, 719–736, 1978.
- Gardiner, C. W.: *Handbook of stochastic methods for physics, chemistry and the natural sciences*, vol. 13, Springer-Verlag, 2004.
- Gerbi, G. P., Trowbridge, J. H., Terray, E. A., Plueddemann, A. J., and Kukulka, T.: Observations of turbulence in the ocean surface boundary layer: Energetics and transport, *Journal of Physical Oceanography*, 39, 1077–1096, 2009.
- Gordon, H. R., Brown, O. B., Evans, R. H., Brown, J. W., Smith, R. C., Baker, K. S., and Clark, D. K.: A semianalytic radiance model of ocean color, *Journal of Geophysical Research: Atmospheres*, 93, 10 909–10 924, 1988.
- Grant, H., Stewart, R., and Moilliet, A.: Turbulence spectra from a tidal channel, *Journal of Fluid Mechanics*, 12, 241–268, 1962.

- Gruber, N.: Warming up, turning sour, losing breath: ocean biogeochemistry under global change, *Philosophical Transactions of the Royal Society A: Mathematical, Physical and Engineering Sciences*, 369, 1980–1996, 2011.
- Gurvich, A.: Frequency spectra and distribution functions of vertical wind components, *Izvestia ANSSSR Geophys Ser*, 7, 1042, 1960.
- Hales, B., Strutton, P. G., Saraceno, M., Letelier, R., Takahashi, T., Feely, R., Sabine, C., and Chavez, F.: Satellite-based prediction of pCO₂ in coastal waters of the eastern North Pacific, *Progress in Oceanography*, 103, 1–15, 2012.
- Hill, P. S.: Controls on floc size in the sea, *Oceanography*, 11, 13–18, 1998.
- Hsieh, C.-h., Glaser, S. M., Lucas, A. J., and Sugihara, G.: Distinguishing random environmental fluctuations from ecological catastrophes for the North Pacific Ocean, *Nature*, 435, 336–340, 2005.
- Huang, N. E. and Wu, Z.: A review on Hilbert-Huang transform: Method and its applications to geophysical studies, *Reviews of Geophysics*, 46, 2008.
- Huang, N. E., Shen, Z., Long, S. R., Wu, M. C., Shih, H. H., Zheng, Q., Yen, N.-C., Tung, C. C., and Liu, H. H.: The empirical mode decomposition and the Hilbert spectrum for nonlinear and non-stationary time series analysis, in: *Proceedings of the Royal Society of London A: Mathematical, Physical and Engineering Sciences*, vol. 454, pp. 903–995, The Royal Society, 1998.
- Huang, N. E., Shen, Z., and Long, S. R.: A new view of nonlinear water waves: The Hilbert Spectrum 1, *Annual review of fluid mechanics*, 31, 417–457, 1999.
- Huang, Y., Schmitt, F. G., Lu, Z., and Liu, Y.: An amplitude-frequency study of turbulent scaling intermittency using Empirical Mode Decomposition and Hilbert Spectral Analysis, *EPL*, 84, 40 010, 2008.
- Huang, Y., Schmitt, F. G., Hermand, J.-P., Gagne, Y., Lu, Z., and Liu, Y.: Arbitrary-order Hilbert spectral analysis for time series possessing scaling statistics: Com-

- parison study with detrended fluctuation analysis and wavelet leaders, *Physical Review E*, 84, 016 208, 2011.
- Huang, Z.-C., Lenain, L., Melville, W. K., Middleton, J. H., Reineman, B., Statom, N., and McCabe, R. M.: Dissipation of wave energy and turbulence in a shallow coral reef lagoon, *Journal of Geophysical Research: Oceans*, 117, 2012.
- Jackson, G. A., Maffione, R., Costello, D. K., Alldredge, A. L., Logan, B. E., and Dam, H. G.: Particle size spectra between 1 μm and 1 cm at Monterey Bay determined using multiple instruments, *Deep Sea Research Part I: Oceanographic Research Papers*, 44, 1739–1767, 1997.
- Jeffrey, S. and LeRoi, J.: Simple procedures for growing SCOR reference microalgal cultures., in: *Phytoplankton pigments in oceanography, Monographs on oceanographic methodology 10*, edited by Jeffrey, S., Mantoura, R., and S.W., W., pp. 181–205, UNESCO, France, 1997.
- Jiang, Q. and Logan, B. E.: Fractal dimensions of aggregates determined from steady-state size distributions, *Environmental Science & Technology*, 25, 2031–2038, 1991.
- Jonasz, M.: Particle-size distributions in the Baltic, *Tellus B*, 35, 346–358, 1983.
- Jonasz, M. and Fournier, G.: *Light Scattering by Particles in Water: Theoretical and Experimental Foundations: Theoretical and Experimental Foundations*, Academic Press, 2011.
- Jouon, A., Ouillon, S., Douillet, P., Lefebvre, J. P., Fernandez, J. M., Mari, X., and Froidefond, J.-M.: Spatio-temporal variability in suspended particulate matter concentration and the role of aggregation on size distribution in a coral reef lagoon, *Marine Geology*, 256, 36–48, 2008.
- Kader, B. and Yaglom, A.: Turbulent Structure of an Unstable Atmospheric Layer, in: *Nonlinear and Turbulent Processes in Physics*, edited by Z., S. R., pp. 829–845, Harwood Academic, Boston, 1984.

- Kamont, A.: On the fractional anisotropic Wiener field, *Probability and Mathematical Statistics-PWN*, 16, 85–98, 1995.
- Katul, G. and Chu, C.-R.: A theoretical and experimental investigation of energy-containing scales in the dynamic sublayer of boundary-layer flows, *Boundary-Layer Meteorology*, 86, 279–312, 1998.
- Katul, G. G., Chu, C. R., Parlange, M. B., Albertson, J. D., and Ortenburger, T. A.: Low-wavenumber spectral characteristics of velocity and temperature in the atmospheric surface layer, *Journal of Geophysical Research: Atmospheres*, 100, 14 243–14 255, 1995.
- Kerman, B. R.: A multifractal equivalent of the Beaufort scale for sea-state, *Geophysical Research Letters*, 20, 297–300, 1993.
- Kestin, J., Khalifa, H. E., and Correia, R. J.: Tables of the dynamic and kinematic viscosity of aqueous NaCl solutions in the temperature range 20–150 C and the pressure range 0.1–35 MPa, *Journal of physical and chemical reference data*, 10, 71–88, 1981.
- Kirk, J. T. O.: *Light and photosynthesis in aquatic ecosystems*, Cambridge University Press, 1994.
- Kitchen, J., Zaneveld, J. R. V., and Pak, H.: Effect of particle size distribution and chlorophyll content on beam attenuation spectra, *Applied Optics*, 21, 3913–3918, 1982.
- Kolmogorov, A. N.: The Wiener spiral and some other interesting curves in Hilbert space, *Dokl. Akad. Nauk SSSR*, 26, 115–118, 1940.
- Kolmogorov, A. N.: Local turbulence structure in incompressible fluids at very high Reynolds numbers, *Dokl. Akad. Nauk SSSR*, 30, 299–303, 1941a.
- Kolmogorov, A. N.: Dissipation of energy in locally isotropic turbulence, *Dokl. Akad. Nauk SSSR*, 32, 16–18, 1941b.

- Kolmogorov, A. N.: A refinement of previous hypotheses concerning the local structure of turbulence in a viscous incompressible fluid at high Reynolds number, *Journal of Fluid Mechanics*, 13, 82–85, 1962.
- Korotenko, K., Sentchev, A., and Schmitt, F. G.: Effect of variable winds on current structure and Reynolds stresses in a tidal flow: analysis of experimental data in the eastern English Channel, *Ocean Science*, 8, 1025–1040, 2012.
- Kranck, K. and Milligan, T.: Characteristics of suspended particles at an 11-hour anchor station in San Francisco Bay, California, *Journal of Geophysical Research: Oceans*, 97, 11 373–11 382, 1992.
- Kuipers, B., Witte, H., and Gonzalez, S.: Zooplankton distribution in the coastal upwelling system along the Banc d'Arguin, Mauritania, *Hydrobiologia*, 258, 133–149, 1993.
- Lass, H., Schmidt, M., Mohrholz, V., and Nausch, G.: Hydrographic and current measurements in the area of the Angola-Benguela front, *Journal of Physical Oceanography*, 30, 2589–2609, 2000.
- Lefebvre, J.-P., Ouillon, S., Vinh, V. D., Arfi, R., Panché, J.-Y., Mari, X., Van Thuoc, C., and Torréton, J.-P.: Seasonal variability of cohesive sediment aggregation in the Bach Dang–Cam Estuary, Haiphong (Vietnam), *Geo-Marine Letters*, 32, 103–121, 2012.
- Levin, S. and Whitfield, M.: Patchiness in marine and terrestrial systems: from individuals to populations [and Discussion], *Philosophical Transactions of the Royal Society of London. Series B: Biological Sciences*, 343, 99–103, 1994.
- Lévy, P. and Borel, M. É.: *Théorie de l'addition des variables aléatoires*, vol. 1, Gauthier-Villars Paris, 1954.
- Li, D. H. and Ganczarczyk, J.: Fractal geometry of particle aggregates generated in water and wastewater treatment processes, *Environmental science & technology*, 23, 1385–1389, 1989.

- Lien, R.-C. and D'Asaro, E. A.: Measurement of turbulent kinetic energy dissipation rate with a Lagrangian float, *Journal of Atmospheric and Oceanic Technology*, 23, 964–976, 2006.
- Litzow, M. A. and Ciannelli, L.: Oscillating trophic control induces community reorganization in a marine ecosystem, *Ecology Letters*, 10, 1124–1134, 2007.
- Logan, B. E. and Wilkinson, D. B.: Fractal dimensions and porosities of *Zoogloea ramigera* and *Saccharomyces cerevisiae* aggregates, *Biotechnology and bioengineering*, 38, 389–396, 1991.
- Loisel, H. and Morel, A.: Non-isotropy of the upward radiance field in typical coastal (Case 2) waters, *International Journal of Remote Sensing*, 22, 275–295, 2001.
- Loisel, H., Nicolas, J.-M., Sciandra, A., Stramski, D., and Poteau, A.: Spectral dependency of optical backscattering by marine particles from satellite remote sensing of the global ocean, *Journal of Geophysical Research: Oceans*, 111, C09 024, 2006.
- Loisel, H., Mériaux, X., Berthon, J.-F., and Poteau, A.: Investigation of the optical backscattering to scattering ratio of marine particles in relation to their biogeochemical composition in the eastern English Channel and southern North Sea, *Limnology and Oceanography*, 52, 739–752, 2007.
- Loisel, H., Vantrepotte, V., Dessailly, D., and Mériaux, X.: Assessment of the colored dissolved organic matter in coastal waters from ocean color remote sensing, *Optics Express*, 22, 13 109–13 124, 2014.
- Lovejoy, S. and Schertzer, D.: Multifractals, cloud radiances and rain, *Journal of Hydrology*, 322, 59–88, 2006.
- Lovejoy, S. and Schertzer, D.: Haar wavelets, fluctuations and structure functions: convenient choices for geophysics, *Nonlinear Processes in Geophysics*, 19, 513–527, 2012.

- Lovejoy, S. and Schertzer, D.: The weather and climate: emergent laws and multifractal cascades, Cambridge University Press, 2013.
- Lovejoy, S., Currie, W., Tessier, Y., Claereboudt, M., Bourget, E., Roff, J., and Schertzer, D.: Universal multifractals and ocean patchiness: phytoplankton, physical fields and coastal heterogeneity, *Journal of Plankton Research*, 23, 117–141, 2001a.
- Lovejoy, S., Schertzer, D., Tessier, Y., and Gaonac’h, H.: Multifractals and resolution-independent remote sensing algorithms: the example of ocean colour, *International Journal of Remote Sensing*, 22, 1191–1234, 2001b.
- Lubchenco, J. and Petes, L.: The interconnected biosphere: science at the ocean's tipping points, *Oceanography*, 23, 115–129, 2010.
- Lucas, A. J., Guerrero, R. A., Mianzan, H. W., Acha, E. M., and Lasta, C. A.: Coastal oceanographic regimes of the northern Argentine Continental Shelf (34–43 S), *Estuarine, Coastal and Shelf Science*, 65, 405–420, 2005.
- Madhupratap, M., Kumar, S. P., Bhattathiri, P., Kumar, M. D., Raghukumar, S., Nair, K., and Ramaiah, N.: Mechanism of the biological response to winter cooling in the northeastern Arabian Sea, *Nature*, 384, 549–552, 1996.
- Mandelbrot, B. B.: Intermittent turbulence in self-similar cascades: divergence of high moments and dimension of the carrier, *Journal of Fluid Mechanics*, 62, 331–358, 1974.
- Mandelbrot, B. B. and Van Ness, J. W.: Fractional Brownian motions, fractional noises and applications, *SIAM review*, 10, 422–437, 1968.
- McCave, I. N.: Particulate size spectra, behavior, and origin of nepheloid layers over the Nova Scotian continental rise, *Journal of Geophysical Research*, 88, 7647–7666, 1983.

- McCave, I. N.: Size spectra and aggregation of suspended particles in the deep ocean, *Deep Sea Research Part A. Oceanographic Research Papers*, 31, 329–352, 1984.
- McGillicuddy, D., Kosnyrev, V., Ryan, J., and Yoder, J.: Covariation of mesoscale ocean color and sea-surface temperature patterns in the Sargasso Sea, *Deep Sea Research Part II: Topical Studies in Oceanography*, 48, 1823–1836, 2001.
- Meeuwis, J. and Lutjeharms, J.: Surface thermal characteristics of the Angola-Benguela front, *South African Journal of Marine Science*, 9, 261–279, 1990.
- Mikkelsen, O. and Pejrup, M.: The use of a LISST-100 laser particle sizer for in-situ estimates of floc size, density and settling velocity, *Geo-Marine Letters*, 20, 187–195, 2001.
- Mikkelsen, O. A., Hill, P. S., and Milligan, T. G.: Single-grain, microfloc and macrofloc volume variations observed with a LISST-100 and a digital floc camera, *Journal of Sea Research*, 55, 87–102, 2006.
- Mitchell, J. G., Yamazaki, H., Seuront, L., Wolk, F., and Li, H.: Phytoplankton patch patterns: seascape anatomy in a turbulent ocean, *Journal of Marine Systems*, 69, 247–253, 2008.
- Mobley, C., Boss, E., and Roesler, C.: *Ocean optics web book*, 2011.
- Mobley, C. D.: *Light and water: Radiative transfer in natural waters*, Academic Press, 1994.
- Montera, L. d., Jouini, M., Verrier, S., Thiria, S., and Crépon, M.: Multifractal analysis of oceanic chlorophyll maps remotely sensed from space, *Ocean Science*, 7, 219–229, 2011.
- Morel, A. and Gentili, B.: Diffuse reflectance of oceanic waters: its dependence on Sun angle as influenced by the molecular scattering contribution, *Applied optics*, 30, 4427–4438, 1991.

- Morel, A. and Gentili, B.: Diffuse reflectance of oceanic waters. III. Implication of bidirectionality for the remote-sensing problem, *Applied Optics*, 35, 4850–4862, 1996.
- Moroshkin, K., Bubnov, V., and Bulatov, R.: Water circulation in the eastern South Atlantic Ocean, *Oceanology*, 10, 27–34, 1970.
- Muzy, J.-F., Sornette, D., Delour, J., and Arneodo, A.: Multifractal returns and hierarchical portfolio theory, *Quantitative Finance*, 1, 131–148, 2001.
- Nakao, H.: Multi-scaling properties of truncated Lévy flights, *Physics Letters A*, 266, 282–289, 2000.
- Neukermans, G., Loisel, H., Mériaux, X., Astoreca, R., and McKee, D.: In situ variability of mass-specific beam attenuation and backscattering of marine particles with respect to particle size, density, and composition, *Limnology and Oceanography*, 57, 124–144, 2012a.
- Neukermans, G., Ruddick, K., Loisel, H., and Roose, P.: Optimization and quality control of suspended particulate matter concentration measurement using turbidity measurements, *Limnology and Oceanography: Methods*, 10, 1011–1023, 2012b.
- Nicolis, O., Ramírez-Cobo, P., and Vidakovic, B.: 2D wavelet-based spectra with applications, *Computational Statistics & Data Analysis*, 55, 738–751, 2011.
- Nieves, V., Llebot, C., Turiel, A., Solé, J., García-Ladona, E., Estrada, M., and Blasco, D.: Common turbulent signature in sea surface temperature and chlorophyll maps, *Geophysical Research Letters*, 34, L23 602, 2007.
- Novikov, E. and Stewart, R.: The intermittency of turbulence and the spectrum of energy dissipation fluctuations, *Izv. Geophys. Ser.*, 3, 408–413, 1964.
- O’Reilly, J., Maritorena, S., Siegel, D., O’Brien, M., Toole, D., Mitchell, B., Kahru, M., Chavez, F., Strutton, P., Cota, G., et al.: Ocean color chlorophyll a algorithms

- for SeaWiFS, OC2, and OC4: version 4, SeaWiFS Postlaunch Calibration and Validation Analyses, Part, 3, 9–23, 2000.
- Obukhov, A.: On the distribution of energy in the spectrum of turbulent flow, Dokl. Akad. Nauk SSSR, 32, 22–24, 1941a.
- Obukhov, A.: Spectral energy distribution in a turbulent flow, Dokl. Akad. Nauk SSSR, 32, 22–24, 1941b.
- Obukhov, A.: Structure of the temperature field in turbulent flows, Izv. Nauk. SSSR, Geogr. i. Geofiz, 13, 58–69, 1949.
- Obukhov, A.: Some specific features of atmospheric turbulence, Journal of Fluid Mechanics, 13, 77–81, 1962.
- Panchev, S.: Random Functions and Turbulence, American Journal of Physics, 40, 927–927, 1972.
- Pedlosky, J.: Geophysical fluid dynamics, vol. 1, Springer-Verlag, 1982.
- Perry, A., Henbest, S., and Chong, M.: A theoretical and experimental study of wall turbulence, Journal of Fluid Mechanics, 165, 163–199, 1986.
- Piontkovski, S., Williams, R., Peterson, W., Yunev, O., Minkina, N., Vladimirov, V., and Blinkov, A.: Spatial heterogeneity of the planktonic fields in the upper mixed layer of the open ocean, Marine ecology progress series, 148, 145–154, 1997.
- Pope, S. B.: Turbulent flows, Cambridge University Press, 2000.
- Pottier, C., Turiel, A., and Garçon, V.: Inferring missing data in satellite chlorophyll maps using turbulent cascading, Remote Sensing of Environment, 112, 4242–4260, 2008.
- Powell, T. M.: Physical and biological scales of variability in lakes, estuaries, and the coastal ocean, in: Ecological time series, pp. 119–138, Springer, 1995.

- Raine, R., White, M., and Dodge, J.: The summer distribution of net plankton dinoflagellates and their relation to water movements in the NE Atlantic Ocean, west of Ireland, *Journal of plankton research*, 24, 1131–1147, 2002.
- Renosh, P. R., Schmitt, F. G., Loisel, H., Sentchev, A., and Mériaux, X.: High frequency variability of particle size distribution and its dependency on turbulence over the sea bottom during re-suspension processes, *Continental Shelf Research*, 77, 51–60, 2014.
- Renosh, P. R., Schmitt, F. G., and Loisel, H.: Scaling analysis of ocean surface turbulent heterogeneities from satellite remote sensing: use of 2D structure functions., *PLoS ONE*, In press, 2015.
- Reynolds, R., Stramski, D., Wright, V., and Woźniak, S.: Measurements and characterization of particle size distributions in coastal waters, *Journal of Geophysical Research: Oceans*, 115, C08 024, 2010.
- Richardson, L. F.: *Weather prediction by numerical process*, Cambridge University Press, 1922.
- Riley, G. A.: Organic aggregates in seawater and the dynamics of their formation and utilization, *Limnology and Oceanography*, 8, 372–381, 1963.
- Schertzer, D. and Lovejoy, S.: Physical modeling and analysis of rain and clouds by anisotropic scaling multiplicative processes, *Journal of Geophysical Research: Atmospheres*, 92, 9693–9714, 1987.
- Schertzer, D. and Lovejoy, S.: Nonlinear variability in geophysics: Multifractal simulations and analysis, in: *Fractals Physical Origin and Properties*, edited by Pietronero, L., pp. 49–79, Springer, 1989.
- Schertzer, D. and Lovejoy, S.: Hard and soft multifractal processes, *Physica A: Statistical Mechanics and its Applications*, 185, 187–194, 1992.

- Schertzer, D., Lovejoy, S., Schmitt, F., Chigirinskaya, Y., and Marsan, D.: Multifractal cascade dynamics and turbulent intermittency, *Fractals*, 5, 427–471, 1997.
- Schmitt, F., Schertzer, D., Lovejoy, S., and Brunet, Y.: Multifractal temperature and flux of temperature variance in fully developed turbulence, *EPL*, 34, 195, 1996.
- Schmitt, F., Schertzer, D., and Lovejoy, S.: Multifractal analysis of foreign exchange data, *Applied stochastic models and data analysis*, 15, 29–53, 1999.
- Schmitt, F., Schertzer, D., and Lovejoy, S.: Multifractal fluctuations in finance, *International Journal of Theoretical and Applied Finance*, 3, 361–364, 2000.
- Schmitt, F. G. and Huang, Y.: *Stochastic Analysis of Scaling Time Series: from turbulence theory to applications*, In press, Cambridge University Press, 2015.
- Schmitt, F. G. and Seuront, L.: Intermittent turbulence and copepod dynamics: increase in encounter rates through preferential concentration, *Journal of Marine Systems*, 70, 263–272, 2008.
- Schmitt, F. G., Huang, Y., Lu, Z., Brizard, S. Z., Molinero, J. C., and Liu, Y.: Analysis of nonlinear biophysical time series in aquatic environments: scaling properties and empirical mode decomposition, in: *Nonlinear Dynamics in Geosciences*, edited by Tsonis, A. and Elsner, J., pp. 261–280, Springer, 2007.
- Schmitt, F. G., Huang, Y., Lu, Z., Liu, Y., and Fernandez, N.: Analysis of velocity fluctuations and their intermittency properties in the surf zone using empirical mode decomposition, *Journal of Marine Systems*, 77, 473–481, 2009.
- Sethuraman, S., Meyers, R., and Brown, R.: A comparison of a Eulerian and a Lagrangian time scale for over-water atmospheric flows during stable conditions, *Boundary-Layer Meteorology*, 14, 557–565, 1978.
- Seuront, L. and Schmitt, F. G.: Multiscaling statistical procedures for the exploration of biophysical couplings in intermittent turbulence. Part II. Applications, *Deep Sea Research Part II: Topical Studies in Oceanography*, 52, 1325–1343, 2005.

- Seuront, L., Schmitt, F., Lagadeuc, Y., Schertzer, D., Lovejoy, S., and Frontier, S.: Multifractal analysis of phytoplankton biomass and temperature in the ocean, *Geophysical Research Letters*, 23, 3591–3594, 1996a.
- Seuront, L., Schmitt, F., Schertzer, D., Lagadeuc, Y., Lovejoy, S., et al.: Multifractal intermittency of Eulerian and Lagrangian turbulence of ocean temperature and plankton fields, *Nonlinear processes in Geophysics*, 3, 236–246, 1996b.
- Seuront, L., Schmitt, F., Lagadeuc, Y., Schertzer, D., and Lovejoy, S.: Universal multifractal analysis as a tool to characterize multiscale intermittent patterns: example of phytoplankton distribution in turbulent coastal waters, *Journal of Plankton Research*, 21, 877–922, 1999.
- She, Z.-S. and Leveque, E.: Universal scaling laws in fully developed turbulence, *Physical review letters*, 72, 336, 1994.
- She, Z.-S. and Waymire, E. C.: Quantized energy cascade and log-Poisson statistics in fully developed turbulence, *Physical Review Letters*, 74, 262, 1995.
- Sheldon, R., Prakash, A., and Sutcliffe, W.: The size distribution of particles in the ocean, *Limnology and Oceanography*, 17, 327–340, 1972.
- Squires, K. D. and Eaton, J. K.: Preferential concentration of particles by turbulence, *Physics of Fluids A*, 3, 1169–1178, 1991.
- Sreenivasan, K. and Kailasnath, P.: An update on the intermittency exponent in turbulence, *Physics of Fluids A: Fluid Dynamics*, 5, 512–514, 1993.
- Sreenivasan, K. R. and Antonia, R.: The phenomenology of small-scale turbulence, *Annual review of fluid mechanics*, 29, 435–472, 1997.
- Stedmon, C. A., Markager, S., Tranvik, L., Kronberg, L., Slätis, T., and Martinsen, W.: Photochemical production of ammonium and transformation of dissolved organic matter in the Baltic Sea, *Marine Chemistry*, 104, 227–240, 2007.
- Steele, J. H.: The ocean 'landscape', *Landscape Ecology*, 3, 185–192, 1989.

- Steele, J. H.: Can ecological theory cross the land-sea boundary?, *Journal of Theoretical Biology*, 153, 425–436, 1991.
- Stramski, D. and Kiefer, D. A.: The size distribution of particles in the ocean, *Progress in Oceanography*, 28, 343–383, 1991.
- Stramski, D., Boss, E., Bogucki, D., and Voss, K. J.: The role of seawater constituents in light backscattering in the ocean, *Progress in Oceanography*, 61, 27–56, 2004.
- Sullivan, J. M., Twardowski, M. S., Donaghay, P. L., and Freeman, S. A.: Use of optical scattering to discriminate particle types in coastal waters, *Applied Optics*, 44, 1667–1680, 2005.
- Svendsen, I. A.: Analysis of surf zone turbulence, *Journal of Geophysical Research: Oceans*, 92, 5115–5124, 1987.
- Tessier, Y., Lovejoy, S., and Schertzer, D.: Universal multifractals: theory and observations for rain and clouds, *Journal of Applied Meteorology*, 32, 223–250, 1993.
- Thomson, J., Polagye, B., Durgesh, V., and Richmond, M. C.: Measurements of turbulence at two tidal energy sites in Puget Sound, WA, *Oceanic Engineering, IEEE Journal of*, 37, 363–374, 2012.
- Traykovski, P., Latter, R. J., and Irish, J. D.: A laboratory evaluation of the laser in situ scattering and transmissometry instrument using natural sediments, *Marine Geology*, 159, 355–367, 1999.
- Turiel, A., Grazzini, J., and Yahia, H.: Multiscale techniques for the detection of precipitation using thermal IR satellite images, *Geoscience and Remote Sensing Letters, IEEE*, 2, 447–450, 2005.
- Turiel, A., Nieves, V., García-Ladona, E., Font, J., Rio, M.-H., and Larnicol, G.: The multifractal structure of satellite sea surface temperature maps can be used to obtain global maps of streamlines, *Ocean Science*, 5, 447–460, 2009.

- Twardowski, M. S., Boss, E., Macdonald, J. B., Pegau, W. S., Barnard, A. H., and Zaneveld, J. R. V.: A model for estimating bulk refractive index from the optical backscattering ratio and the implications for understanding particle composition in case I and case II waters, *Journal of Geophysical Research: Oceans*, 106, 14 129–14 142, 2001.
- Umlauf, L. and Burchard, H.: Second-order turbulence closure models for geophysical boundary layers. A review of recent work, *Continental Shelf Research*, 25, 795–827, 2005.
- Van der Lee, E., Bowers, D., and Kyte, E.: Remote sensing of temporal and spatial patterns of suspended particle size in the Irish Sea in relation to the Kolmogorov microscale, *Continental Shelf Research*, 29, 1213–1225, 2009.
- Van Leussen, W.: Aggregation of particles, settling velocity of mud flocs a review, in: *Physical processes in estuaries*, pp. 347–403, Springer, 1988.
- Vantrepotte, V., Brunet, C., Mériaux, X., Lécuyer, E., Vellucci, V., and Santer, R.: Bio-optical properties of coastal waters in the Eastern English Channel, *Estuarine, Coastal and Shelf Science*, 72, 201–212, 2007.
- Velegakis, A., Michel, D., Collins, M., Lafite, R., Oikonomou, E., Dupont, J., Huault, M., Lecouturier, M., Salomon, J., and Bishop, C.: Sources, sinks and resuspension of suspended particulate matter in the eastern English Channel, *Continental Shelf Research*, 19, 1933–1957, 1999.
- Verrier, S., Crépon, M., and Thiria, S.: Scaling and stochastic cascade properties of NEMO oceanic simulations and their potential value for GCM evaluation and downscaling, *Journal of Geophysical Research: Oceans*, 119, 6444–6460, 2014.
- Vulpiani, A. and Livi, R.: *The Kolmogorov legacy in physics*, Springer Science & Business Media, 2003.

- Wang, L.-P., Wexler, A. S., and Zhou, Y.: Statistical mechanical description and modelling of turbulent collision of inertial particles, *Journal of Fluid Mechanics*, 415, 117–153, 2000.
- Wells, M. L. and Goldberg, E. D.: Marine submicron particles, *Marine Chemistry*, 40, 5–18, 1992.
- Wolanski, E. and Gibbs, R. J.: Flocculation of suspended sediment in the Fly River estuary, Papua New Guinea, *Journal of Coastal Research*, pp. 754–762, 1995.
- Wollast, R.: Evaluation and comparison of the global carbon cycle in the coastal zone and in the open ocean, *The Sea*, 10, 213–252, 1998.
- Wu, M. K. and Friedlander, S. K.: Note on the power law equation for fractal-like aerosol agglomerates, *Journal of Colloid and interface Science*, 159, 246–248, 1993.
- Xu, H. and Bodenschatz, E.: Motion of inertial particles with size larger than Kolmogorov scale in turbulent flows, *Physica D: Nonlinear Phenomena*, 237, 2095–2100, 2008.
- Yaglom, A.: The influence of fluctuations in energy dissipation on the shape of turbulence characteristics in the inertial interval, in: *Soviet Physics Doklady*, vol. 11, pp. 26–30, 1966.
- Yahia, H., Turiel, A., Chrysoulakis, N., Grazzini, J., Prastacos, P., and Herlin, I.: Application of the multifractal microcanonical formalism to the detection of fire plumes in NOAA–AVHRR data, *International Journal of Remote Sensing*, 29, 4189–4205, 2008.
- Yoder, J. A., Ackleson, S. G., Barber, R. T., Flament, P., and Balch, W. M.: A line in the sea, *Nature*, 371, 689–692, 1994.
- Yonghe, L., Kexin, Z., Wanchang, Z., Yuehong, S., Hongqin, P., and Jinming, F.:

Multifractal analysis of 1-min summer rainfall time series from a monsoonal watershed in eastern China, *Theoretical and applied climatology*, 111, 37–50, 2013.

Yoshimoto, H. and Goto, S.: Self-similar clustering of inertial particles in homogeneous turbulence, *Journal of Fluid Mechanics*, 577, 275–286, 2007.

APPENDICES

Appendix A: Curriculum Vitae of the author

Mr. Renosh PANNIMPULLATH REMANAN

CONTACT INFORMATION

Lille-1 University of Science and Technology, CNRS,
Laboratory of Oceanology and Geosciences, UMR 8187 LOG,
32 Avenue Foch, 62930 Wimereux, France.
E-mail: pr.renosh@gmail.com
Phone: +33 76 25 15 099

PERSONAL INFORMATION

Date of birth : 30-October-1982
Place of birth : Pallipuram
Gender : Male
Marital status : Married
Languages known : English, Malayalam and Hindi
Nationality : Indian

EDUCATION

**Ph.D. student at Lille-1 University of Science and Technology,
Lille, France. Degree awarded on 07 April 2015**

- Title of the Thesis: *Characterisation of the coupling between oceanic turbulence and the variability of coastal waters optical properties, using in situ measurements and satellite data.*
- Advisors: **Prof. Francois G. Schmitt, Ph.D.** and **Prof. Hubert Loisel, Ph.D.**
- **Laboratory of Oceanology and Geosciences (LOG)**, Wimereux, France.

M. Sc., Physical Oceanography, 2005-2007

- CGPA: 7.30/10
- Dissertation Topic: *Study on salt-silt wedge and Identification of Turbidity Maxima in a Tropical Estuary during Pre-monsoon Period*
- Advisor: Dr. K Rasheed, Ph.D.
- **Cochin University of Science and Technology (CUSAT)**, Cochin, Kerala, India.

B. Sc., Physics, 2000-2003

- Percentage :74.1%
- *Sree Narayana College, Nattika*
- **University of Calicut**, Malappuram, Kerala, India.

RESEARCH
EXPERIENCE

CSIR-UGC Fellow

July 2011 to February 2012

- Dept. of Marine Sciences, Goa University
Goa University, Goa, India.

Research Fellow

January 2008 to June 2011

- Project Title : Bio-optical properties of the coastal waters off the west coast for modeling, illumination and retrieval of ocean colour components through OCM onboard IRS - P4.
Dept. of Marine Sciences, Goa University
Goa University, Goa, India.

Laboratory Assistant (Physics)

2003 to 2005

- Vidya Academy of Science and Technology (VAST)
VAST, Thalakkottukara, Thrissur, India.

AWARDS AND
FELLOWSHIPS

- Awarded CSIR-NET (Eligibility for Lectureship) (Rank-13) by Council of scientific and Industrial Research, India (June 2010).
- Awarded JRF-UGC-NET (Rank-87) by Council of scientific and Industrial Research, India (December 2010).
- Awarded JRF-UGC-NET (Rank-56) by Council of scientific and Industrial Research, India (June 2011).

CRUISE
PARTICIPATIONS

- Research cruise: Onboard BTV Sagar Manjusha during month of April 2008 in eastern Arabian Sea.
- Research cruise: Onboard CRV Sagar Purvi during the month of November 2008 in eastern Arabian Sea.
- Research cruise: Onboard FORV Sagar Sampada during month of April 2009 in eastern Arabian Sea.
- Research cruise: Participated research cruise in Bay of Bengal conducted by INCOIS india during October 2008 in ORV Sagar Kanya.
- Research cruise: Participated in ICARB-W conducted by ISRO from 27-December-2008 to 30-January-2009 in entire Bay of Bengal in ORV Sagar Kanya.
- Research cruise: Onboard FORV Sagar Sampada during the month of April 2010 in eastern Arabian Sea.
- Field Trips: Participated many field trips in Zuari and Mandovi Estuaries in West coast of India.

TRAININGS AND
WORKSHOPS

- Attended **COHERENS** (COupled Hydrodynamical Ecological model for REgioNal Shelf seas) model Training Programme organized by MUMM, Brussels and NIO, Goa at the International Centre Goa during 30 Nov - 4 Dec 2009.
- Attended two days **training course on time series analysis** (17-18 Sept. 2012) organised by IFREMER and Europole Mer, Moulin Mer in Logonna Daoulas, France.
- Attended one day **short course on Observational approaches in Ocean Optics** (7 Oct. 2012), Glasgow, Scotland.
- Attended one day **workshop on LISST-HOLO** (19 Oct. 2012), Barcelona, Spain.
- Attended four days **4eme Atelier National Couleur de l'Ocan** (3-5 Feb. 2014) Nausicaa, Boulogne-sur-Mer, France.
- Attended one day **workshop on Ocean Optics Protocols** (25 Oct. 2014), Portland, Maine.
- Attended one day **short course on SeaDAS** (26 Oct. 2014), Portland, Maine.

POSTER
PRESENTATIONS

- H. B. Menon, **Renosh, P. R.**, N.Sangekar, S.Halarnekar and S.Nulageri Spatial variability of bio-optical properties and algorithm development to retrieve algal bloom data from coastal waters of the eastern Arabian sea. SAFARI Symposium on Remote sensing and Fisheries, 15-17 Feb. 2010, Kochi, India.
- **Renosh, P. R.**, F.G. Schmitt, H. Loisel, X. Meriaux and A. Sentchev. Analysis of a high frequency time series of bio-optical properties in complex coastal waters: couplings with turbulence. Time Series analysis in marine science and applications for Industry, 19-21 Sept. 2012, Logonna Daoulas, Brest, France.
- **Renosh, P. R.**, H. Loisel, F.G. Schmitt, X. Meriaux, A. Sentchev and G. Lacroix. Origin of the high frequency variability of bio-optical properties in complex coastal environments. Ocean Optics Conference XXI, 8-12 Oct. 2012, Glasgow, Scotland.
- Renosh, P. R., **F.G. Schmitt**, H. Loisel and X. Meriaux. Multiscaling properties of coastal waters particle size distribution from LISST in situ measurements. AGU fall meeting 2013, 9-13 Dec. 2013, San Francisco, California.
- **Renosh, P. R.**, F.G. Schmitt and H. Loisel. Multi-Scale analysis of MODIS-Aqua Chlorophyll-a and Sea Surface Temperature: statistical characterization using turbulence tools. Ocean Optics XXII, 27-31 Oct. 2014, Portland, Maine.
- **Renosh, P. R.**, F.G. Schmitt and H. Loisel. Multi-Scale analysis of MODIS-Aqua Chlorophyll-a and Sea Surface Temperature: statistical characterization using turbulence tools. Journe Thmatique du Programme National de Tldtection Spatiale: 13 November -2014, Paris.

ORAL
PRESENTATIONS

- **Renosh, P. R.**, F.G. Schmitt, H. Loisel, X. Meriaux and A. Sentchev. High frequency variability of particle size distributions and its dependency to turbulence in the optically complex coastal environment of the English Channel. Particles in Europe -2012, 17-19 Oct. 2012, Barcelona, Spain.
- **Renosh, P. R.**, F.G. Schmitt, H. Loisel, A. Sentchev and X. Meriaux (2014). High frequency variability of particle size distribution and its dependency on turbulence over the sea bottom during re-suspension processes. 4eme Atelier National Couleur de l'Océan (3-5 Feb. 2014) Nausicaa, Boulogne-sur-Mer, France.

PUBLICATIONS

1. **Renosh, P. R.**, F. G. Schmitt, H. Loisel (2015) Scaling Analysis of Ocean Surface Turbulent Heterogeneities from Satellite Remote Sensing: Use of 2D Structure Functions. **PLoS ONE** 10(5): e0126975.
2. **Renosh, P. R.**, F. G. Schmitt, H. Loisel, A. Sentchev and X. Meriaux (2014). High frequency variability of particle size distribution and its dependency on turbulence over the sea bottom during re-suspension processes. **Continental Shelf Research**, 77, 51-60.
3. **Renosh, P. R.**, K. Rasheed and A. N. Balchand (2010), Studies on tide depended salt-silt wedge and identification of turbidity maxima in Cochin estuary. **Indian Journal of Marine Sciences**, 39(1), 136-142.

SUBMITTED
PAPER

1. **Renosh, P. R.**, F. G. Schmitt and H. Loisel. Intermittent particle dynamics in marine coastal waters. Submitted to **Nonlinear Processes in Geophysics**.

PAPERS UNDER
PREPARATION

1. **Renosh, P. R.**, F. G. Schmitt and H. Loisel. Multi-Scale analysis of ocean colour and sea surface temperature images of MODIS-Aqua: statistical characterization using turbulence tools. Prepared for **Remote Sensing of Environment**.

Appendix B: Published papers



Contents lists available at ScienceDirect

Continental Shelf Research

journal homepage: www.elsevier.com/locate/csr

Research papers

High frequency variability of particle size distribution and its dependency on turbulence over the sea bottom during re-suspension processes

P.R. Renosh^a, François G. Schmitt^{a,*}, Hubert Loisel^b, Alexei Sentchev^b, Xavier Mériaux^b^a CNRS, University of Lille-1, Laboratory of Oceanology and Geosciences, CNRS UMR 8187 LOG, 32 Avenue Foch, 62930 Wimereux, France^b ULCO, Laboratory of Oceanology and Geosciences, UMR 8187 LOG, 32 Avenue Foch, 62930 Wimereux, France

ARTICLE INFO

Article history:

Received 22 August 2013

Received in revised form

21 January 2014

Accepted 27 January 2014

Available online 5 February 2014

Keywords:

Particle size distribution

Turbulence

Spectral analysis

Stokes number

Re-suspension processes

ABSTRACT

The impact of tidal current, waves and turbulence on particles re-suspension over the sea bottom is studied through Eulerian high frequency measurements of velocity and particle size distribution (PSD) during 5 tidal cycles (65 h) in a coastal environment of the eastern English Channel. High frequency variability of PSD is observed along with the velocity fluctuations. Power spectral analysis shows that turbulent velocity and PSD parameters have similarities in their spectral behaviour over the whole range of examined temporal scales. The low frequency variability of particles is controlled by turbulence ($\beta \approx -5/3$) and the high frequency is partly driven by dynamical processes impacted by the sea bottom interactions with turbulence (wall turbulence). Stokes number (St), rarely measured in situ, exhibits very low values, emphasizing that these particles can be considered as passive tracers. The effect of tide and waves on turbidity and PSD is highlighted. During slack tide, when the current reaches its minimum value, we observe a higher proportion of small particles compared to larger ones. To a lower extent, high significant wave heights are also associated with a greater concentration of suspended sediments and the presence of larger particles (larger Sauter's diameter D_A , and lower PSD slope ξ).

© 2014 Elsevier Ltd. All rights reserved.

1. Introduction

Marine particles cover a broad range in diameters from nanometers, mainly as colloids, to few millimeters and even centimeters in the presence of big *Phaeocystis* colonies, diatoms chains, or cyanobacteria filaments. Intermediate size particles include viruses, heterotrophic bacteria, pico-, nano-, and micro-, phytoplankton, micro-, meso-, and macro-zooplankton, non-living particles, and mineral particles (Stramski et al., 2004). These particles do not solely appear as individual entities in the water column, but are mainly present as marine algal flocs and aggregates (Eisma, 1986; Fowler and Knauer, 1986; Hill, 1998; Boss et al., 2009). The variability of the marine particle size distribution (PSD) impacts the different biological processes occurring in oceanic waters and vice versa. For instance, trophic interactions are tightly linked to the size distribution of the different living and non-living particles involved all over the trophic system (McCave, 1984). In the other way, blooms of specific phytoplankton species modify the general PSD shape by affecting one given size class. Phytoplankton degradation processes as well as zooplankton grazing also affect the PSD shape by promoting the small particles size classes

compared to larger ones. Physical processes occurring in the water column are also related to the PSD. For example, the settling velocity of the suspended matters is strongly controlled by the particles size. In contrast, the size distribution of floc or aggregate depends on the balance between aggregation and breakage, two processes driven by diffusive turbulent transport and differential settling (McCave, 1984). McCave suggested that particles in the Brownian range ($< 1.0 \mu\text{m}$) are pumped rapidly into larger size classes by aggregation. The instantaneous turbulent kinetic energy modifies the proportion between particles/floccule, fine, coarse, microflocs and macroflocs (Lefebvre et al., 2012). The re-suspension of marine sediments is also strongly size dependent (Wells and Goldberg, 1992; Mikkelsen and Pejrup, 2001; Fettweis et al., 2006).

Turbulence is one of the most important physical phenomena which determines the re-suspension and the settling of the suspended particles in the coastal as well as oceanic waters (Eisma, 1986; Van Leussen, 1988; Umlauf and Burchard, 2005; Fettweis et al., 2006; Burchard et al., 2008; Van der Lee et al., 2009). For instance, observations on floc in the field show that smaller flocs occur in high energy environments (Kranck and Milligan, 1992; Berhane et al., 1997). At a critical magnitude of turbulence, shear overcomes the binding strength of flocs and tends to destroy aggregates (Eisma, 1986). For primary (disaggregated) particles significantly larger than $1.0 \mu\text{m}$, and for the process of smaller flocs (microflocs) growing into larger flocs (macroflocs), turbulent shear is thought to be the dominant

* Corresponding author.

E-mail addresses: pr.renosh@gmail.com (P.R. Renosh), francois.schmitt@univ-lille1.fr (F.G. Schmitt).<http://dx.doi.org/10.1016/j.csr.2014.01.024>

0278-4343 © 2014 Elsevier Ltd. All rights reserved.

collision mechanism, except during periods of slack current velocities when differential settling of suspended particles onto one another may be responsible for most of the flocs formation and rapid clearing of the water (Van Leussen, 1988).

Studies done by Wolanski and Gibbs (1995) in Fly River Estuary show that the mean floc size was affected by the turbulence of tidal currents. The largest floc sizes were observed in the low tidal currents (< 0.5 m/s) and comparatively smaller floc sizes were observed in the high tidal currents (> 0.5 m/s).

In the present study, we analyse the dynamics of PSD and its relation with turbulence from in situ measurements. We conducted simultaneous measurements of velocity and PSD from instruments fixed on a frame positioned on the sea floor in the coastal waters of eastern English Channel. This study area, characterized by low depth, exhibits a large range of variability of bio-optical properties related to the occurrence of different phytoplankton blooms, bottom sediments re-suspension confined in the coastal areas, and numerous river inputs (Velegrakis et al., 1999; Loisel et al., 2007; Vantrepotte et al., 2007). The study carried out by Velegrakis et al. (1999) showed that re-suspension of fine-grained particles takes place during the spring tides and correlates well with the distribution of the bottom lithological type. In this paper, we will assess whether the re-suspended particles are passive tracers, or have an inertia that influences their transport by turbulence. For this, we estimate from in situ measurements their Stokes number St , which is a dimensionless number explaining the effect of inertia on the particles in a fluid motion. The impact of hydro-dynamical forcing on the particles behaviour is examined for different size classes of particles (silt/clay, fine, micro/coarse and macro flocs).

In the first section we present the study area as well as the different measurements and methods used to assess the coupling between turbulence and the particles behaviour over the sea bottom. The meteorological and hydrodynamic contexts occurring during the field measurements are then provided in the next section. The velocity field and the particle size distribution variability are described and their relationships are analysed. The Stokes numbers of these different particles, rarely measured in situ, are also estimated.

2. Data and methods

2.1. Study area

The measurements were conducted in the coastal waters of the eastern English Channel at a fixed station ($50^{\circ}45.676$ N, $01^{\circ}35.117$ E) from 25 to 28 June 2012 (Fig. 1A). The different instruments (explained in the data section) are fixed on a structure which was positioned on the seafloor. The English Channel is a mega tidal sea having a tidal range that varies from 3 to 9 m, and experiencing a tidal current of amplitude close to 1.0 m/s (Desprez, 2000; Seuront and Schmitt, 2005; Korotenko et al., 2012). The biogeochemical environment during the particular sampling period is defined from in situ data collected few days before the experiment (21 June) in the frame of the SOMLIT program in two different areas and in high tide period (Fig. 1B). Significant stratification can be noticed from the surface to the bottom at the coastal station for Chlorophyll-a (Chl-a), particulate organic carbon (POC) and suspended particulate matter (SPM) (Table 1). The SPM and Chl-a values are relatively low for a coastal environment, in good agreement with the summer low fresh water discharge, and the absence of phytoplankton bloom. The POC concentration is however relatively high. Besides, the relatively high POC/Chl-a ratio values, a proxy of the carbon mass of living and non-living organisms with respect to the autotrophic organisms (Loisel et al., 2007), indicate that the particulate organic

Table 1
Biogeochemical data collected from SOMLIT few days before the time series measurements (21 June 2012) from the stations C and L (shown in Fig. 1B).

Site	Depth	Temperature (°C)	Salinity (psu)	POC (µg/l)	SPM (mg/l)	Chl-a (µg/l)
C	Surface	15.83	34.43	341.9	NA	0.5
C	Bottom	14.82	34.76	239.67	1.54	0.5
L	Surface	14.88	34.93	220.9	0.48	1.21
L	Bottom	13.92	35.06	85.804	1.63	0.18

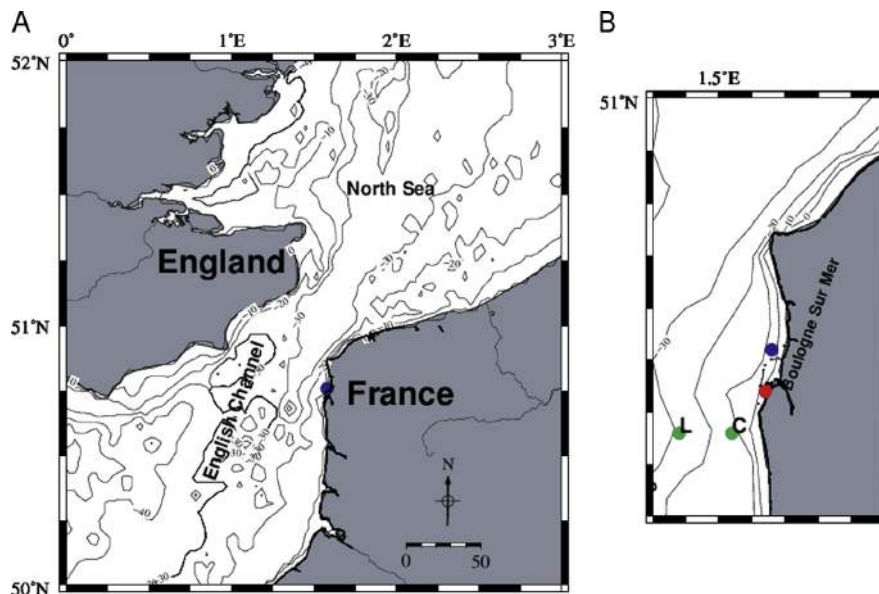


Fig. 1. Location (blue dot) of the sampling area in the eastern English Channel together with the isobaths (A). Zoom on the sampling area (blue dot), the meteorological station (red dot) and SOMLIT stations (green dot) in (B). (For interpretation of the references to colour in this figure caption, the reader is referred to the web version of this paper.)

fraction is largely dominated by detritus and heterotrophic bacteria.

2.2. Data

High frequency time series data were collected at 0.5 m depth above the sea bottom from different instruments fixed on the same platform moored on the sea bed. The three following instruments were used for the present study: a LISST-100x type C (Laser In Situ Scattering and Transmissometry, Sequoia Scientific), a Nortek Vector ADV current meter, and a RDI ADCP. The LISST measures the volume concentration of particles having diameters ranging from 2.5 to 500 μm in 32 size classes in logarithmic scale (Agrawal and Pottsmith, 2000). It also records the beam attenuation (c) at 670 nm (± 0.1 nm) over a 5 cm path length with an acceptance angle of 0.0135° . The particulate beam attenuation coefficient c_p has been derived from c after calibration with MilliQ water before and after the field campaign, using the assumption that chromophoric dissolved organic matter (CDOM) does not absorb the light at 670 nm. The volume concentration and c_p are measured with a sampling frequency of 1.0 Hz. The Nortek Vector ADV current meter measured the North, East and up components of the local velocity components with an accuracy of $\pm 0.5\%$ at 1 Hz. The available range of the velocity value measured by the instrument is from 0.01 to 7.0 m/s (± 0.01 m/s). A 1.2 MHz upward-looking four beam broadband RDI ADCP was also deployed on the bottom, along with the previous cited instruments clubbed in a structure. The ADCP was operated in the fast ping mode, providing two profiles per second. Each velocity was an average of six short pulse measurements over a 2 Hz interval. The velocities were recorded in Cartesian co-ordinates with 0.4 m vertical resolution. The significant wave height H_s , peak wave period T_p , and peak wave direction D_p are derived from the ADCP data using manufacture provided software WavesMon (Teledyne RD Instruments). These wave parameters were computed for 10 min burst duration with a moving window of 5 min interval providing one data point every 5 min. The wind data were provided by the meteorological station of harbour, Boulogne-Sur-Mer light house (Meteo-France) with a temporal resolution of 1 h.

2.3. Methods

Particle size distributions and power law of PSD: The scattering patterns of particles at 670 nm are recorded in 32 logarithmically size scattering angles by the LISST-100X type C (Agrawal and Pottsmith, 2000). This instrument measures the volume concentration $C_{vol,i}$ ($\mu\text{l/l}$) of the particles in 32 size classes from 2.5 to 500 μm through diffraction technique. Because of instability in the smallest and largest size classes, the data recorded in the first five inner and last outer rigs are excluded from further analysis (Traykovski et al., 1999; Jouon et al., 2008; Reynolds et al., 2010; Neukermans et al., 2012a). These instabilities observed in the smaller size classes have also been related to effects of stray light (Reynolds et al., 2010). Due to multiple scattering effects and signal to noise ratio sensitivity, the data for which optical transmission values are less than 30% and greater than 98% are also disregarded from the statistical analysis (personal communication with Ole Mikkelsen).

The volume concentration distributed on a particle size class can also be expressed as the concentration $C_{vol}(\sigma)$ per unit volume per unit bin width (Jouon et al., 2008):

$$C_{vol}(\sigma) = \frac{C_{vol,i}}{\sigma_{\max}(i) - \sigma_{\min}(i)} \quad (1)$$

where σ is the median diameter of the particle size class i , $\sigma_{\max}(i)$ and $\sigma_{\min}(i)$ are, respectively, the maximum and the minimum

particle size of the class i . This resulting volumetric PSD is expressed in $\mu\text{l}^{-1}\mu\text{m}^{-1}$. The number of particles for a size σ of the PSD is estimated by a normalization by their volume (Jouon et al., 2008). We obtain the number density $n(\sigma)$, which is also the product of the probability density function of the size $p(\sigma)$ and the total number of particles N :

$$n(\sigma) = Np(\sigma) = \frac{C_{vol}(\sigma)}{\frac{4}{3}\pi(\sigma/2)^3} \quad (2)$$

The PSD of this density number classically follows a power law distribution for aquatic particles in suspension (Sheldon et al., 1972; Kitchen et al., 1982; Jonasz, 1983; Boss et al., 2001a; Twardowski et al., 2001; Loisel et al., 2006; Reynolds et al., 2010):

$$n(\sigma) \sim K\sigma^{-\xi} \quad (3)$$

where K is a constant and ξ is the PSD slope. The value of $\xi(t)$ is here estimated at each time step (every second) from the LISST measurements, using an automatic regression analysis. The ξ value provides information on the relative concentration of small and large particles: the steeper the slope (the greater the ξ), the more small particles relative to large particles are present in the water (and vice versa).

Mean particulate diameters: Sauter's diameter (D_A) is the mean diameter of an equivalent sphere which has the same specific surface area as that of the PSD. This diameter is commonly used in sedimentology to represent size distribution in fluid flow calculation. Sauter's diameter D_A is also computed from the PSD using the following equations (Neukermans et al., 2012a; Filippa et al., 2012):

$$D_A = \frac{\sum_{i=6}^{31} [AC]_i \sigma_i}{[AC]} = \frac{\int_{\sigma_6}^{\sigma_{31}} n(\sigma) \sigma^3 d\sigma}{\int_{\sigma_6}^{\sigma_{31}} n(\sigma) \sigma^2 d\sigma} = \frac{\int_{\sigma_6}^{\sigma_{31}} p(\sigma) \sigma^3 d\sigma}{\int_{\sigma_6}^{\sigma_{31}} p(\sigma) \sigma^2 d\sigma} \quad (4)$$

$$[AC]_i = \frac{3}{2\sigma_i} C_{vol}(\sigma) \quad (5)$$

where $[AC]_i$ is the cross sectional area concentration of particles in bin i , and $[AC]$ is the total cross sectional area.

The following size classification has been adopted: silt/clay ($< 30 \mu\text{m}$), fine ($< 105 \mu\text{m}$), coarse/micro ($< 300 \mu\text{m}$) and macro-floc ($> 300 \mu\text{m}$) (Lefebvre et al., 2012). The volume concentration of each size class has been analysed using statistical and dynamical approaches.

Stokes number: In turbulent flows, the largest turbulent eddies break-up into smaller eddies through an energy cascade and finally dissipate at small scale due to molecular viscosity. The size of these smallest eddies is the Kolmogorov length scale. The eddies at this scale have typical life time τ_η which is the smallest time scale of turbulence. The Stokes number St is defined as the non-dimensional ratio of an inertial characteristic time scale τ_p to τ_η . It is one of the fundamental parameters characterizing particle-turbulence interactions: for $St \ll 1$, particles follow passively the fluid flow, whereas for $St \gg 1$, large inertia particles are not influenced by turbulence, and follow their own trajectories. It can also be related to the particles and fluid characteristics (Wang et al., 2000; Schmitt and Seuront, 2008; Xu and Bodenschatz, 2008) as follows:

$$St = \frac{\tau_p}{\tau_\eta} = C_p \left(\frac{\sigma}{\eta} \right)^2 \quad (6)$$

with $C_p = B/18$, where $B = \rho_p/\rho$ is the ratio of the particle density to the fluid density, and $\eta = (\nu^3/\epsilon)^{1/4}$ is the Kolmogorov length scale, where ν and ϵ are the kinematic viscosity of the fluid (in $\text{m}^2 \text{s}^{-1}$) and the dissipation rate (in $\text{m}^2 \text{s}^{-3}$), respectively.

The value of the dissipation rate ϵ is estimated using the power spectrum of the velocity time series, assuming a local isotropic

Kolmogorov relation of the form (Pope, 2000)

$$E(k) = C\epsilon^{2/3}k^{-5/3} \quad (7)$$

where $E(k)$ is the Fourier power spectrum, $C=1.5$ is a constant and k is the wavenumber. Since the power spectrum is here estimated from a time series in a fixed point, we estimate $E(f)$ where f is the frequency. Frequency and wavenumber are related with the horizontal component of the velocity V : $k=2\pi f/V$. This gives the following estimation of the dissipation from the power spectrum (Sethuraman et al., 1978; Lien and D'Asaro, 2006; Gerbi et al., 2009; Huang et al., 2012; Thomson et al., 2012):

$$\epsilon = \left(\frac{C_0}{C}\right)^{3/2} \left(\frac{2\pi}{\sigma_V}\right)^{5/2} \quad (8)$$

where σ_V is the standard deviation of V and C_0 is the constant such that $E(f) = C_0 f^{-5/3}$ is a best fit estimated over a range of frequencies corresponding to the inertial range.

3. Results

3.1. Meteorological and hydrodynamic conditions

Fig. 2 shows the hydrodynamic conditions prevailing in the study area during the observations. The significant wave height H_s exhibits relatively large variability in its magnitude during the entire time series observation (from 0.18 to 0.84 m). The mean and standard deviation values of H_s are 0.41 and 0.14 m, respectively. The peak wave period, T_p , also presents a relatively great variability from few seconds to 20 s, with a mean and standard deviation values of 6.41 and 2.44 s, respectively. In contrast, the peak wave direction, D_p , is almost constant during the entire experiment, with a mean value around 268° , which reveals that the waves are coming from the West. The water level shows typical semi-diurnal tidal characteristics with a period of 12.5 h. The total water column depth observed during the low tide time and the high tide time is 3.74 m and 10.07 m, respectively, revealing the spring tide conditions.

Relatively large wind fluctuations in terms of amplitude and direction are observed during the experiment. Relatively high wind speed values (above 4 m s^{-1}) are generally associated with South West wind (except at the end of the experiment), whereas relatively low wind speeds values (less than 4 m s^{-1}) are generally associated with South East wind.

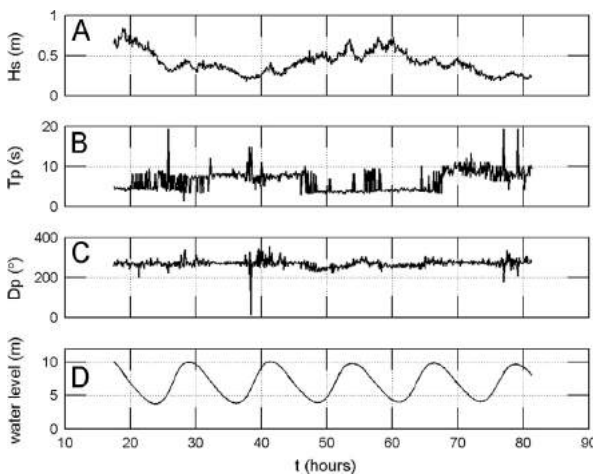


Fig. 2. Time series of (A) the significant wave height H_s , (B) peak wave period T_p , (C) peak wave direction D_p , and (D) water level.

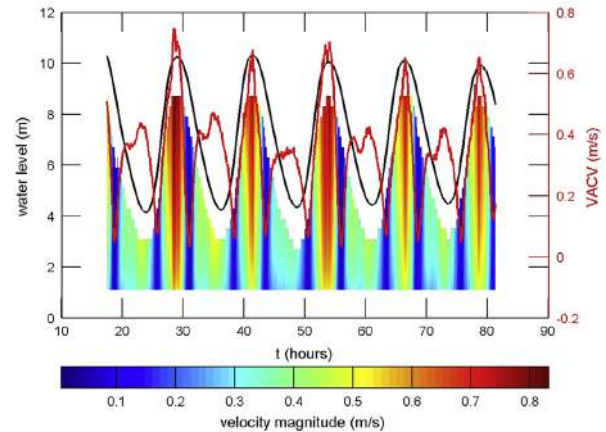


Fig. 3. Time series of water level evolution along with tide (black line), time series of VACV (in red) and contour map showing the vertical structure of the current velocity. (For interpretation of the references to colour in this figure caption, the reader is referred to the web version of this paper.)

From the water level evolution and current data set provided by ADCP, the effect of tidal current on the PSD can be analysed. The interval when the speed of the tidal current is very weak or zero usually refers to the period of reversal between ebb and flood currents, and also refers to the slack tide. The vertically averaged current velocity (VACV) has been derived for the entire time series (Fig. 3). VACV shows minimum values during the current reversal time, and two maxima, the main ones corresponding to the high tide (high water), and the second ones, reached at low tide (low water) (Fig. 3). The consecutive intervals of time between flood to ebb and ebb to flood are (7–7.34 h) greater than ebb to flood and flood to ebb (5.1–5.42 h), evidencing a pronounced asymmetry of tidal currents (Fig. 3).

3.2. Stokes number

The estimation of horizontal power spectra (U and V components) was used to estimate the constant C_0 in Eq. (8) and hence the dissipation rate. The mean value of the dissipation rate over the sampling day is $\epsilon = 7.65 \times 10^{-7} \text{ m}^2 \text{ s}^{-3}$. Since the mean temperature value is $T = 16.11^\circ \text{C} (\pm 0.10)$, the viscosity value is fixed at $\nu = 1.133 \times 10^{-6} \text{ m}^2 \text{ s}^{-1}$ (Kestin et al., 1981) and hence the Kolmogorov dissipation length scale $\eta = (\nu^3/\epsilon)^{1/4} = 1.2 \text{ mm}$. Because the mass density is not measured in the present study, two extreme values are imposed to assess the ratio of the particle density to the fluid density, B . The mass density of mineral and organic particles is $\rho_p = 2.7 \pm 0.15 \text{ g cm}^{-3}$ and $\rho_p = 1.06 \pm 0.03 \text{ g cm}^{-3}$, respectively (Chiappa-Carrara et al., 2006), resulting in B values of 2.7 ± 0.15 and 1.06 ± 0.03 , respectively. Using Eq. (6), these range of values for B , the estimation of ϵ and the range of particle sizes detected by the LISST (6.20–390 μm), we obtain Stokes numbers ranging from 6.8×10^{-7} to 0.03 for mineral particles and from 2.66×10^{-7} to 0.01 for organic particles. The largest values of the Stokes number are found for the largest particles ($\sim 0.39 \text{ mm}$), which are still almost four times smaller than the Kolmogorov scale. This shows that the Stokes numbers are here always very small, and that these particles are likely to be passive tracers and move along with the fluids.

3.3. Temporal variability of the velocity field

The time series of along-shore (U) and cross-shore (V) components of the velocity and their corresponding power spectra were estimated using the ADV data (Fig. 4). The along and cross shore

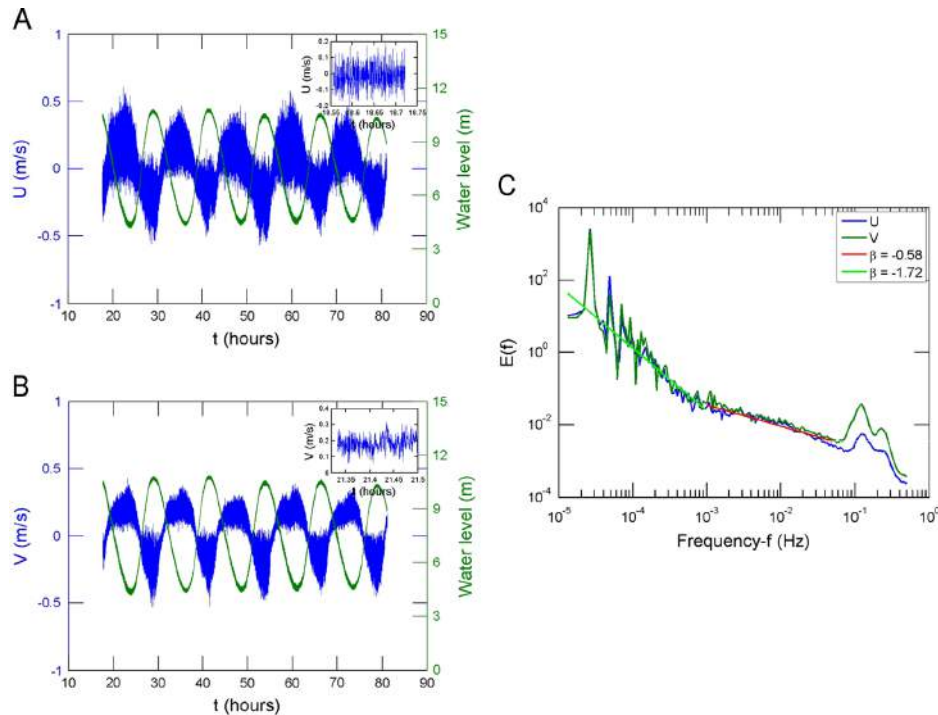


Fig. 4. Time series of U (A) and V (B). The insets represent a small portion of the time series to show the fluctuations. (C) Power spectra of U (blue curve) and V (green curve). The two straight lines correspond to two different scales with slopes of -1.72 (near to $-5/3$ slope of Kolmogorov) in light green and -0.58 in red and the humps in the energy value at high frequency represents a small scale forcing of high energy wave breaking. (For interpretation of the references to colour in this figure caption, the reader is referred to the web version of this paper.)

velocity components are characterized by a periodicity of 12.5 h, and a large small scale variability with a coefficient of variation (i.e., a ratio of standard deviation to the mean value of the absolute velocity also called as turbulent intensity) value for the along-shore and cross-shore components of 64.28 and 50.48%, respectively (Fig. 4A, B). These velocity records are tightly linked to the tidal cycle which also exhibits a period of 12.5 h. The along-shore component is characterized by a higher variability compared to the cross-shore component. The variability patterns of U and V are analysed through their power spectra (Fig. 4C). At low frequency scaling ranges, the power spectra of the two horizontal components (U and V) are characterized by a power law with a slope (β) close to $-5/3$ associated with 3D homogeneous turbulence (Kolmogorov scaling). From $T = 1000$ s \sim 17 min there is a transition to a regime for which the power spectra are characterized by a lower slope value (close to -0.6). Similar kind of β value has been observed in the 1-min summer rainfall time series data with a scaling regime from 1 h to 1 day (Yonghe et al., 2013). At high frequencies (0.1–0.3 Hz, hence on the range 3–10 s), the energy spectra exhibit the impact of a localized forcing. Such forcing has previously been attributed to the high energy associated with wave breaking scales (Schmitt et al., 2009).

3.4. Temporal variability patterns of particles concentration and size parameters in relation with hydrodynamical forcing

The size parameters considered here are the slope ξ of the PSD, as well as D_A and the normalized volume concentration of different size classes (silt/silt, fine, coarse/micro and macro-floc) of aggregates (Lefebvre et al., 2012). The turbidity dynamics is also considered through the particulate attenuation coefficient, $c_p(670)$, which is proportional to the particle concentration, at

first order (Neukermans et al., 2012b). The number of particles in size class i per unit volume and per unit diameter increment $n(\sigma)$ is computed for the entire size classes at each time step (Fig. 5). The PSD of the present data set is well represented by a power-law distribution throughout the whole time series. The slope values, ξ , of the particulate size distribution range between 2.57 and 3.94, with a mean value of 2.9 and a standard deviation of 0.16. These values are in good agreement with previous studies (Jonasz, 1983; Boss et al., 2001b; Loisel et al., 2006; Buonassissi and Dierssen, 2010; Reynolds et al., 2010; Neukermans et al., 2012a).

The Probability Density Function (PDF) of the concentrations and size parameters followed non-Gaussian distributions (Fig. 6). The inset of each panel in Fig. 6 shows the PDF and the Gaussian fit in a semi-log scale in order to emphasize extreme values. All the parameters show an asymmetry, and some are showing a heavy tail in their distribution (Fig. 6C–E). In addition, chi-square goodness-of-fit tests have been performed to test the normal distribution; the test result rejects the null hypothesis that these parameters come from a normal distribution with a mean and a variance computed from these parameters, at 5% significance level with a p -value of 0 and $h = 1$.

The temporal variability of $\xi(t)$ is analysed along with the vertically averaged current velocity (VACV) showing the tidal information as well as the current reversal (Fig. 7A). At the time of the current reversal, that is when VACV is minimum, $\xi(t)$ generally exhibits a well pronounced peak. This pattern indicates that the proportion of small particles compared to larger ones increases at this particular time. The mean diameter D_A , estimated for each time step, exhibits strong high frequency variability and has a mean value of $116.57 \mu\text{m}$ and standard deviation of $\pm 20.43 \mu\text{m}$ (Fig. 7B). D_A presents a well pronounced trough in

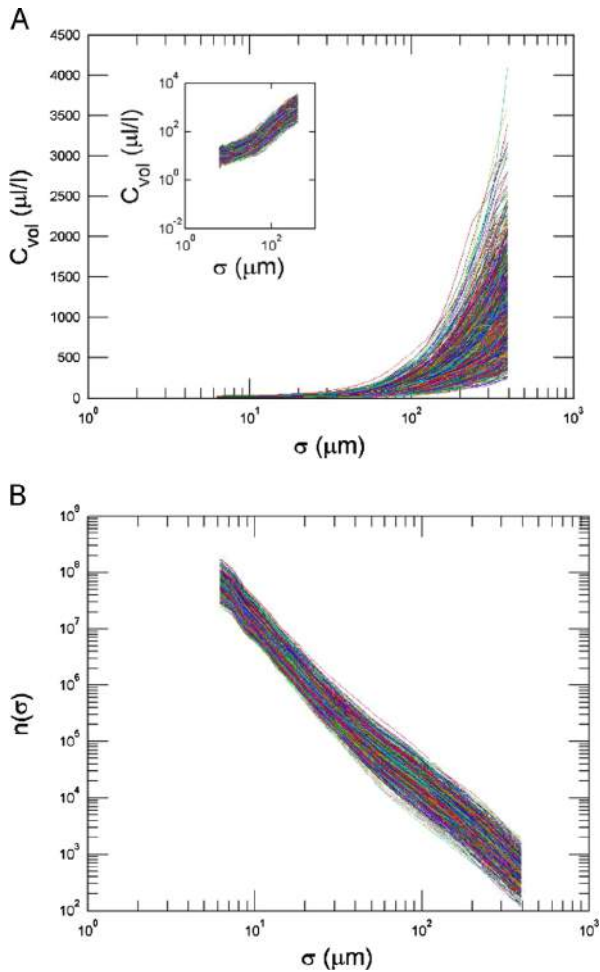


Fig. 5. PSD for volume concentration (A) and for number concentration (B). The inset in (A) is a log–log plot emphasizing the power-law relations for the volume concentrations.

magnitude during the current reversal time in agreement with the $\xi(t)$ patterns. This impact of current reversal on particles size distribution is also well evidenced through the temporal evolution of the normalized volume concentration of each considered size class (Fig. 7D–G). During slack tide the normalized volume concentration presents relatively higher values (a peak) in the lower size classes (silt/clay and fine) (Fig. 7D, E) and lower values (a trough) in the complementary higher size classes (coarse/micro and macro-flocs) (Fig. 7F, G). The time series of $c_p(670)$, a proxy of the suspended particulate concentration, exhibits strong high frequency variability (coefficient of variation of 53%), with numerous peaks which generally occur when the VACV is maximum (Fig. 7C). The mean and the standard deviation of $c_p(670)$ are 10.38 and 5.53 m^{-1} , respectively.

Besides the apparent impact of the vertically averaged current velocity on the particles concentration and size distribution, the significant wave height also slightly contributes to the re-suspension effects ($r^2=0.23$). The larger the mean significant wave height, the more the concentration of re-suspended particles (Fig. 8A). Moreover, significant wave height seems to affect PSD by promoting the concentration of larger particles compared to smaller ones (Fig. 8B). However, according to the low determination coefficient value additional data are needed to confirm this last point.

Since we have high frequency time series of $\xi(t)$, $D_A(t)$, $c_p(670)(t)$ and normalized volume concentration of each size classes of particles, we can explore their dynamical properties. The dynamics of ξ , D_A and $c_p(670)$ has been estimated through power spectral analysis (Fig. 9A–C). Two scaling regimes characterized by different slope values are observed on either side of the period of $T=1000$ s, similar to the velocity period. These parameters in the low frequency regime present the same spectral slope (β close to $-5/3$) similar to the velocity field, indicating that the dynamics of the particles is influenced by turbulence at low frequencies. At higher frequencies, the slope values of these parameters and velocity field are significantly different but remain similar to the velocity spectra. With a slope value close to -0.8 in the frequency range $[0.001; 0.1 \text{ s}^{-1}]$, the dynamics of the particles seems to be partly driven by dynamical processes likely impacted by the interaction with the sea floor for which a slope of -1.0 is expected (Perry et al., 1986; Katul et al., 1995; Katul and Chu, 1998). Similar power spectra are also observed in the case of normalized volume concentrations of different size classes of particles (Fig. 9D).

4. Discussion and conclusion

Large temporal variability in the hydrodynamic fields, particle concentration and size distribution was observed during the in situ experiment reported here. The hydrodynamic conditions, along with the high turbulence level encountered, provide favourable conditions for the re-suspension of particle. The present data set has shown that tidal current and waves have a significant role in the particle re-suspension and further water column turbidity. This is in good agreement with Velegrakis et al. (1999) who observed large scale particle re-suspension processes generated by the tidal current and coastal waves for the same region. During the current reversal, when the VACV is minimum, all the size parameters examined here indicate a modification in the particle size distribution. The proportions of small particles tend to increase compared to bigger ones (Fig. 7). Two processes can explain this pattern. First, hydrodynamic forcing is not sufficient to re-suspend large particulate assemblages from the bottom. Second, during the period of slack current, the differential settling of particles one over the other takes place inducing a washing of the water column, especially of heavy flocs. These observations agree with the study carried out by Van Leussen (1988). To a lesser extent, the occurrence of waves induces an increase of the suspended particulate matter concentration (i.e. $c_p(670)$), and especially of large particulate assemble (Fig. 8).

Turbulence has been extracted from the along shore and cross-shore components of the current velocity, which show periodic fluctuations in their magnitude. The power spectra of velocity components follow three different regimes depending on the scale. The first one, with typical inertial range, has a slope close to $-5/3$. The second one is characterized by a flatter slope of -0.6 with a transition scale of 1000 s. At last, the energy spectra at high frequencies (3–10 s) show a localized forcing attributed to waves forcing, similar to the previous results obtained in the same region (Schmitt et al., 2009). From $T=1000 \text{ s} \sim 17 \text{ min}$ there is a transition to a regime for which the power spectra are characterized by a lower slope value (close to -0.6). While there is still no theoretical explanation of such low slope value, theoretical studies have shown that the power spectra of velocities close to the sea floor may be characterized by a slope value of -1.0 (Panchev, 1971; Kader and Yaglom, 1984; Katul and Chu, 1998). The theoretical and experimental studies carried out by Perry et al. (1986), Katul et al. (1995), and Katul and Chu (1998) showed that the

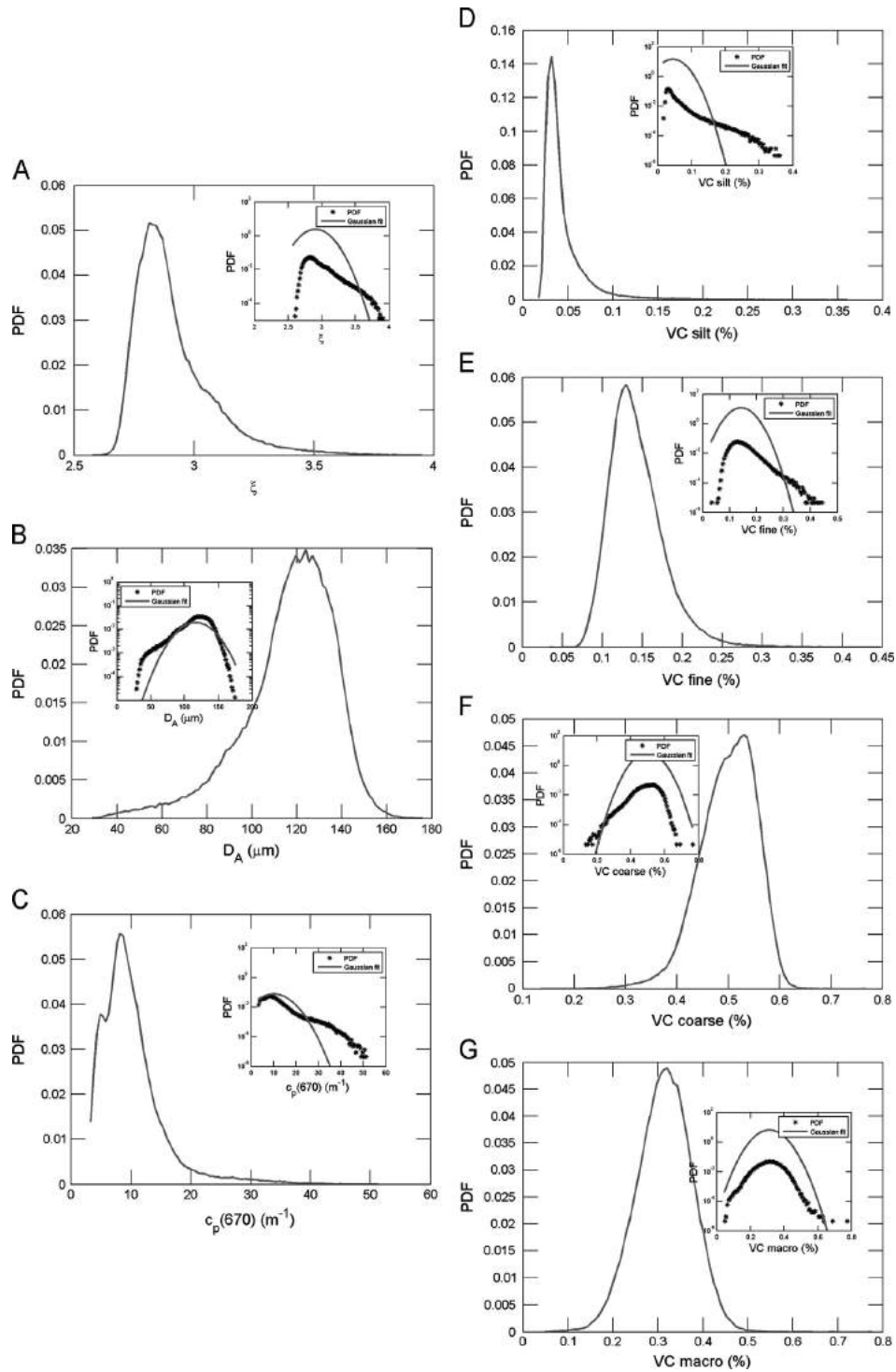


Fig. 6. The PDF of (A) ξ , (B) D_A , (C) $c_p(670)$ and normalized volume concentration of the different size classes of particles (VC silt (D), VC fine (E), VC coarse (F) and VC macro (G)), superposed to a Gaussian fit with the same mean and variance. The inset in all figures is a semi-log plot emphasizing extremes, showing that all PDFs are non-Gaussian.

turbulent boundary layer was characterized by a power-spectral slope of -1.0 at the low wave number values.

Thus, the power spectra of size parameters and $c_p(670)$ exhibit very similar turbulent scaling in the lower and higher frequency

regions compared to the velocity field. The Stokes number derived from the present measurements exhibits very low values ($\ll 1$), showing that the particles in the fluid motion behave like tracers and move along with the fluid.

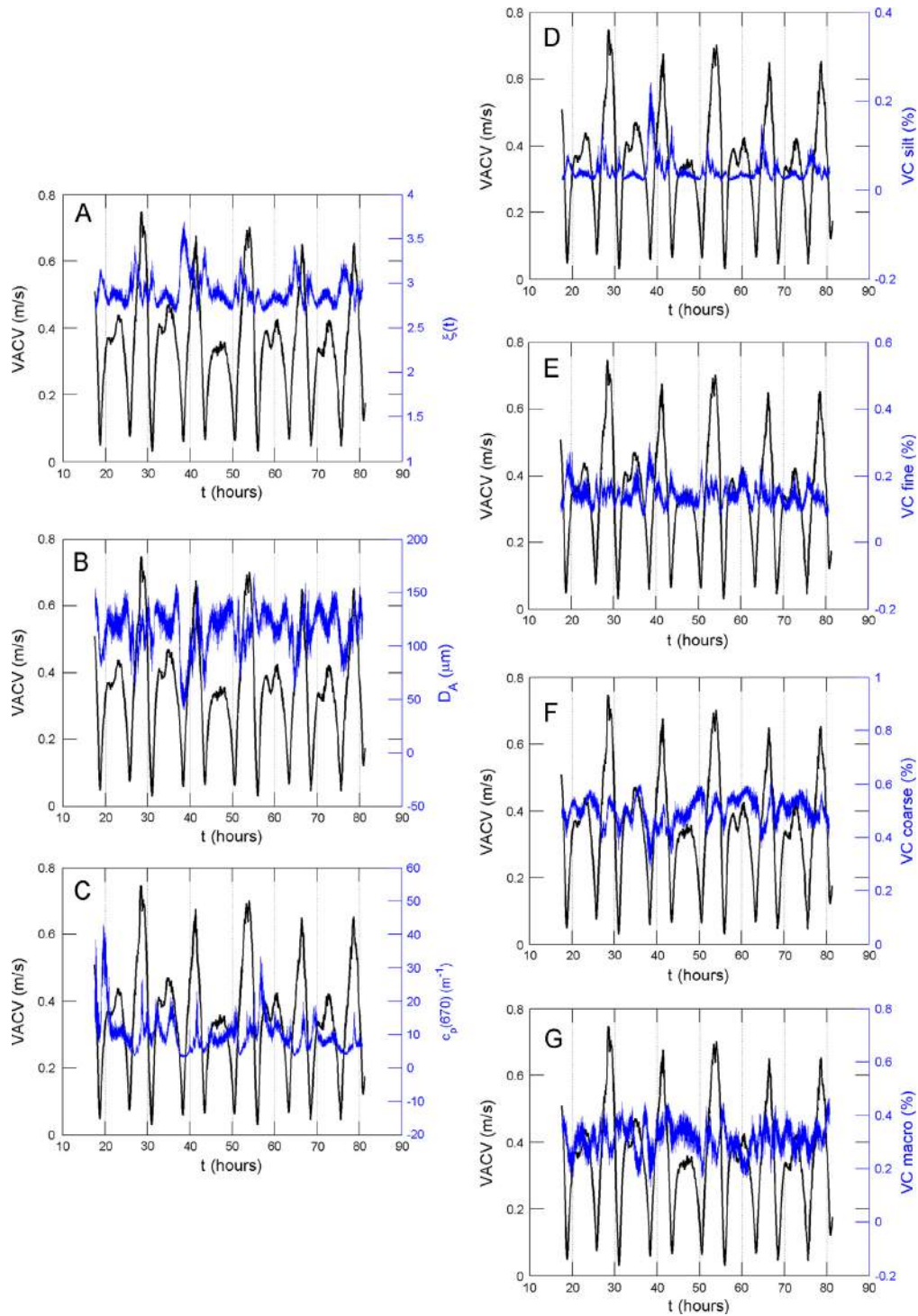


Fig. 7. Time series of (A) $\xi(t)$, (B) D_A , (C) $c_p(670)$ and the normalized volume concentration of different size classes of particles (VC silt (D), VC fine (E), VC coarse (F) and VC macro (G)) superposed to VACV data.

We found that turbulence has a great role in the dynamics of the particles in the present region. Low frequency variability of the particles is controlled by the turbulence ($\beta \approx -5/3$) and high frequency variability is controlled by the physical processes which

are related to the sea bottom interactions (wall turbulence), tidal currents and waves. A next step related to this work will be to analyze the turbulent intermittency scaling of these parameters using empirical mode decomposition (Huang et al., 2008). Other

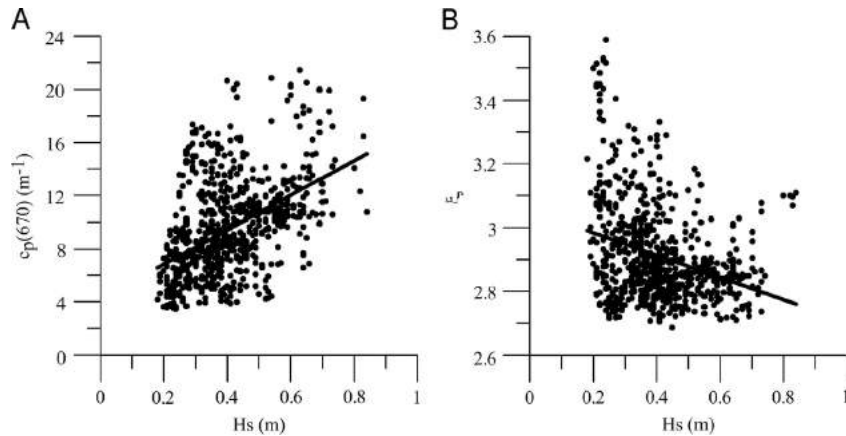


Fig. 8. (A) Scatter plot of $c_p(670)$ versus H_s and (B) ξ versus H_s .

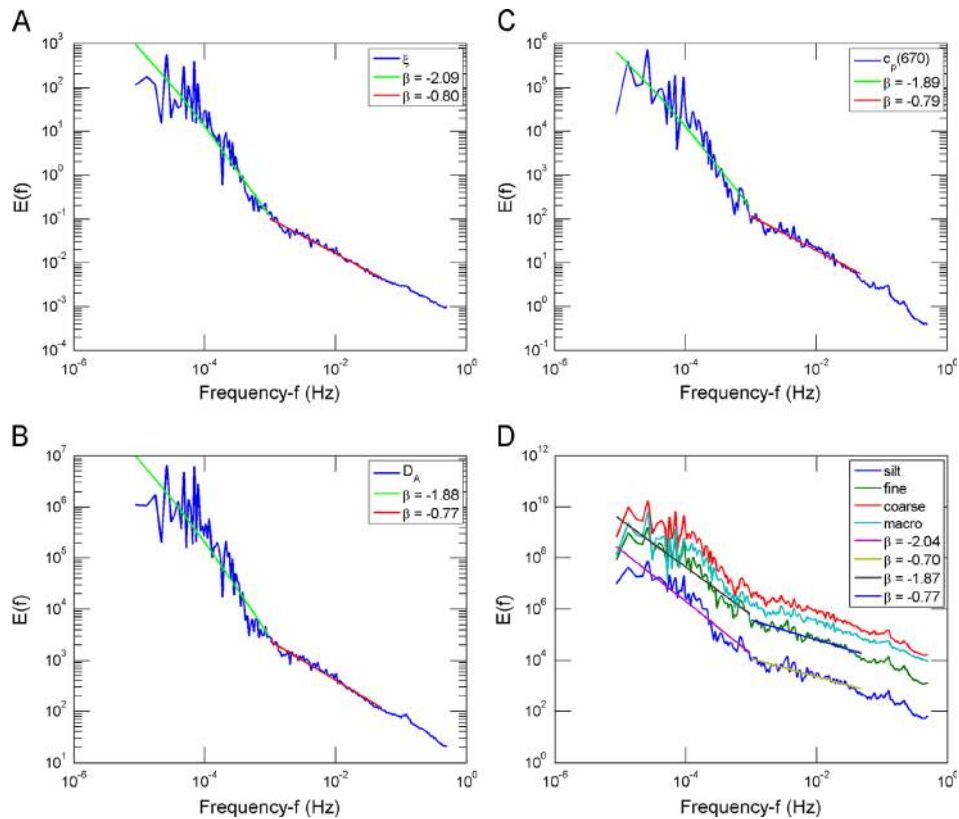


Fig. 9. Power spectra of ξ , D_A , $c_p(670)$ and the total volume concentrations of different size classes of particles showing different scale regimes as indicated by the different slope values for different frequency ranges.

measurement campaigns will be performed in coastal waters to compare with the present study and assess its possible universality.

Acknowledgements

Centre National d'Etudes Spatiales (CNES) and Centre National de la Recherche Scientifique (CNRS) are acknowledged for the funding of P.R. Renosh's Ph.D thesis. Météo France is acknowledged for providing wind data. The biogeochemical data were provided

by Service d'Observation en Milieu Littoral, INSU-CNRS, Wimereux. This study is performed in the frame of the COULCOT-2 project, funded by the CNES/TOSCA program.

References

Agrawal, Y.C., Pottsmith, H.C., 2000. Instruments for particle size and settling velocity observations in sediment transport. *Mar. Geol.* 168, 89–114.

- Berhane, I., Sternberg, R.W., Kineke, G.C., Milligan, T.G., Kranck, K., 1997. The variability of suspended aggregates on the Amazon Continental Shelf. *Cont. Shelf Res.* 17, 267–285.
- Boss, E., Pegau, W.S., Gardner, W.D., Zaneveld, J.R.V., Barnard, A.H., Twardowski, M.S., Dickey, T.D., 2001a. Spectral particulate attenuation and particle size distribution in the bottom boundary layer of a continental shelf. *J. Geophys. Res.* 106 (C5), 9509–9516.
- Boss, E., Twardowski, M.S., Herring, S., 2001b. Shape of the particulate beam attenuation spectrum and its inversion to obtain the shape of the particulate size distribution. *Appl. Opt.* 40, 4885–4893.
- Boss, E., Slade, W., Hill, P., 2009. Effect of particulate aggregation in aquatic environments on the beam attenuation and its utility as a proxy for particulate mass. *Opt. Express* 17, 9408–9420.
- Buonassissi, C.J., Dierssen, H.M., 2010. A regional comparison of particle size distributions and the power law approximation in oceanic and estuarine surface waters. *J. Geophys. Res.* 115, C10028.
- Burchard, H., Craig, P.D., Gemrich, J.R., van Haren, H., Mathieu, P.P., Meier, H.E., Wijesekera, H.W., 2008. Observational and numerical modeling methods for quantifying coastal ocean turbulence and mixing. *Prog. Oceanogr.* 76, 399–442.
- Chiappa-Carrera, X., Rioja-Nieto, R., Mascaro, M., 2006. Mass density assessment: comparison of three methods using *Oikopleura dioica* (Appendicularia) as a model system. *Caribbean J. Sci.* 42, 231–238.
- Desprez, M., 2000. Physical and biological impact of marine aggregate extraction along the French coast of the Eastern English Channel: short- and long-term post-dredging restoration. *ICES J. Mar. Sci.* 57, 1428–1438.
- Eisma, D., 1986. Flocculation and de-flocculation of suspended matter in estuaries. *Neth. J. Sea Res.* 20, 183–199.
- Fettweis, M., Francken, F., Pison, V., Van den Eynde, D., 2006. Suspended particulate matter dynamics and aggregate sizes in a high turbidity area. *Mar. Geol.* 235, 63–74.
- Filippa, L., Trento, A., Alvarez, A.M., 2012. Sauter mean diameter determination for the fine fraction of suspended sediments using a LISST-25X diffractometer. *Measurement* 45, 364–368.
- Fowler, S.W., Knauer, G.A., 1986. Role of large particles in the transport of elements and organic compounds through the oceanic water column. *Prog. Oceanogr.* 16, 147–194.
- Gerbi, G.P., Trowbridge, J.H., Terray, E.A., Plueddemann, A.J., Kukulka, T., 2009. Observations of turbulence in the ocean surface boundary layer: energetics and transport. *J. Phys. Oceanogr.* 39, 1077–1096.
- Hill, P.S., 1998. Controls on floc size in the sea. *Oceanography* 11, 13–18.
- Huang, Z.C., Lenain, L., Melville, W.K., Middleton, J.H., Reineman, B., Statom, N., McCabe, R.M., 2012. Dissipation of wave energy and turbulence in a shallow coral reef lagoon. *J. Geophys. Res.* 117, C03015.
- Huang, Y.X., Schmitt, F.G., Lu, Z.M., Liu, Y.L., 2008. An amplitude–frequency study of turbulent scaling intermittency using empirical mode decomposition and Hilbert spectral analysis. *EPL* 84, 40010.
- Jonasz, M., 1983. Particle-size distributions in the Baltic. *Tellus B* 35, 346–358.
- Jouan, A., Ouilon, S., Douillet, P., Lefebvre, J.P., Fernandez, J.M., Mari, X., Froidefond, J.M., 2008. Spatio-temporal variability in suspended particulate matter concentration and the role of aggregation on size distribution in a coral reef lagoon. *Mar. Geol.* 256, 36–48.
- Kader, B.A., Yaglom, A.M., 1984. Turbulent structure of an unstable atmospheric layer. In: Sagdeyev, R.Z. (Ed.), *Nonlinear and Turbulent Processes in Physics*, vol. 2. Harwood Academic, Boston, pp. 829–845.
- Katul, G., Chu, C.R., 1998. A Theoretical and experimental investigation of energy-containing scales in the dynamic sublayer of boundary-layer flows. *Boundary-Layer Meteorol.* 86, 279–312.
- Katul, G.G., Chu, C.R., Parlange, M.B., Albertson, J.D., Ortenburger, T.A., 1995. Low-wavenumber spectral characteristics of velocity and temperature in the atmospheric surface layer. *J. Geophys. Res.* 100 (D7), 14243–14255.
- Kestin, J., Khalifa, H.E., Correia, R.J., 1981. Tables of the dynamic and kinematic viscosity of aqueous NaCl solutions in the temperature range 20–150 °C and the pressure range 0.1–35 MPa. *Am. Chem. Soc. Amer. Inst. Phys. Natl. Bur. Stand.* 10, 71–87.
- Kitchen, J.C., Zaneveld, J.R.V., Pak, H., 1982. Effect of particle size distribution and chlorophyll content on beam attenuation spectra. *Appl. Opt.* 21, 3913–3918.
- Korotenko, K.A., Sentchev, A.V., Schmitt, F.G., 2012. Effect of variable winds on current structure and Reynolds stresses in a tidal flow: analysis of experimental data in the eastern English Channel. *Ocean Sci.* 8, 1025–1040.
- Kranck, K., Milligan, T.G., 1992. Characteristics of suspended particles at an 11 hour anchor station in San Francisco Bay, California. *J. Geophys. Res.* 97 (C7), 11373–11382.
- Lefebvre, J.P., Ouilon, S., Vinh, V.D., Arfi, R., Panché, J.Y., Mari, X., Torrétou, J.P., 2012. Seasonal variability of cohesive sediment aggregation in the Bach Dang-Cam Estuary, Haiphong (Vietnam). *Geo-Mar. Lett.* 32, 103–121.
- Lien, R.C., D'Asaro, E.A., 2006. Measurement of turbulent kinetic energy dissipation rate with a Lagrangian float. *J. Atmos. Ocean. Technol.* 23, 964–976.
- Loisel, H., Mériaux, X., Berthon, J.F., Poteau, A., 2007. Investigation of the optical backscattering to scattering ratio of marine particles in relation to their biogeochemical composition in the eastern English Channel and southern North Sea. *Limnol. Oceanogr.* 52, 739–752.
- Loisel, H., Nicolas, J.M., Sciandra, A., Stramski, D., Poteau, A., 2006. Spectral dependency of optical backscattering by marine particles from satellite remote sensing of the global ocean. *J. Geophys. Res.* 111, C09024.
- McCave, I.N., 1984. Size spectra and aggregation of suspended particles in the deep ocean. *Deep Sea Res. A. Oceanogr. Res. Pap.* 31, 329–352.
- Mikkelsen, O., Pejrup, M., 2001. The use of a LISST-100 laser particle sizer for in-situ estimates of floc size, density and settling velocity. *Geo-Mar. Lett.* 20, 187–195.
- Neukermans, G., Loisel, H., Mériaux, X., Astoreca, R., McKee, D., 2012a. In situ variability of mass-specific beam attenuation and backscattering of marine particles with respect to particle size, density, and composition. *Limnol. Oceanogr.* 57, 124–144.
- Neukermans, G., Ruddick, K., Loisel, H., Roose, P., 2012b. Optimization and quality control of suspended particulate matter concentration measurement using turbidity measurements. *Limnol. Oceanogr.: Methods* 10, 1011–1023.
- Panchev, S., 1971. *Random Functions and Turbulence*. Pergamon Press, Oxford p. 443.
- Perry, A.E., Henbest, S., Chong, M.S., 1986. A theoretical and experimental study of wall turbulence. *J. Fluid Mech.* 165, 163–199.
- Pope, S.B., 2000. *Turbulent Flows*. Cambridge University Press, Cambridge p. 770.
- Reynolds, R.A., Stramski, D., Wright, V.M., Wozniak, S.B., 2010. Measurements and characterization of particle size distributions in coastal waters. *J. Geophys. Res.* 115, C08024.
- Schmitt, F.G., Huang, Y., Lu, Z., Liu, Y., Fernandez, N., 2009. Analysis of velocity fluctuations and their intermittency properties in the surf zone using empirical mode decomposition. *J. Mar. Syst.* 77, 473–481.
- Schmitt, F.G., Seuront, L., 2008. Intermittent turbulence and copepod dynamics: increase in encounter rates through preferential concentration. *J. Mar. Syst.* 70, 263–272.
- Sethuraman, S., Meyers, R.E., Brown, R.M., 1978. A comparison of a Eulerian and a Lagrangian time scale for over-water atmospheric flows during stable conditions. *Boundary-Layer Meteorol.* 14, 557–565.
- Seuront, L., Schmitt, F.G., 2005. Multiscale statistical procedures for the exploration of biophysical couplings in intermittent turbulence. Part II. Applications. *Deep Sea Res. II* 52, 1325–1343.
- Sheldon, R.W., Prakash, A., Sutcliffe, W.H., 1972. The size distribution of particles in the ocean. *Limnol. Oceanogr.* 17, 327–340.
- Stramski, D., Boss, E., Bogucki, D., Voss, K.J., 2004. The role of seawater constituents in light backscattering in the ocean. *Prog. Oceanogr.* 61, 27–56.
- Thomson, J., Polagye, B., Durgesh, V., Richmond, M.C., 2012. Measurements of turbulence at two tidal energy sites in Puget Sound, WA. *IEEE J. Ocean. Eng.* 37, 363–374.
- Traykovski, P., Latter, R.J., Irish, J.D., 1999. A laboratory evaluation of the laser in situ scattering and transmissometry instrument using natural sediments. *Mar. Geol.* 159, 355–367.
- Twardowski, M.S., Boss, E., Macdonald, J.B., Pegau, W.S., Barnard, A.H., Zaneveld, J.R.V., 2001. A model for estimating bulk refractive index from the optical backscattering ratio and the implications for understanding particle composition in case I and case II waters. *J. Geophys. Res.: Oceans* 106 (C7), 14129–14142.
- Umlauf, L., Burchard, H., 2005. Second-order turbulence closure models for geophysical boundary layers. A review of recent work. *Cont. Shelf Res.* 25, 795–827.
- Van der Lee, E.M., Bowers, D.G., Kyte, E., 2009. Remote sensing of temporal and spatial patterns of suspended particle size in the Irish Sea in relation to the Kolmogorov microscale. *Cont. Shelf Res.* 29, 1213–1225.
- Van Leussen, W., 1988. Aggregation of particles, settling velocity of mud flocs a review. In: Dronkers, J., Van Leussen, W. (Eds.), *Physical Processes in Estuaries*. Springer, Berlin, Heidelberg, pp. 347–403.
- Vantropotte, V., Brunet, C., Mériaux, X., Lécuyer, E., Vellucci, V., Santer, R., 2007. Bio-optical properties of coastal waters in the Eastern English Channel. *Estuar. Coast. Shelf Sci.* 72, 201–212.
- Velegrakis, A.F., Michel, D., Collins, M.B., Lafite, R., Oikonomou, E.K., Dupont, J.P., Bishop, C., 1999. Sources, sinks and resuspension of suspended particulate matter in the eastern English Channel. *Cont. Shelf Res.* 19, 1933–1957.
- Wang, L.P., Wexler, A.S., Zhou, Y., 2000. Statistical mechanical description and modelling of turbulent collision of inertial particles. *J. Fluid Mech.* 415, 117–153.
- Wells, M.L., Goldberg, E.D., 1992. Marine submicron particles. *Mar. Chem.* 40, 5–18.
- Wolanski, E., Gibbs, R.J., 1995. Flocculation of suspended sediment in the Fly River estuary, Papua New Guinea. *J. Coast. Res.* 11, 754–762.
- Xu, H., Bodenschatz, E., 2008. Motion of inertial particles with size larger than Kolmogorov scale in turbulent flows. *Physica D* 237, 2095–2100.
- Yonghe, L., Kexin, Z., Wanchang, Z., Yuehong, S., Hongqin, P., Jinming, F., 2013. Multifactorial analysis of 1-min summer rainfall time series from a monsoonal watershed in eastern China. *Theor. Appl. Climatol.* 111 (1–2), 37–50.

RESEARCH ARTICLE

Scaling Analysis of Ocean Surface Turbulent Heterogeneities from Satellite Remote Sensing: Use of 2D Structure Functions

P. R. Renosh¹, Francois G. Schmitt^{2*}, Hubert Loisel³

1 University of Lille, Laboratory of Oceanology and Geosciences, UMR 8187 LOG CNRS/Univ Lille/ULCO, Wimereux, France, **2** CNRS, Laboratory of Oceanology and Geosciences, UMR 8187 LOG CNRS/Univ Lille/ULCO, Wimereux, France, **3** ULCO, Laboratory of Oceanology and Geosciences, UMR 8187 LOG CNRS/Univ Lille/ULCO, Wimereux, France

* francois.schmitt@log.cnrs.fr



OPEN ACCESS

Citation: Renosh PR, Schmitt FG, Loisel H (2015) Scaling Analysis of Ocean Surface Turbulent Heterogeneities from Satellite Remote Sensing: Use of 2D Structure Functions. PLoS ONE 10(5): e0126975. doi:10.1371/journal.pone.0126975

Academic Editor: Shang-Ping Xie, University of California San Diego, UNITED STATES

Received: January 16, 2015

Accepted: April 9, 2015

Published: May 27, 2015

Copyright: © 2015 Renosh et al. This is an open access article distributed under the terms of the [Creative Commons Attribution License](http://creativecommons.org/licenses/by/4.0/), which permits unrestricted use, distribution, and reproduction in any medium, provided the original author and source are credited.

Data Availability Statement: Synthetic data are generated using the algorithms described in the paper. The satellite image data are freely available through NASA's Ocean Color web site: <http://oceancolor.gsfc.nasa.gov/cms/>.

Funding: PRR received funding for his PhD thesis from Centre National de la Recherche Scientifique (<http://www.cnrs.fr>) and Centre National d'Etudes Spatiales (<http://www.cnes.fr>). The funders had no role in study design, data collection and analysis, decision to publish, or preparation of the manuscript.

Abstract

Satellite remote sensing observations allow the ocean surface to be sampled synoptically over large spatio-temporal scales. The images provided from visible and thermal infrared satellite observations are widely used in physical, biological, and ecological oceanography. The present work proposes a method to understand the multi-scaling properties of satellite products such as the Chlorophyll-a (Chl-a), and the Sea Surface Temperature (SST), rarely studied. The specific objectives of this study are to show how the small scale heterogeneities of satellite images can be characterised using tools borrowed from the fields of turbulence. For that purpose, we show how the structure function, which is classically used in the frame of scaling time series analysis, can be used also in 2D. The main advantage of this method is that it can be applied to process images which have missing data. Based on both simulated and real images, we demonstrate that coarse-graining (CG) of a gradient modulus transform of the original image does not provide correct scaling exponents. We show, using a fractional Brownian simulation in 2D, that the structure function (SF) can be used with randomly sampled couple of points, and verify that 1 million of couple of points provides enough statistics.

Introduction

One of the main features of geophysical fields is their huge fluctuations occurring over wide ranges of spatio-temporal scales. Here we consider the heterogeneities and intermittencies in 3D ocean turbulence. We use for this the framework of homogeneous and locally isotropic turbulence that originated in the work of Kolmogorov [1]. In this framework, energy is supplied, introduced or produced in the fluid at a relatively large scale, and is successively passed by interactions between eddies or their instabilities. This is performed through a spectrum of smaller and smaller eddies where inertial forces are dominant. After successive cascades steps, these eddies are conveyed to eddies of size comparable to the Kolmogorov length scale η , where

Competing Interests: The authors have declared that no competing interests exist.

viscosity plays a major role in transferring their kinetic energy into heat. This was formalised using the velocity fluctuations at scale l ; for time series it writes $\Delta V_l = |V(x+l) - V(x)|$ (V is the velocity); and for an isotropic 2D field it can be written $\Delta V_l = \|V(M) - V(N)\|$, where M and N are two points and $l = d(M,N)$:

$$\langle \Delta V_l \rangle = C\epsilon^{1/3}l^{1/3} \tag{1}$$

where $\langle \rangle$ means statistical average, C is a constant and ϵ represents the dissipation. This can also be written in the spectral space as follows [2]:

$$E_v(k) = C_1\epsilon^{2/3}k^{-5/3} \tag{2}$$

where C_1 is another constant, $E_v(k)$ is the Fourier spectral energy of velocity, and k is the wave number. This corresponds to a situation of scale invariance: velocity fluctuation have no characteristic scale with a power-law scale dependence. A similar scale dependence can be obtained for a passive scalar θ , with a power-law of the form [3, 4]:

$$E_\theta(k) = C_2\epsilon^{-1/3}\chi k^{-5/3} \tag{3}$$

where $E_\theta(k)$ is the Fourier spectral energy of passive scalar, C_2 is another constant, and χ is the dissipation of scalar variance (analogous to ϵ as dissipation of kinetic energy). It is now realized for a long time that turbulence produces intermittency, i.e. huge local fluctuations in energy and passive scalar fluxes ϵ and χ , and large variations in velocity and passive scalars [5]. Since the proposals of Obukhov and Kolmogorov in 1962 [6, 7] those quantities are characterized using local averages ϵ_l and χ_l at scale l :

$$\epsilon_l(x) = \frac{1}{a_l} \int_{B_l(x)} \epsilon(x') dx'; \quad \chi_l(x) = \frac{1}{a_l} \int_{B_l(x)} \chi(x') dx' \tag{4}$$

where $B_l(x)$ is a bowl of radius l centered in x and $a_l = \frac{4}{3}\pi l^3$ is its volume. This is called the “coarse graining” method (CG). This method is used to change the resolution of a positive, intermittent field. These local averages have scaling statistical properties of the form [5, 8]:

$$\langle \epsilon_l^q \rangle \approx l^{-K_\epsilon(q)}; \quad \langle \chi_l^q \rangle \approx l^{-K_\chi(q)} \tag{5}$$

where q is the statistical moment, $K_\epsilon(q)$ and $K_\chi(q)$ are scale invariant moment functions; these are also second Laplace characteristic function and as such are convex functions. They verify $K_\epsilon(1) = 0$ and $K_\chi(1) = 0$ by conservation of fluxes. Another approach to characterize intermittency and local fluctuations in the studied fields is to directly characterize the fluctuations of velocity and passive scalar using structure functions [5]:

$$\langle \Delta V_l^q \rangle \approx I_v^q(q); \quad \langle \Delta \theta_l^q \rangle \approx I_\theta^q(q) \tag{6}$$

where $\zeta_v(q)$ and $\zeta_\theta(q)$ are the scaling moment functions that characterize the fluctuations of velocity and passive scalar [9]. This is called the structure function method (SF). In the following, we focus on the passive scalar case, since we will consider Chlorophyll-a and Sea Surface Temperature, which are transported scalars and may be compared to passive scalars. The scaling moment functions for both CG and SF methods are derived using remotely sensed 2D Chl-a and SST images from MODIS Aqua.

In the next section we present the two-dimensional data analysis techniques using CG and SF methods. The next section deals with the test of these two methods for various 2D stochastic simulations. Finally as an illustration, the methods are applied to two real images (Chl-a and SST) measured from MODIS Aqua. An often assumed link between scaling exponents

estimated using CG and SF methods is tested on these images and shown to be wrong except for low order moments.

Methods

Data analysis techniques

Multifractal methods have been widely applied to time series, but there are not many studies applying such approaches to 2D data, especially in the field of ocean color remote sensing. Some of them considered a local gradient transform in order to identify currents and oil spills [10–13]. Other studies transformed satellite Chl-a or SST image data into a positive singular field using a gradient modulus transform [14, 15]. Below we will consider this method and compare it to the structure functions method.

Coarse Graining (CG) method. One method which has been applied in several studies is to produce a positive field, called “multifractal random measure”, from a non stationary field such as Temperature and Chlorophyll-a [10, 11, 14]. For that purpose, the gradient modulus of the field θ is calculated as follows:

$$\varphi = \sqrt{\left(\frac{\partial\theta}{\partial x}\right)^2 + \left(\frac{\partial\theta}{\partial y}\right)^2} \tag{7}$$

using at the smallest resolution the discrete transformation:

$$\varphi_{ij}^2 = \left(\frac{\theta_{i+1j} - \theta_{ij}}{a}\right)^2 + \left(\frac{\theta_{ij+1} - \theta_{ij}}{a}\right)^2 \tag{8}$$

where a is a constant corresponding to grid size and θ_{ij} is the value of the field θ at pixel position (i,j) . This relates a fluctuating field θ (a passive scalar) to an intermittent and passive field φ . The latter is taken as the multifractal measure at the best resolution l_0 . The field φ_l at larger scales $l \geq l_0$ is then estimated by coarse graining:

$$\varphi_l(x, y) = \frac{1}{a_l} \int_{B_l(x,y)} \varphi(x_0, y_0) dx_0 dy_0 \tag{9}$$

This is usually done by taking an image of size $2^n \times 2^n$, and degrading the resolution in p steps until scale $l = 2^p l_0$ ($2 \leq p \leq n$). At each step, one goes from resolution l to $2l$ by taking a local average in a square of 4 values and giving to the larger scale cell this average value. The resolution is degraded recursively. As given by Eq (5), the scale-dependant field has scaling statistics with a scale invariant moment function $K(q)$, $\langle \varphi_l^q \rangle \approx l^{-K(q)}$. Experimentally, the function $K(q)$ is estimated as the regression of $\log\langle \varphi_l^q \rangle$ versus $\log(l)$, for each value of q (in practice $q \geq 0$ varies from 0 to 5).

Structure Function (SF) method. In fact the application of the gradient modulus method is not necessary to consider the intermittency properties of a 2D field, θ , such as temperature and Chlorophyll-a. Let us consider two points M and N belonging to the field, and their distance $d(M,N)$. The moments $\langle |\theta(M) - \theta(N)|^q \rangle$ versus $d(M,N)$ are considered. This can be estimated directly by taking all couple of points (M,N) in the 2D domain and discretizing the distance $d(M,N)$ in small intervals. A log-log regression of $\langle |\theta(M) - \theta(N)|^q \rangle$ versus $d(M,N)$ gives the exponent ζ_θ , following the law

$$\langle |\theta(M) - \theta(N)|^q \rangle \approx d(M, N)^{\zeta_\theta(q)} \tag{10}$$

where “ \approx ” means scaling relation. In practice, for an image of size $n \times n$, M is chosen among

$n \times n$ values and the same for N , which corresponds to consider n^4 couple of points. If $n = 10^3$, this will provide 10^{12} couple of points, which is usually much too computationally expensive, even for modern computers. It is then necessary to use a numerical method to optimize the computations. M and N are here randomly taken. The N_p number of couple of points ($N_p \ll n^4$) are taken small enough for a computational realistic time (less than half an hour for each image for a powerful personal computer), and large enough to have converged statistics. The exponent function $\zeta_\beta(q)$ is directly estimated from such images using the randomly selected couple of points, N_p .

Tests on 2D stochastic simulation

CG Method. In the following, the coarse graining method is tested in 2D with two classical cascade models: the β model and the Log-normal model.

β model 2D cascade. This is one of the first and simplest cascade models to describe the intermittency in turbulence, also called as the black and white model [16]. This model was introduced under this name by Frisch et al. [16], but it has already been discussed by Mandelbrot [17] using a “pulses into pulses” approach originally proposed by Novikov and Stewart [18]. The β -model is a discrete multiplicative model. The multiplicative cascade yields a small scale field $\epsilon(x)$ at the smallest scale, as the product

$$\epsilon(x) = \prod_{i=1}^n W_{i,x} \tag{11}$$

of n independent realisations $W_{i,x}$ of a random variable W (here x is the position and i is the level in the cascade).

The β -model is a binomial model with only 2 possibilities for the value of W ($0 < \beta < 1$):

$$\begin{cases} \Pr(W = 0) = 1 - \beta \\ \Pr\left(W = \frac{1}{\beta}\right) = \beta \end{cases} \tag{12}$$

We can verify that such field is normalized:

$$\langle W \rangle = \sum W_i \Pr(W_i) = \left(\frac{1}{\beta}\right)\beta = 1 \tag{13}$$

The statistical moments of the random variable W are:

$$\langle W^q \rangle = \int W^q \Pr(W)dw = \sum_{i=1}^n W_i^q \Pr(W_i) = \beta^{1-q} \tag{14}$$

The cascade field ϵ is built by multiplying n independent realisations of W . Hence its moments write:

$$\langle \epsilon^q \rangle = \left\langle \left(\prod_{i=1}^n W_{i,x} \right)^q \right\rangle = \prod_{i=1}^n \langle (W_{i,x})^q \rangle = \langle W^q \rangle^n = \beta^{(1-q)n} \tag{15}$$

Since each cascade step is associated with a scale ratio of 2 from one scale to the next, we have $\lambda = 2^n$, where λ is the total scale ratio. Hence we have the scaling relation for moments $\langle \epsilon^q \rangle = \lambda^{K(q)}$ with $K(q) = c(q - 1)$, where $c = -\log_2 \beta$ is the co-dimension. Which give rise to Eq (5) by coarse-graining. The scaling moment function $K(q)$ is linear, and corresponds to a

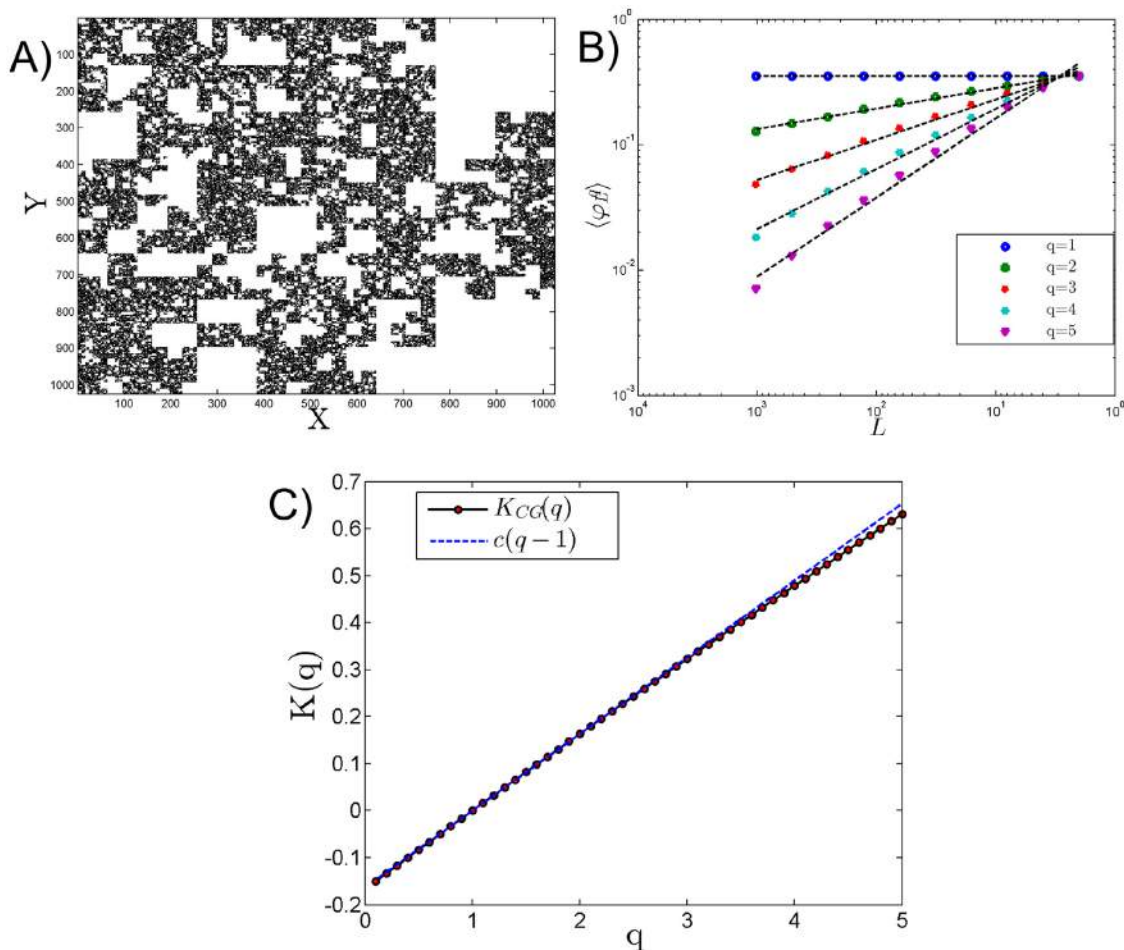


Fig 1. A) simulation of a 2D β model with $n = 2^{10}$ and $\beta = 0.9$ (ϵ is displayed), B) coarse grained moments for $q = 1$ to 5 and C) moment scaling function $K(q)$, where the experimental estimation is shown in dots compared to the theoretical prediction as a dotted line, with $c = 0.15$.

doi:10.1371/journal.pone.0126975.g001

mono-fractal process. A realisation with $n = 10$ and $\beta = 0.9$ is shown in Fig 1A. Fig 1B shows the CG method applied to this field and Fig 1C, the scaling moment function.

Log-normal 2D cascade. The cascade generation for the log-normal model is similar to the β model cascade. The only difference is that here we use $W = e^g$, where g is Gaussian. As above, the scaling moment function for the dissipation is $\langle \epsilon^q \rangle = \lambda^{K(q)}$, where $K(q) = \log_2 \langle W^q \rangle$. To understand the scaling moment function, some basic characteristics of a log-normal random variable are now provided. The moment generating function of a log-normal series (X) of mean m and standard deviation σ (of $\log X$) is $\langle X^q \rangle = \exp(qm + q^2 \sigma^2 / 2)$. This can be applied to the moment generating function for dissipation:

$$K(q) = \log_2 \langle W^q \rangle = \frac{qm + q^2 \sigma^2 / 2}{\log 2} \tag{16}$$

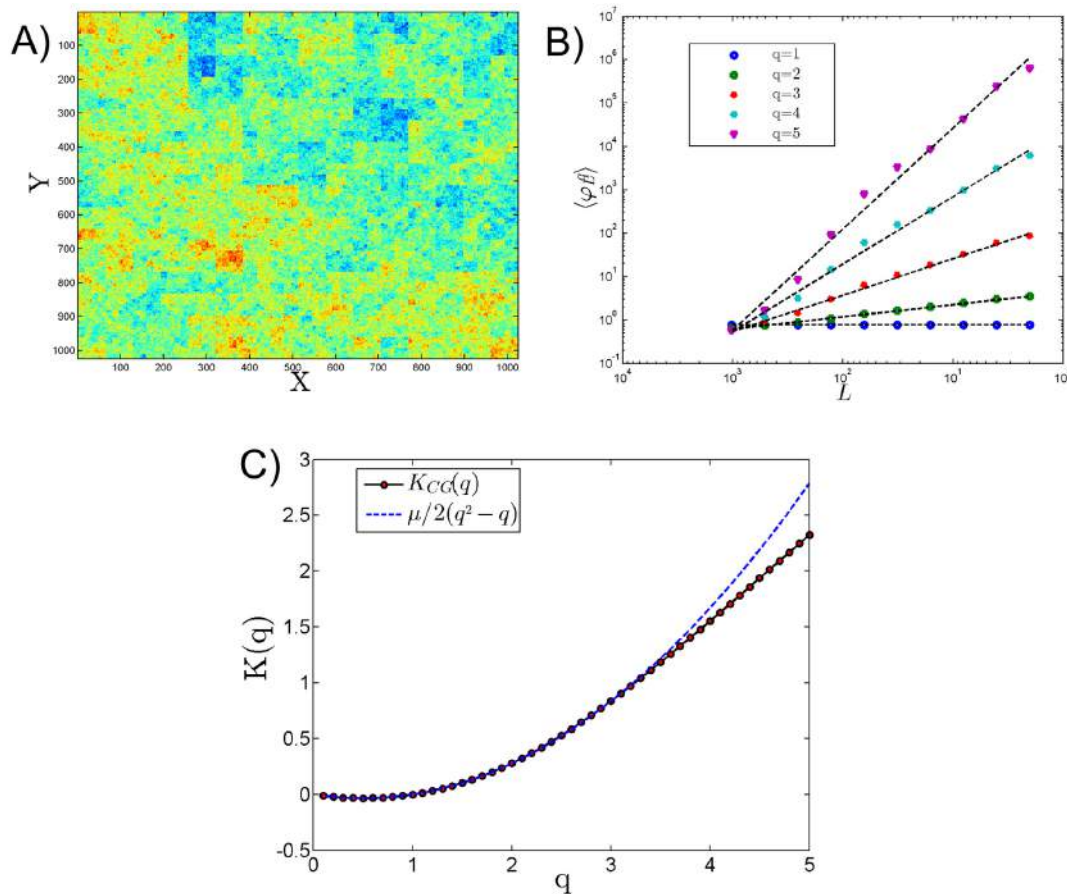


Fig 2. A) Simulation of a 2D log-normal image using a discrete cascade model with $\mu = 0.3$, B) coarse grained moments from $q = 1$ to 5 and C) the corresponding moment scaling function experimentally estimate as dots and theoretical value $K(q) = \frac{\mu}{2}(q^2 - q)$ as a dotted line.

doi:10.1371/journal.pone.0126975.g002

Since we want to have $K(q) = \frac{\mu}{2}(q^2 - q)$, where $\mu = K(2)$ is the intermittency parameter, the adequate choice for the discrete log-normal cascade is to take for g , a Gaussian random variable of mean $m = \frac{-\mu \log 2}{2}$ and variance $\sigma^2 = \mu \log 2$.

A realisation of discrete log-normal cascade has been produced with $n = 10$ and $\mu = 0.3$ (Fig 2A). The coarse-gaining method is applied to this image in Fig 2B, and the resulting $K(q)$ function provided by Eq (16) in Fig 2C. The agreement is excellent until moment of order 3; this is a statistical bound of the estimation of moments which is theoretically predicted [19].

SF Method. The proposed structure function method has been validated with a 2D fractional Brownian field with H value varying from 0.1 to 0.9 with an increment of 0.1.

Fractional Brownian motion (fBm). A generalization of Brownian motion, was introduced by Kolmogorov in 1940 [20]. This has been extensively studied by Mandelbrot and his co-workers in 1960s [21] and since then, it is considered as a classical scaling stochastic process for time series analysis. For time series, a *fBm*, denoted by $B_H(t)$, is a zero-mean Gaussian

process with stationary increments characterized by the self-similarity parameter H , also known as the Hurst exponent. It possesses the following rescaling property:

$$B_H(\Lambda t) \stackrel{d}{=} \Lambda^H B_H(t), \quad \forall \Lambda > 0 \tag{17}$$

Where $\stackrel{d}{=}$ means equality of probability distributions. It leads to linear moment functions using structure functions Eq (6): $\zeta(q) = qH$. This can be done also in 2D. The bi-dimensional isotropic fractional Brownian motion with Hurst parameter H is a centered Gaussian field B_H with an autocorrelation function [22]:

$$\langle B(\vec{x})B(\vec{y}) \rangle \propto \|\vec{x}\|^{2H} + \|\vec{y}\|^{2H} - \|\vec{x} - \vec{y}\|^{2H}; \quad 0 < H < 1 \tag{18}$$

where $\vec{x}, \vec{y} \in R^2$ and $\|\cdot\|$ is the usual Euclidean norm.

In the present study we simulated 2D fractional Brownian field for various H values ($H = 0.1, 0.2, \dots, 0.9$) using an algorithm and code described in recent works [23, 24] (Fig 3A). These images are analysed using 2D SF method for various randomly selected data ($N_p = 0.1$ million, 0.5 million, 1.0 million, 5.0 million and 10.0 million). The scaling moment function has been derived for each image for different iteration number. H has been derived from the moment scaling function using $H = \zeta(1)$. Since satellite images often have missing values due to cloud coverage, we have also applied the SF approach to irregular images, where some part of the image have been removed. Fig 3A shows some simulations for various values of H and Fig 3B compares H estimations for full images and for images with some rectangles removed. This is tested for various values of N_p . We see that for $N_p = 10^6$ the method works very well (with an error of 3.88%) even when there are missing values, and the estimated exponents are very precise. In the following we thus choose $N_p = 10^6$, since it is computationally reasonable and provide converged statistics for scaling exponents. To estimate the standard deviation of the estimated values with respect to full image and percentage of missing values will need a systematic study, which will be the topic of a future work.

Comparison of the CG and SF methods

Two recent studies have proposed to analyse the scaling of satellite images by applying first a gradient modulus approach [12, 14], in order to have a positive intermittent field, and then applying the CG method. The $K_{CG}(q)$ exponent function is retrieved and the authors assume that:

$$K_{CG}(q) = qH - \zeta(q) \tag{19}$$

where $\zeta(q)$ is the scaling exponent characterizing the Chl-a or SST fluctuations. Based on one simulated image, and two real satellite images we compare this latter approach with the one proposed here. We extract $K_{CG}(q)$ as described above, and we directly estimate $\zeta(q)$ using the 2D structure functions. We then compute $K_{CG}(q) + \zeta(q)$: if Eq 19 is correct this should be linear ($= qH = q\zeta(1)$).

Multifractal field from cascade and fractional integration

We first test Eq 19 using a multifractal simulation done by performing a cascade and then a fractional integration [25]. As done in Lovejoy et al. [15], we simulate a 2D log-normal multifractal image with $H = 0.35$ and $\mu = 0.1$ [26] (Fig 4A). The SF is directly applied to the image itself and the CG is applied to its gradient modulus. The scaling moment spectrum is derived for each method (Fig 4B and 4C). The moment scaling functions for both SF and CG are derived for various moments from 0.1 to 5 with an interval of 0.1. $K_{CG}(q)$ is non-linear and $\zeta(q)$ is

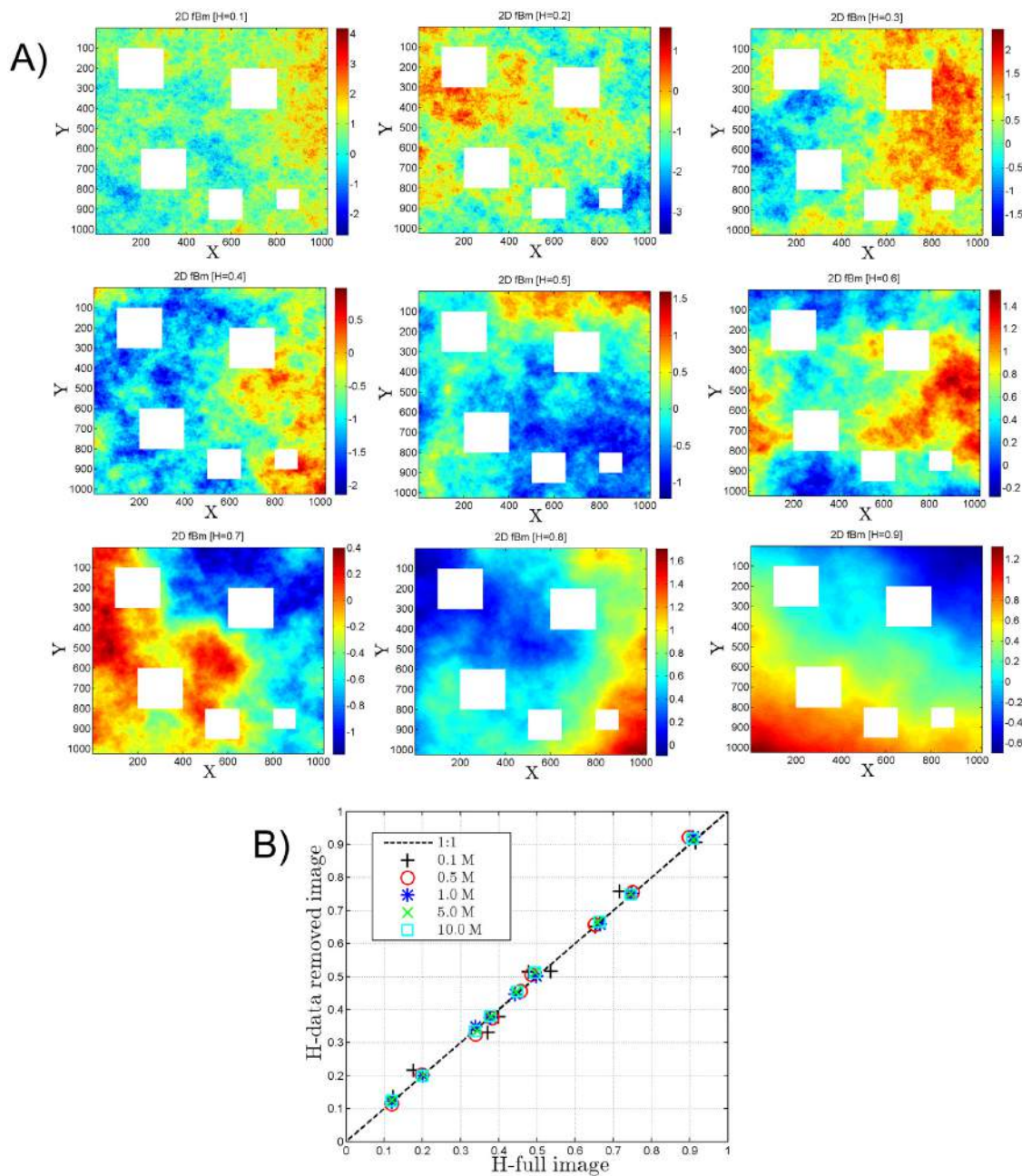


Fig 3. A) Simulation of 2D fractional Brownian motion for various Hurst exponents ($H = 0.1, 0.2, \dots, 0.9$). The white rectangles are the space where the data have been removed to test this method for deriving H using spatial Structure function method. The 2D structure function was applied to each full image and also to the same image with white rectangles removed, in order to show that this scaling method can be applied to irregular images. **B) For each image, comparison of the H value estimated using the structure function for the full image and for images with missing values.**

doi:10.1371/journal.pone.0126975.g003

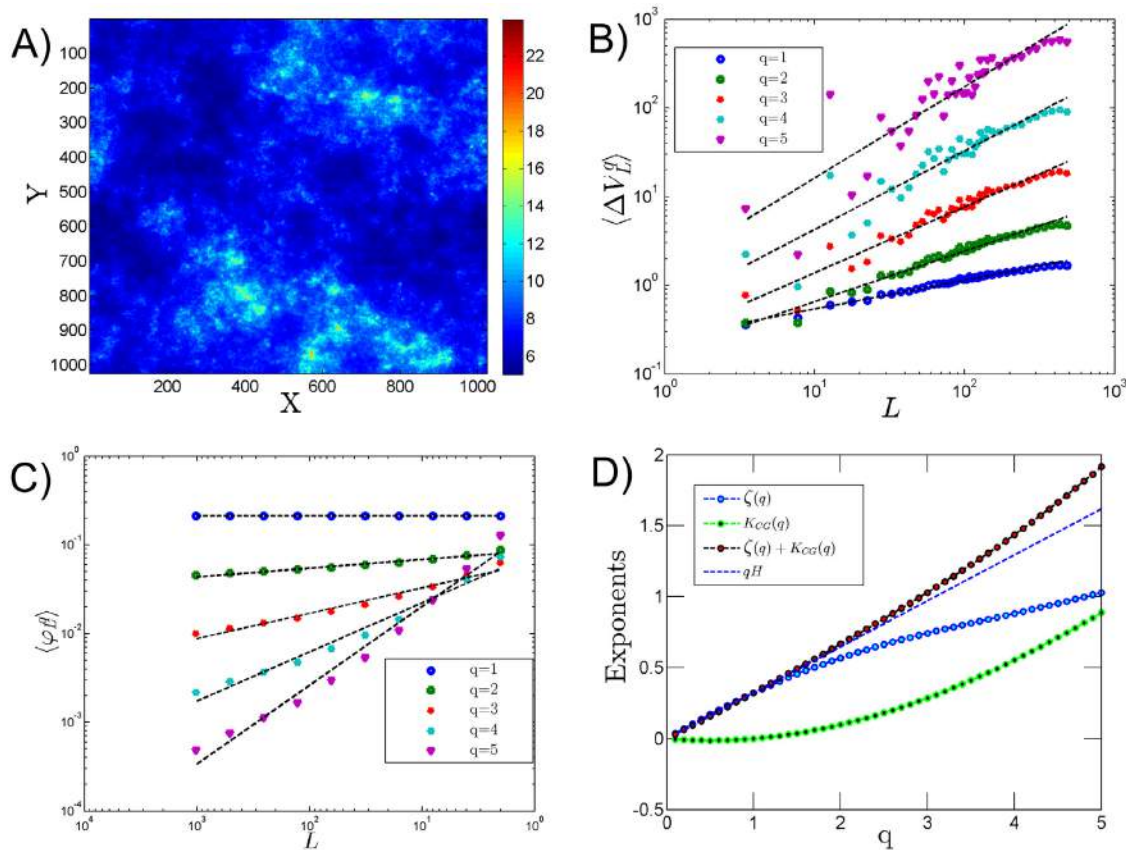


Fig 4. A) Simulation of a 2D log-normal multifractal image with $H = 0.35$ and $\mu = 0.1$. B) Scaling of the SF; C) Scaling analysis when gradient modulus is applied on the image shown in A; D) representation of different exponents.

doi:10.1371/journal.pone.0126975.g004

almost linear and Eq 19 is not verified: $K_{CG}(q) + \zeta(q)$ is close to qH for $q \leq 2$ but for larger moments it is no more the case (Fig 4D).

Scaling analysis on a Chl-a image of MODIS aqua

The standard MODIS Chl-a imagery available from the Goddard Space Flight Centre is produced via OC3M algorithm [27] has been used for the present study. The OC3M algorithm is a fourth order polynomial equation and applies the maximum ratio of the remote sensing reflectance at 443 nm (blue) to 550 nm (green) or 490 nm (blue) to 550 nm (green). These proposed methods have been applied to real images of Chl-a from the Mauritanian coast sampled on 11-March-2003 (Fig 5A). A cloud free image (512×512 pixels) has been extracted for the analysis (square region marked in Fig 5A). The gradient modulus of Chl-a (Δ Chl-a) has been derived from the Chl-a image (Fig 5B). This gradient modulus generates a positive field, the CG method is adopted for analysing this positive field. The SF method has been applied directly to

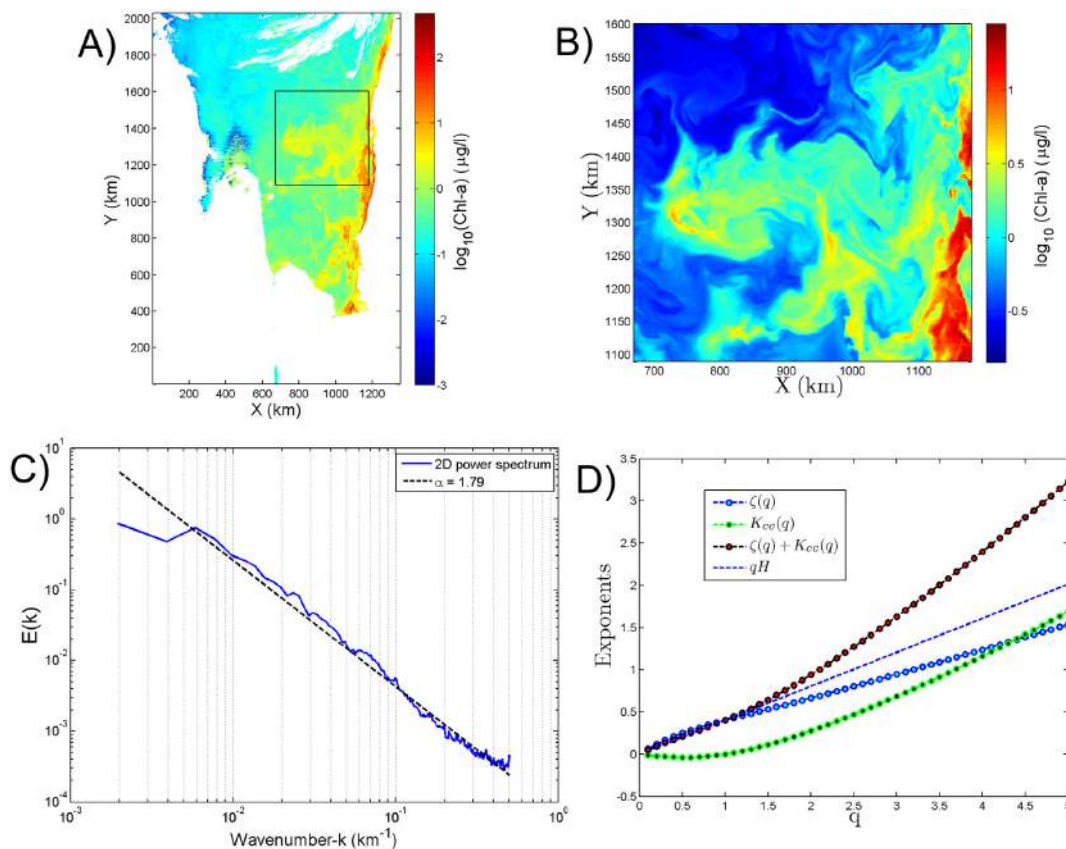


Fig 5. A) Chl-a image from MODIS Aqua from the Mauritanian coast sampled on 11 March 2003; the square indicates the 512 × 512 pixel of cloud free image chosen for the analysis of Chl-a. B) Gradient modulus estimated for the latter square image. C) Power-spectrum of the Chl-a image showing a scaling exponent $\alpha = 1.79$. D) Moment scaling function for the square image, using the CG and SF methods. Eq 19 is tested and found not to be correct for $q \geq 1.7$.

doi:10.1371/journal.pone.0126975.g005

the Chl-a image. We have chosen the random picking method tested in section 2 with $N_p = 10^6$ couple of points. Here also we could observe the power-law behaviour of the SF. The radially summed power-spectra of the Chl-a image has been derived for the cloud free part of the image (512 × 512 pixel). The derived spectral exponent α for the radially summed image is 1.79 (Fig 5C). The constants derived for the Chl-a image are shown in Table 1. The $\zeta(q)$ derived for the Chl-a image also follows a non-linear convex curve showing intermittency in the spatial distribution of Chl-a (Fig 5C). Fig 5D shows that Eq 19 is not verified for $q \geq 1.7$.

Table 1. The exponents (H and α) derived for Chl-a and SST images for Mauritanian region. The Hurst exponent H derived through SF ($H = \zeta(1)$).

Region	Sampling date	Parameter	H	α
Mauritanian Coast	11-Mar-2003	Chl-a	0.37	1.79
Mauritanian Coast	11-Mar-2003	SST	0.41	1.80

doi:10.1371/journal.pone.0126975.t001

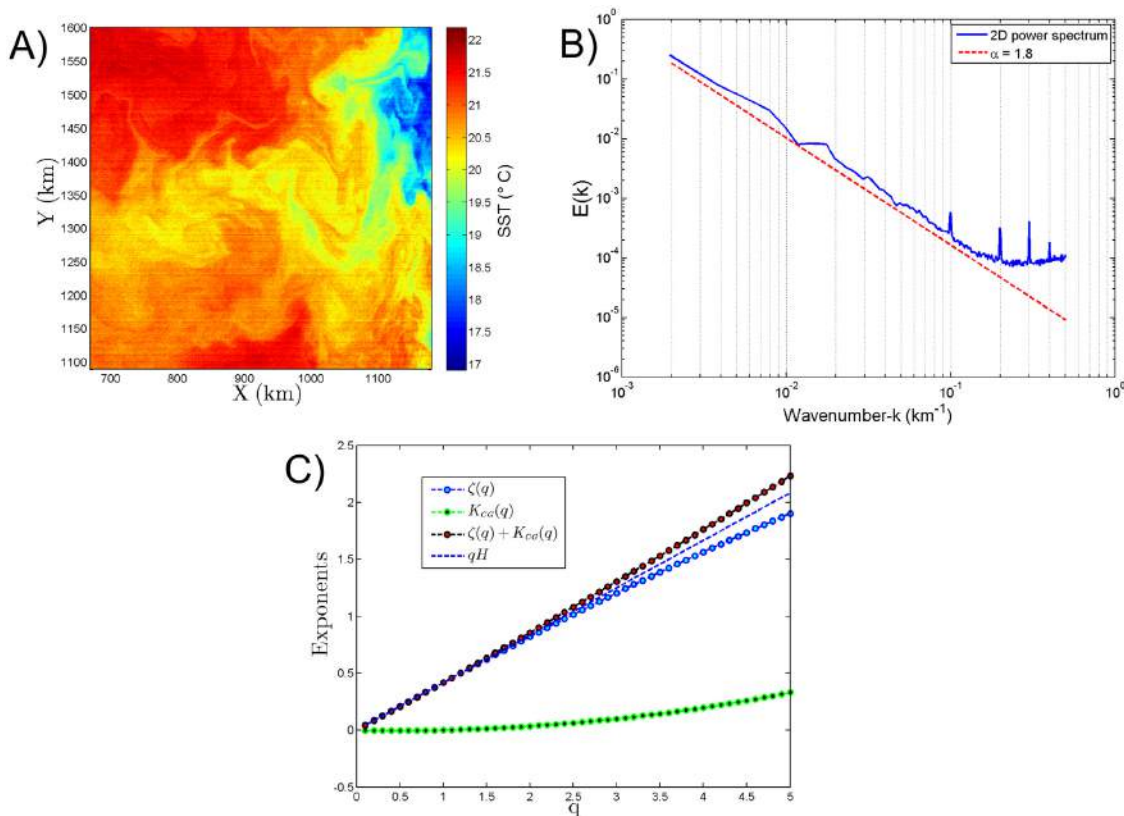


Fig 6. A) SST image from MODIS from the Mauritanian coast sampled on 11 March 2003. B) 2D power-spectrum of the image showing a scaling exponent $\alpha = 1.80$. C) Moment scaling function, using the CG and SF method. Eq 19 is approximately valid, coming from the fact the $K_{GG}(q)$ is very small, corresponding to a very regular field.

doi:10.1371/journal.pone.0126975.g006

Scaling analysis of MODIS SST

These proposed methods (CG and SF) have also been applied to an image of SST sampled simultaneously with Chl-a from the Mauritanian coast on 11-March-2003. A cloud free image (512×512 pixels) has been extracted for the analysis (Fig 6A). The 2D power-spectra of the SST image has been derived. It follows a power-law behaviour with a spectral slope $\alpha = 1.8$ (Fig 6B) with some noise observed at smaller scales. Similarly to Chl-a, the gradient modulus of the SST has been derived and CG method applied. Here also the scaling moment function derived for the SST follows a non-linear concave curve showing the spatial intermittent characteristics of SST (Fig 6C). However its small value shows that this field is not very intermittent. The proposed SF method has been directly applied to the SST image. The moment scaling function of SST image derived follows a non-linear convex shape, showing the intermittent characteristics of the spatial distribution of the SST (Fig 6C). The H derived through the SF method is $H = 0.41$ ($H = \zeta(1)$). The constants derived for the SST image are shown in Table 1. Here we can also see that these two exponents fall away from the typical linear qH line for $q \geq 1.5$.

The values of the spectral exponent α derived here for the Chl-a and SST satellite images are in good agreement with the range of α values derived from in situ measurements of fluorescence (as a proxy of Chl-a) and temperature [28]. The estimated values of the scaling parameter H for Chl-a and SST show also very good agreement with previous studies [28–30]. Concerning the μ value, let us note that this intermittency parameter could be more sensitive to the local conditions. It can be estimated using structure functions as $\mu = K_{CG}(2) = 2\zeta(1) - \zeta(2)$. For Chl-a and SST we obtain here 0.13 and 0.012 respectively. For Chl-a, this value is larger than the one estimated from Eulerian time series, ranging from 0.065 to 0.074 [28, 31]. On the other hand, the SST field considered here seems smoother than found in other studies since $\mu = K_{CG}(2)$ in other published studies range from 0.05 to 0.19 [28–32].

Discussion: the role of signs

We have considered here the scaling exponent $K_{CG}(q)$ obtained by coarse-graining a positive field, and the exponent $\zeta(q)$ obtained directly through structure functions. We found, using a simulation and two satellite images, that Eq 19 is not verified, an equation assuming that the gradient modulus applied to a non-stationary field retrieves the basic scaling information. In fact, such relation is not verified because the local sign contains information; when performing a gradient modulus, the sign information is lost. We check this hypothesis here by considering a fBm simulation with $H = 0.6$. We estimated a sign information from the 2D fBm simulation as follows. We computed the two components of the gradient (in the x and y directions) and took the sum of the two terms. If this sum is positive, we choose to consider a sign information as 1 and 0 if the sum is negative. This way the sign information of the gradient is transformed into a matrix containing only 0 and 1 values. The figure obtained (Fig 7A) does not seem to be a noise; to check this we consider its scaling by using a coarse-graining (Fig 7B). We obtain a scaling law of the form $\mu(q - 1)$ with $\mu = 0.09$. This is similar with β -model and shows that the sign information has a structure; such structure is lost when performing a modulus and we can assume the same property for real images: such analysis is left for future studies.

Conclusion

We have considered here several methods to estimate the scaling properties of ocean colour images, in relation with turbulence. We have first recalled data analysis methods, mainly coarse graining after taking the gradient modulus, and 2D structure functions. Similar to many atmospheric processes, oceanic processes are also governed by complex turbulent processes. These processes cannot be fully characterised by a single scaling exponent such as α . Additional multifractal parameters are required to fully characterise these multi-scaling properties. Even though the CG method is successful in many applications, it suffers from several approximations that can add some uncertainties in the estimation of multifractal parameters. In this context, we highlighted here an alternative tool such as 2D structure function to overcome the approximations related to the CG method. This method of 2D structure functions has rarely been documented and studied for geophysical image analysis due to computational complexity constraints. We have obtained several results in this framework:

- Since the structure function approach needs to consider n^4 couple of points, where n is the linear size (in pixels) of an image, it is too much computer time consuming. We shown using fBm simulations that taking 10^6 couple of points randomly is enough for an adequate estimation of the structure function scaling exponents. We showed also that this method works for images with missing data, an important aspect since many real images have missing pixels due to cloud coverage.

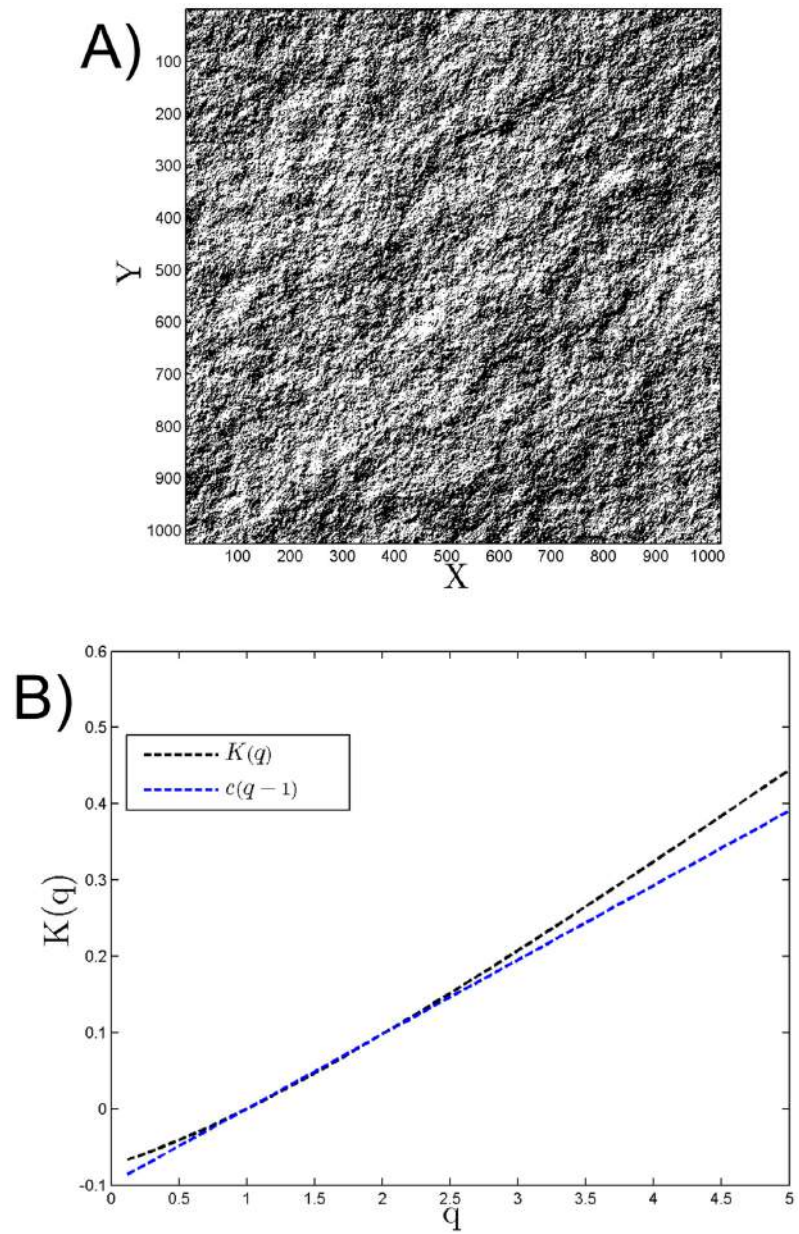


Fig 7. The gradient sign information of the 2D fBm derived for $H = 0.6$ in A) and its moment scaling function in B).

doi:10.1371/journal.pone.0126975.g007

- We compared the Coarse graining scaling exponent $K_{CG}(q)$ from the gradient modulus, to $qH - \zeta(q)$, and found that such relation is not verified, indicating that the gradient modulus loses information (the signs have a scaling structure) and hence this method cannot be safely used instead of SF.
- We considered two images from MODIS Aqua (Chl-a and SST) and showed on these examples that scaling approach using SF and $N_p = 10^6$ couple of points is adequate; we also showed that the spectral exponent for these examples is close to 5/3 characteristic of passive scalar fully developed turbulence. Such 2D multifractal property of Chl-a and SST is a 2D generalistic of previous results obtained for time series [28, 31, 32].
- Since Chl-a and SST are not conservative, Chl-a can be influenced by biological activities and SST can be influenced by the surface heat flux. These biological and physical processes can have influence on the scaling exponents. These two parameters may show different scaling properties for in situ measurements as shown in other studies [28, 31]. The spectral exponent α derived for Chl-a and SST satellite images are in good agreement with the in situ measurements of fluorescence by Chl-a and temperature [28, 31, 32].
- The present paper compared CG and SF methods on a real image. We have considered here the question of missing data on a synthetic fBm field; the same has been done on real images and it was confirmed that the method is also providing the same scaling exponents for real images (not shown here).

Let us note that this method can also be applied to the 2D velocity field obtained from altimeter data, since the velocity can also be intermittent and scaling. As a perspective, in a following work, we will use the SF method with $N_p = 10^6$ couple of points, to estimate the $\zeta(q)$ function, fit with the data using a log-normal approximation with 2 parameters ($H = \zeta(1)$ and $\mu = 2H - \zeta(2)$) and consider the values of these parameters in several locations (open ocean, coastal waters, upwelling region, etc.). For that purpose, several images collected over different oceanic regions characterised by contrasted biological and physical environment will have to be studied.

Author Contributions

Conceived and designed the experiments: FGS. Performed the experiments: PRR. Analyzed the data: FGS PRR HL. Contributed reagents/materials/analysis tools: FGS PRR HL. Wrote the paper: FGS PRR HL.

References

1. Kolmogorov AN. Dissipation of energy in locally isotropic turbulence. Dokl. Akad. Nauk SSSR. 1941; 32: 16–18.
2. Obukhov AM. Spectral energy distribution in a turbulent flow. Dokl. Akad. Nauk SSSR. 1941; 32(1): 22–24.
3. Obukhov AM. Structure of the temperature field in a turbulent flow. Izv. Acad. Nauk SSSR Ser. Geog. Geofiz. 1949; 13: 58–69.
4. Corrsin S. On the spectrum of isotropic temperature fluctuations in an isotropic turbulence. J. Appl. Phys. 1951; 22(4): 469–473. doi: [10.1063/1.1699986](https://doi.org/10.1063/1.1699986)
5. Frisch U. Turbulence: the legacy of AN Kolmogorov. Cambridge University Press; 1995.
6. Obukhov AM. Some specific features of atmospheric turbulence. J. Fluid Mech. 1962; 13: 77–81. doi: [10.1017/S0022112062000506](https://doi.org/10.1017/S0022112062000506)

7. Kolmogorov AN. A refinement of previous hypotheses concerning the local structure of turbulence in a viscous incompressible fluid at high Reynolds number. *J. Fluid Mech.* 1962; 13: 82–85. doi: [10.1017/S0022112062000518](https://doi.org/10.1017/S0022112062000518)
8. Lovejoy S, Schertzer D. *The weather and climate: emergent laws and multifractal cascades.* Cambridge University Press; 2013.
9. Schmitt F, Schertzer D, Lovejoy S, Brunet Y. Multifractal temperature and flux of temperature variance in fully developed turbulence. *Europhys. Lett.* 1996; 34(3): 195–200. doi: [10.1209/epl/i1996-00438-4](https://doi.org/10.1209/epl/i1996-00438-4)
10. Turiel A, Grazzini J, Yahia H. Multiscale techniques for the detection of precipitation using thermal IR satellite images. *IEEE Geosci. Remote Sens. Lett.* 2005; 2(4): 447–450. doi: [10.1109/LGRS.2005.852712](https://doi.org/10.1109/LGRS.2005.852712)
11. Turiel A, Nieves V, García-Ladona E, Font J, Rio MH, Larnicol G. The multifractal structure of satellite sea surface temperature maps can be used to obtain global maps of streamlines. *Ocean Sci.* 2009; 5(4): 447–460. doi: [10.5194/os-5-447-2009](https://doi.org/10.5194/os-5-447-2009)
12. Nieves V, Llebot C, Turiel A, Sole J, Garcia-Ladona E, Estrada M, et al. Common turbulent signature in sea surface temperature and chlorophyll maps. *Geophys. Res. Lett.* 2007; 34(23). doi: [10.1029/2007GL030823](https://doi.org/10.1029/2007GL030823)
13. Yahia H, Turiel A, Chrysoulakis N, Grazzini J, Prastacos P, Herlin I. Application of the multifractal micro-canonical formalism to the detection of fire plumes in NOAA-AVHRR data. *Int. J. Remote Sens.* 2008; 29(14): 4189–4205. doi: [10.1080/01431160701840174](https://doi.org/10.1080/01431160701840174)
14. Montera LD, Jouini M, Verrier S, Thiria S, Crépon M. Multifractal analysis of oceanic chlorophyll maps remotely sensed from space. *Ocean Sci.* 2011; 7(2): 219–229. doi: [10.5194/os-7-219-2011](https://doi.org/10.5194/os-7-219-2011)
15. Lovejoy S, Schertzer D, Tessier Y, Gaonac'h H. Multifractals and resolution-independent remote sensing algorithms: the example of ocean colour. *Int. J. Remote Sens.* 2001; 22(7): 1191–1234. doi: [10.1080/01431160151144314](https://doi.org/10.1080/01431160151144314)
16. Frisch U, Sulem PL, Nelkin M. A simple dynamical model of intermittent fully developed turbulence. *J. Fluid Mech.* 1978; 87(4): 719–736. doi: [10.1017/S0022112078001846](https://doi.org/10.1017/S0022112078001846)
17. Mandelbrot BB. Intermittent turbulence in self-similar cascades: divergence of high moments and dimension of the carrier. *J. Fluid Mech.* 1974; 62(2): 331–358. doi: [10.1017/S0022112074000711](https://doi.org/10.1017/S0022112074000711)
18. Novikov EA, Stewart RW. The intermittency of turbulence and the spectrum of energy dissipation fluctuations. *Izv. Geophys. Ser.* 1964; 3: 408–413.
19. Schertzer D, Lovejoy S. Hard and soft multifractal processes. *Phys. A-Statistical Mechanics and its Applications.* 1992; 185(1): 187–194. doi: [10.1016/0378-4371\(92\)90455-Y](https://doi.org/10.1016/0378-4371(92)90455-Y)
20. Kolmogorov AN. The Wiener spiral and some other interesting curves in Hilbert space. *Dokl. Akad. Nauk SSSR.* 1940; 26(2): 115–118.
21. Mandelbrot BB, Van Ness JW. *Fractional Brownian Motions, Fractional Noises and Applications.* SIAM Rev. 1968; 10: 422–437. doi: [10.1137/1010093](https://doi.org/10.1137/1010093)
22. Kamont A. *On the Fractional Anisotropic Wiener Fields.* *J. Probab. Math. Statist.* 1996; 16(1): 85–98.
23. Barriere, O. *Synthese et estimation de mouvements Browniens multifractionnaires et autres processus a regularite prescrite. Definition du processus autoregule multifractionnaire et applications,* Doctoral dissertation, Univ. Nantes. 2007.
24. Nicolis O, Ramirez-Cobo P, Vidakovic B. 2D wavelet-based spectra with applications. *Comput. Stat. Data Anal.* 2011; 55(1): 738–751. doi: [10.1016/j.csda.2010.06.020](https://doi.org/10.1016/j.csda.2010.06.020)
25. Schertzer D, Lovejoy S, Schmitt F, Chigirinskaya Y, Marsan D. Multifractal cascade dynamics and turbulent intermittency. *Fractals.* 1997; 5(03): 427–471. doi: [10.1142/S0218348X97000371](https://doi.org/10.1142/S0218348X97000371)
26. Schertzer D, Lovejoy S. *Nonlinear variability in geophysics: multifractal simulations and analysis.* In: *Fractals Physical Origin and Properties,* edited by Pietronero L.. Springer; 1989. pp. 49–79.
27. O'Reilly JE, Maritorena S, Seigel DA, O'Brien MC, Toole D, Mitchell BC et al. Ocean color chlorophyll a algorithms for SeaWiFS, OC2, and OC4: Version 4. *SeaWiFS postlaunch calibration and validation analyses,* 2000; 3: 9–23.
28. Seuront L, Schmitt F, Lagadeuc Y, Schertzer D, Lovejoy S, Frontier S. Multifractal structure of phytoplankton biomass and temperature in the ocean. *Geophys. Res. Lett.* 1996; 23: 3591–3594. doi: [10.1029/96GL03473](https://doi.org/10.1029/96GL03473)
29. Lovejoy S, Currie WJS, Tessier Y, Claereboudt MR, Bourget E, Roff JC, et al. Universal multifractals and ocean patchiness: phytoplankton, physical fields and coastal heterogeneity. *J. Plankton Res.* 2001; 23(2): 117–141. doi: [10.1093/plankt/23.2.117](https://doi.org/10.1093/plankt/23.2.117)

30. Verrier S, Crépon M, Thiria S. Scaling and stochastic cascade properties of NEMO oceanic simulations and their potential value for GCM evaluation and downscaling. *J. Geophys. Res. Oceans.* 2014; 119 (9): 6444–6460. doi: [10.1002/2014JC009811](https://doi.org/10.1002/2014JC009811)
31. Seuront L, Schmitt F, Schertzer D, Lagadeuc Y, Lovejoy S. Multifractal intermittency of Eulerian and Lagrangian turbulence of ocean temperature and plankton fields. *Nonlinear Process. Geophys.* 1996; 3: 236–246. doi: [10.5194/npg-3-236-1996](https://doi.org/10.5194/npg-3-236-1996)
32. Seuront L, Schmitt F, Lagadeuc Y, Schertzer D, Lovejoy S. Multifractal analysis as a tool to characterize multiscale inhomogeneous patterns. Example of phytoplankton distribution in turbulent coastal waters. *J. Plankton Res.* 1999; 21: 877–922. doi: [10.1093/plankt/21.5.877](https://doi.org/10.1093/plankt/21.5.877)

Appendix C: Submitted paper

Manuscript prepared for Nonlin. Processes Geophys.
with version 2015/04/24 7.83 Copernicus papers of the L^AT_EX class copernicus.cls.
Date: 21 May 2015

Intermittent particle dynamics in marine coastal waters

P. R. Renosh¹, F. G. Schmitt^{2*}, and H. Loisel³

¹University of Lille, UMR 8187, Laboratory of Oceanology and Geosciences, 28 Avenue Foch, 62930 Wimereux, France

²CNRS, UMR 8187, Laboratory of Oceanology and Geosciences, 28 Avenue Foch, 62930 Wimereux, France

³ULCO, UMR 8187, Laboratory of Oceanology and Geosciences, 32 Avenue Foch, 62930 Wimereux, France

Correspondence to:

F. G. Schmitt*

(francois.schmitt@cnrs.fr)

P. R. Renosh

(pr.renosh@gmail.com)

Abstract. Marine coastal processes are highly variable over different space and time scales. In this paper we analyse the intermittency properties of particle size distribution (PSD) recorded every second using a LISST instrument (Laser In-Situ Scattering and Transmissometry). The particle concentrations have been recorded over 32 size classes from 2.5 to 500 μm , at 1 Hz resolution. Such information is used to estimate at each time step the hyperbolic slope of the particle size distribution, and to consider its dynamics. Shannon entropy, as an indicator of the randomness, is estimated at each time step and its dynamics is analysed. Furthermore, particles are separated into four classes according to their size, and the intermittent properties of these classes are considered. The empirical mode decomposition (EMD) is used, associated with arbitrary order Hilbert spectral analysis (AHSA), in order to retrieve scaling multi-fractal moment functions, for scales from 10 *sec* to 8 minutes. The intermittent properties of two other indicators of particle concentration are also considered on the same range of scales: the total volume concentration $C_{vol-total}$ and the particulate beam attenuation coefficient $c_p(670)$. Both show quite similar intermittent dynamics and are characterized by the same exponents. Globally we find here negative Hurst exponents for each time series considered, and nonlinear moment functions.

1 Introduction

Ocean data fields show a high variability over many different time and space scales. Such variability is often associated with turbulence, and multi-scaling properties of oceanic fields have been reported and studied in many previous studies: sea state (Kerman, 1993); phytoplankton concentration (Seuront et al., 1996a, b, 1999; Lovejoy et al., 2001a); rainfall and cloud radiance (Tessier et al., 1993;

Lovejoy and Schertzer, 2006); satellite images of ocean colour, chlorophyll-a and sea surface temperature (Lovejoy et al., 2001b; Nieves et al., 2007; Pottier et al., 2008; Turiel et al., 2009; Montera et al., 2011; Renosh et al., 2015). Here we focus on coastal waters and consider particles transported by oceanic currents in this highly energetic medium (Svendsen, 1987; Schmitt et al., 2009). The solid phases in the environment has been described by hyperbolic particle size distributions (PSD) of clay aggregates in water (Amal et al., 1990), biological aggregate and marine snow (Jiang and Logan, 1991; Logan and Wilkinson, 1991), aerosol agglomerates (Wu and Friedlander, 1993) and flocs produced in the water and waste water discharge (Li and Ganczarzyk, 1989).

PSD has major influence in biological, physical and chemical processes in the aquatic environment (Boss et al., 2001; Twardowski et al., 2001; Reynolds et al., 2010). For instance, PSD is strongly involved in the trophic interaction within the plankton community and in the chemical/geological aspects. The shape of the PSD is also uses in computing the sinking rate of the sediment fluxes. The study carried out by Renosh et al. (2014) using the same in situ data set than the present study showed that the dynamics of the PSD is controlled by many oceanographic parameters like tidal currents, waves and turbulence. The present study is a continuation of this work.

All environmental and geophysical data sets are nonlinear and non-stationary at many different scales of time and space. Intermittency is a property that occurs in fully developed turbulence ranging between the large scale injection and the small scale dissipation (Frisch, 1995; Pope, 2000). The main objective of this study is to analyse the intermittency properties of particle size distribution (PSD). In this study we mainly focus on the dynamics of the PSD along with the velocity data. For that we decomposed the PSD into different size classes and also derived the Shannon entropy from the probability density function (PDF) of the PSD.

Empirical Mode of Decomposition (EMD) together with Hilbert spectral analysis (HSA) is a well-known time-frequency analysis method for non-stationary and nonlinear time series (Huang et al., 1998, 1999). Such analysis is done in two parts: the EMD is an algorithm to decompose a time series into a sum of mono-chromatic modes, and HSA extends for each mode into characteristic amplitude and frequency. Hence this method is a time-amplitude-frequency analysis, which is recalled in appendices A and B. This approach can be generalised to extract intermittency exponents (Huang et al., 2008, 2011). This is presented in Appendix C.

The first part of the paper present the study area and in-situ data, which contains the separation of different size classes and the hyperbolic shape shape of the PSD. Intermittency analysis using the EMD-AHSA method (presented in the appendices) are then provided in the next section followed by the conclusion.

2 In-situ data

55 The measurements were conducted above (50 cm) from the bottom of coastal waters of the eastern English Channel at a fixed station (50°45.676 N, 01°35.117 E) from the 25-28 of June 2012 (Figure 1).

Figure 1

We consider here simultaneous measurements of velocity and particle concentrations. The in-situ
60 sampling of Laser In-Situ Scattering and Transmissometry (LISST 100x type C) has been carried out at 1.0 Hz. The main part of the instrument is a collimated laser diode and a specially constructed annular ring detector. The primary information collected by the LISST is the scattering of the laser at 32 angles, which are converted into size distribution using an inverting method. The size distribution is presented as volume concentration with units of micro-litres per litre ($\mu\text{l.l}^{-1}$). The LISST
65 measures the volume concentration $C_{vol,i}$ of particles having diameters ranging from 2.5 to 500 μm in 32 size classes in logarithmic scale (Agrawal and Pottsmith, 2000). Because of instability in the smallest and largest size classes, the data recorded in the inner and outer rings are excluded from further analysis (Traykovski et al., 1999; Jouon et al., 2008; Neukermans et al., 2012). The LISST also records the beam attenuation (c) at 670 nm ($\pm 0.1\text{nm}$) over a 5 cm path length with an acceptance
70 angle of 0.0135° . The particulate attenuation coefficient c_p has been derived from c after calibration with MilliQ water before and after the field campaign, using the assumption that chromophoric dissolved organic matter (CDOM) does not absorb the light at 670 nm. $c_p(670)$ is an important parameter which has a direct link to the suspended particulate matter (SPM) of the water body (Boss et al., 2009; Neukermans et al., 2012). Simultaneously, velocity time series are measured using a
75 Nortek Vector ADV current meter fixed on the same platform along with the LISST at 0.5 m above the sea bottom. The ADV measured the North, East and Up components of velocity components with an accuracy of $\pm 0.5\%$.

2.1 Separation into size classes

The volume concentration distributed of a particle size class can also be expressed as the concentra-
80 tion $C_{vol}(\sigma)$ per unit volume per unit bin width (Jouon et al., 2008):

$$C_{vol}(\sigma) = \frac{C_{vol,i}}{\sigma_{\max}(i) - \sigma_{\min}(i)} \quad (1)$$

where σ is the median diameter of the particle size class i , $\sigma_{\max}(i)$ and $\sigma_{\min}(i)$ are respectively the maximum and minimum particle size of the class i . This resulting volumetric PSD is expressed in

$\mu l.l^{-1}.\mu m^{-1}$. The total volume concentration of the PSD ($C_{vol-total}$) has been derived at each time
85 step:

$$C_{vol-total}(t) = \sum_{i=6}^{31} C_{vol,i}(t) \quad (2)$$

This quantity gives the total volume of the particles in $\mu l/l$. For the present study we deal with
4 different size classes, using the following classification: Silt/Clay ($\sigma < 30\mu m$), Fine ($30 < \sigma$
 $< 105\mu m$), Coarse/Micro ($105 < \sigma < 300\mu m$) and Macro flocs/particles ($\sigma > 300\mu m$) (Lefebvre
90 et al., 2012; Renosh et al., 2014). Figure 2 shows the time series of normalized volume concentrations
(VC) of different size classes of PSD. All 4 size classes are showing large temporal fluctuations in
their magnitude. Their statistical and dynamical properties are considered below.

Figure 2

2.2 PSD slope (ξ)

95 The particle size distribution in the ocean, which describes the particle concentration as a function
of particle size/number, typically shows a rapid decrease in concentration with increasing size from
a sub-micrometer range to hundreds of micrometers. This feature is common to all the suspended
particles and also for plankton micro-organisms (Sheldon et al., 1972; McCave, 1983; Stramski and
Kiefer, 1991; Jackson et al., 1997). The number of particles for a given size σ is estimated by a
100 normalisation by their volume (Jouon et al., 2008). We obtain the number density $n(\sigma)$, which is
also the product of the probability density function of the size, $p(\sigma)$, times N , the total number of
particles:

$$n(\sigma) = Np(\sigma) = \frac{C_{vol}(\sigma)}{\frac{4}{3}\pi(\sigma/2)^3} \quad (3)$$

The PSD of this density number classically follows a power law distribution for aquatic particles in
105 suspension (Sheldon et al., 1972; Kitchen et al., 1982; Jonasz, 1983; Boss et al., 2001; Twardowski
et al., 2001; Loisel et al., 2006; Reynolds et al., 2010; Renosh et al., 2014):

$$n(\sigma) \sim K\sigma^{-\xi} \quad (4)$$

where K is a constant and $\xi > 0$ is the PSD hyperbolic slope. Since the LISST provides size class
information at each time step, the power-law distribution can be fitted at each time step, providing
110 the exponent as a time series $\xi(t)$. The ξ value provides information on the relative concentration
of small and large particles: the steeper the slope (the greater ξ), the more small particles relative
to large particles are present in the water (and vice versa). A small portion of 3000 samples of ξ is
shown in Figure 3A: large temporal fluctuations in its magnitude are visible. When considering all

size classes in all the time steps, a hyperbolic PDF is also obtained, represented in Figure 3B with a slope value of $\bar{\xi} = 2.9 \pm 0.16$.

Figure 3

The study carried out by Renosh et al. (2014) considered the dynamics of the $\xi(t)$ in relation with different hydrodynamic quantities like waves, tidal currents and turbulence. It showed that turbulence has a major role in the re-suspension of the particles in the aquatic environment. It also showed that along-shore (U) and cross-shore (V) components of velocity have power spectra showing different scaling regimes in low frequency and high frequency regions (Figure 4). At low frequency scale there is a typical Kolmogorov $-5/3$ slope and at high frequency a scaling regime with a 0.6 slope. For high frequencies there is a hump like structure, which can be identified as the high energy associated with surf zone wave breaking (Schmitt et al., 2009).

The study of Renosh et al. (2014) showed that the low frequency variability of $\xi(t)$ and $c_p(670)$ are controlled by turbulence and that the high frequency part is related to dynamical processes impacted by the sea bottom. The present study is a continuation of Renosh et al. (2014); it considers the high frequency scaling regimes and studies the intermittency of particle concentration in this range of scales.

3 Intermittent dynamics

3.1 Velocity intermittency

We first consider here the scaling and intermittency properties of the velocity. Figure 4A shows the Fourier and Hilbert (HSA) estimation of the U and V components of the velocity. Scaling range are found from 20 to 500 seconds with a slope of about -0.6. In this range of scales the AHSA method has been applied to characterise intermittency in a multi-fractal framework (see Appendix C for the AHSA method). First a negative Hurst exponent is found: $H_U = -0.26$ and $H_V = -0.24$. Such negative sign for H values indicates that small scales show larger fluctuations than the larger scales in a scaling way (Lovejoy and Schertzer, 2012). Both curves become quite different for larger moments: the U curve is more nonlinear, associated to larger intermittency (Figure 4B).

Figure 4

3.2 Dynamics of the entropy of particle size

The LISST system records at each time step a discretized PDF of the particle size. Hence it is possible to estimate at all time step the entropy of the particle size distribution as:

$$S(t) = - \sum_{i=6}^{31} P_i(t) \log P_i(t) \quad (5)$$

145 where $P_i(t) = n(\sigma_i(t))/N(t)$. The Shannon Entropy $S(t)$ is estimated at each time step; it possesses some variability with value centered around $\bar{S} = 1.59 \pm 0.03$. Figure 5A shows a sample of $S(t)$ and Figure 5B shows its PDF, which is centered around \bar{S} with values ranging mainly between 1.5 and 1.7. As a stochastic process, in order to consider the dynamics of $S(t)$, we plot in Figure 5C the autocorrelation of $S(t)$. A memory time of the entropy series can be estimated as:

$$150 \quad T = \int_0^{T_0} C_s(t) dt \quad (6)$$

where T_0 is the first time for which $C_s(t) = 0$; we find here $T_0 = 7826s$ and we compute $T = 2176s = 36.26min$. This characteristic time scale could be related to the transition scale (Figure 4A) between two scaling regimes of low frequency injection scale and high frequency wave breaking scale.

155 The entropy of particle sizes characterises the “disorder” of the size distribution, its information content. We showed here that the dynamics of such quantity can be considered by using LISST data. One of the very interesting feature of LISST measurements is hence to be able to characterise nonlinear classical indicators such as the Shannon entropy, in a dynamical way.

Figure 5

160 3.3 Intermittent dynamics of different size classes

As explained above, the PSD is decomposed into 4 different size classes of particles (Silt/Clay, Fine particles, Coarse/Micro particles and Macro particles/flocs). The power spectra of these 4 size classes have been derived using Fourier as well as Hilbert transform (Figure 6) for understanding the turbulent characteristics. Similar spectra are found from Fourier and Hilbert transform and there is a good power-law behaviour observed in the high frequency region (0.09Hz - 0.002Hz).

Figure 6

This scale range has been taken for the extraction of the scaling exponents. The scaling exponent function $\xi(q)$ has been extracted for all size classes using arbitrary order Hilbert spectral analysis (Appendix C). The exponent $\zeta(q) = \xi(q) - 1$ is computed. Nonlinear functions are visible for each size classes (Figure 7). The Hurst number $H = \zeta(1) = \xi(1) - 1$ is estimated for each classes: we find $H = -0.17; -0.19; -0.38; -0.26$ for increasing size classes. The high H values are observed in the larger size classes and low H values are observed in lower size classes. This parameter determines the rate at which mean fluctuations grow ($H > 0$) or decrease ($H < 0$) with the scale. We found negative H values in the present study. Negative H values have not been found in many studies. Recently in 175 Lovejoy and Schertzer (2012, 2013) it was argued that Haar wavelet analysis can be used to extract the H values with any sign for the exponent ($-1 < H < 1$). Such sign indicate that small scales show larger fluctuation than large scales. If $\zeta(q)$ is linear, the statistical behaviour is mono-scaling; if $\zeta(q)$ is nonlinear and concave/convex, the behaviour is defined as multi-scaling, corresponding

to a multi-fractal process. The concavity of this function is a characteristic of the intermittency: the more concave is the curve, the more intermittent is the process (Frisch, 1995; Schertzer et al., 1997; Vulpiani and Livi, 2003; Lovejoy and Schertzer, 2012). The slight curvature which is found here for all size classes (Figure 7) is hence a signature of intermittency in the particle dynamics.

Figure 7

3.4 Intermittent concentration dynamics

We perform here an analysis of intermittency of concentration dynamics considering two indicators of this particle concentration: $c_p(670)$ and total volume concentration ($C_{vol-total}$). At first order, $c_p(670)$ is driven by the suspended particulate matter (SPM). We observe here a large variability in the $c_p(670)$ data (Figure 8A). The total volume concentration of the PSD has been derived for each time step using equation 2. The derived $C_{vol-total}$ shows large fluctuation in its magnitude (Figure 8B). The turbulent power spectrum derived for these series shows 2 scaling regimes similar to the size classes (Figure 8C and 8D). A good scaling between 0.002Hz - 0.09Hz is observed (Figure 8C and 8D). Hence the region between 0.002 to 0.09 Hz (10 sec. to 8 min.) has been identified for the multi-scaling analysis. The structure function scaling moment function derived for this series shows a nonlinearity and concavity in its shape (Figure 8E). The H value derived for the $C_{vol-total}$ is slightly negative; $H = -0.08$. The scaling moment function of the $c_p(670)$ showed a nonlinearity in its behaviour showing its intermittent characteristics (Figure 8E). We find here $H = -0.06$ which is quite similar to $C_{vol-total}$. Globally, for power spectra as well as for their intermittency properties, both proxies of SPM show similar scaling properties. These two different indicators of particle concentrations show quite similar dynamics and statistical intermittent properties.

Figure 8

4 Conclusions

This work analysed the intermittency and scaling properties of particles using the AHSA method. The intermittent transport of particles in complex flows, like in coastal waters, is very important for the study of partition dynamics, erosion processes, ecosystem modelling, sediment transport and turbidity dynamics. Suspended particle dynamics in turbulent flows are complex; some studies showed preferential concentration (Eaton and Fessler, 1994; Squires and Eaton, 1991) and some other studies showed multifractal repartition according to the Stokes number (Bec, 2005; Yoshimoto and Goto, 2007). We thus expect here also, in the natural environment to find intermittent particle dynamics.

This work has analysed the intermittency and scaling properties of the PSD using different aspects. We have time series of normalized volume concentration of different size classes of PSD and Shannon entropy which have been derived from number density of PSD. Here we showed the in-

termittency of particles for different size classes. The $c_p(670)$, a proxy of the suspended sediment concentration, and the total volume concentration ($C_{vol-total}$) showed an intermittent and multiscaling properties in their dynamics.

Turbulent scaling of these parameters has been derived through both Fourier power spectra and spectra derived through HSA. The scaling moment function derived for $C_{vol-total}$ and $c_p(670)$ are showing similar nonlinear curve stressing the intermittency in their dynamics. The scaling moment functions derived for each size class of the particle are also nonlinear. The curvature of the spectrum for various size class shows the intermittency of the particles dynamics in different sizes.

We may note also that the Hurst exponent derived for the velocity components and the particle concentrations are negative. This negative sign indicates that small scales show larger fluctuations than large scales. We have here no theoretical interpretation to propose to these values, which could be related to the particular statistical characteristics of a bottom boundary layer flow.

This multi-scaling analysis has been tested only in the bottom of the highly dynamic coastal waters of the Eastern English channel. Such analysis is an illustration of the potential provided by LISST data, with many particle size classes recorded at each time steps. It may be applied to other time series in the open ocean, coastal waters and also fresh water situations, in order to provide comparison and help to look for universal properties.

230 **Appendix A: Empirical Mode of Decomposition (EMD)**

Hilbert Spectral Analysis (HSA) and Empirical Mode of Decomposition (EMD) have been introduced by Norden Huang and collaborators in the end of the 1990s (Huang et al., 1998) to locally extract amplitude and frequency information in a time series. It was mainly introduced for nonlinear and non-stationary time series. The first step of this approach is EMD. The objective of the EMD method is to decompose a signal into a series of modes. Each component is defined as an intrinsic mode function (IMF) satisfying the following conditions: (1) In the whole data set, the number of extrema and the number of zero crossings must either equal or differ at most by one. (2) The mean value of the envelope defined using the local maxima and the envelope defined using the local minima are zero (Huang et al., 1998; Huang and Wu, 2008). An iterative algorithm was proposed to extract successive IMF from time series. We do not reproduce all the details of this algorithm here and refer to original publications (Huang et al., 1998, 1999).

The decomposition process stops when the residue, r_n , becomes a monotonic function or a function with only one extrema from which no more IMF can be extracted. At the end of the decomposition, the original time series $x(t)$ is decomposed into a sum of n modes and a residue:

$$245 \quad x(t) = \sum_{j=1}^n c_j(t) + r_n(t) \quad (\text{A1})$$

where $c_j(t)$ are IMFs and $r_n(t)$ is the residue. In this decomposition, each mode has a decreasing characteristic frequency. If N is the number of points of the original series, we have: $n \approx \log_2(N)$, hence in general, $10 \leq n < 20$ (Flandrin and Goncalves, 2004; Huang et al., 2008).

Appendix B: Hilbert Spectral Analysis (HSA)

250 Hilbert Spectral Analysis (HSA) is the second step of the analysis, which is applied to each mode $c_j(t)$ extracted for the time series $x(t)$ using the procedure discussed in Appendix A. For any function $x(t)$, its Hilbert transform $y(t)$ is written as:

$$y(t) = H\{x\}(t) = \frac{1}{\pi} \int_{-\infty}^{+\infty} \frac{x(\tau)}{t - \tau} d\tau \quad (\text{B1})$$

The analytic function $z(t)$ estimated from $x(t)$ using the Hilbert transform $y(t)$:

$$255 \quad z(t) = x(t) + iy(t) = x(t) + iH\{x\}(t) \quad (\text{B2})$$

where $i = \sqrt{-1}$. The analytical function is estimated for each mode and at each time step. For each mode and each time step a local amplitude a and phase function θ can be estimated:

$$a(t) = (x^2 + y^2)^{1/2} \quad (\text{B3})$$

$$\theta(t) = \tan^{-1}(y/x) \quad (\text{B4})$$

260 The local frequency is estimated from the phase function:

$$\omega = \frac{d\theta}{dt} \quad (\text{B5})$$

The *HSA* represents a time-amplitude-frequency analysis. This helps to estimate a joint PDF $p(\omega, A)$ of frequency and amplitude. From this, a marginal spectrum is estimated:

$$h(\omega) = \int_0^{\infty} p(\omega, A) A^2 dA \quad (\text{B6})$$

265 This $h(\omega)$ spectral analysis is done through a Hilbert transform and can be compared to the Fourier spectrum $E(f)$ obtained through the classical Fourier analysis (Huang et al., 2008).

Appendix C: Arbitrary order Hilbert Spectral Analysis (AHSA)

The equation obtained in the previous section giving $h(\omega)$ is a second order statistical moment; it can be generalised into arbitrary order moment (Huang et al., 2008, 2011), by taking a moment of order q :

$$L_q(\omega) = \int_0^{\infty} p(\omega, A) A^q dA \quad (\text{C1})$$

where $q \geq 0$. In case of scale invariance we can write

$$L_q(\omega) \approx \omega^{-\xi(q)} \quad (\text{C2})$$

where $\xi(q)$ is the corresponding scaling exponent, which is related to the classical structure function by $\xi(q) = 1 + \zeta(q)$ (Huang et al., 2008). For example for a fractional Brownian motion $\xi(q) = 1 + qH$. Here we are interested by the ‘‘Hurst’’ exponent given by $H = \zeta(1) = \xi(1) - 1$. H can positive or negative and it characterises the degree of stationarity of the scaling process. The nonlinearity of $\zeta(q)$ is related to the intermittency of the time series: the more nonlinear the scaling exponent $\zeta(q)$, the more intermittent is the series (Schmitt and Huang, In press 2015).

Acknowledgements. Centre National d’Etudes Spatiales (CNES) and Centre National de la Recherche Scientifique (CNRS) are acknowledged for the funding of P.R. Renosh’s Ph.D. thesis. This study is performed in the frame of the COULCOT-2 project, funded by the CNES/TOSCA program.

References

- Agrawal, Y. and Pottsmith, H.: Instruments for particle size and settling velocity observations in sediment
285 transport, *Marine Geology*, 168, 89–114, 2000.
- Amal, R., Raper, J. A., and Waite, T. D.: Fractal structure of hematite aggregates, *Journal of Colloid and inter-
face Science*, 140, 158–168, 1990.
- Bec, J.: Multifractal concentrations of inertial particles in smooth random flows, *Journal of Fluid Mechanics*,
528, 255–277, 2005.
- 290 Boss, E., Pegau, W. S., Gardner, W. D., Zaneveld, J. R. V., Barnard, A. H., Twardowski, M. S., Chang, G., and
Dickey, T.: Spectral particulate attenuation and particle size distribution in the bottom boundary layer of a
continental shelf, *Journal of Geophysical Research: Oceans*, 106, 9509–9516, 2001.
- Boss, E., Slade, W., and Hill, P.: Effect of particulate aggregation in aquatic environments on the beam attenu-
ation and its utility as a proxy for particulate mass, *Optics Express*, 17, 9408–9420, 2009.
- 295 Eaton, J. K. and Fessler, J.: Preferential concentration of particles by turbulence, *International Journal of Mul-
tiphase Flow*, 20, 169–209, 1994.
- Flandrin, P. and Goncalves, P.: Empirical Mode Decompositions as Data Driven Wavelet-Like Expansions,
JWMIP, 2(4), 477–496, 2004.
- Frisch, U.: *Turbulence: the legacy of AN Kolmogorov*, Cambridge University Press, 1995.
- 300 Huang, N. E. and Wu, Z.: A review on Hilbert-Huang transform: Method and its applications to geophysical
studies, *Reviews of Geophysics*, 46, 2008.
- Huang, N. E., Shen, Z., Long, S. R., Wu, M. C., Shih, H. H., Zheng, Q., Yen, N.-C., Tung, C. C., and Liu, H. H.:
The empirical mode decomposition and the Hilbert spectrum for nonlinear and non-stationary time series
analysis, *Proceedings of the Royal Society of London A*, 454, 903–995, 1998.
- 305 Huang, N. E., Shen, Z., and Long, S. R.: A new view of nonlinear water waves: The Hilbert Spectrum 1, *Annual
Review of Fluid Mechanics*, 31, 417–457, 1999.
- Huang, Y., Schmitt, F. G., Lu, Z., and Liu, Y.: An amplitude-frequency study of turbulent scaling intermittency
using Empirical Mode Decomposition and Hilbert Spectral Analysis, *EPL*, 84, 40 010, 2008.
- Huang, Y., Schmitt, F. G., Hermand, J.-P., Gagne, Y., Lu, Z., and Liu, Y.: Arbitrary-order Hilbert spectral
310 analysis for time series possessing scaling statistics: Comparison study with detrended fluctuation analysis
and wavelet leaders, *Physical Review E*, 84, 016 208, 2011.
- Jackson, G. A., Maffione, R., Costello, D. K., Alldredge, A. L., Logan, B. E., and Dam, H. G.: Particle size spec-
tra between 1 mm and 1 cm at Monterey Bay determined using multiple instruments., *Deep-Sea Research I*,
44, 1739–1767, 1997.
- 315 Jiang, Q. and Logan, B. E.: Fractal dimensions of aggregates determined from steady-state size distributions,
Environmental Science & Technology, 25, 2031–2038, 1991.
- Jonasz, M.: Particle-size distributions in the Baltic, *Tellus B*, 35, 346–358, 1983.
- Jouon, A., Ouillon, S., Douillet, P., Lefebvre, J. P., Fernandez, J. M., Mari, X., and Froidefond, J.-M.: Spatio-
temporal variability in suspended particulate matter concentration and the role of aggregation on size distri-
320 bution in a coral reef lagoon, *Marine Geology*, 256, 36–48, 2008.
- Kerman, B. R.: A multifractal equivalent of the Beaufort scale for sea-state, *Geophysical Research Letters*, 20,
297–300, 1993.

- Kitchen, J., Zaneveld, J. R. V., and Pak, H.: Effect of particle size distribution and chlorophyll content on beam attenuation spectra, *Applied Optics*, 21, 3913–3918, 1982.
- 325 Lefebvre, J.-P., Ouillon, S., Vinh, V. D., Arfi, R., Panché, J.-Y., Mari, X., Van Thuoc, C., and Torrétton, J.-P.: Seasonal variability of cohesive sediment aggregation in the Bach Dang–Cam Estuary, Haiphong (Vietnam), *Geo-Marine Letters*, 32, 103–121, 2012.
- Li, D. H. and Ganczarzyk, J.: Fractal geometry of particle aggregates generated in water and wastewater treatment processes, *Environmental Science & Technology*, 23, 1385–1389, 1989.
- 330 Logan, B. E. and Wilkinson, D. B.: Fractal dimensions and porosities of *Zoogloea ramigera* and *Saccharomyces cerevisiae* aggregates, *Biotechnology and Bioengineering*, 38, 389–396, 1991.
- Loisel, H., Nicolas, J.-M., Sciandra, A., Stramski, D., and Poteau, A.: Spectral dependency of optical backscattering by marine particles from satellite remote sensing of the global ocean, *Journal of Geophysical Research: Oceans*, 111, C09 024, 2006.
- 335 Lovejoy, S. and Schertzer, D.: Multifractals, cloud radiances and rain, *Journal of Hydrology*, 322, 59–88, 2006.
- Lovejoy, S. and Schertzer, D.: Haar wavelets, fluctuations and structure functions: convenient choices for geophysics, *Nonlinear Processes in Geophysics*, 19, 513–527, 2012.
- Lovejoy, S. and Schertzer, D.: *The weather and climate: emergent laws and multifractal cascades*, Cambridge University Press, 2013.
- 340 Lovejoy, S., Currie, W., Tessier, Y., Claereboudt, M., Bourget, E., Roff, J., and Schertzer, D.: Universal multifractals and ocean patchiness: phytoplankton, physical fields and coastal heterogeneity, *Journal of Plankton Research*, 23, 117–141, 2001a.
- Lovejoy, S., Schertzer, D., Tessier, Y., and Gaonac’h, H.: Multifractals and resolution-independent remote sensing algorithms: the example of ocean colour, *International Journal of Remote Sensing*, 22, 1191–1234,
- 345 2001b.
- McCave, I. N.: Particulate size spectra, behavior, and origin of nepheloid layers over the Nova Scotian continental rise, *Journal of Geophysical Research*, 88, 7647–7666, 1983.
- Montera, L. d., Jouini, M., Verrier, S., Thiria, S., and Crépon, M.: Multifractal analysis of oceanic chlorophyll maps remotely sensed from space, *Ocean Science*, 7, 219–229, 2011.
- 350 Neukermans, G., Loisel, H., Mériaux, X., Astoreca, R., and McKee, D.: In situ variability of mass-specific beam attenuation and backscattering of marine particles with respect to particle size, density, and composition, *Limnology and Oceanography*, 57, 124–144, 2012.
- Nieves, V., Llebot, C., Turiel, A., Solé, J., García-Ladona, E., Estrada, M., and Blasco, D.: Common turbulent signature in sea surface temperature and chlorophyll maps, *Geophysical Research Letters*, 34, L23 602, 2007.
- 355 Pope, S. B.: *Turbulent flows*, Cambridge University Press, 2000.
- Pottier, C., Turiel, A., and Garçon, V.: Inferring missing data in satellite chlorophyll maps using turbulent cascading, *Remote Sensing of Environment*, 112, 4242–4260, 2008.
- Renosh, P. R., Schmitt, F. G., Loisel, H., Sentchev, A., and Mériaux, X.: High frequency variability of particle size distribution and its dependency on turbulence over the sea bottom during re-suspension processes,
- 360 *Continental Shelf Research*, 77, 51–60, 2014.
- Renosh, P. R., Schmitt, F. G., and Loisel, H.: Scaling analysis of ocean surface turbulent heterogeneities from satellite remote sensing: use of 2D structure functions., *PLoS ONE*, In press, 2015.

- Reynolds, R., Stramski, D., Wright, V., and Woźniak, S.: Measurements and characterization of particle size distributions in coastal waters, *Journal of Geophysical Research: Oceans*, 115, C08 024, 2010.
- 365 Schertzer, D., Lovejoy, S., Schmitt, F., Chigirinskaya, Y., and Marsan, D.: Multifractal cascade dynamics and turbulent intermittency, *Fractals*, 5, 427–471, 1997.
- Schmitt, F. G. and Huang, Y.: *Stochastic Analysis of Scaling Time Series: from turbulence theory to applications*, Cambridge University Press, In press 2015.
- Schmitt, F. G., Huang, Y., Lu, Z., Liu, Y., and Fernandez, N.: Analysis of velocity fluctuations and their inter-
- 370 mittency properties in the surf zone using empirical mode decomposition, *Journal of Marine Systems*, 77, 473–481, 2009.
- Seuront, L., Schmitt, F., Lagadeuc, Y., Schertzer, D., Lovejoy, S., and Frontier, S.: Multifractal analysis of phytoplankton biomass and temperature in the ocean, *Geophysical Research Letters*, 23, 3591–3594, 1996a.
- Seuront, L., Schmitt, F., Schertzer, D., Lagadeuc, Y., Lovejoy, S., et al.: Multifractal intermittency of Eulerian
- 375 and Lagrangian turbulence of ocean temperature and plankton fields, *Nonlinear processes in Geophysics*, 3, 236–246, 1996b.
- Seuront, L., Schmitt, F., Lagadeuc, Y., Schertzer, D., and Lovejoy, S.: Universal multifractal analysis as a tool to characterize multiscale intermittent patterns: example of phytoplankton distribution in turbulent coastal waters, *Journal of Plankton Research*, 21, 877–922, 1999.
- 380 Sheldon, R., Prakash, A., and Sutcliffe, W.: The size distribution of particles in the ocean, *Limnology and Oceanography*, 17, 327–340, 1972.
- Squires, K. D. and Eaton, J. K.: Preferential concentration of particles by turbulence, *Physics of Fluids A*, 3, 1169–1178, 1991.
- Stramski, D. and Kiefer, D. A.: The size distribution of particles in the ocean, *Progress in Oceanography*, 28,
- 385 343–383, 1991.
- Svendsen, I. A.: Analysis of surf zone turbulence, *Journal of Geophysical Research: Oceans*, 92, 5115–5124, 1987.
- Tessier, Y., Lovejoy, S., and Schertzer, D.: Universal multifractals: theory and observations for rain and clouds, *Journal of Applied Meteorology*, 32, 223–250, 1993.
- 390 Traykovski, P., Latter, R. J., and Irish, J. D.: A laboratory evaluation of the laser in situ scattering and transmission instrument using natural sediments, *Marine Geology*, 159, 355–367, 1999.
- Turiel, A., Nieves, V., García-Ladona, E., Font, J., Rio, M.-H., and Larnicol, G.: The multifractal structure of satellite sea surface temperature maps can be used to obtain global maps of streamlines, *Ocean Science*, 5, 447–460, 2009.
- 395 Twardowski, M. S., Boss, E., Macdonald, J. B., Pegau, W. S., Barnard, A. H., and Zaneveld, J. R. V.: A model for estimating bulk refractive index from the optical backscattering ratio and the implications for understanding particle composition in case I and case II waters, *Journal of Geophysical Research: Oceans*, 106, 14 129–14 142, 2001.
- Vulpiani, A. and Livi, R.: *The Kolmogorov legacy in physics*, Springer Science & Business Media, 2003.
- 400 Wu, M. K. and Friedlander, S. K.: Note on the power law equation for fractal-like aerosol agglomerates, *Journal of Colloid and interface Science*, 159, 246–248, 1993.

Yoshimoto, H. and Goto, S.: Self-similar clustering of inertial particles in homogeneous turbulence, *Journal of Fluid Mechanics*, 577, 275–286, 2007.

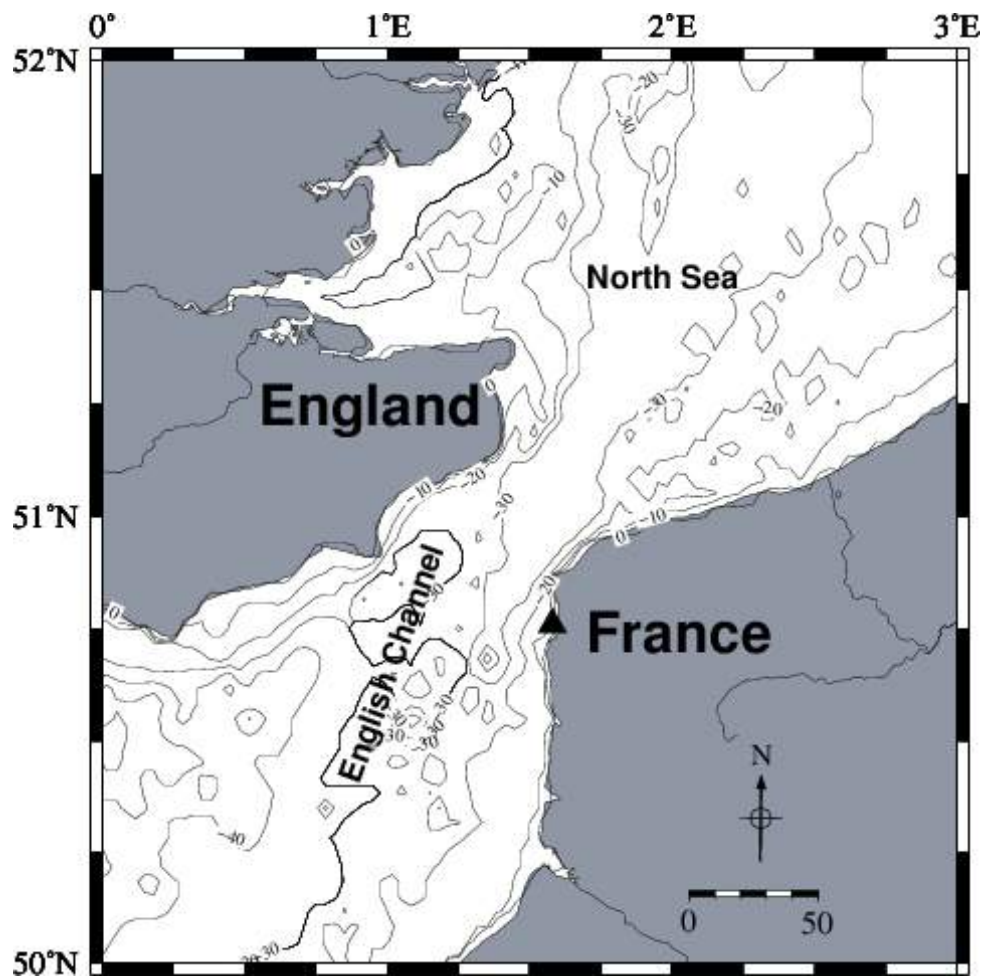


Figure 1. Location (black triangle) of the sampling station in the eastern English Channel together with the isobaths.

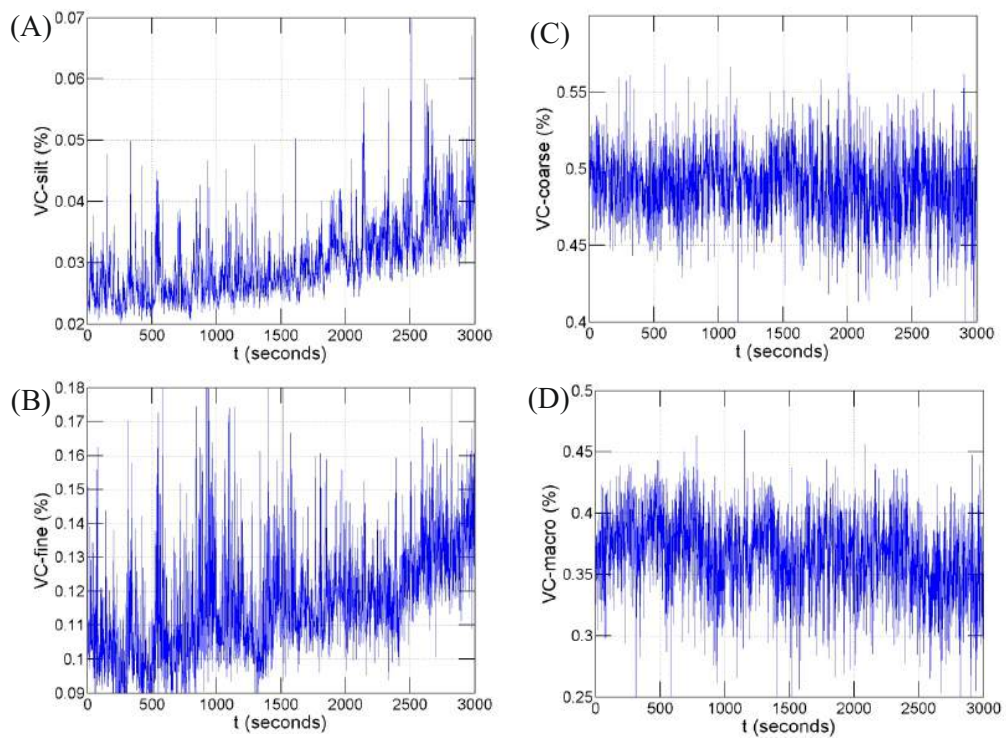


Figure 2. Time series of 3000 samples of volume concentrations of different size classes of *PSD*. (A) Silt/Clay, (B) Fine particles, (C) Coarse/Micro particles (D) Macro particles/flocs.

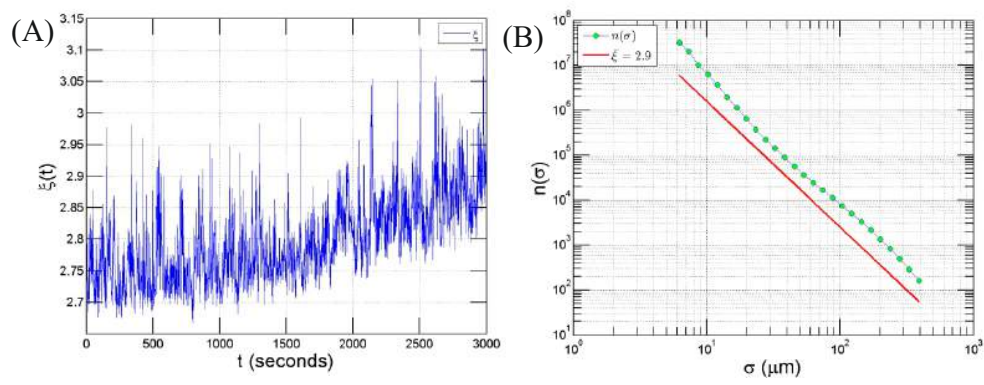


Figure 3. Time series of 3000 samples of PSD slope (ξ) (A) and PSD slope of the entire dataset with a power-law fit of slope $\bar{\xi} = 2.9 \pm 0.16$ (B).

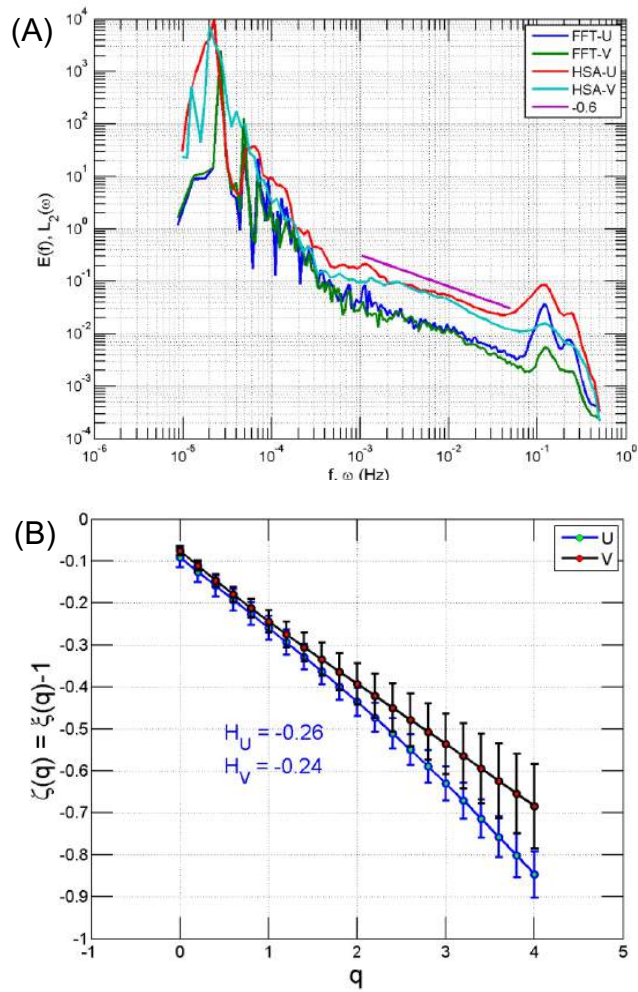


Figure 4. Turbulent power spectra of U and V components of velocity fields showing different scaling regimes same for both FFT and HSA (A). The scaling exponents estimated using the HSA method: the curve for U is more nonlinear than the one for V. The Hurst exponents H_U and H_V are negative (B).

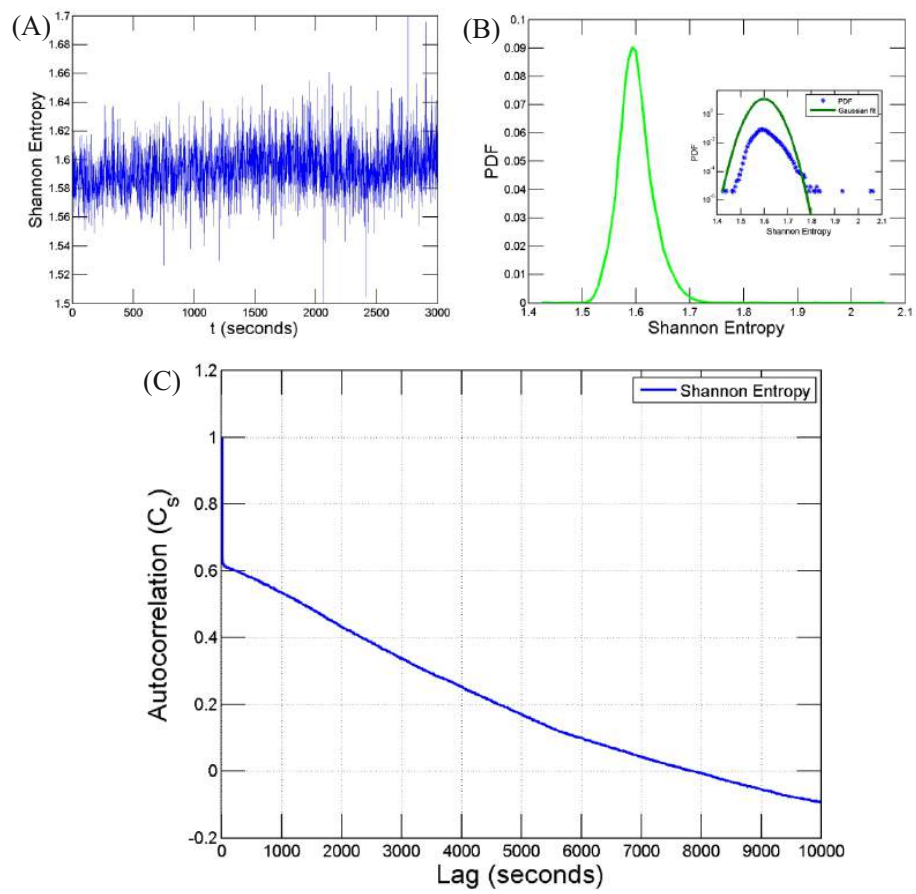


Figure 5. Time series of 3000 samples of Shannon entropy in (A), PDF of Shannon entropy along with a Gaussian fit in semilog plot (inset) in (B) and the Autocorrelation of Shannon entropy in (C).

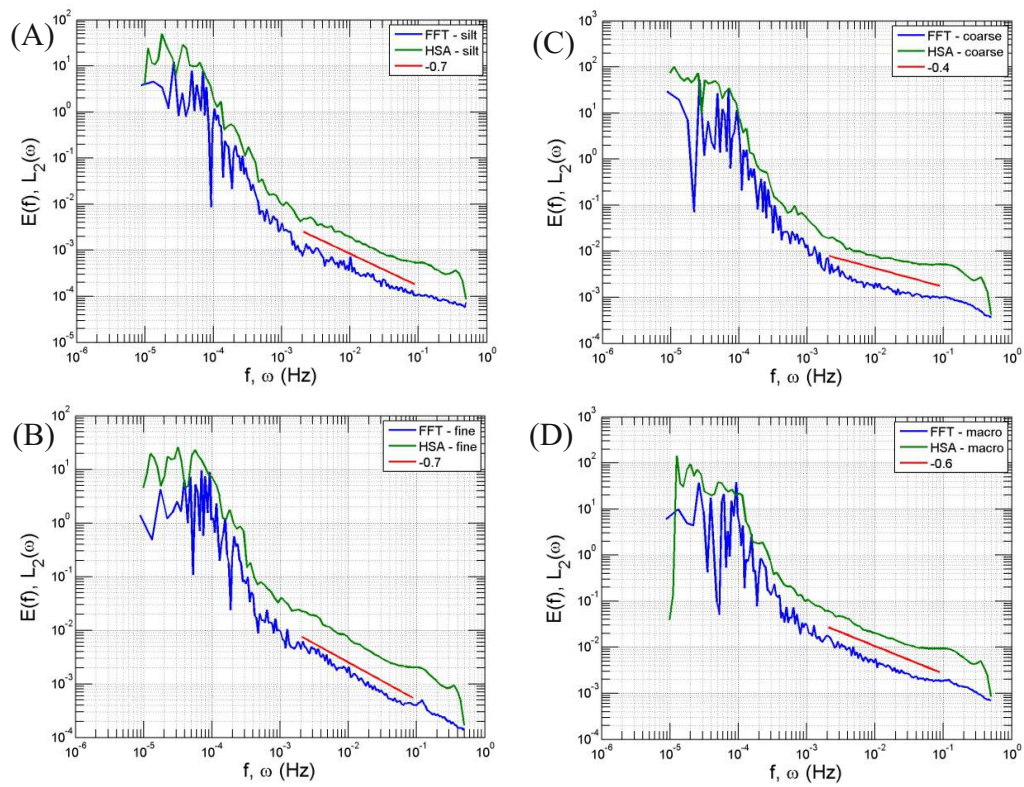


Figure 6. Power spectra for different size classes of PSD estimated for Fourier and Hilbert transform Silt/Clay (A), Fine (B), Coarse/Micro (C) and Macro particles/flocs (D). The red lines shows the scaling range and the slope of the best fit in this range.

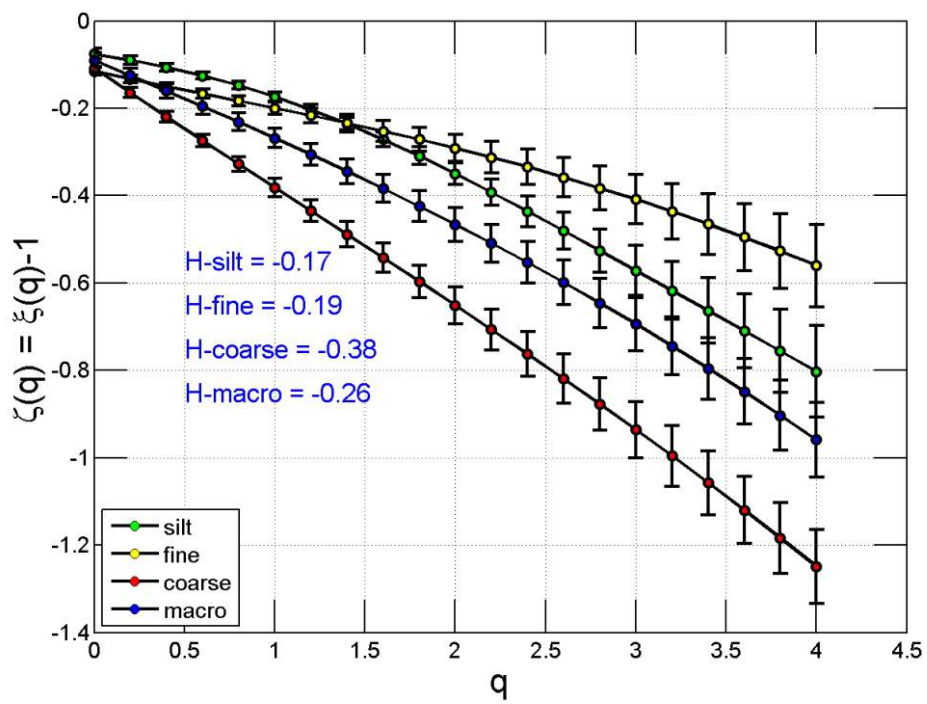


Figure 7. Scaling exponents $\zeta(q)$ estimated for different particle sizes, using the HSA method. In all cases the Hurst exponent is negative, with values between -0.17 and -0.38. The curves are all slightly nonlinear, sign of intermittency.

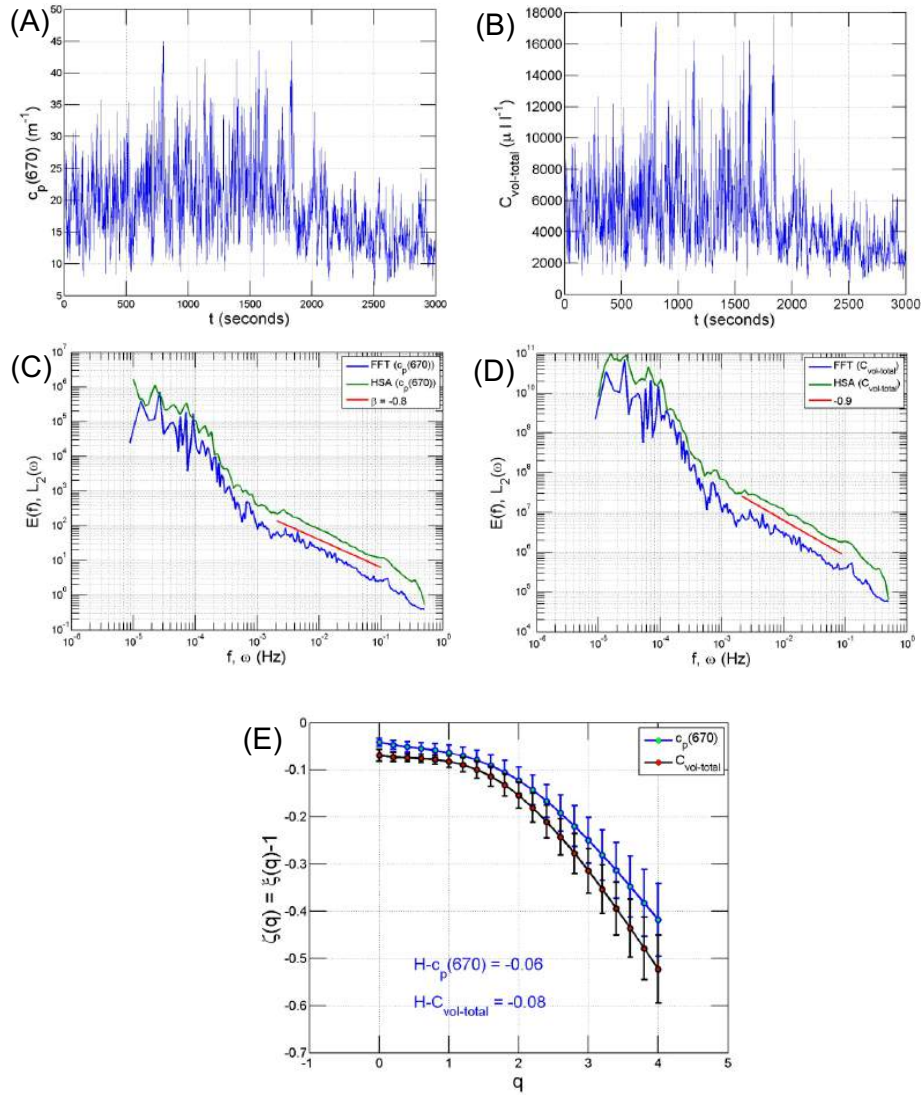


Figure 8. Time series of 3000 samples of $c_p(670)$ in (A), Time series of 3000 samples of $C_{vol-total}$ in (B), Turbulent power spectrum of $c_p(670)$ and turbulent power spectrum of $C_{vol-total}$ showing different scaling regimes (The scaling regime indicated as red is used for the scaling exponent computation) in (C and D) and scaling moment function of $c_p(670)$ and $C_{vol-total}$ in (E). The Hurst exponent values are very small but the curve is strongly nonlinear.